Luisa Tolle

Doktorarbeit in Physik
angefertigt im Physikalischen Institut

vorgelegt der
Mathematisch-Naturwissenschaftlichen Fakultät
der
Rheinischen Friedrich-Wilhelms-Universität
Bonn

Juli 2025

I hereby declare that this thesis was formulated by myself and that no sources or tools other than those cited were used.

Bonn, ...
Date Signature

1. Gutachterin: Prof. Dr. Corinna Kollath
2. Gutachter: Prof. Dr. Thierry Giamarchi

Steady state and dynamic properties of fermionic many-body systems coupled to a dissipative cavity

List of publications associated with this thesis

Fluctuation induced bistability of fermionic atoms coupled to a dissipative cavity
Luisa Tolle[1], Ameneh Sheikhan[1], Thierry Giamarchi[2], Corinna Kollath[1] and Catalin-Mihai Halati[2].
Phys. Rev. Lett., 134:133602, Mar 2025. [1]

Nonequilibrium dynamics of long-range interacting fermions
T. Zwettler[3], G. Del Pace[3], F. Marijanovic[4], S. Chattopadhyay[4,5], T. Bühler[3], L.Skolc[4], C.-M. Halati[2], **Luisa Tolle**[1], V. Helson[3], G. Bolognini[3], A. Fabre[3], S. Uchino[6], T. Giamarchi[2], E. Demler[4] and J. P. Brantut[3].
Phys. Rev. X, 15:021089, Jun 2025. [2]

Level statistics of the one-dimensional ionic hubbard model
Jeannette De Marco[1], **Luisa Tolle**[1], Catalin-Mihai Halati[2], Ameneh Sheikhan[1], Andreas M. Läuchli[3,7] and Corinna Kollath[1].
Phys. Rev. Res., 4:033119, Aug 2022. [3]

[1]Physikalisches Institut, University of Bonn, Nussallee 12, 53115 Bonn, Germany
[2]Department of Quantum Matter Physics, University of Geneva, Quai Ernest-Ansermet 24, 1211 Geneva, Switzerland
[3]Institute of Physics, Ecole Polytechnique Fédérale de Lausanne (EPFL), CH-1015 Lausanne, Switzerland
[4]Institute for Theoretical Physics, ETH Zürich, CH-8093 Zürich, Switzerland
[5]Lyman Laboratory, Department of Physics, Harvard University, Cambridge, Massachusetts 02138, USA
[6]Faculty of Science and Engineering, Waseda University, Tokyo 169-8555, Japan
[7]Laboratory for Theoretical and Computational Physics, Paul Scherrer Institute, CH-5232 Villigen, Switzerland

Abstract

Strongly correlated quantum many-body systems feature a competition of various energy scales as well as a large number of degrees of freedom. The interplay between them leads to a complex variety of quantum phases, while at the same time yielding the possibility to tune them through external perturbations. A way to gain control over the behavior of these quantum systems, is the engineering of couplings to an external bath. Controlling the dissipative coupling of the system to the environment while introducing a coherent drive allows to tailor quantum many-body phases of matter and light with some desired properties, an approach that has been applied to both ultracold atoms and solid state systems.

The system that is central to this work is a system of ultracold interacting fermionic atoms on an optical lattice that are globally coupled to a dissipative optical cavity mode. It features an intricate interplay of energy scales, among which are the atomic short-range interactions, a cavity mediated global interaction and the kinetic motion of the atoms. This results in complex quantum phases and self-ordering processes occurring in the system and makes it a perfect platform to study them.

This thesis approaches the many-body atom-cavity coupled system and the possible manifestation of non-trivial quantum phases in two main ways. On one hand, we investigate the steady state phase diagram using our method of many-body adiabatic elimination that goes beyond standard mean-field methods. By including fluctuations in the atoms-cavity coupling in our analytical model we are able to show their importance to determine the mixed state character of the self-ordering phase transition. We identify many-body processes within the self-ordered phase that strongly influence the physical nature of the steady states. Our method captures cavity cooling as well as many-body cooling resonances, as well as a novel mechanism, the fluctuation-induced bistability, that emerges from the excited eigenstate spectrum of the effective Hamiltonian. We provide arguments, that these phenomena can be generalized to a large class of atoms-cavity models with comparable atomic and photonic energy scales.

On the other hand, we investigate the dynamics across the self-ordering transition using newly developed numerically exact tensor-network based algorithms.

Acknowledgments

First of all, I want to thank Corinna Kollath and Thierry Giamarchi for offering welcoming me in their groups and giving me the opportunity to work with them. I am very grateful for their continued support, advice and encouragement during the last years. I learned a great amount from the many insightful and inspiring discussions that helped me for both this thesis and my future research endeavors. I know I grew a lot as a scientist under your supervision. All the members of both the Kollath group in Bonn and the Giamarchi group in Geneva made the time of my thesis a great experience and I was happy to interact and work with such amazing people. I will always think fondly of our joined breaks, evenings at the lake or hiking adventures. Of course I would like to thank everyone who helped me improve my thesis, Catalin-Mihai Halati, Ameneh Sheikhan, Simon Jaeger, Anne-Maria Visuri, Franco Lisandrini and Jeannette De Marco. I would like to especially express my gratitude to Catalin-Mihai Halati and Ameneh Sheikhan for their commitment to our joint projects and the time they took to answer my every question. Thank you so much for your help.

I would like to thank Ilona Vorobjova for her work and support in all administrative matters. Many thanks also to Oliver Freyermuth and Peter Wienemann for their help in getting my numerical simulations to run on the cluster. I would like to also thank the collaborators with whom I had the opportunity to work with across the projects I tackled in the last years, Jean-Philippe Brantut from EPFL Lausanne and Andreas Laeuchli from the Paul-Scherrer-Institute and EPFL.

I would like to thank all my friends for their support in the last few years and for providing me with alternatives to working on my thesis, in order to make the most of my "non-physics" life in Bonn and Geneva. And last but certainly not least I want to thank my family, my parents and sister for always being reliable sources of encouragement and support. I'm truly grateful to have all of you in my life.

Contents

Chapter 1

Introduction

In recent years, many fascinating discoveries were made in the research of non-equilibrium properties of a multitude of quantum systems, both in complex solid state and ultracold atom systems. A perfect platform to probe the non-equilibrium physics and emerging phenomena is the class of open systems that couple to an external environment with many degrees of freedom via dissipation. An asset of these systems is the introduced attractor dynamics that lead to an exponentially fast decay of the dynamics towards the steady state. Controlling the interplay between driving and dissipation in the system can thus allow to access quantum states with sought-out properties [4], which generates a platform for quantum simulations [5–7]. By manipulating the exchanges between a system and its environment, reservoir-engineering techniques allow to realize previously inaccessible quantum phases of matter and stabilize phases without an equilibrium counterpart.

For years, the regime of strong coupling of quantum matter and quantum light has been explored on a variety of platforms. These range from atomic Bose gases or fermionic ensembles coupled to a dissipative cavity [8–10] to electronic systems coupled to THz cavities [11–13]. For atomic systems some experimentally as well as theoretically investigated examples systems where the bosonic atoms are three-dimensional Bose-Einstein Condensates [14–20], or confined to an external optical lattice structure [9, 21–23]. The external lattice enables tuning of the atoms interaction strength over a wide parameter range and leads to an emerging band structure. More recently, there have been advances in the realization of ultra-cold fermionic gases coupled to a cavity field [24–28]. The cavity setups permit to access the strong coupling regime and gain precise control over the collective matter-light coupling.

For these light matter coupled setups the formation of self-organized density patterns has been theoretically predicted and observed when tuning the coupling across the Dicke superradiant transition. Some work has previously been done on various models that feature atoms in a cavity transversally driven by a laser field [29–32]. The atomic ensemble can spontaneously form spatially ordered structures such as checkerboard patterns. This occurs when the laser intensity exceeds a threshold value and results from the mechanical forces on the atoms associated with superradiant scattering into the cavity mode. This was confirmed by experiments on thermal clouds as well as Bose-Einstein Condensates [33, 34] and atoms on an underlying optical lattice [21]. An equivalence to the superradiant transition in an effective Dicke-model has since been stated [35–38]. This opens up many possibilities to investigate out-of-equilibrium and strongly correlated light-matter effects. This includes driven-dissipative phase transitions [39, 40] and Mott insulator transitions in self-organized lattices [41]. Further effects like emerging topological phases [42] or the engineering of tunable range interactions in multi-mode cavities also have been investigated [16].

In the past years theoretical studies for involving fermionic atomic subsystems have predominantly focused on either the properties of the self-ordering phase transition with both longitudinal and transversal pumping [43–50], aspects of the non-equilibrium dynamics [51, 52], super-fluid pairing [53, 54] or topological effects that can occur in this class of system [42, 55–59]. Further, a point of interest has been the possibility of stabilizing various exotic states of matter via the attractor dynamics [60–68], and synthetic gauge fields [69] or the emergence of skin effects [70]. Most of the theoretical approaches to the light-matter coupled systems rely on a decoupling

of the atomic degrees of freedom from the photonic sector and subsequent adiabatic elimination of the cavity field [45, 46, 49, 71, 72]. So far, not many theoretical methods exist that allow to treat ensembles of interacting particles globally coupled to a dissipative bosonic field on a level beyond this mean field approximation. Therefore, it is of high interest to develop methods that are able to describe the competing long and short-range interaction present in the system under consideration of fluctuation effects and to investigate how they can explain the new phases that were observed in experiments. Here, concerning the steady state quantum phases, we want to focus on effects like multi-stable behavior and cooling effects.

Cavity cooling is an important process in the preparation of ultracold atomic systems and relies on the broadening of the spectrum of the light scattered by a moving particle relative to the incident light. It contains both lower- and higher-frequency components, corresponding to an increase or decrease of the particle's kinetic energy, respectively. By tuning the cavity to higher frequencies, it is possible to efficiently cool an atomic system via light scattering into the cavity [73]. This was confirmed by theoretical works and seminal experiments, which demonstrated cavity cooling of single atoms [74] as well as the center-of-mass mode of an atomic ensemble [75] or many non-interacting atoms [76]. Efficient cavity-assisted laser cooling of an atomic ensemble [77–80] utilizes the decay of an optical resonator instead of atomic spontaneous emission for energy dissipation. It is based on the preferential coherent emission of laser photons into an optical cavity. However, cooling resonances in the context of interacting atomic systems remain mostly unexplored. We investigate those many-body cooling processes that play a crucial role in the emergence of a fluctuation-induced bistability.

The emergence of a bistability or multistability is a fascinating effect often occurring in nature. Systems that can reach several stable states are often seen in nature and are explored in many scientific fields such as chemistry, biology, engineering, or physics. Which state the system evolves towards might be influenced by the previous dynamics, the preparation of the initial state or other. Since presence of a bistability can induce a high sensitivity of the system dynamics to the initial conditions and external perturbations, it can yield profound implications for the overall behavior of the system. In physics, a very well-known bistability is the optical bistability [81], where two stable states that are characterized by different light intensities emerge. This is typically caused by nonlinear effects, for example in a cavity containing a nonlinear optical medium with a refractive index depending on the light intensity. For fermionic atoms in optical cavities an underlying non-linearity can also appear throughout the BEC-BCS crossover [24, 44] induced by the optomechanical interactions of the cold atomic gas coupled to an optical cavity field [78]. The influence of dissipation on the existence of bistabilities remains an important question. Bistable behaviors emerging in the vicinity of a dissipative phase transition are typically ascribed to the first order character of the transition [18, 40, 82–90], or to the spontaneous breaking of a weak-symmetry [14, 32, 78, 91–99]. If it behaves as a first order transition often a hysteresis behavior in the dynamics across the phase transition is observed. The transition point between the two competing phases depends on the initially prepared state and parameter protocol. But in most of these cases the bistability is only obtained within a mean-field approach. Considering quantum fluctuations around the mean-field solutions the competing bistable states resolve to meta-stable states [92, 100–102] that are admixed in the density matrix, leading to a unique steady state in the quantum dynamics. This is to be differentiated from multiple stable steady states observed within each symmetry sector in the presence of a strong symmetry of the dissipative system [103–106]. For instance, fluctuations don't always counteract bistability. There are cases where fluctuations have been shown to change the nature of a phase transition from second-order to a first-order character. This has been observed in equilibrium, for classical setups or systems that can be described by Ginzburg-Landau type theories such as superconductors, magnets or liquid crystals [107–111]. A coexistence of phases around the critical point is possible [112].

Beyond the unveiling of the steady state phase diagram, many intriguing phenomena can be expected in the real time dynamics of these atom-cavity coupled systems [52, 113]. Nevertheless, most theoretical and experimental research on these systems thus far focus on the description of steady states. While this, as we demonstrated above, yields many intriguing phenomena that warrant further investigation, the quantum time evolution of these complex systems also remains to be explored.

Theoretically, interacting many-body quantum systems that are isolated from their environment already pose a great challenge when aiming to resolve its quantum dynamics towards the steady state. The dimension of the Hilbert space associated with the many-body system grows at an exponential rate with the number of particles to be considered, since the quantum state of the system is generally in a superposition of all possible configurations at varying weights. Therefore, one quickly reaches the limit of exactly solvable system sizes. An analytical solution can only be found on few special cases, for more general approaches we need to develop efficient computational

methods that are able to give numerically exact results. A lot of effort has been put into the development of algorithms that simulate the numerically exact time evolution of complex quantum system [114–120] or search for their ground state [121–124] using tensor network methods. Various time evolution methods have been developed to treat closed quantum many body systems. The most prominent are the Trotter-Suzuki-algorithm [125, 126], that relies on an approximate decomposition of the time evolution operator into short-range terms, the Time Dependent Variational Principle (TDVP) [127–130] or time-dependent Density Matrix Renormalization Group (tDMRG) methods [115, 131].

When treating the time evolution of open quantum systems, more challenges arise. If they are described by Lindbladian dynamics, the dynamics is determined by the density matrix instead of state vectors. This results in an effectively squared Hilbert space dimension compared to the dimension of the original space. To overcome this challenge, some algorithms have been developed, such as the purification-algorithm [132–134]. Alternatively, the Lindbladian dynamics are imitated through stochastic unraveling of the Lindblad master equation using quantum trajectories. The evolution of the density matrix is modeled by means of Monte-Carlo averages over the time-evolution of many different trajectories in phase space [135–145]. The Monte-Carlo Wavefunction (MCWF) approach has been applied to a bosonic many-body system globally coupled to a dissipative cavity field [102]. The performance of both methods has been compared for short-range interacting systems [139, 145]. How these results hold up in systems that feature a long- or global range interaction remains to be explored and in this thesis we take first steps towards it.

The development of our newly constructed algorithm permits us to determine the evolution of local observables as well as correlation functions. We can then quantitatively characterize new evolution regimes and identify the processes governing the dynamics in large interacting open quantum systems. Especially the dynamics as the system transitions to the self-ordered phase that is predicted for the atoms-cavity coupled systems are of great interest. Further, this class of systems can exhibit persistent oscillations [104, 146, 147], that we also observe in the specific model we consider in this thesis.

In this work, we focus on the coupling of spinful fermions to a single mode of a transversely pumped dissipative cavity. An equivalent system with bosons was described and investigated beyond the mean field level using analytical and numerical methods in our group [102, 106, 148–151]. We want to provide multiple newly developed and applied methods that allow us to gain a broad understanding of the intricate steady state phase diagrams as well as out-of-equilibrium dynamics of such a driven dissipative many-body atomic system coupled to a cavity mode. We focus on the treatment of a spinful fermionic ensemble of atoms, though we occasionally extend our methods to bosons for comparative purposes and to provide arguments for the generality of the described phenomena beyond our specific model.

The outline of the thesis is as follows:

Chapter 2: We begin by providing an introduction to the model that is central to the here presented methods. Here we derive the system Hamiltonian in second quantization and corresponding Lindbladian differential equation that determines the dynamics of the full atoms-cavity coupled system towards its steady state.

Chapter 3: This is followed up by our newly developed analytical methods. Going beyond standard mean field methods our approach considers fluctuations in the coupling to the photonic mode [Sec. 3.1]. The fluctuations cause the system to thermalize towards steady states with a self-consistently determined effective temperature. The method is complemented by various limit considerations, notably a weak tunneling perturbation going to the thermodynamic limit [Sec. 3.2], that proves to be valid in a regime of the steady state phase diagrams that exhibits intriguing fluctuation-induced bistability at low fillings. Notably the results in this limit can be generalized for higher dimensions. The stability of the obtained solutions in the mean field approach is evaluated using a thermal stability condition that will be presented in Sec. 3.3. With this, we have a variety of analytical tools at hand that allow us to efficiently compute the steady state behavior of the effective driven dissipative atoms-cavity coupled system.

Chapter 4: We further want to present the newly developed quasi-exact numerical algorithms based on tensor network methods. They allow to perform an efficient real time evolution of the many-body fermionic system with global photon-mediated interactions on top of the short-range interactions between the different spin species. Further the Lindbladian dynamics that are introduced to the system by taking into account the dissipative nature of the cavity in the numerical simulations. We begin by introducing the basics of Matrix-product state methods,

including tensor-train decomposition, representation and application of operators. Then we go through the full algorithm, introducing the used methods at each step. These include time evolution with the Trotter-Suzuki-method or using the Time-Dependent-Variational principle as well as Purification or Monte-Carlo-Wavefunctions combined with stochastic sampling to evolve dissipative systems. We provide an analysis of the dependence of the numerical convergence of our results on various parameters for all of the previously presented methods [Sec. 4.3]. The validity of the obtained results is confirmed by comparing the measured observables from the independently implemented methods in various limits.

Chapter 5: Since our complex effective model takes the form of a ionic Hubbard model with self-consistently determined staggering in the lattice potential we first provide an overview on the standard ionic Hubbard model in order to facilitate the interpretation of the obtained result. We examine both the ground state phase diagrams at quarter and half-filling as well as the excitation spectra that contribute to the finite temperature steady states [Sec. 5.2], which will serve as a basis for the interpretation of the phases and physical processes observed in the effective model. Further, we present our work on the level statistics of the one-dimensional ionic Hubbard model Ref. [3] in Sec. 5.3. We analyze the energy level spacings in detail, demonstrating the breaking of the integrability, which is a property of the Fermi-Hubbard model, in the presence of a finite potential staggering. Special focus is put on the importance of considering symmetries of the Hamiltonian in the statistics to obtain reliable results. The chaotic nature of the ionic Hubbard Hamiltonian extends to our effective model capturing the atoms-cavity coupled system and supports our assumption of a thermal atomic steady state.

Chapter 6: In the light of all these analytical considerations, we present the obtained steady state results. We differentiate between the atomic densities of quarter filling [Sec. 6.1] and half (commensurate) filling [Sec. 6.2] that show fundamentally different behavior both at the self-ordering transition and within the self-ordered phase. Special focus is put on the discussion of the self-ordering transition [Sec. 6.1.1 & 6.2.1] where the atoms spontaneously order and a finite cavity field emerges. We contrast the physical properties of the steady states across the phase transition taking into account fluctuations in the coupling with the ground states obtained at the bare mean field level. Additionally analytical approximations for the critical coupling at which the self-ordering takes place are provided over a wider range of system parameters.
Within the self-ordered phase, we discuss the influence of atomic resonances on the obtained effective temperature of the steady state and find regimes where cavity cooling resonances allow for an efficient energy transfer from the atomic ensemble to the dissipative cavity mode. We further identify many-body cooling resonances that involve the interacting character of the fermionic system. Further a saturation in the cavity field observables deep in the self-ordered regime is observed. We provide the derivation of a universal scaled photon number in the large temperature limit.
Within the self-ordered regime at quarter filling, we identify a novel mechanism, a region where multiple stable steady state solutions appear. We call this *fluctuation-induced bistability* Ref. [1] since it relies on level-crossings in the excitation spectrum of the effective *dissipative quantum* model thus can not prevail at zero temperature. We identify this phenomenon in Sec. 6.3 for interacting spinful fermionic atoms confined to optical lattices and coupled to the field of a dissipative cavity and provide a detailed analysis concerning the generating processes, dependence on the system parameters and physical properties of the individual stable solutions. Our specific setup can serve a paradigmatic example of an open quantum system. In the strong atoms-cavity coupling regime two (multiple) self-organized steady state solutions are obtained, that are characterized by different effective self-consistently determined temperatures and cavity field order parameters. While the dominant (lowest energy) contribution remains the same in all solutions, the difference lies in the nature of the admixed excited states. More specifically, in the second steady solution associated with the stronger cavity field, excited states containing double occupancies become crucial. A many-body cooling mechanism emerges due to resonant photon-assisted transitions between states with and without double occupied sites. We are thus able to attribute the origin of the bi (multi)-stability to the interplay between the cavity-photon mediated *global-range* coupling and the *short-range* atomic interactions. In the weak hopping perturbation, where the fluctuation-induced bistability appears, its existence is independent of the dimensionality of the atomic gas or fermionic nature of the atoms. We therefore expect that the underlying mechanism exists in a large class of atoms-cavity models with equivalent competing photonic and atomic energy scales. The necessity of fluctuations around the mean-field solution is an astonishing property, since it is widely believed that mean-field methods remain valid for long-range couplings. This is differentiated from the bistable behavior at the self-ordering transition at commensurate filling in Sec. 6.2.1 that is connected to a level crossing in the ground state of the effective model. The discussion of the fluctuations induced bistability is complemented by equivalent results for a bosonic many-body system coupled to a dissipative cavity mode in Sec. 6.3.1. Here

we identify a similar behavior in the steady state within the self-ordered phase with a filling of on average one atom for every two lattice sites. The bistability repeats for higher numbers of the on-site occupations and therefore strengthens our arguments for the mechanism that causes the bistability to appear.

Chapter 7: After discussing the steady state results obtained using analytical mean field based methods, we proceed to show some real time results. As with the analytical methods we make the distinction between systems at quarter filling and half filling. To complement the numerical results, in Sec. 7.3 we show the time evolution as the coupling strength is ramped up to a final value within the self-ordered state at various speeds. In Ref. [2] this was investigated for a variety of experimental and theoretical models to determine a scaling law. Finally, we connect our analytical insights into the steady state phase diagrams in the framework of adiabatic elimination to the numerically obtained long-time results to provide a first step towards the interpretation of the steady state of the full Lindbladian model in Sec. 7.4. We focus here on the regime where the fluctuation-induced bistability was observed with the analytical ansatz and pinpoint how it manifests in the statistics of the Monte-Carlo trajectories.

The thesis is concluded in **Chapter 8**, where we summarize the main findings.

Chapter 2

Fermi gas on an optical lattice coupled to a dissipative cavity mode

Exploring the dynamics as well as steady states emerging from the coupling of interacting particles to a dissipative mode has attracted a lot of interest in recent years. One can expect numerous exciting phenomena to emerge in these systems due to an involved competition of various energy scales such as long- and short range interactions, external drive and dissipation. Examples of setups for this class of models that have been investigated both theoretically and experimentally are ultracold atomic gases interacting with a dissipative optical cavity mode [8–10] or equivalently gases of electrons coupled to a long-lived phonon mode [11, 12]. A schematic depiction of a general one dimensional system of interacting particles globally coupled to a bosonic field that exhibits dissipation is shown in Fig. 2.1.

Ultracold atoms coupled to the light-mode of optical cavities have proven to be a suitable platform to study various dissipative phenomena [78, 152], which is experimentally well-founded with systems of bosonic atoms placed in cavities. For these atomic systems three-dimensional Bose-Einstein condensates [14–20], as well as atoms confined to an underlying external optical lattice [9, 21–23] have been realized. More recently much effort has been made to realize a coupling between cold fermionic gases and a cavity field, which has thus far been realized by a few groups [24–28].

Generally, this class of systems undergo a *self-ordering* phase transition, transitioning from a so-called normal phase without occupation of the cavity mode to and a self-organized phase characterized by the emergence of a finite cavity field [78]. In the past years theoretical studies for involving fermionic atomic subsystems have predominantly focused on either the properties of the self-ordering phase transition [43, 45–50], aspects of the non-equilibrium dynamics [51, 52], super-fluid pairing [54] or topological effects that can occur in this class of system [42, 55–59]. Further, a point of interest has been the possibility of stabilizing various exotic states of matter via the attractor dynamics [60–68].

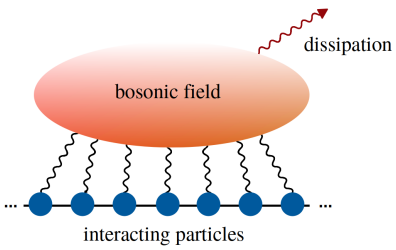

Fig. 2.1: Schematic depiction of a one dimensional system of interacting particles globally coupled to a dissipative bosonic quantum mode that mediates global all-to-all interactions between the particles.

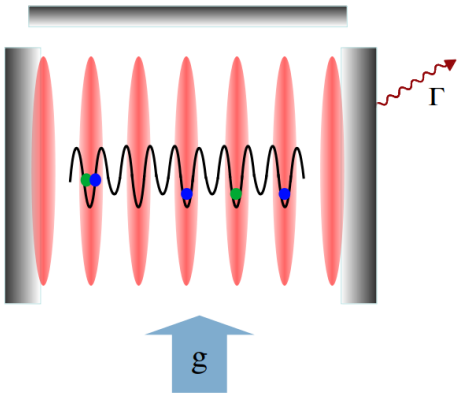

Fig. 2.2: Schematic depiction of the Fermi-Hubbard chain globally coupled to a single dissipative cavity mode. The spin $1/2$ atoms exhibit on-site-interactions of strength U and nearest neighbor hopping J. To globally couple them to the cavity mode the atoms are subjected to a transversal pump beam with amplitude g. Losses from the cavity field through the end mirrors is dissipative through photon losses through the mirrors with losses accounted for by the dissipation rate Γ.

The particular realization we investigate in this work is an ultracold quantum gas of interacting particles confined to an underlying external optical lattice that couples globally to a dissipative optical cavity mode [152]. This setup provides multiple intriguing possibilities to gain better understanding of light-matter interactions as well as out-of equilibrium processes. While the confinement to the external lattice allows for an externally tunable atom-atom interaction up to the strongly interacting regime, the global coupling of the single-mode cavity field couples to all lattice sites homogeneously, introducing an effective global interaction between the atoms. This is depicted schematically in Fig. 2.2. We choose a realization with fermionic atoms confined to an optical cavity, that in the normal phase is well described by a Fermi-Hubbard-Model, to see how the Fermi-statistics and correlations influence the physical behavior. Driving the system with a transverse pump beam introduces the photon-mediated long-range interaction, that is enhanced by the optical cavity. The small probability of a scattered photon to be re-scattered is increased by the many passings of the individual cavity-photons through the atomic system. The re-scattering of the cavity photons from an arbitrary atom within the ensemble mediates the all-to-all atomic interactions within the system. The setup thus opens possibilities to enter into the regime of strong light-matter interactions [153].

In this chapter, we introduce the theoretical model our further investigations will base on in Sec. 2.1. The equations capturing the dynamics of the open coupled atom-cavity system are subsequently presented in Sec. 2.2. To see the analytical methods we develop to allow an efficient treatment of the highly complex quantum many-body system refer to the next Chapter 3.

2.1 The Hamiltonian model

As stated above, we want to analyze a system of ultracold interacting fermionic atoms confined to a an external optical lattice. It is transversely pumped by a retro-reflected standing-wave laser field driving a cavity-assisted two-photon Raman transition during which the atoms can emit photons into the cavity mode. Consequently, a global photon-mediated atomic interaction is introduced to the atomic ensemble. The coupled system is subjected to energy losses via dissipation of the cavity mode, which opens the possibility to stabilize out-of equilibrium steady states. Additionally, since in realistic experiments such cavity systems can never be decoupled from their environment completely, the assumption of photon losses contributes to a more true-to nature description, while at the same time providing a quantum non-demolition measurement access via detection of the leakage photons. The model we consider therefore exhibits the nature of an open system with attractor dynamics, stabilizing complex modes of the interacting light-matter system. The setup we consider provides a comparably good external access to tuning the global coupling strength by varying the intensity or detuning of the transversal laser beam. This therefore allows makes the investigation of the dissipative phase transition possible over a broad range of parameters.

In the derivation of our model we follow analogous to the formulation provided in Ref. [31], adapting it to the here considered spinful fermionic atoms in the process.

To begin with, we divide the system Hamiltonian into several terms that either act on the atomic system, the cavity field or describe the coupling of the two subsystems

$$\hat{H} = \hat{H}_{\text{atom}} + \hat{H}_{\text{cav}} + \hat{H}_{\text{ac}} \tag{2.1}$$

Here, the atomic part includes short-range atom-atom interaction as well kinetic terms that capture their movement within the lattice. We consider an internal 2-level structure for the individual atoms in the ensemble, where they can reside in either the ground (g) or excited (e) state, split by an energy $\hbar\omega_{\text{ge}}$, This can generally be written as

$$\begin{aligned}\hat{H}_{\text{atom}} = \sum_{\sigma} \int d\mathbf{r}\, \hat{\psi}^{\dagger}_{g,\sigma}(\mathbf{r}) \Big[-\frac{\hbar^2}{2m}\nabla^2 + \frac{U}{2}\hat{\psi}^{\dagger}_{g,\bar{\sigma}}(\mathbf{r})\hat{\psi}_{g,\bar{\sigma}}(\mathbf{r}) + V_g(\mathbf{r}) \Big] \hat{\psi}_{g,\sigma}(r) \\ + \hat{\psi}^{\dagger}_{e,\sigma}(\mathbf{r}) \Big[-\frac{\hbar^2}{2m}\nabla^2 + V_e(\mathbf{r}) - \hbar\delta_a \Big] \hat{\psi}_{e,\sigma}(\mathbf{r})\end{aligned} \tag{2.2}$$

where the dynamics are described using the atomic field operators $\hat{\psi}_{g(e),\sigma}(\mathbf{r})$ that remove an atom in spin state σ and at position $\mathbf{r}$ (for now in arbitrary spatial dimension d) from the ground (excited) state respectively. The corresponding creation field operators are defined by the hermitian conjugates. Note, the field operators for the state $s, s' \in \{e, g\}$ obey the fermionic anti-commutation relations

$$\big[\hat{\psi}_{s,\sigma}(\mathbf{r}), \hat{\psi}^{\dagger}_{s',\sigma'}(\mathbf{r}')\big]_{+} = \delta^d(\mathbf{r}-\mathbf{r}')\delta_{s,s'}\delta_{\sigma,\sigma'} \tag{2.3a}$$

$$\big[\hat{\psi}_{s,\sigma}(\mathbf{r}), \hat{\psi}_{s',\sigma'}(\mathbf{r}')\big]_{+} = \big[\hat{\psi}^{\dagger}_{s,\sigma}(\mathbf{r}), \hat{\psi}^{\dagger}_{s',\sigma'}(\mathbf{r}')\big]_{+} = 0 \tag{2.3b}$$

Further the coupling constant for the two-body contact interaction is introduced as $U = 4\frac{\pi a_s \hbar^2}{m}$, where a_s is the s-wave scattering length and m the atomic weight. For now we consider a general spatially varying external trapping potential imposed on the atoms by the external optical lattice. While we still consider that atoms in ground- or excited state respectively might experience different effective potentials $V_{g(e)}(\mathbf{r})$, we assume it to be independent of the atomic spin degree of freedom σ and the detuning between the pump beam and the atomic resonance $\delta_a = \omega_{\text{pump}} - \omega_{\text{ge}}$.

The second terms appearing in Eq. (2.1) is $\hat{H}_{\text{cav}}$. It represents the energy stored in the bosonic field and accounts for energy changes to the overall system occurring when photons are added (via 2-photon Raman processes) or removed (via re-absorption by the atoms or dissipation) from the cavity mode. Here we perform a rotating wave-approximation, moving to the rotating frame of the external standing-wave coherent pump beam. In this basis we introduce δ as the detuning between the frequency supported by the single cavity mode and the frequency of the pump $\delta = \omega_{\text{cav}} - \omega_{\text{pump}}$. With this we obtain

$$\hat{H}_{\text{cav}} = \hbar\delta\hat{a}^{\dagger}\hat{a} \tag{2.4}$$

where $\hat{a}(\hat{a}^{\dagger})$ are the photonic (annihilation)(creation) operators.

Probably the most intriguing term in Eq. (2.1) is $\hat{H}_{\text{ac}}$ which captures the global coupling of the bosonic field to the atomic ensemble. For the limiting case of non-interacting atoms one recovers the Jaynes-Cummings Hamiltonian for the dynamics of the individual two-level systems. This model was first introduced and described in Ref. [154]. This model atom-cavity interaction can now be extended to the case of N two-level atoms coupled to a cavity field that is characterized by a given mode structure via an coherent external pump. We assume, that the pump field couples equally to all atomic spin species. Considering these assumptions, the atoms-cavity interaction can be expressed by the Hamiltonian [152, 155]

$$\hat{H}_{\text{ac}} = \hbar \sum_{\sigma} \int \mathrm{d}\mathbf{r}\, \hat{\psi}^{\dagger}_{e,\sigma}(\mathbf{r}) \big[h(\mathbf{r}) + g(\mathbf{r})\hat{a} \big] \hat{\psi}_{g,\sigma}(\mathbf{r}) + H.c. \tag{2.5}$$

The spatially dependent function $g(\mathbf{r})$ here describes the mode structure of the cavity field and $h(\mathbf{r})$ the mode-function of the coherent transverse pump with respect to the atoms.

Since we are interested in the observation of quantum effects, the system should be at reasonably low temperatures. Therefore, heating needs to be limited and the parameters should be chosen in a way that lets the atoms accumulate in the individual two-level ground state. One can achieve this by ensuring that the atomic excitation energy is far detuned from the other involved energy scales $\omega_{\text{eg}} \ll \omega_{\text{cav}}, \omega_{\text{pump}}$. In this dispersive regime the atoms are only virtually excited within the gap and subsequently decay back to the ground state without macroscopically occupying the excited state. We therefore approximate the system by adiabatically eliminating the excited state of the two-level atoms. Instead, it takes a steady state form depending on the ground state and the mode structure of pump and cavity field [31]

$$\bar{\psi}_{e,\sigma}(\mathbf{r}) \simeq \frac{1}{\delta_a}\left[h(\mathbf{r}) + g(\mathbf{r})\hat{a}\right]\hat{\psi}_{g,\sigma}(\mathbf{r}). \tag{2.6}$$

Atomic spontaneous emission can also be neglected due to the large detuning of the pump beam from the atomic resonance.

Inserting this expression for the field operators acting on the excited state in the previously derived Hamiltonian terms and restricting to terms up to $\mathcal{O}(1/\delta_a)$ in the perturbation yields for the atomic part

$$\begin{aligned}\hat{H}_{\text{atom}} = &\sum_{\sigma}\int d\mathbf{r}\,\hat{\psi}^{\dagger}_{g,\sigma}(\mathbf{r})\Big[-\frac{\hbar^2}{2m}\nabla^2 + \frac{U}{2}\hat{\psi}^{\dagger}_{g,\bar{\sigma}}(\mathbf{r})\hat{\psi}_{g,\bar{\sigma}}(\mathbf{r}) + V_g(\mathbf{r})\Big]\hat{\psi}_{g,\sigma}(r)\\ &-\frac{\hbar}{\delta_a}\hat{\psi}^{\dagger}_{g,\sigma}(\mathbf{r})\left[h(\mathbf{r}) + g(\mathbf{r})\hat{a}^{\dagger}\right]\left[h(\mathbf{r}) + g(\mathbf{r})\hat{a}\right]\hat{\psi}_{g,\sigma}(\mathbf{r})\end{aligned}$$

and the atoms-cavity coupling

$$\hat{H}_{\text{ac}} = \hbar\sum_{\sigma}\int \mathrm{d}\mathbf{r}\,\frac{1}{\delta_a}\hat{\psi}^{\dagger}_{g,\sigma}(\mathbf{r})\left[h(\mathbf{r}) + g(\mathbf{r})\hat{a}^{\dagger}\right]\left[h(\mathbf{r}) + g(\mathbf{r})\hat{a}\right]\hat{\psi}_{g,\sigma}(\mathbf{r}) + H.c.\,.$$

Expanding the bracket expressions and simplifying the resulting full Hamiltonian $\hat{H} = \hat{H}_{\text{atom}} + \hat{H}_{\text{cav}} + \hat{H}_{\text{ac}}$ one obtains two coupled differential equations, the Heisenberg equations of motion, that determine the dynamics of the atomic field operator in the ground state $\hat{\psi}_{\sigma} \equiv \hat{\psi}_{g,\sigma}$ and of the cavity field operator $\hat{a}$

$$\begin{aligned}i\hbar\frac{\partial\hat{\psi}_{\sigma}(\mathbf{r})}{\partial t} = &\Big[-\frac{\hbar^2}{2m}\nabla^2 + U\hat{\psi}^{\dagger}_{\bar{\sigma}}(\mathbf{r})\hat{\psi}_{\bar{\sigma}}(\mathbf{r}) + V(\mathbf{r}) + \frac{\hbar}{\delta_a}h(\mathbf{r})^2 + \frac{\hbar}{\delta_a}g(\mathbf{r})^2\hat{a}^{\dagger}\hat{a}\\ &+\frac{\hbar}{\delta_a}h(\mathbf{r})g(\mathbf{r})(\hat{a}+\hat{a}^{\dagger})\Big]\hat{\psi}_{\sigma}(\mathbf{r}) \qquad (2.7a)\\ i\hbar\frac{\partial\hat{a}}{\partial t} = &-\frac{\hbar}{\delta_a}\Big[\delta - \int \mathrm{d}\mathbf{r}\,g(\mathbf{r})^2\hat{\psi}^{\dagger}_{\sigma}(\mathbf{r})\hat{\psi}_{\sigma}(\mathbf{r})\Big]\hat{a} + \frac{\hbar}{\delta_a}\int \mathrm{d}\mathbf{r}\,h(\mathbf{r})\hat{\psi}^{\dagger}_{\sigma}(\mathbf{r})\hat{\psi}_{\sigma}(\mathbf{r}). \qquad (2.7b)\end{aligned}$$

Note that since the model no longer depends on $V_e(\mathbf{r})$ we identified $V_g(\mathbf{r}) \equiv V(\mathbf{r})$ for simplicity. From these we find an effective Hamiltonian that simplifies the individual two-level atoms to effective one level systems, operating in the dispersive regime

$$\begin{aligned}\hat{H}_{\text{eff}} = &\sum_{\sigma}\int \mathrm{d}\mathbf{r}\,\hat{\psi}^{\dagger}_{\sigma}(\mathbf{r})\Big[-\frac{\hbar^2}{2m}\nabla^2 + V(\mathbf{r})\Big]\hat{\psi}_{\sigma}(\mathbf{r}) \qquad (2.8)\\ &+\int \mathrm{d}\mathbf{r}\,\frac{U}{2}\hat{\psi}^{\dagger}_{\sigma}(\mathbf{r})\hat{\psi}^{\dagger}_{\bar{\sigma}}(\mathbf{r})\hat{\psi}_{\bar{\sigma}}(\mathbf{r})\hat{\psi}_{\sigma}(\mathbf{r})\\ &+\int \mathrm{d}\mathbf{r}\,\frac{\hbar}{\delta_a}\hat{\psi}^{\dagger}_{\sigma}(\mathbf{r})\big[h(\mathbf{r})^2 + g(\mathbf{r})^2\hat{a}^{\dagger}\hat{a} + h(\mathbf{r})g(\mathbf{r})(\hat{a}+\hat{a}^{\dagger})\big]\hat{\psi}_{\sigma}(\mathbf{r})\\ &-\hbar\delta\hat{a}^{\dagger}\hat{a}.\end{aligned}$$

While the derivation up until here has been kept mostly general concerning the geometry of the atomic system, pump beam and cavity mode, we want to now specify the model toward our interests. We want to initially restrict to low dimensions, confining the atomic motion along the cavity axis which we define as x in Cartesian coordinates. We consider a single cavity mode with an intensity profile along the cavity axis described by the mode function $g(x) = G_0^2\cos^2(k_{\text{cav}}x)$, with maximal coupling to the cavity mode G_0 and cavity wave vector k_{cav}. For the single

mode setup we assume the mode profile along the transverse field axis to be seen as homogeneous in the one-dimensional atomic chain and omit the spatial dependence along the other dimensions y, z.

To specify the mode function of the transverse pump laser, we take it to be aligned with the y axis and approximate it by $h(y) = \Omega_0^2 \cos^2(k_\mathrm{p} y)$ with maximal Rabi-frequency from the coupling to the atoms Ω_0 and the wave vector of the pump k_p. We assume the field to show a homogeneous profile along the cavity axis throughout the atomic system located at $y = 0$, leading to a fixed coupling to all atoms. It can be rewritten in terms of a constant energy offset and can thus be omitted in the further treatment of the model.

We want to subject the atoms to a strong external static trapping potential in direction of the cavity axis $V(x) = V_0 \cos^2(k_\mathrm{l} x)$ with periodicity characterized by the wave-vector k_l. Since the atoms are strongly confined along two of the three spatial dimensions, the scattering length in the contact-interactions needs to be adjusted correspondingly, leading to a coupling strength of g_1D for the effective one dimensional system. For sufficiently large V_0, effects of the pump beam and emerging cavity field above the self-ordering transition do not affect the periodicity of the static lattice to first order. We aim to design a staggered coupling of the atoms to the cavity field, i.e. the sign of the coupling term between neighboring lattice sites for square lattices in arbitrary dimension should alternate. This would effectively create a bipartite lattice with neighboring sites belonging to different sublattices A and B and a coupling of the cavity field to the imbalance between the occupation of the different sublattices $\hat{\Delta}$. This can be achieved by adjusting k_l so that the lattice spacing is commensurate with half the wavelength of the cavity mode in each lattice direction (here 1D). In this special case, the cavity mode function $G_0 \cos(k_\mathrm{cav} x)$ can be translated to an effective pump strength $\pm g$ with its sign depending on the respective sublattice [31]. We note that we do not consider in $\hat{H}_\mathrm{ac}$ the dispersive coupling $\propto \hat{a}^\dagger \hat{a} \hat{\Delta}$ [78], which often leads to bistabilities due to optical non-linearities.

In the so-called tight binding limit, the fermionic field operators $\hat{\psi}_\sigma(x)$ can be expanded in the basis of the well known single-particle Wannier functions

$$\hat{\psi}_\sigma(x) = \sum_j \sum_\sigma \hat{c}_{j\sigma} w(x - x_j). \tag{2.9}$$

In the process, we introduced fermionic annihilation ($\hat{c}_{j\sigma}$) and creation operators $\hat{c}^\dagger_{j\sigma}$ that remove/add a fermion in spin state $\sigma \in \{\uparrow, \downarrow\}$ at a site of the external lattice labeled by j. Note, these operators satisfy the fermionic anti-commutation relations

$$\begin{aligned} \left[\hat{c}_{i\sigma}, \hat{c}^\dagger_{j\sigma'}\right]_+ &= \delta_{ij}\delta_{\sigma\sigma'} \\ \left[\hat{c}_{i\sigma}, \hat{c}_{j\sigma'}\right]_+ &= \left[\hat{c}^\dagger_{i\sigma}, \hat{c}^\dagger_{j\sigma'}\right]_+ = 0. \end{aligned}$$

The local density operator can be expressed in terms of these operators $\hat{n}_{j\sigma} = \hat{c}^\dagger_{j\sigma}\hat{c}_{j\sigma}$. We further restricted the model to the lowest energy band since the eigenenergies of the model hamiltonian can be assumed to be small compared to the band gap. In a next step, the Wannier-expansion is inserted for the field operators in the effective Hamiltonian [first two lines of Eq. (2.8)]. If only dominant terms are retained, one arrives at the Fermi-Hubbard model, that is a very well known many-body system

$$\hat{H}_\mathrm{atom} = \hat{H}_\mathrm{FH} = -J \sum_{\langle j,l\rangle,\sigma} \left(\hat{c}^\dagger_{j\sigma}\hat{c}_{l\sigma} + \mathrm{H.c.}\right) + U \sum_j \hat{n}_{j\uparrow}\hat{n}_{j\downarrow}. \tag{2.10}$$

Here the sum runs over neighboring sites with indices $\langle j, l\rangle$ within the chain of length L that contains a total number of N atoms.

The introduced parameters are J, tunneling amplitude that determines the hopping rate between neighboring lattice sites, and $U > 0$ the repulsive on-site interaction between different spin species. They are defined from overlap integrals of the Wannier functions.

$$\begin{aligned} J_{jk} &= -\int dx\, w_j^*(x)\big[-\frac{\hbar^2}{2m}\partial_x^2 + V(x)\big] w_k(x) \\ U_j &= g_\mathrm{1D} \int dx\, |w_j(x)|^4 \end{aligned}$$

One restricts to contributions from adjacent lattice sites (j,k) since processes at larger distance are suppressed exponentially in the atomic system. Further, due to the presence of a discrete translation invariance within the system along the lattice, one assumes the tunneling amplitude and on-site interaction strength to be homogeneous, identifying $J \equiv J_{jk}$ and $U \equiv U_j$.

With the expansion in Wannier basis and the introduction of the fermionic annihilation and creation operators, the entire Hamiltonian in second quantization can be written as

$$\hat{H} = \hat{H}_{\text{FH}} + \hat{H}_{\text{cav}} + \hat{H}_{\text{ac}} \tag{2.11a}$$

$$\hat{H}_{\text{FH}} = -J \sum_{\langle j,l\rangle,\sigma} \left(\hat{c}^\dagger_{j\sigma}\hat{c}_{l\sigma} + \text{H.c.}\right) + U\sum_j \hat{n}_{j\uparrow}\hat{n}_{j\downarrow} \tag{2.11b}$$

$$\hat{H}_{\text{cav}} = \hbar\delta\hat{a}^\dagger\hat{a} \tag{2.11c}$$

$$\hat{H}_{\text{ac}} = -\frac{\hbar g}{\sqrt{L^d}}(\hat{a}+\hat{a}^\dagger)\hat{\Delta}, \quad \hat{\Delta} = \sum_{j\in A,\sigma} \hat{n}_{j\sigma} - \sum_{l\in B,\sigma} \hat{n}_{l\sigma} \tag{2.11d}$$

We will briefly comment on the influence of the individual terms on the physical state of the system to clarify their role in the overall model description. While the second line is the well know Fermi-Hubbard model containing next-neighbor tunneling with amplitude J and inter-spin-species on-site interaction U, the cavity term $\hat{H}_{\text{cav}}$ in the third line accounts for the energy stored in the cavity field relative to the rotating frame of the pump beam. Here, δ is the detuning between the pump frequency and the single mode cavity resonance. Note, that in the following discussions we will sometimes simply refer to this as "pump-detuning" or "detuning". Lastly, the cavity mediated global range atomic interaction is represented in the last line via coupling of the cavity field operator $(\hat{a}+\hat{a}^\dagger)$ to the density occupation imbalance between the two sublattices A and B. For a one dimensional atomic system this would result in a staggered density $\sum_{j,\sigma}(-1)^j\hat{n}_{j\sigma}$, a checkerboard pattern in two dimensions and correspondingly for higher dimensional external lattices. We note that Hamiltonian is invariant under simultaneous mapping

$$\begin{cases} \hat{a} \to -\hat{a}, \\ \hat{\Delta} \to -\hat{\Delta} \end{cases}$$

which is a $\mathbb{Z}_2$ symmetry of the model. Further, the Hamiltonian exhibits a $U(1)$ gauge symmetry and is thus invariant under a global phase shift χ, $\hat{c}_{j\sigma} \to \hat{c}'_{j\sigma} = \exp(i\chi)\hat{c}_{j\sigma}$. Another symmetry of the model is a $SU(2)$ spin symmetry we will comment on in later chapters.

2.2 Open system dynamics

So far, we only considered the part of the model setup as sketched in Fig. 2.2 that is energy-conserving. We now aim to include a single dissipation channel (due to the single-mode nature of the considered cavity field) in the description of the system.

The dissipative system is characterized by the coupling to a large external bath, also called the environment. The system, consisting of system and environment, is thus defined on the full Hilbert space $\mathcal{H}_S \otimes \mathcal{H}_E$. Assuming that the coupling to the bath does not have a memory, i.e. the next time step proceeding from a current state does not depend on the previous time evolution and the trajectory to reach this specific state, one can perform a Born approximation and describe the dissipative dynamics by a Markovian master-equation. This is a sensible assumption if the thermalization of the large environment happens at scales much faster than the interactions with the system that is subject to dissipation. We take this to be true if the coupling of the cavity field to the environment is weak.

To this end, the full system-environment density matrix, tracing out the environment degrees of freedom, is reduced to an effective subsystem with a time evolution that is no longer unitary. The dissipative dynamics of the entire model with the cold atomic gas in an optical cavity, subjected to a coherent transverse pump beam, can then be described by a Markovian quantum master equation in Lindblad form [4, 31, 78, 152, 156]

$$\frac{d}{dt}\hat{\rho} = -\frac{i}{\hbar}[\hat{H},\hat{\rho}] + \frac{\Gamma}{2}\left(2\hat{a}\hat{\rho}\hat{a}^\dagger - \hat{a}^\dagger\hat{a}\hat{\rho} - \hat{\rho}\hat{a}^\dagger\hat{a}\right). \tag{2.12}$$

Here the density matrix $\hat{\rho}$ contains all atomic and photonic degrees of freedom. The Hamiltonian provides an equation of motion $\hat{\rho}$ as determined by a typical von Neumann-equation $\frac{d}{dt}\hat{O} = -\frac{i}{\hbar}[\hat{H}, \hat{O}]$. This is completed by the second term appearing in Eq. 2.12, the so-called dissipator. It describes the dissipation via the application of a "jump operator", in this specific case the photon annihilation jump operator $\hat{a}$, at rate $\Gamma/2$. These non-linear differential equations determine the full system dynamics for the density matrix.

We note that in open systems like the one considered here, a symmetry in the Hamiltonian does not necessarily imply a conserved quantity [104, 157]. For so-called strong symmetries that do correspond to a conserved quantity the condition that the symmetry generator commutes with all jump operators defined in the dissipator has to additionally be fulfilled. For the $\mathbb{Z}_2$ symmetry, this is not true, since the corresponding generator does not commute with the photon annihilation operator. It is therefore called a weak symmetry of the Lindbladian model.

Looking at the equations describing the model, above a critical pump strength and, thus, global interaction strength, the atoms are expected to transition to a density-modulated phase by spontaneously ordering on one of the sublattices of the static optical lattice. The initially empty cavity field becomes macroscopically occupied, introducing an additional dynamical lattice on top of the static one [71, 158]. Recall, that the cavity field wave vector is chosen to be commensurate with half the site-spacing of the external optical lattice by choosing the wavelength of the lattice beam and the cavity length correspondingly.

Before moving on to the development of analytical methods that allow us to solve the presented equations, we want to comment on the physical process one expects for the self-ordering phase transition at a critical coupling strength. Without the pump beam and thus without coupling to the cavity mode the atoms are in a many-body steady state as predicted for the standard Fermi-Hubbard model, characterized by a homogeneous density distribution (neglecting finite size effects). However, the local densities are typically not static but subject to quantum fluctuations whose strength depends on various parameters such as the relative strength of the on-site interactions U/J and the overall atomic density. Turning on the transversely applied, standing wave laser, these local density fluctuations can lead to temporary sublattice density imbalances that consequently stimulate a process in which an atom absorbs a photon from the pump field, gets virtually excited and immediately decays back to the ground state, emitting a photon into the cavity mode. Once there are a finite number of photons in the cavity field, they can be re-absorbed by any (other) atom mediating the global range interaction that allows the system to collectively order. This process self-amplifies the density fluctuations in the atomic ensemble. Once the coupling strength determined by the pump intensity and detuning from the cavity mode exceeds a critical value, the atoms are able to collectively order and the system undergoes a self-ordering quantum-phase transition to a steady state where occupations of one sublattice are favored while they are suppressed for the other one. Here, the cavity setup effectively amplifies light-matter interaction cross-section via multiple passings of each photon through the atomic ensemble.

Summary

In this chapter we outlined the derivation of the Hamiltonian describing the quantum many body system of fermions with global coupling to a dissipative cavity field via transverse pumping. We included the open nature of the model in the framework of Markovian quantum master equations in Lindblad form. Having introduced this model, that serves as a starting point for our investigations, we want to present the analytical methods we employ in order to gain a detailed understanding of the processes driving the complex system towards its steady state in the following Chapter 3. While we focus mostly on the steady state phase diagrams in these analytical derivations, we also investigate the quasi-exact numerical time evolution of the system using our newly developed tensor-network methods we will introduce in Chapter 4.

Chapter 3

Many body adiabatic elimination technique for atoms-cavity coupled systems

Our fermionic quantum-many body system globally coupled to a dissipative cavity mode is quite involved and can only be solved exactly for very small system sizes. Therefore, strategies are needed in order to derive the system dynamics and steady state behavior. In this chapter we introduce the analytical approximation methods used to determine the steady state solutions [Sec. 3.1] of the driven dissipative atoms-cavity coupled system. Our approach takes into account fluctuations in the coupling of the atomic ensemble to the cavity field, going beyond standard mean field methods. Further we perform a perturbation in the kinetic energy, deriving a system of equations in the thermodynamic limit [Sec. 3.2] that can be solved numerically. We comment on its validity for atomic systems of arbitrary dimensions.

For both approaches we provide a stability condition for the steady-state solutions that determines the robustness against small perturbations in the cavity field. We derive the condition for general mixed atomic states [Sec. 3.3] and later evaluate it for the case of a thermal atomic state. Finally we briefly show the influence of the total spin symmetry sector on the solutions [Sec. 3.4].

An introduction to the implemented numerical tensor network methods will be provided in Chapter 4. This allows us to obtain the quasi exact dynamics of the complex quantum many-body system.

3.1 Derivation of the energy-transfer equation

In this section, we outline the derivation of an energy transfer equation for a many-body atomic subsystem that includes the dissipative character of the model via an effective coupling of the atoms to a static cavity field. The final result of the calculations is shown in Eq. (3.14). We apply the framework of many-body adiabatic elimination, which allows us to consider fluctuations on top of the standard mean-field approximation of the atoms-cavity coupling term Eq. (2.11d). The adiabatic elimination of the cavity dynamics via mean-field decoupling typically leads to a static coupling between the atoms and the cavity mode, decoupling photonic and atomic degrees of freedom completely [78]. In contrast to this, the adiabatic elimination method for many-body quantum systems we developed captures fluctuations in the atom-cavity dynamics via perturbative coupling of the decoherence free subspace of the Lindblad master equation to dissipative subspaces [159–163]. Here we follow this mean-field treatment, including the fluctuations in the atoms-cavity coupling perturbatively by initially starting from the states resulting from a mean-field decoupling of the photonic and atomic subsystems. This method has been developed by our group and collaborators in Refs. [150, 164], where additional benchmarks for its validity have been provided. Importantly, our approach does not involve a mean-field treatment of the atomic part of the system and still contains the full Fermi-Hubbard dynamics resulting from the interplay of the tunneling amplitude with the on-site interactions between different spin species.

We start our derivations from the non-dissipative part of our model which is given by the Hamiltonian Eq. (2.11a)

$$\hat{H} = \hat{H}_{\text{FH}} + \hbar\delta\hat{a}^\dagger\hat{a} - \frac{\hbar g}{\sqrt{L^d}}(\hat{a} + \hat{a}^\dagger)\hat{\Delta}$$

as introduced in Sec. 2.1.

Here, the last term represents the laser-assisted atoms-cavity coupling $\hat{H}_{\text{ac}}$ that couples to neighboring sites belonging to different sublattices A, B in opposite ways. This staggered coupling effectively shifts the lattice potential the atoms see, creating a bipartite lattice with potential offset $\frac{\hbar g}{\sqrt{L^d}}(\hat{a} + \hat{a}^\dagger)$. We can interpret this as a coupling of the cavity mode to the imbalance between the atomic densities on the individual sublattices $\hat{\Delta} = \sum_{j\in A,\sigma}\hat{n}_{j\sigma} - \sum_{l\in B,\sigma}\hat{n}_{l\sigma}$ [31]. Since in our setup we choose to pump the system transversely, the dispersive coupling $\propto \hat{a}^\dagger\hat{a}\hat{\Delta}$ [78] is not present in $\hat{H}_{\text{ac}}$. Therefore, we do not observe bistabilities due to optical non-linearities that often result from this direct coupling to the light field intensity. Instead, other interesting phenomena emerge that have not been widely explored up until now.

As stated above, a standard approach to simplify these complex cavity-atoms systems is to perform an adiabatic elimination of the cavity mode. In the process the atoms-cavity coupling term $\hat{H}_{\text{ac}}$ is replaced by a static mean-field value depending on the parameter configuration for the system. In the following discussion we will refer to this method as *zero-temperature mean-field method* ($T = 0$ MF)] [78, 152]. Since typically the cavity-field dynamics occur at rates that are significantly faster than any processes in the atomic system, the photons are assumed to quickly decay to a coherent state.

While this approach is already able to provide some insights into the system, in various system setups it was demonstrated that taking into account fluctuations in the coupling fundamentally alters the steady state properties and we therefore can not assume the phase diagrams determined at $T = 0$ MF level to correctly represent the physical processes leading to the steady state that is close to the full system solution [102, 106, 149, 164–167]. One thus needs to go beyond the standard methods, which we do by applying an approach, that was recently developed based on a so-called *many-body adiabatic elimination technique* [159–163, 168], to include perturbatively the fluctuations in the atoms-cavity coupling on top of the mean-field [106, 164].

Since our method is based on the mean field approximation, we start by providing the corresponding equations for our specific model. We assume the cavity field to be in a coherent state $|\alpha\rangle$ with $\alpha = \langle\hat{a}\rangle$. The steady state condition for the time evolution of this operator with respect to the Hamiltonian Eq. (2.11a) is given by

$$\frac{\partial}{\partial t}\langle\hat{a}\rangle = i\frac{g}{\sqrt{L^d}}\langle\hat{\Delta}\rangle - \left(i\delta + \frac{\Gamma}{2}\right)\langle\hat{a}\rangle \stackrel{!}{=} 0. \tag{3.1}$$

Solving for the steady state results in

$$\langle\hat{a}\rangle = \frac{g/\sqrt{L^d}}{\delta - i\Gamma/2}\langle\hat{\Delta}\rangle. \tag{3.2}$$

Using this result, we define the system parameter λ which describes the cavity field in the coupling term

$$\lambda(\Delta) \equiv \frac{\langle\hat{a} + \hat{a}^\dagger\rangle}{\sqrt{L^d}} = \frac{2g\delta}{\delta^2 + (\Gamma/2)^2}\frac{\langle\hat{\Delta}\rangle}{L^d}. \tag{3.3}$$

Utilizing this result obtains an effective Hamiltonian $\hat{H}_{\text{eff}}$ that contains a coupling term depending on a static coherent cavity-field

$$\hat{H}_{\text{eff}} = \hat{H}_{\text{FH}} - \hbar g\lambda(\Delta)\hat{\Delta} \quad \text{with} \quad \hat{H}_{\text{FH}} = -J\sum_{\langle j,l\rangle,\sigma}\left(\hat{c}^\dagger_{j\sigma}\hat{c}_{l\sigma} + \text{h.c.}\right) + U\sum_j \hat{n}_{j\uparrow}\hat{n}_{j\downarrow} - \mu\sum_{j,\sigma}\hat{n}_{j,\sigma}. \tag{3.4}$$

For completeness, here a chemical potential term $\propto \mu$ is included that controls the energy change in the atomic system when adding or removing a particle from the system. In the following we are only focusing on particle-number conserving systems and restrict losses to the cavity field. Therefore, this term will generally drop out of the steady state description. For the purposes of this work it will however become important when going to the thermodynamic limit. In this approach we don't explicitly define basis states that satisfy the particle conservation

(as in small system case that is solved using exact diagonalization of $\hat{H}_{\text{eff}}$) but rather conserve it on average using the chemical potential [see Sec. 3.2]. The sublattice density imbalance appearing in the coupling term $\lambda(\Delta)$ is calculated self-consistently with respect to the corresponding atomic states using Eq. (3.3). We note that the MF treatment breaks the weak $\mathbb{Z}_2$ symmetry of the model, $(\hat{a}, \hat{\Delta}) \to (-\hat{a}, -\hat{\Delta})$, thus, in the following we restrict ourselves to the solution with $\langle \hat{a} \rangle \geq 0$, resulting in the A-sublattice to have the lower energy. There is a drawback to the MF approach. The mean-field decoupling steady state equation is solved by any eigenstate of $\hat{H}_{\text{eff}}$ and therefore, one needs to make a somehow arbitrary choice for the atomic state that is not well-determined. One common step, which we choose here, is to take the ground state of the effective atomic Hamiltonian [78, 152].

We expand this approach now by taking into account the fluctuations in the atom-cavity coupling $\delta\hat{H}_{\text{ac}}$ via perturbation theory [150, 164], which is defined as the deviation between mean field and full dynamic coupling.

$$\delta\hat{H}_{\text{ac}} = -\hbar g\Big(\frac{(\hat{a}+\hat{a}^\dagger)}{\sqrt{L^d}} - \lambda\Big)\hat{\Delta} \tag{3.5}$$

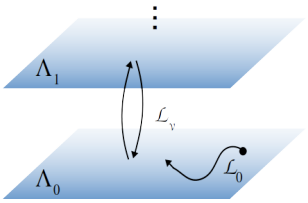

Fig. 3.1: Sketch of the decoherence free (Λ_0) and lowest decaying (Λ_1) Liouvillian subspaces. Dynamics in Λ_0 are captured by the unperturbed Liouvillian $\mathcal{L}_0$, while the perturbation $\mathcal{L}_\nu$ couples to decaying subspaces.

We apply in the many-body adiabatic elimination framework the perturbation theory for density matrices onto our Lindbladian model. To this end we determine the decoherence free and lowest lying dissipative subspaces of the unperturbed Liouvillian $\mathcal{L}_0$, as shown in the sketch in Fig. 3.1. For our specific model, the resulting equation is given by

$$\mathcal{L}_0\hat{\rho} = -\frac{i}{\hbar}[\hat{H}_{\text{eff}} + \hbar\delta\hat{a}^\dagger\hat{a}, \hat{\rho}] + \frac{\Gamma}{2}\left(2\hat{a}\hat{\rho}\hat{a}^\dagger - \hat{a}^\dagger\hat{a}\hat{\rho} - \hat{\rho}\hat{a}^\dagger\hat{a}\right). \tag{3.6}$$

Note that the eigenvalues of $\mathcal{L}_0$ have the form $\mathcal{L}_0\hat{\rho}_\lambda = (-\lambda^R + i\lambda^I)\hat{\rho}_\lambda$, where $\lambda^R \geq 0$ and λ^I are real numbers. This can be seen in Fig. 3.2, where we show the Lindbladian eigenvalues for a system of size $L = 4$, $N = 2$. Already for this minimal size, the dimension of the matrix one needs to diagonalize is of order $\sim 10^5$, which strengthens our motivation to find more efficiently computable representations of the system that allow us to investigate larger system sizes. We see that, since the dissipator defined for our system is determined by the dissipation rate $\Gamma/2$ the real part of the eigenvalues λ^R lie in bands separated by gaps of order $O(\Gamma)$ if the dissipation rate is the largest energy scale in the system $\Gamma \gg g, U/\hbar, \delta$. As the coupling increases other effects "disturb" this ordering starting from the highest dissipative subspaces. However, since we restrict our description to the low-lying decaying subspaces in our derivation and neglect the fast decaying higher ones, the most relevant part of the Lindbladian is that with $\lambda^R \sim 0$.

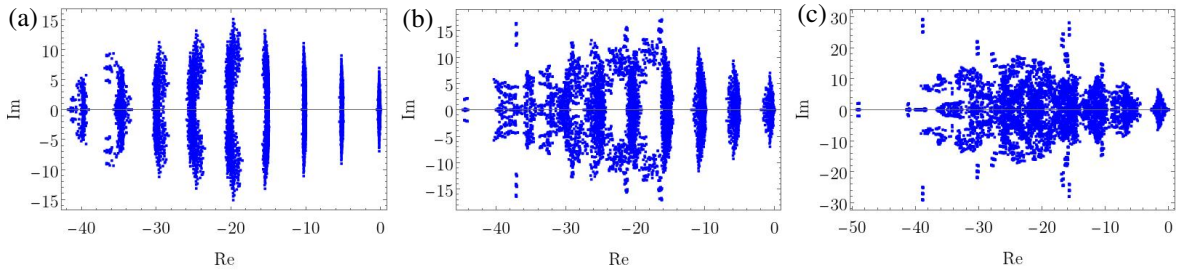

Fig. 3.2: We show the Lindbladian eigenvalue spectrum $\mathcal{L}_0\hat{\rho}_\lambda = (-\lambda^R + i\lambda^I)\hat{\rho}_\lambda$ at system size $L = 4$ and quarter filling. The parameters used are $U/J = 2$, $\hbar\delta/J = 2$, $\hbar\Gamma/J = 10$ and $\hbar g/J = \{0.5, 1.0, 2.0\}$.

Λ_α is defined as the subspace of right eigenvectors that share a real part λ_α^R. Note that in this notation, Λ_0 is the decoherence free subspace that is characterized by $\lambda_0^R = 0$. We assume that the eigenstates of $\mathcal{L}_0$ obtained by solving $\mathcal{L}_0\hat{\rho}^0 = \lambda_0\hat{\rho}^0$ are well described by product states between the atomic and cavity-field subspaces

$$\hat{\rho}^0 = \hat{\rho}^0_{\text{FH}} \otimes \hat{\rho}^0_{\text{cav}}, \qquad \text{with} \quad \hat{\rho}^0_{\text{FH}} = |n_1(\lambda)\rangle \langle n_2(\lambda)|, \qquad \hat{\rho}^0_{\text{cav}} = |\alpha(\Delta)\rangle \langle \alpha(\Delta)|. \tag{3.7}$$

The atomic part is here built from eigenstates of $\hat{H}_{\text{eff}}$ which we write in the number basis as states $|n(\lambda)\rangle$ with energy $E_n(\lambda)$. For the cavity state $\hat{\rho}^0_{\text{cav}}$ we stay with the coherent state assumption due to the fast atomic time scale with the field depending on the atomic state via the sublattice density imbalance

$$\frac{\alpha(\Delta)}{\sqrt{L^d}} = \frac{g}{\delta - i\Gamma/2} \frac{\langle \hat{\Delta} \rangle}{L^d}.$$

As groundwork for the following derivation, we provide some relevant eigenstates of the unperturbed Liouvillian $\mathcal{L}_0$ showing the lowest decay rates. To simplify the calculation, we perform a basis shift by the steady mean field value of the cavity operator $\alpha = \langle \hat{a} \rangle$. The photonic states are from here on thus written as

$$\begin{aligned} &\tilde{a} = \hat{a} - \alpha, \quad \tilde{a}^\dagger = \hat{a}^\dagger - \alpha^*, \quad (\tilde{a} + \tilde{a}^\dagger)/\sqrt{L^d} = (\hat{a} + \hat{a}^\dagger)/\sqrt{L^d} - \lambda, \\ &|0\rangle \equiv |\alpha\rangle, \quad \tilde{a}|0\rangle = 0, \quad |1\rangle \equiv \tilde{a}^\dagger |0\rangle, \text{ with } \langle 0|1\rangle = 0, \end{aligned} \tag{3.8}$$

using the shifted oscillator basis, the most relevant eigenstates yield

$$\begin{aligned} \mathcal{L}_0(|n,0\rangle \langle m,0|) &= -i(E_n - E_m)/\hbar \, |n,0\rangle \langle m,0| \\ \mathcal{L}_0(|n,0\rangle \langle m,1|) &= [-i((E_n - E_m)/\hbar - \delta) - \Gamma/2] \, |n,0\rangle \langle m,1|, \\ \mathcal{L}_0(|n,1\rangle \langle m,0|) &= [-i((E_n - E_m)/\hbar + \delta) - \Gamma/2] \, |n,1\rangle \langle m,0|. \end{aligned} \tag{3.9}$$

Here, we wrote $E_n(\lambda) = E_n$, $n(\lambda) = n$ etc. for simplicity. From these equations it becomes apparent, that the decoherence free subspace Λ_0 is spanned by states $|n,0\rangle \langle m,0|$ where the cavity field takes the mean field value α. Using this result, a state in the decoherence free subspace can generally be written as

$$\hat{\rho}^0 = |\alpha(\Delta)\rangle \langle \alpha(\Delta)| \otimes \hat{\rho}^{\text{at}}(\lambda), \quad \text{with} \quad \hat{\rho}^{\text{at}} = \sum_{n_1,n_2} c(n_1,n_2) \, |n_1(\lambda)\rangle \langle n_2(\lambda)|. \tag{3.10}$$

In contrast to this, the excited subspaces $\Lambda_{\alpha\neq 0}$ contain states with a deviation from the coherent state, representing excitations of the cavity field. For the subspace Λ_1 considered here, these would be states containing one photonic excitation [see Eq. (3.9)]. Since these states decay exponentially at a rate $O(\Gamma)$ as they evolve in time, it is possible to adiabatically eliminate contributions from Λ_1. By doing this we perturbatively include the effect of the decaying subspace in an effective description of the decoherence free subspace. The elimination is done as follows.

The considered perturbation couples Λ_0 to Λ_1 via action of $\delta\hat{H}_{\text{ac}}$ defined in Eq. (3.5)

$$\mathcal{L}_\nu(\hat{\rho}) = -\frac{i}{\hbar}[\delta\hat{H}_{\text{ac}}, \hat{\rho}]. \tag{3.11}$$

Using this one arrives at an equation capturing the effective dynamics within the decoherence free subspace [162, 163] which allows us to compute the steady state by using projectors $\hat{P}_0$ and $\hat{P}_1$ that project to the respective subspaces Λ_0 and Λ_1. This yields

$$\frac{\partial}{\partial t}\hat{\rho}^0 = \mathcal{L}_0\hat{\rho}^0 + \frac{1}{\hbar^2}\hat{P}_0 \left[\delta\hat{H}_{\text{ac}}, (\mathcal{L}_0^{\Lambda_1})^{-1}\hat{P}_1 \left[\delta\hat{H}_{\text{ac}}, \hat{\rho}^0\right]\right], \tag{3.12}$$

where for simplicity we identify $\hat{\rho}^0 \equiv \hat{\rho}^{\Lambda_0}$.

We use Eq. (3.9) to obtain an explicit expression for the steady state of Eq. (3.12). Note that a drawback from the perturbative expansion is that the equations we obtain are no longer restricted to positive semi-definite solutions. One thus needs to carefully check the physicality of the obtained results. The atomic density matrix obtained from solving Eq. (3.12) is parameterized by by a coefficient matrix whose dimension scales with the dimension of the atomic Hilbert space. The number of coefficients thus grows quadratically.

To overcome these issues we further approximate our system by reducing the number of atomic degrees of freedom of the resulting system of equations and restricting to solutions with physical density matrices. We assume, that the atomic system can be described by a thermal state [150, 164], which is justified if the thermalization time of the atomic system is shorter than the disordering process from coupling to photon fluctuations. We provide arguments for the validity of the thermal state approximation by showing that the level spacing distribution in each symmetry block of $\hat{H}_{\text{eff}}$ obey Gaussian orthogonal ensemble (GOE) statistics in the presence of the staggered potential (see Sec. 5.3, published in Ref. [3]). In general, we would have to consider a generalized Gibbs ensemble state for the atoms to take into account all symmetries [106, 168]. However, in our case of an underlying staggered potential, if we consider just a single symmetry sector or a chaotic system we can describe the atomic density matrix by the thermal state

$$\hat{\rho}_{\text{at}} \sim e^{-\beta \hat{H}_{\text{eff}}(\lambda)}/Z. \tag{3.13}$$

Here, the effective inverse temperature $\beta = 1/k_B T$ at which the atomic system thermalizes in the steady state is determined by the fluctuations in the atoms-cavity coupling. The finite temperature causes the admixture of excited states of the effective Hamiltonian in the density matrix of the system, in contrast to the pure state obtained from the $T = 0$ MF method. The thermal atomic state only depends on a single parameter and can thus be determined using the equation of motion of a single observable, namely the energy transfer, which in Lehmann-representation is given by [150, 164]

$$\begin{aligned}\frac{\partial}{\partial t}\langle \hat{H}_{\text{eff}}\rangle_T &= \frac{\hbar^2 g^2 \Gamma}{L^d Z}\sum_{n,m}|\Delta_{m,n}|^2 e^{-\beta E_m}\frac{E_n - E_m}{(E_n - E_m + \hbar\delta)^2 + (\hbar\Gamma/2)^2}. \\ &= \frac{\hbar^2 g^2 \Gamma}{L^d Z}\sum_{n,m>n}|\Delta_{m,n}|^2 (E_n - E_m)\left[\frac{e^{-\beta E_m}}{(E_n - E_m + \hbar\delta)^2 + (\hbar\Gamma/2)^2} - \frac{e^{-\beta E_n}}{(E_n - E_m - \hbar\delta)^2 + (\hbar\Gamma/2)^2}\right],\end{aligned} \tag{3.14}$$

with E_n being the energy of the eigenstate $|n\rangle$ of $\hat{H}_{\text{eff}}$ and $\Delta_{nm} = \langle n|\,\hat{\Delta}\,|m\rangle$.

In the steady state, since all transition rates balance, the left hand side vanishes and we only have to solve for β by additionally fulfilling the self-consistency condition Eq. (3.3).

In some cases, it is favorable to rewrite the spectral energy transfer equations as a function of the retarded susceptibility $\chi(\omega)$

$$\frac{\partial}{\partial t}\langle \hat{H}_{\text{eff}}\rangle_T = \frac{2\hbar g^2}{L^d Z_{1\text{D}}}\int d\omega \frac{\hbar\omega}{1 - e^{-\beta\hbar\omega}}\,\text{Im}\left[\chi_T(\omega)\right]\frac{\Gamma/(2\pi)}{(\omega+\delta)^2 + (\Gamma/2)^2}, \tag{3.15}$$

where [169]

$$\chi_T(\omega) = -\frac{i}{\hbar}\int_0^\infty dt e^{i(\omega + i\epsilon)t}\left\langle\left[\hat{\Delta}(t), \hat{\Delta}(0)\right]\right\rangle_T.$$

The subscript T here emphasizes the evaluation of the expectation values with respect to the thermal steady states. The integrand exhibits a main peak at $\hbar\omega = \pm 2g\lambda$ with secondary peaks around $\hbar\omega = \pm U$. Generally, the secondary peaks are suppressed by a factor of $J^2/\hbar g\lambda$ due to their dependence on second order hopping processes. Since the contribution of specific processes in Eq. (3.15) is proportional to the energy transfer in the atomic system ΔE_{nm}, transitions without energy transfer are additionally suppressed.

The effective inverse temperature β and the cavity field strength λ are simultaneously determined self-consistently from the mean-field relation and the steady state condition of the energy transfer. We want to note that in the normal phase below the self-ordering transition, the atoms still couple to the cavity field fluctuations despite the vanishing average density imbalance, which determines an effective finite temperature. However, care is needed when using the thermal state ansatz in this regime, since the effective atomic Hamiltonian reduces to the integrable Fermi-Hubbard model. Therefore, one would need to resort to a generalized Gibbs ensemble state that includes the conservation laws [106, 168, 170]. As we are mostly interested in the features present in the self-organized phase, where the effective model is the ionic Hubbard model [see Chapter 5], employing such an ansatz is beyond the scope of the current work.

In the self-ordered phase we can solve the system of equations Eqs. (3.3) & (3.14) via exact diagonalization to find the effective Hamiltonian that satisfies the self-consistency condition. Note that the number of states of the respective basis set $\{n\}$ here typically limits the solvable system size. Due to the large Hilbert space we consider $L = 8$ for quarter filling and $L = 6$ for half filling to obtain spin-balanced states with $S^z = 0$. We will comment briefly on the influence of the total spin in Sec. 3.4.

Large temperature limit

We can identify regimes, where the effective temperature is almost exclusively determined by the cavity field and very weakly depends on microscopic details of the atomic subsystem. Important limits of the derived equations where this is the case are that of large dissipation $\Gamma, \Gamma^2/\delta \gg J/\hbar, U/\hbar, g\lambda$ or large pump-cavity detuning $\hbar\delta \gg U, J, \hbar g\lambda$. These limits are directly linked to a large effective temperature. It proves to be useful for the understanding of some of the explicit results presented in Chapter 6. Since in the considered limit $\mathrm{Im}[\chi_T(\omega)]$, which appears as a factor in Eq. (3.15), decays rapidly for $\hbar\omega > J, U, \hbar g\lambda$ further approximations can be made. We obtain for the remaining factor

$$\delta_\Gamma(\omega+\delta) \equiv \frac{\Gamma/2\pi}{\delta^2(1+\omega/\delta)^2+(\Gamma/2)^2} \approx \frac{\Gamma/2\pi}{\delta^2+(\Gamma/2)^2} - \frac{\omega\delta\Gamma/\pi}{(\delta^2+(\Gamma/2)^2)^2}.$$

Typically, in the large dissipation or large detuning limit the effective temperature is large compared to the other energy scales in the system. Therefore, we can simultaneously take the high temperature limit $\beta \to 0$, which permits us to approximate part of the integrand appearing in the energy transfer equation Eq. (3.15) by

$$\left(1-e^{-\beta\hbar\omega}\right)^{-1} \approx 1/2+1/\beta\hbar\omega.$$

In the integral over the resulting approximate integrand $\delta_\Gamma(\omega+\delta)\left(1-e^{-\beta\hbar\omega}\right)^{-1}$ odd functions in frequency ω drop out when integrating over the symmetric interval. We are therefore left with the even terms, which in leading order terms are independent of the frequency, as given below

$$\frac{\Gamma/4\pi}{\delta^2+(\Gamma/2)^2} - \frac{\delta\Gamma/\pi}{\hbar\beta(\delta^2+(\Gamma/2)^2)^2}.$$

In order to satisfy the steady state condition for the effective Hamiltonian $\frac{\partial}{\partial t}\langle\hat{H}_{\text{eff}}\rangle = 0$, the integrand needs to vanish. This results in a condition that we can solve for β

$$\beta \approx \frac{4\delta/\hbar}{\delta^2+(\Gamma/2)^2}. \tag{3.16}$$

We thus find an approximate analytical equation for the effective temperature in the large temperature, large dissipation limit that does not explicitly depend on the cavity field parameter λ.

3.2 Thermodynamic limit in the weak tunneling perturbation

We want to obtain analytical equations in the thermodynamic limit that allow us to estimate finite size effects that still prevail in the maximal system sizes we can solve within the exact-diagonalization approach. Further this provides us with an analytical base for the identification of physical processes driving the system towards its steady state in the low hopping limit (part of this section has been published in Ref. [1] and its Supplemental). Additionally, treating the kinetic term in the Hamiltonian as a perturbation permits to generalize our findings to higher dimensional systems. This approach is generally valid for slightly altered models in parameter regimes where the dominating terms in the respective Hamiltonian commutes with the atomic operator the cavity field couples to, i.e. here the sublattice imbalance $\hat{\Delta}$.

Starting from Eq. (3.14) we describe our analytical steps taken to finally reach Eq. (3.25a) based on a perturbation theory in the kinetic energy, assuming that the hopping amplitude J is the smallest energy scale in the system. Ultimately, interpreting the resulting energy transfer equations allows us to gain a better understanding of the physical processes which cause the fluctuation-induced bistability, as described in Sec. 6.3.

We split the effective Hamiltonian into an 'unperturbed' part $\tilde{H}_0$ and the perturbative kinetic part $\hat{H}_{\text{kin}}$

$$\hat{H}_{\text{eff}} = \tilde{H}_0 + \hat{H}_{\text{kin}} \quad \text{with} \quad \begin{aligned} \tilde{H}_0 &= U\sum_j \hat{n}_{j\uparrow}\hat{n}_{j\downarrow} - \hbar g\lambda\hat{\Delta} - \mu\sum_{j,\sigma}\hat{n}_{j,\sigma} \\ \hat{H}_{\text{kin}} &= -J\sum_{\langle j,l\rangle,\sigma}\left(\hat{c}^\dagger_{j\sigma}\hat{c}_{l\sigma} + \text{h.c.}\right). \end{aligned} \tag{3.17}$$

Note that we added a chemical potential term in $\tilde{H}_0$ in order to adjust the correct atomic filling that was previously implemented directly in the generation of the basis states. The susceptibility $\chi_T(\omega)$ appearing in Eq. (3.15) can be rewritten in terms of the perturbation $\hat{H}_{\text{kin}}$ as shown in the following. We will provide here an outline of the calculation. First, the equation of motion for the operator $\hat{\Delta}$ is computed. Since $\hat{\Delta}$ is diagonal in the basis of local densities all terms of $\hat{H}_{\text{eff}}$ except for the kinetic part commute with it and we obtain

$$\begin{aligned}\frac{\partial}{\partial t}\hat{\Delta}(t) &= \frac{\partial}{\partial t}e^{i\hat{H}_{\text{eff}}t/\hbar}\hat{\Delta}e^{-i\hat{H}_{\text{eff}}t/\hbar} = -\frac{i}{\hbar}e^{i\hat{H}_{\text{eff}}t/\hbar}\big[\hat{H}_{\text{eff}},\hat{\Delta}\big]e^{-i\hat{H}_{\text{eff}}t/\hbar} \\ &= -\frac{i}{\hbar}e^{i\tilde{H}_0t/\hbar}\big[\hat{H}_{\text{kin}},\hat{\Delta}\big]e^{-i\tilde{H}_0t/\hbar} = -\frac{i}{\hbar}\big[\hat{H}_{\text{kin}},\hat{\Delta}\big](t).\end{aligned} \tag{3.18}$$

Inserting this result into our expression for the susceptibility yields

$$\begin{aligned}\chi_T(\omega) &= -\frac{i}{\hbar}\int_0^\infty dt e^{i(\omega+i\epsilon)t}\big\langle\big[\hat{\Delta}(t),\hat{\Delta}(0)\big]\big\rangle_T = -\frac{1}{\hbar\omega}\int_0^\infty dt\frac{\partial}{\partial t}\big(e^{i(\omega+i\epsilon)t}\big)\big\langle\big[\hat{\Delta}(t),\hat{\Delta}(0)\big]\big\rangle_T \\ &\overset{P.I.}{=} -\frac{1}{\hbar\omega}\Big[e^{i(\omega+i\epsilon)t}\big\langle\big[\hat{\Delta}(t),\hat{\Delta}(0)\big]\big\rangle_T\Big]_0^\infty + \frac{1}{\hbar\omega}\int_0^\infty dt e^{i(\omega+i\epsilon)t}\frac{\partial}{\partial t}\big\langle\big[\hat{\Delta}(t),\hat{\Delta}(0)\big]\big\rangle_T \\ &= -\frac{i}{\hbar^2\omega}\int_0^\infty dt e^{i(\omega+i\epsilon)t}\big\langle\big[\big[\hat{H}_{\text{kin}},\hat{\Delta}\big](t),\hat{\Delta}(0)\big]\big\rangle_T \\ &= -\frac{1}{\hbar^2\omega^2}\int_0^\infty dt\frac{\partial}{\partial t}\big(e^{i(\omega+i\epsilon)t}\big)\big\langle\big[\big[\hat{H}_{\text{kin}},\hat{\Delta}\big](t),\hat{\Delta}(0)\big]\big\rangle_T \\ &\overset{P.I.}{=} -\frac{i}{\hbar^3\omega^2}\int_0^\infty dt e^{i(\omega+i\epsilon)t}\big\langle\big[\big[\hat{H}_{\text{kin}},\hat{\Delta}\big](t),\big[\hat{H}_{\text{kin}},\hat{\Delta}\big](0)\big]\big\rangle_T.\end{aligned} \tag{3.19}$$

In this calculation we used the time-translational symmetry $\big[\hat{\Delta}(t),\hat{\Delta}(0)\big] = \big[\hat{\Delta}(0),\hat{\Delta}(-t)\big]$ and performed partial integration (P.I.). One can then perform the perturbation theory starting from the susceptibility written with the double commutator expression. The evaluation of the thermal expectation values defined by $\langle ...\rangle_T = \text{Tr}\left[e^{-\beta\tilde{H}_0}...\right]$ is done with respect to the unperturbed Hamiltonian $\tilde{H}_0$, resulting in an expression that is perturbative in the kinetic terms to second order $\mathcal{O}(J^2)$. Explicitly calculating the commutators and expectation values yields

$$\big[\hat{H}_{\text{kin}},\hat{\Delta}\big](t) = e^{i\tilde{H}_0t/\hbar}\big[\hat{H}_{\text{kin}},\hat{\Delta}\big](0)e^{-i\tilde{H}_0t/\hbar} = 2Je^{i\tilde{H}_0t/\hbar}\Big(\sum_{\substack{\langle j,l\rangle,\alpha\\ j\in A}}\hat{c}^\dagger_{j\alpha}\hat{c}_{l\alpha} - \sum_{\substack{\langle j,l\rangle,\alpha\\ j\in B}}\hat{c}^\dagger_{j\alpha}\hat{c}_{l\alpha}\Big)e^{-i\tilde{H}_0t/\hbar}. \tag{3.20}$$

As we already established, the dominating unperturbed part of the Hamiltonian $\tilde{H}_0$ is only dependent on local densities, causing all contributions from processes that ultimately leave the initial density distribution in the evaluation of the expectation values $\big\langle\big[\big[\hat{H}_{\text{kin}},\hat{\Delta}\big](t),\big[\hat{H}_{\text{kin}},\hat{\Delta}\big](0)\big]\big\rangle_T$ to vanish. Therefore, we can discard most of the terms in the trace. For (hyper-)cubic lattices arbitrary dimensions, as we consider only terms up to $\mathcal{O}(J^2)$, we can do the following decomposition

$$\big\langle\big[\big[\hat{H}_{\text{kin}},\hat{\Delta}\big](t),\big[\hat{H}_{\text{kin}},\hat{\Delta}\big](0)\big]\big\rangle_T = \sum_s\big\langle\big[\big[\hat{H}^s_{\text{kin}},\hat{\Delta}\big](t),\big[\hat{H}^s_{\text{kin}},\hat{\Delta}\big](0)\big]\big\rangle_T. \tag{3.21}$$

Here, we separate the terms in each direction s of the hopping $\hat{H}_{\text{kin}}$ and rewrite them with the sum over s.

Before explicitly calculating the expectation value we rewrite the time dependent operators in order to avoid calculations with the operators in the time-evolution operator exponent. The fermionic annihilation operators evolving with the unperturbed Hamiltonian $\tilde{H}_0$ can be rewritten exactly by considering their action on the set of local basis states $\{|0\rangle, |\uparrow\rangle, |\downarrow\rangle, |\uparrow\downarrow\rangle\}$. We obtain

$$\hat{c}_{j\alpha}(t) = e^{it(g\lambda(-1)^j+\mu/\hbar)}\hat{c}_{j\alpha}\big(1-\hat{n}_{j\bar{\alpha}}+e^{iUt/\hbar}\hat{n}_{j\bar{\alpha}}\big).$$

Inserting this in Eq. (3.21) results the expectation value

$$\begin{aligned}\left\langle\left[\left[\hat{H}_{\text{kin}},\hat{\Delta}\right](t),\left[\hat{H}_{\text{kin}},\hat{\Delta}\right](0)\right]\right\rangle_T = -\frac{2iJ^2}{Z_d}\sum_{\substack{\langle j,l\rangle,\alpha\\ j<l}}&\sin\big(2g\lambda(-1)^j t\big)\left\langle(1-\hat{n}_{j\bar{\alpha}}-\hat{n}_{l\bar{\alpha}}+2\hat{n}_{j\bar{\alpha}}\hat{n}_{l\bar{\alpha}})(\hat{n}_{j\alpha}-\hat{n}_{l\alpha})\right\rangle_T\\ &+\sin\big((2g\lambda(-1)^j-U/\hbar)t\big)\left\langle\hat{n}_{j\bar{\alpha}}(1-\hat{n}_{l\bar{\alpha}})(\hat{n}_{j\alpha}-\hat{n}_{l\alpha})\right\rangle_T\\ &+\sin\big((2g\lambda(-1)^j+U/\hbar)t\big)\left\langle\hat{n}_{l\bar{\alpha}}(1-\hat{n}_{j\bar{\alpha}})(\hat{n}_{j\alpha}-\hat{n}_{l\alpha})\right\rangle_T,\end{aligned} \tag{3.22}$$

where Z_d is the partition function defined on the basis set of the d-dimensional unit cell, containing 2^d lattice sites.

In the following section we focus on the special case of a one-dimensional atomic system, as we treat it in our full effective model via exact diagonalization (ED), and explicitly compute the susceptibility and resulting energy transfer equation. We further derive the self-consistency equation and a condition for the particle number conservation at the same approximation level. We generalize the result by providing arguments for its validity also for two-dimensions and make predictions for higher dimensional cases in Sec. 3.2.2.

3.2.1 Results for a one-dimensional atomic system

In the thermodynamic limit, considering the kinetic terms to the order of $\mathcal{O}(J^2)$, the one-dimensional system is effectively reduced to a two-site unit cell. Since only processes that ultimately restore the initial density distribution have a finite contribution in the equations, the maximal distance process covered by a second order hopping process is 1. Since from here, all expectation values are calculated with respect to the thermal state we will drop the index T. Evaluating Eq. (3.22) in the one dimensional lattice, which is oriented in the direction of the cavity axis, the expectation values are given by

$$\begin{aligned}\left\langle\left[\left[\hat{H}_{\text{kin}},\hat{\Delta}\right](t),\left[\hat{H}_{\text{kin}},\hat{\Delta}\right](0)\right]\right\rangle = \frac{16iJ^2}{Z_{\text{1D}}}\Big[&2\sin(2g\lambda t)\big(e^{\beta\mu}+e^{\beta(3\mu-U)}\big)\sinh(\beta\hbar g\lambda)\\ &-\sin((2g\lambda-U/\hbar)t)e^{2\beta\mu}\big(1-e^{\beta(2\hbar g\lambda-U)}\big)\\ &+\sin((2g\lambda+U/\hbar)t)e^{2\beta\mu}\big(1-e^{-\beta(2\hbar g\lambda+U)}\big)\Big].\end{aligned} \tag{3.23}$$

We now insert this result into the expression for the susceptibility Eq. (3.19)

$$\begin{aligned}\chi_T(\omega) = \frac{16J^2}{\hbar^3\omega^2 Z_{\text{1D}}}\int_0^\infty dt e^{i(\omega-i\epsilon)t}\Big[&2\sin(2g\lambda t)\big(e^{\beta\mu}+e^{\beta(3\mu-U)}\big)\sinh(\beta\hbar g\lambda)\\ &-\sin((2g\lambda-U/\hbar)t)e^{2\beta\mu}\big(1-e^{\beta(2\hbar g\lambda-U)}\big)\\ &+\sin((2g\lambda+U/\hbar)t)e^{2\beta\mu}\big(1-e^{-\beta(2\hbar g\lambda+U)}\big)\Big]\\ = \frac{16J^2}{\hbar^3\omega^2 Z_{\text{1D}}}\Bigg[&\frac{2g\lambda}{(\omega+i\epsilon)^2-(2g\lambda)^2}\big(e^{\beta\mu}+e^{\beta(3\mu-U)}\big)\sinh(\beta\hbar g\lambda)\\ &-\frac{(2g\lambda-U/\hbar)}{(\omega+i\epsilon)^2-(2g\lambda-U/\hbar)^2}e^{2\beta\mu}\big(1-e^{\beta(2\hbar g\lambda-U)}\big)\\ &+\frac{(2g\lambda+U/\hbar)}{(\omega+i\epsilon)^2-(2g\lambda+U/\hbar)^2}e^{2\beta\mu}\big(1-e^{-\beta(2\hbar g\lambda+U)}\big)\Bigg].\end{aligned} \tag{3.24}$$

The energy transfer equation for the effective Hamiltonian, Eq. (3.15) is calculated in this perturbative approach where we used $\frac{A}{(\omega+i\epsilon)^2-A^2} = \frac{1}{2}\big(\frac{1}{\omega+i\epsilon-A}-\frac{1}{\omega+i\epsilon+A}\big)$ and $\lim_{\epsilon\to 0^+}\left[\text{Im}\left[\frac{1}{x+i\epsilon}\right]\right] = -\pi\delta(x)$ in order to simplify the expression. We finally arrive at

$$\frac{\partial}{\partial t}\langle \hat{H}_{\text{eff}}\rangle \propto J^2\Bigg[\left(\frac{-\exp(\beta\hbar g\lambda)}{(2\hbar g\lambda+\hbar\delta)^2+(\hbar\Gamma/2)^2}+\frac{\exp(-\beta\hbar g\lambda)}{(2\hbar g\lambda-\hbar\delta)^2+(\hbar\Gamma/2)^2}\right)\frac{e^{\beta\mu}+e^{\beta(3\mu-U)}}{2\hbar g\lambda} \tag{3.25a}$$
$$+\left(\frac{-\exp[\beta(2\hbar g\lambda-U)]}{(2\hbar g\lambda-U+\hbar\delta)^2+(\hbar\Gamma/2)^2}+\frac{1}{(2\hbar g\lambda-U-\hbar\delta)^2+(\hbar\Gamma/2)^2}\right)\frac{e^{2\beta\mu}}{2\hbar g\lambda-U}$$
$$+\left(\frac{-\exp[\beta(2\hbar g\lambda+U)]}{(2\hbar g\lambda+U+\hbar\delta)^2+(\hbar\Gamma/2)^2}+\frac{1}{(2\hbar g\lambda+U-\hbar\delta)^2+(\hbar\Gamma/2)^2}\right)\frac{e^{2\beta\mu}}{2\hbar g\lambda+U}\Bigg],$$

We also calculate the mean-field self consistency condition and the total particle-number per unit cell in the same local basis, which allows to determine the chemical potential μ required to fix the particle density to the desired filling as well as λ.

$$\langle\hat{n}\rangle=\frac{1}{Z_{1D}}\left(\cosh(\beta\hbar g\lambda)\left(e^{\beta\mu}+e^{\beta(3\mu-U)}\right)+e^{2\beta\mu}\left(2+e^{-\beta U}\cosh(2\beta\hbar g\lambda)\right)+e^{\beta(4\mu-2U)}\right) \tag{3.25b}$$

$$\lambda=\frac{2g\delta}{\delta^2+(\Gamma/2)^2}\frac{\langle\hat{\Delta}\rangle}{L^d}=\frac{1}{Z_{1D}}\frac{4g\delta}{\delta^2+(\Gamma/2)^2}\left(\sinh(\beta\hbar g\lambda)\left(e^{\beta\mu}+e^{\beta(3\mu-U)}\right)+e^{\beta(2\mu-U)}\sinh(2\beta\hbar g\lambda)\right) \tag{3.25c}$$

The partition function defined on the one dimensional two-site unit cell is given by

$$Z_{1D}=1+4\cosh(\beta\hbar g\lambda)\left(e^{\beta\mu}+e^{\beta(3\mu-U)}\right)+2e^{2\beta\mu}\left(2+e^{-\beta U}\cosh(2\beta\hbar g\lambda)\right)+e^{\beta(4\mu-2U)}. \tag{3.25d}$$

The steady state solutions in this thermodynamic low-hopping limit presented in Chapter 6, are obtained by simultaneously solving the coupled self-consistent equations Eqs. (3.25) for (μ,β,λ). Note that at the special case of commensurate filling $(N/L=1)$ with fixed on-site interactions the chemical potential takes a constant value of $\mu=U/2$, consequently reducing the system of equations to self-consistency and energy transfer equations.

3.2.2 The case of higher dimensional atomic lattices

Since we constrict to kinetic processes up to order $\mathcal{O}(J^2)$ it is reasonable to expect one can retrieve results that are qualitatively similar to the previously presented case of a one-dimensional atomic system for configurations with a higher dimensional underlying lattice. Note that in an experimental setup one would need to ensure a lattice and pump geometry that ensures the staggered coupling to the field with respect to neighboring sites in opposite fashion. In two dimensions, this could be achieved by a relative angle of the lattice axes relative to the cavity axis and a corresponding adjustment of the cavity resonance and lattice spacing. If one goes to higher dimensions or slightly altered lattice geometries one might need to resort to a configuration involving multiple pump beams. We sketch the layout for one and two dimensions involving a single pump beam below, where circles represent lattice sites. Neighboring sites are located on either an intensity maximum or minimum of the nodes of the standing-wave cavity field.

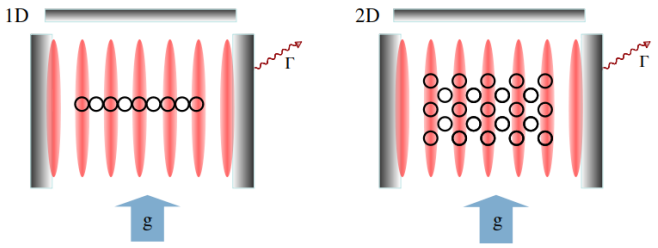

In Eq. (3.21) the commutators entering the calculation of the susceptibility $\chi_T(\omega)$ can be decomposed into independent contributions stemming from each direction of the external lattice the atoms are confined to. Any hopping processes involving a tunneling of the atoms along more than one lattice direction and still fulfilling the condition that they need to return to the initial density distribution are of higher order of the hopping, at least $\mathcal{O}(J^4)$. We therefore expect dimensionality to enter via a multiplicative factor in the susceptibility, leaving the overall shape of the equations unchanged. The factor entering dependent on the dimension in which the atoms are confined could be interpreted as a rescaled tunneling amplitude J'.

As we are mainly interested in the steady state solution of the energy transfer Eq. (3.25a), the steady state solution remains unaffected by the specific lattice dimension. However, the dynamics of these systems could very well differ even at the same level of approximation since the rates of the processes driving the system towards the steady state very much depend on both the dimensionality and lattice coordination number Z. Generally, one would expect a higher dimensional system to thermalize more quickly since it suffers less from Pauli-blocking than the one dimensional chain.

The agreement of the steady state results is explicitly confirmed by us for the case of a two-dimensional square lattice as sketched above. Here, one reduces the system description to local 2×2-site unit cells in Eq. (3.22) and, by noting that the partition function is $Z_{\mathrm{2D}} = Z_{\mathrm{1D}}^2$, the obtained equations are proportional to those presented for the one-dimensional case Eqs. (3.25). Details of the calculation are provided in Appendix A.2.

3.2.3 Role of individual terms in the energy transfer equation

In this section we want to provide some details on how we solve the system of equations Eqs. (3.25) and look at the analytical properties of the individual terms appearing in the energy transfer equation.

We did confirm that for the parameter range shown in the following Chapter 6 the results obtained using the system of equations Eqs. (3.25) agree with those obtained going to higher order in the perturbation theory [see Appendix A.3 for details] within the limits of the numerical accuracy reached. Therefore, since the calculation without corrections is faster and more stable, we will use the system of equations Eqs. (3.25) if not stated otherwise.

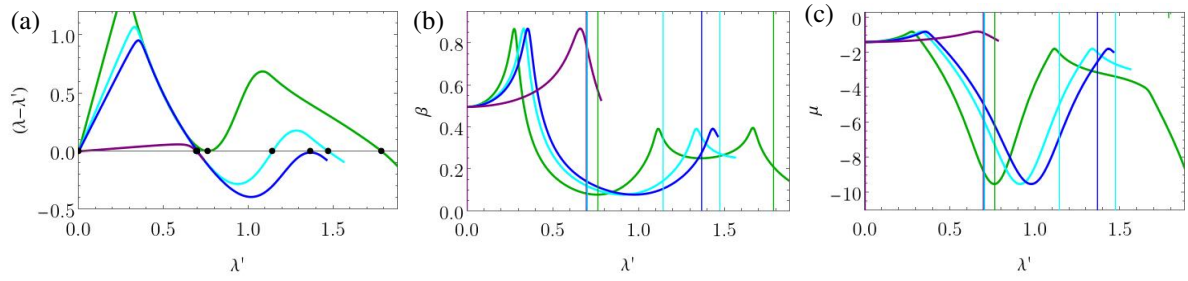

Fig. 3.3: Graphical solution of the self-consistency condition for several values of the atom-cavity coupling $\hbar g/J$ across the bistability region. (a) Self-consistency condition Eq. (3.25c), (b) effective temperature β and (c) chemical potential μ solving Eq. (3.25a) & (3.25b). The system of infinite size is at quarter-filling with $U/J = 40$, $\hbar\delta/J = 8$, $\hbar\Gamma/J = 1$. The values of $\hbar g/J$ are colored as follows: 6.0 (purple), 11.2 (blue), 12.0 (cyan), 14.4 (green). Vertical lines in (b),(c) denote solutions of the self-consistency condition at the respective $\hbar g/J$. Note all curves are plotted up to the maximal value $\lambda'_{\mathrm{max}} = \frac{2g\delta}{\delta^2+(\Gamma/2)^2}\frac{N}{L}$.

The system of equations is solved numerically by simultaneously determining the parameter set (μ, β, λ) that satisfies all three equations. To determine the solution points, several zero-point methods have been tested of which the "ConjugateGradient"-algorithm showed to be the most stable one. We typically generate random initial values $(\mu_0, \beta_0, \lambda_0)$ within a given interval and check to see if the system of equations is solved to the requested accuracy, which we set to $\epsilon = 10^{-12}$. If it fails to converge, the step is repeated with altered initial values. We monitor the algorithms by explicitly solving the particle conservation equation and energy transfer equation at varying given values of λ' and graphically solving the resulting curve for the self-consistency condition that is fulfilled at its zero crossings where $\lambda' = \lambda$ [see Fig. 3.3]. Increasing $\hbar g/J$ one typically moves from one zero-crossing at $\lambda = 0$, which is the trivial solution, to two crossings (purple line) at a value we will refer to as g_{cr} in the following Chapter 6. There we present our results and provide insight into the physical processes. Depending on the relative system parameters, one either remains with the two solutions, or enters an interval $[g_{\mathrm{bi},1}, g_{\mathrm{bi},2}]$ where multiple zero-crossings occur. For the parameters shown in the figure, at $\hbar g_{\mathrm{bi},1}/J \approx 11.2$ (blue curve) the second local maximum developing in the self-consistency curve touches 0 around $\lambda = 1.37$. Increasing the coupling further the maximum moves across the 0-axis, entering the regime with 4 solutions (cyan curve) until the intermediate minimum moves up and becomes positive around $\hbar g_{\mathrm{bi},1}/J \approx 14.4$ (green curve).

As derived in Sec. 3.2.1, the energy transfer in this perturbative approach is given by Eq. (3.25a). Here, comparing to the spectral representation of the full energy transfer equation Eq. (3.14), one can interpret the contributions in

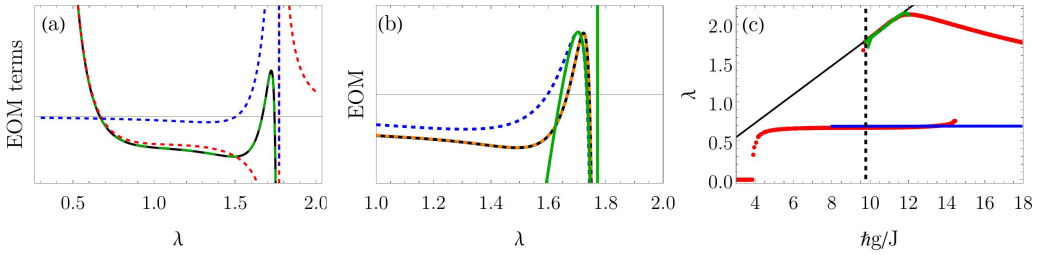

Fig. 3.4: Sign of the terms $\propto 1/(2g\lambda - U/\hbar)$ in Eq. (3.25a) line 2, showing whether the processes heat (red) or cool (blue) the atomic subsystem and the numerical solution to the full system of equations Eqs. (3.25a)-(3.25c) (black).

the upper line as originating from eigenstates of $\hat{H}_{\text{eff}}$, which are singly occupied on the lower potential or upper potential sub-lattice, i.e. $E_n - E_m \approx 2\hbar g\lambda$, and the lower lines stemming from states with double occupancies, or two singly occupied sites where the interaction energy is important, i.e. $E_n - E_m \approx 2\hbar g\lambda \mp U$.

The sign of the terms in Eq. (3.25a) implies either a cooling or a heating nature of the processes in the self-consistent dynamics towards the steady state. In the exemplary parameter region we show here, multiple stable solutions $\lambda_{1,2}$ exist at one pump strength $\hbar g/J$ [see black curve in Fig. 3.4]. For the first solution (low λ_1) the terms $\propto 1/(2g\lambda)$ are sufficient to reproduce the full solution. The temperature to balance the cooling (first term upper line) and heating (second term upper line) is relatively high $k_B T_1 > 8J$. In contrast, for the second, higher photon density solution, the effective temperature is much lower and also the states with double occupancies captured by the second line $\propto 1/(2g\lambda - U/\hbar)$ in Eq. (3.25a) become important. In particular, the efficient transfer of heat from the atoms to the photonic degrees of freedom, due to the resonances between excited states and the photonic energy, leads to a cooling mechanism which drives the atoms to a steady state with a much lower temperature in the bistable region. We will comment on this in more detail and also provide a clear picture of the resulting physical processes in Chapter 6. Since $2g\lambda_2 > U/\hbar$ the process reducing sublattice imbalance $\hat{\Delta}$ while creating a double occupancy on the low potential sublattice while simultaneously adding a photon to the cavity field heats the system while the same process simultaneously removing a photon cools it.

We further look at the weight of the individual basis state configurations of the 2-site unit cell in our perturbative approach [see Fig. 3.5]. This is done by evaluating $\langle \exp[-\beta \hat{H}_{\text{eff}}] \rangle_{2j,2j+1} / Z_{1\text{D}}$ with respect to every two-site configuration on $|2j, 2j+1\rangle$ where $Z1\text{D}$ is the partition function defined on the unit cell [see Eq. (3.25d)]. Note that, without loss of generality, we only show two-site configurations where the first site belongs to the low potential sublattice. However, since at the here considered level of perturbation in the hopping, the states $|n_1, n_2\rangle_{2j,2j+1}$ and $|n_2, n_1\rangle_{2j-1,2j}$ would yield the same contribution we omit from explicitly showing them. The most relevant density-matrix elements are shown as a function of both the externally given coupling strength $\hbar g/J$ [Fig. 3.5 (a)] as well as the resulting self-consistently determined atom-cavity coupling $\hbar g\lambda/J$ [Fig. 3.5 (b)]. We note that for the parameters in the large interaction limit $U/J = 40$ at quarter filling, the basis states that carry the largest probability weights remain those with either the empty unit cell $|0, 0\rangle_{2j,2j+1}$ or singly occupied low potential sublattice site $|\uparrow, 0\rangle_{2j,2j+1}$; $|\downarrow, 0\rangle_{2j,2j+1}$. Most interestingly, extreme points seem to be directly connected to special points like $2g\lambda = \delta$ (cyan dashed vertical line in Fig. 3.5 (b)) or $2g\lambda = U \pm \delta$ (orange dashed vertical lines). The significance of these cavity and many-body resonances and their influence on the physical properties of the steady state will be one of the main focus points of the results presented in Chapter 6.

3.3 Stability condition for in many-body adiabatic elimination

In order to determine which of the self-consistent solutions from our self-consistent equations of motion are stable, we check the stability against small perturbations in the cavity field for both the full effective model at finite size [Sec. 3.3.1] and in the thermodynamic low hopping limit [Sec. 3.3.2]. For atomic systems in a pure state a stability condition has previously been derived, see e.g. in Refs. [78, 171, 172]. Here, we again want to go beyond the $T = 0$ MF approach by extending the derivation for systems where the atomic state is described by a density matrix, more specifically, by a thermal state.

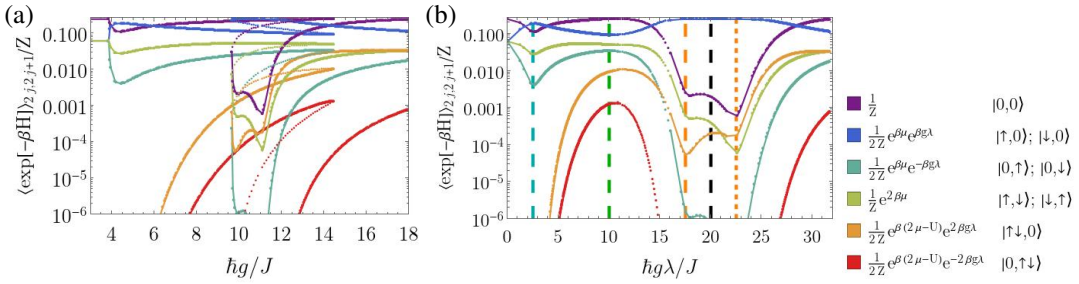

Fig. 3.5: Most relevant elements of the density matrix $\langle \exp[-\beta \hat{H}_{\text{eff}}] \rangle_{2j,2j+1}/Z$ as a function of (a) the coupling strength $\hbar g/J$ and (b) the effective lattice imbalance $\hbar g\lambda/J$ in logarithmic scale for $L = 8$ at quarter filling. The color legend shows the term in the energy transfer equation Eq. (3.25a) in the thermodynamic limit and the corresponding occupations of the two-site unit cell where the first site is the low-potential site $|2j, 2j+1\rangle$. The parameters used are $U/J = 40$, $\hbar\delta/J = 5$, $\hbar\Gamma/J = 3$. Vertical lines in (b) denote the resonances, $2g\lambda_1 = \delta$ (cyan), $2g\lambda = U/\hbar$ (black, dashed), $2g\lambda_2 = U/\hbar \pm \delta$ (orange, short/long-dashed), $4g\lambda_2 = U/\hbar - \delta$ (green, dashed).

3.3.1 Derivation of the stability condition

To determine the stability, we consider the behavior of the inverse temperature $\beta(\lambda)$, the eigenenergies of the corresponding atomic effective Hamiltonian $E_n(\beta, \lambda)$ and the matrix elements $\Delta_{nm}(\lambda)$ of the imbalance operator under linear deviations of the cavity field $\tilde{\lambda}$. In this section, all expectation values are evaluated using the self-consistently determined thermal steady states. As in the previous section to simplify the notation we drop the sub-index $\langle ... \rangle_T = \langle ... \rangle$. The equations of motion for the quadratures of the cavity field are defined as

$$\lambda = \langle \hat{a}^\dagger + \hat{a} \rangle / \sqrt{L^d}, \qquad p = i \langle \hat{a}^\dagger - \hat{a} \rangle / \sqrt{L^d}. \tag{3.26}$$

Using the known dynamics of the jump operator $\hat{a}$, given by

$$\frac{d}{dt}\langle \hat{a} \rangle = -i\delta \langle \hat{a} \rangle - \frac{\Gamma}{2}\langle \hat{a} \rangle + i\frac{g}{\sqrt{L^d}} \langle \hat{\Delta} \rangle^{(s)},$$

one easily obtains the equations for the quadratures

$$\frac{d\lambda}{dt} = -\frac{\Gamma}{2}\lambda + \delta p, \qquad \frac{dp}{dt} = -\delta\lambda - \frac{\Gamma}{2}p + \frac{2g}{L^d}\langle \hat{\Delta} \rangle^{(s)},$$

where the expectation value $\langle ... \rangle^{(s)}$ is computed in the steady state thermal density matrix.

The stationary solutions of the equations can be calculated as

$$\lambda^{(s)} = \frac{2\delta g}{\delta^2 + (\Gamma/2)^2} \frac{\langle \hat{\Delta} \rangle^{(s)}}{L^d}, \qquad p^{(s)} = \frac{\Gamma g}{\delta^2 + (\Gamma/2)^2} \frac{\langle \hat{\Delta} \rangle^{(s)}}{L^d}. \tag{3.27}$$

To study the stability linear fluctuations around the stationary solutions marked by (s) are taken into account

$$\lambda = \lambda^{(s)} + \tilde{\lambda}, \qquad p = p^{(s)} + \tilde{p}, \qquad \langle \hat{\Delta} \rangle = \langle \hat{\Delta} \rangle^{(s)} + \frac{\mathrm{d}\langle \hat{\Delta} \rangle^{(s)}}{\mathrm{d}\lambda^{(s)}} \tilde{\lambda}. \tag{3.28}$$

The derivative of the expectation value of the atomic imbalance, obtained in the self-consistent thermal state $\langle \hat{\Delta} \rangle^{(s)} = \frac{1}{Z_d(\lambda)} \sum_n e^{-\beta(\lambda)E_n(\lambda)} \Delta_{nn}$, with respect to the stationary solution yields

$$\begin{aligned} \frac{\mathrm{d}\langle \hat{\Delta} \rangle^{(s)}}{\mathrm{d}\lambda^{(s)}} &= \frac{1}{Z_d(\lambda)^2} \sum_n \frac{\partial}{\partial\lambda} \left[e^{-\beta(\lambda)E_n(\lambda)} \Delta_{nn}(\lambda) \right] Z_d(\lambda) + \left[e^{-\beta(\lambda)E_n(\lambda)} \Delta_{nn}(\lambda) \right] \frac{\partial}{\partial\lambda} Z_d(\lambda) \\ &= \frac{1}{Z_d} \sum_n e^{-\beta E_n} \left[\frac{\partial \Delta_{nn}}{\partial\lambda} - \Delta_{nn} \left(\frac{\partial\beta}{\partial\lambda} E_n + \beta \frac{\partial E_n}{\partial\lambda} \right) \right] + \frac{1}{Z_d^2} \sum_{n,m} e^{-\beta(E_n+E_m)} \Delta_{nn} \left(\frac{\partial\beta}{\partial\lambda} E_m + \beta \frac{\partial E_m}{\partial\lambda} \right). \end{aligned} \tag{3.29}$$

The dynamics resulting from the inclusion of linear fluctuations is given by

$$\frac{d\tilde{\lambda}}{dt} = -\frac{\Gamma}{2}\tilde{\lambda} + \delta\tilde{p}, \qquad \frac{d\tilde{p}}{dt} = -\delta\lambda - \frac{\Gamma}{2}\tilde{p} + \frac{2g}{L^d}\frac{\mathrm{d}\langle\hat{\Delta}\rangle^{(s)}}{\mathrm{d}\lambda^{(s)}}\tilde{\lambda}. \tag{3.30}$$

We aim do derive a condition that determines whether the fluctuations are suppressed in the dynamics, leading to a stable steady state, as opposed to the case where slight deviations from the steady state value diverge. This can be achieved by putting a constraint on the Jacobian eigenvalues for the system of equations Eqs. (3.30) given by

$$k_\pm = -\frac{\Gamma}{2} \pm \sqrt{-\delta^2 + \frac{2g\delta}{L^d}\frac{\mathrm{d}\langle\hat{\Delta}\rangle^{(s)}}{\mathrm{d}\lambda^{(s)}}}. \tag{3.31}$$

For a stable solution, the eigenvalues must satisfy $\mathrm{Re}\{k_\pm\} < 0$. Since here we consider the pump laser to be red detuned from the cavity resonance we can assume $\delta \geq 0$. With Eq. (3.31) this results in the condition

$$\begin{aligned}\frac{\delta^2 + (\Gamma/2)^2}{2\delta g} > &\frac{1}{L^d Z_d}\sum_n \mathrm{e}^{-\beta E_n}\left[\frac{\partial\Delta_{nn}}{\partial\lambda} - \Delta_{nn}\left(\frac{\partial\beta}{\partial\lambda}E_n + \beta\frac{\partial E_n}{\partial\lambda}\right)\right] \\ &+ \frac{1}{L^{2d}Z_d^2}\sum_{n,m}\mathrm{e}^{-\beta(E_n+E_m)}\Delta_{nn}\left(\frac{\partial\beta}{\partial\lambda}E_m + \beta\frac{\partial E_m}{\partial\lambda}\right).\end{aligned} \tag{3.32}$$

This condition distinguishes between stable and unstable thermal steady states under fluctuations of the cavity field. Since it depends on multiple derivatives the numerical convergence when calculating the right hand side needs to be carefully monitored. Especially around the special points where the number of solutions to the self-consistency condition changes and therefore the slope of the function around the solution-points becomes really flat, some convergence issues might arise.

For completeness we state here the stability condition at the $T = 0$ MF level

$$\frac{\delta^2 + (\Gamma/2)^2}{4\delta g} > \frac{\mathrm{d}\langle\hat{\Delta}\rangle^{(s)}}{\mathrm{d}\lambda^{(s)}}. \tag{3.33}$$

This will mostly be applied in the discussion of our results at half filling Sec. 6.2.

3.3.2 Stability condition in the thermodynamic limit in the weak tunneling perturbation

By evaluating the obtained stability condition in the local unit cell basis as introduced in Sec. 3.2, we obtain an analytical equation determining the stability in the thermodynamic low-hopping limit. It results in solving

$$\frac{\delta^2 + (\Gamma/2)^2}{2\delta g} > \frac{\mathrm{d}\langle\hat{\Delta}\rangle^{(s)}}{\mathrm{d}\lambda^{(s)}} = \left(\frac{\partial\mathrm{Tr}\left[e^{-\beta\tilde{H}_0}\hat{\Delta}\right]}{\partial\lambda^{(s)}}Z_{1D} - \frac{\partial Z_{1D}}{\partial\lambda^{(s)}}\mathrm{Tr}\left[e^{-\beta\tilde{H}_0}\hat{\Delta}\right]\right)/(Z_{1D}^2) \tag{3.34}$$

with

$$\begin{aligned}\frac{\partial\mathrm{Tr}\left[e^{-\beta\tilde{H}_0}\hat{\Delta}\right]}{\partial\lambda^{(s)}} =& \left(g\frac{\partial\beta}{\partial\lambda^{(s)}}\cosh(\beta g\lambda) + \sinh(\beta g\lambda)\left(\frac{\partial\beta}{\partial\lambda^{(s)}}\mu + \beta\frac{\partial\mu}{\partial\lambda^{(s)}}\right)\right)e^{\beta\mu} \\ &+3\left(g\frac{\partial\beta}{\partial\lambda^{(s)}}\cosh(\beta g\lambda) + \sinh(\beta g\lambda)\left((3\mu - U)\frac{\partial\beta}{\partial\lambda^{(s)}} + 3\beta\frac{\partial\mu}{\partial\lambda^{(s)}}\right)\right)e^{\beta(3\mu-U)} \\ &+\left(2g\frac{\partial\beta}{\partial\lambda^{(s)}}\cosh(2\beta g\lambda) + \sinh(2\beta g\lambda)\left(\frac{\partial\beta}{\partial\lambda^{(s)}}(2\mu - U) + 2\beta\frac{\partial\mu}{\partial\lambda^{(s)}}\right)\right)e^{\beta(2\mu-U)}\end{aligned} \tag{3.34a}$$

$$\begin{aligned}\frac{\partial Z_{1D}}{\partial\lambda^{(s)}} =& 4\cosh(\beta g\lambda)\left(e^{\beta\mu}\left(\frac{\partial\beta}{\partial\lambda^{(s)}}\mu + \beta\frac{\partial\mu}{\partial\lambda^{(s)}}\right) + e^{\beta(3\mu-U)}\left(\frac{\partial\beta}{\partial\lambda^{(s)}}(3\mu - U) + 3\beta\frac{\partial\mu}{\partial\lambda^{(s)}}\right)\right) \\ &+2\left(\frac{\partial\beta}{\partial\lambda^{(s)}}(2\mu - U) + 2\beta\frac{\partial\mu}{\partial\lambda^{(s)}}\right)\left(\cosh(2\beta g\lambda)e^{\beta(2\mu-U)} + e^{2\beta(2\mu-U)}\right) \\ &-4\frac{\partial\beta}{\partial\lambda^{(s)}}g\left(\sinh(\beta g\lambda)\left(e^{\beta\mu} + e^{\beta(3\mu-U)}\right) + \sinh(2\beta g\lambda)e^{\beta(2\mu-U)}\right) \\ &+8e^{2\beta\mu}\left(\frac{\partial\beta}{\partial\lambda^{(s)}}\mu + \beta\frac{\partial\mu}{\partial\lambda^{(s)}}\right).\end{aligned} \tag{3.34b}$$

3.3.3 Computation

In practice, due to their complexity, we numerically evaluate the condition in Eq. (3.32) for the solutions of Eqs. (3.25) for both the small system exact-diagonalization and in perturbative approach in the thermodynamic limit. In order to obtain more robust numerical results we evaluate the derivatives using a five-point finite differences scheme with a small step size ϵ

$$f'(\lambda) = \frac{-f(\lambda+2\epsilon) + 8f(\lambda+\epsilon) - 8f(\lambda-\epsilon) + f(\lambda-2\epsilon)}{12\epsilon}. \tag{3.35}$$

We evaluate the condition for various step sizes to ensure the convergence of the derivation scheme. Note however, that in some parameter configurations the vanishing slope of one of the curves, especially around the bistability edges can make it difficult to obtain reliable results. This mostly is the case around parameters where the number of solutions to the self-consistency changes. In the results presented, whenever the stability can not be clearly determined we present the points as *unstable* or *ambiguous*.

3.4 Symmetry sectors

We note that in our exact-diagonalization calculations we generally investigate the case of equal number of spin up and down but do not consider explicitly the total spin quantum number symmetry. Numerically, we checked the temperature in each symmetry sector separately and obtain agreeing results for $s < s_{\max}$, while the sector with $s = s_{\max}$ reproduces the $U \to \infty$ results, since no on-site interaction is possible. This is shown for exemplary parameters in Fig. 3.6 for the pair of parameters (β, λ) that determine the steady state of our effective model. We constrict to $S^z = 0$ and show the solutions to Eq. (3.3) & (3.14) within the individual S^2 symmetry sectors with quantum numbers $s(s+1)$.

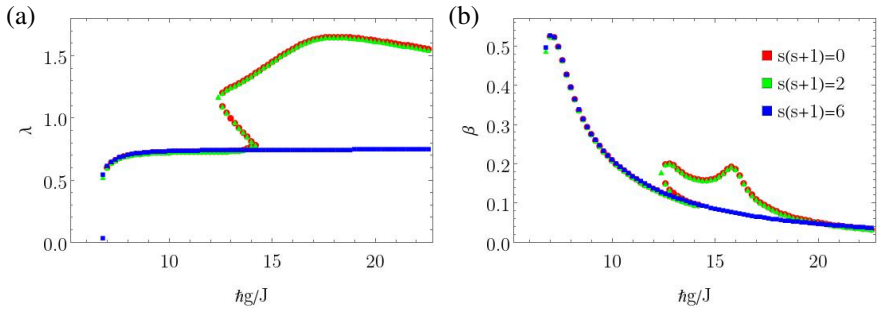

Fig. 3.6: (a) cavity field order parameter $\lambda = \langle \hat{a}^\dagger + \hat{a} \rangle / \sqrt{L}$, (b) effective inverse temperature β as a function of the atom-cavity coupling strength $\hbar g/J$ for $S_z = 0$ in individual S^2 symmetry sectors with quantum number $s(s+1)$. Parameters used are $U/J = 40$, $\hbar\Gamma/J = 3$, $\hbar\delta/J = 10$.

Summary

In this chapter we presented the derivation of our analytical method, the *many-body adiabatic elimination*, that allows us to go beyond standard mean field approaches by taking into account fluctuations in the atom-cavity coupling. With a thermal state assumption for the atomic subsystem, we arrived at a coupled system of equations that determines the steady state of the effective model by two parameters, namely the cavity field order parameter λ and the effective inverse temperature of the atoms β. It can be solved via exact diagonalization of the effective Hamiltonian for finite system sizes.

We further derived a thermodynamic limit in the weak tunneling perturbation that results in numerically solvable equations that show to be valid in arbitrary dimensions. Additionally, a condition for stability of the thermal steady state solutions under variations in the cavity field were established for both the full effective model and in the perturbation. These prove to be valuable to determine whether an obtained solution is physical.

Finally, we briefly commented on the influence of the total spin quantum number on the found steady states.

Chapter 4

Numerical tensor network methods

We present our implementation of the many-body atoms-cavity coupled model introduced in Chapter 2 in the framework of tensor network states. This chapter introduces the techniques and limits of using tensor networks to simulate the dynamics of large globally interacting many-body systems in contact with a Markovian environment. The numerically exact time evolution is a powerful tool that can be applied to a broad class of complex quantum systems to gain information about the dynamics on short time scales as well as in the long time limit. It is therefore generally interesting to develop new methods in this framework and find algorithms that allow to efficiently evolve systems that feature an intricate interplay of energy scales. In our specific case the comparison to the steady state analytic results is further motivation to develop these methods, since they take all correlations of the system into account. Therefore, it allows us to gain insight into the out-of equilibrium dynamics across the self-ordering transition, the influence of correlations in the long time limit and much more.

We introduce our new algorithm for the spinful fermionic systems. While it is based on a combination of several already established methods [119, 120], we brought it over to the fermionic coupled system and merged them in an efficient code using the iTensor library [173] that tackles the most challenging points of the time evolution of globally interacting dissipative systems.

Following the steps of our algorithm, we introduce the most important methods used. To begin with, the representation of quantum states with matrix product states (MPS) is shown in Sec. 4.1. This allows to perform a quasi exact simulation of the time evolution dynamics of complex, interacting quantum many-body systems. We further introduce some of the standard algorithms, like a variational ground state search for closed systems [Sec. 4.2.2] that we use to initialize our simulation. The time evolution is based on either Trotterization combined with swap gates [Sec. 4.2.3] or the time dependent variational principle (TDVP) [Sec. 4.2.4].

Completing the algorithm, we show how to account for the Lindbladian dynamics with non-unitary time evolution by implementing and comparing two main methods [Sec. 4.2]. To begin with, an algorithm using purification of the density matrix is outlined in Sec. 4.2.6. To our knowledge, this is the first implementation of the purification ansatz for the atom-cavity coupled system. Due to the drastic enlargement of the explored Hilbert space with this method, we are however restricted to very small system sizes. To reach larger systems, an algorithm using Monte-Carlo-Wavefunctions (MCWF) is introduced in Sec. 4.2.5.

4.1 Matrix product states (MPS) representation of quantum states

Matrix product states (MPS) are an efficient way to approximately represent the quantum many body wavefunction of a one-dimensional system. Its large set of degrees of freedom that grows exponentially with the system size, is reduced to the most important contributions. The goal of matrix products states is to expand the state vector coefficient into a product of local tensors using singular value decomposition (SVD) which is one of the most important, well-known tools in linear algebra. The decomposition of a general matrix $M = M_{i,j}$ of dimension

$n \times m$ is performed as

$$M_{i,j} = \sum_{\alpha} U_{i,\alpha} S_{\alpha} V^{\dagger}_{\alpha,j}. \tag{4.1}$$

Where U and V are matrices of dimensions $n \times n$ and $m \times m$ respectively and $\dagger$ denotes the conjugate transpose. The $n \times m$ singular value matrix is S with non-negative singular values s_α on the diagonal. One can see the singular values in a way as the "weights" of the columns of U and V. In the context of quantum states one often calls it "Schmidt-decomposition" and the singular values "Schmidt coefficients".

For physical states, the weight of the individual states in the wavefunctions is typically given by a high-dimensional coefficient matrix. For a system on a chain of length L this is typically expanded into a product of L local tensors representing the individual system sites via successive application of the singular value decomposition.

$$|\psi\rangle = \sum_{\sigma_1..\sigma_L} c_{\sigma_1..\sigma_L} |\vec{\sigma}\rangle = \sum_{\sigma_1..\sigma_L} \sum_{a_1..a_{L-1}} M^{\sigma_1}_{1,a_1} M^{\sigma_2}_{a_1,a_2} ... M^{\sigma_L}_{a_{L-1},1} |\vec{\sigma}\rangle \tag{4.2}$$

with the local tensors $M^{\sigma_i}_{a_{i-1},a_i}$ and $|\vec{\sigma}\rangle \equiv |\sigma_1, ...\sigma_L\rangle$. Here σ_i is a physical index of dimension d that depends on the atomic degrees of freedom like site-occupation, spin degree of freedom etc. For the here presented case of $spin-1/2$ we have $d=4$ and $\sigma_j \in \{0, \uparrow, \downarrow, \uparrow\downarrow\}$. The a_j are so-called bond indices with dimension determined by the number of singular values obtained in the decomposition. The singular value matrices are contracted to either the left- or right side by multiplying them to the respective matrix, yielding the MPS in left- or right-canonical form. We alternatively call the resulting states left- or right-normalized. The dimension of the matrix product is given by $(1 \times d), (d \times d^2), ..(d^{L/2-1} \times d^{L/2}), (d^{L/2} \times d^{L/2-1}), .., (d \times 1)$, i.e. the dimension of the center bond grows exponentially.

The entanglement between the subsystems left and right of a bond index a_j that connects two site tensors, can be accessed in form of the singular values, and poses a criterion for truncation of the local Hilbert spaces. The bond dimension M' needed to meet the set truncation error strongly depends on the von-Neumann bond entropy $M' \propto \exp(S_{\text{vN}})$. In this context S_{vN} measures the computational entanglement present in the MPS [174, 175]. The lower the entropy, the faster the weight of contributing states decays. The number of relevant Eigenvalues is restricted by the so-called Lieb-Robinson bound. For local Hamiltonians it is restricted to a sub-linear growth as the system evolves in time.

While the decomposition is exact, one typically aims to reduce the dimensionality of the system to increase the computational efficiency. This is achieved by truncating matrix dimensions by only keeping the largest singular values in the decomposition. One can control the truncation error ϵ by setting a limit on either the combined weight of the discarded values or restricting to a maximal number of values to keep.

$$\epsilon_j(M') = \sum_{a_j \geq M'} s^2_{a_j} \tag{4.3}$$

All values that do not fulfill these conditions are set to zero. This reduces the maximal matrix dimensions to rank $M' \leq M$. In an analogous way to the MPS one can define a tensor representation of operators $\hat{O}$ like the Hamiltonian or Lindbladian operators which can in general act on different sites of the wavefunction in tensor network representation. The matrix product operators (MPO) is represented by the product of local rank-4 tensors

$$\hat{O} = \sum_{\substack{\sigma_1,..\sigma_L \\ \sigma'_1,..\sigma'_L}} c^{(\sigma_1,..\sigma_L),(\sigma'_1,..\sigma'_L)} |\vec{\sigma}\rangle \langle\vec{\sigma}| = \sum_{\substack{\sigma_1,..\sigma_L \\ \sigma'_1,..\sigma'_L}} \sum_{b_1,..b_{L-1}} W^{\sigma_1,\sigma'_1}_{1,b_1} W^{\sigma_2,\sigma'_2}_{b_1,b_2} ... W^{\sigma_L,\sigma'_L}_{b_{L-1},1} |\vec{\sigma}\rangle \langle\vec{\sigma}| . \tag{4.4}$$

Here, in correspondence to their "bra" or "ket" counterparts, one calls the indices σ_j acting on the "ket" state physical indices and the indices σ'_j acting on the "bra" state auxiliary indices.

4.1.1 Graphical tensor notation

In order to visually represent complicated tensor-algorithms, we use an intuitive graphical notation proposed by Roger Penrose [176].

As shown below, tensors are represented by squares, while the order of the tensor is given by the number of lines going out. A scalar is thus drawn as a simple square, a vector has one index-line and a matrix two.

This scheme can be continued for arbitrary dimensions. The direction of the lines can be defined to represent indices in the normal and dual vector space. Here, for the physical indices lines coming out the top are indices of the normal space while lines coming out the bottom side are in the dual space. Vertical lines are bond indices as will be introduced in the next section.

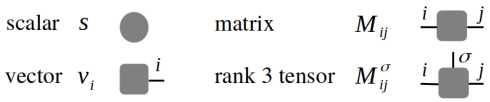

Connecting two lines represents a contraction of the respective indices. Alluding to the graphical notation, indices that are not contracted are also called open indices.

In this framework, the MPS decomposition of a wavefunction Eq. (4.2) for a system with L sites can be written as

and correspondingly for a matrix product operator Eq. (4.4), i.e. an operator that acts on the whole system

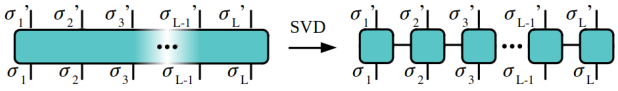

4.1.2 Measuring observables with MPS

A general local operator can be written as $\hat{A}_j = \sum_{\sigma_j,\sigma_j'} A^{\sigma_j,\sigma_j'} |\sigma_j\rangle \langle\sigma_j'|$. Putting the orthogonality center of the MPS $|\psi\rangle$ to site j, all sites to its left are left-normalized and to its right right-normalized. Calculating $\langle\psi| \hat{A}_j |\psi\rangle$ one can efficiently contract all left- and right-normalized tensors respectively.

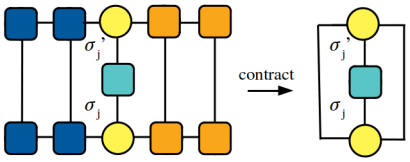

With these basics we now proceed to introduce our newly developed algorithm to perform the time evolution of our interacting fermionic system globally coupled to a dissipative cavity field.

4.2 Time dependent Matrix product state (tMPS) methods for dissipative atoms-cavity coupled systems

The dynamics of an open quantum system are typically characterized by the interplay between the intrinsic unitary dynamics, determined by the Hamiltonian $\hat{H}$, and the coupling to the environment. The environment causes the non-unitary part of the time evolution and quantum jumps, which are captured by the Lindblad operators. In this section we describe state-of-the-art numerically exact methods based on matrix product states (MPS) we developed in order to perform the Lindbladian quantum time evolution of the combined atoms-cavity system presented in Chapter 2. We address the challenges one needs to overcome to efficiently treat the complex system and introduce the utilized methods along the way. All algorithms are implemented using the ITensor library [173].

The *fermionic nature* of the atomic system requires a careful consideration of the anti-commutation relations and basis order, especially when applying long-range operators or measuring distant correlations [see Sec. 4.2.1]. The choice of the initial state [Sec. 4.2.2], that can be prepared restricting to subspaces of the full Hilbert space using quantum numbers or adapted using ground state searching algorithms on parts of the system also greatly influences the efficiency and convergence of the real time evolution. Also, the global coupling of the optical cavity mode to the interacting atoms makes typical algorithms using matrix product operators vastly inefficient. We present in Sec. 4.2.3 how we develop an algorithm that combines a time evolution algorithm based on Trotterization with

the application of swap gates to alter the lattice geometry and effectively create a long-rage interaction. This time evolution method is compared to an alternative approach, the "Time Dependent Variational Principle" (TDVP) [Sec. 4.2.4] that uses variational methods to perform a time step and does not require the insertion of swap gates. Further, the dissipative aspect of the combined system due to the photon losses requires extra care when including it in the numerical method. The time evolution of the density matrix describing the quantum many-body-systems following Lindblad dynamics needs to be determined. Lastly, the Hilbert space of the bosonic cavity field is generally arbitrarily large. We introduce the algorithm to determine the most efficient reducing of the local Hilbert space dimension in Sec. 4.2.7 analogous to the one developed in Ref. [102].

We represent the one dimensional atomic many-body system as a matrix product state as introduced in Eq. (4.2). The cavity mode is introduced to the system in the form of an additional site in front of the first local atomic tensor, which we will in the following call "cavity-site".

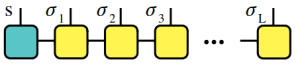

It has been shown for bosonic systems [102] that the specific position of this cavity site does not seem to influence the efficiency or entanglement build up in the system. The physical indices of the j^{th} atomic sites are denoted as σ_j while the cavity index is named s. While the quantum number conserving atomic sites have local physical dimension $d = 4$, the photonic site is non-conserving to respect the dissipative nature of the cavity field, and can generally be of infinite dimension.

4.2.1 Fermionic tensor networks with Jordan-Wigner-Transformation

When implementing matrix product state methods for fermions, one can encounter difficulties since a lot of standard methods are implemented for lattice sites associated with bosonic degrees of freedom. Fermions obey the Pauli exclusion principle as well as anti-commutation relations due to their totally anti-symmetric wavefunction.

To capture the behavior of physical fermionic systems correctly, we introduce the non-local Jordan-Wigner transformation [177], which maps spinful fermionic operators bosonic ones combined with non-local Jordan-Wigner string operators $\hat{F}_j$. The mapping of the fermionic annihilation operators $\hat{c}_{j\sigma}$ acting on site j are defined as

$$\begin{aligned} \hat{c}_{j\uparrow} &= \hat{F}_1\hat{F}_2...\hat{F}_{j-1}\hat{b}_{j\uparrow} \\ \hat{c}_{j\downarrow} &= \hat{F}_1\hat{F}_2...\hat{F}_{j-1}(\hat{F}_j\hat{b}_{j\downarrow}) \end{aligned} \tag{4.5}$$

with $\hat{F}_j = (1-2\hat{n}_{j\uparrow})(1-2\hat{n}_{j\downarrow}) = (-1)^{\sum_\sigma \hat{n}_{j\sigma}}$ [note: $\hat{F}_j^2 = 1$] and $\hat{b}_{j\sigma}$ the corresponding bosonic operators. The additional operator $\hat{F}_j$ in the mapping of spin-down operator $\hat{c}_{j\downarrow}$ as compared to the mapping of $\hat{c}_{j\uparrow}$ comes from the fixed ordering of the basis states.

For some relevant terms in the considered Hubbard model introduced in Sec. 2.1, this mapping results in

$$\begin{aligned} \sum_\sigma \hat{c}^\dagger_{j\sigma}\hat{c}_{j+1\sigma} + \text{H.c.} &= \hat{c}^\dagger_{j\uparrow}\hat{c}_{j+1\uparrow} + \hat{c}^\dagger_{j\downarrow}\hat{c}_{j+1\downarrow} + \text{H.c.} \\ &= (\hat{b}^\dagger_{j\uparrow}\hat{F}_{j-1}..\hat{F}_1)(\hat{F}_1..\hat{F}_{j-1}\hat{F}_j\hat{b}_{j+1\uparrow}) + (\hat{b}^\dagger_{j\downarrow}\hat{F}_j..\hat{F}_1)(\hat{F}_1..\hat{F}_j\hat{F}_{j+1}\hat{b}_{j+1\downarrow}) + \text{H.c.} \\ &= (\hat{b}^\dagger_{j\uparrow}\hat{F}_j\hat{b}_{j+1\uparrow}) + (\hat{b}^\dagger_{j\downarrow}\hat{F}_{j+1}\hat{b}_{j+1\downarrow}) - (\hat{b}_{j\uparrow}\hat{F}_j\hat{b}^\dagger_{j+1\uparrow}) - (\hat{b}_{j\downarrow}\hat{F}_{j+1}\hat{b}^\dagger_{j+1\downarrow}) \end{aligned} \tag{4.6}$$

for the kinetic terms. We used $\hat{F}_j\hat{b}_j = -\hat{b}_j\hat{F}_j$. For the local atomic densities $\hat{n}_{j\sigma}$ one finds $\hat{c}^\dagger_{j\sigma}\hat{c}_{j\sigma} = \hat{b}^\dagger_{j\sigma}\hat{b}_{j\sigma}$.

Replacing all fermionic operators in a system's Hamiltonian with these expressions allows to use the methods predefined for matrix product operators in the ITensor library. The correct implementation of these non-local strings, especially in the context of long-range correlations, is one of the main feats of our new method. We now turn to an example of the specific protocol we follow in the numerical runs.

4.2.2 Preparation of the initial state

We begin by introducing the preparation of the initial state that will be the starting point for the real time evolution. Since we typically aim to quickly converge towards a steady state, a state with symmetric homogeneous density

distribution and sufficiently large bond dimension is favorable. A standard protocol for our algorithm is thus to initialize the wavefunction as a MPS in a simple product state that resides within the desired S^z spin sector. In the tensor network architecture it is very beneficial to include quantum number conservation to reduce computational costs.

Quantum number conservation

If a Hamiltonian is invariant under a symmetry transformation, the corresponding matrix representation can be divided into several symmetry blocks. If it is a strong symmetry, meaning the symmetry generator also commutes with the jump operator defined in the Lindblad equation, it can be associated with a conserved quantity. In that case, the symmetry blocks are labeled by the value the observable associated with the symmetry takes when projected onto the block, defining a quantum number (QN).

We consider good quantum numbers of the atomic many-body system into account to reduce computational costs by block-diagonalizing with respect to the corresponding symmetry sectors. These are the conservation of the number of particles in the individual spin species as well as the total $\hat{S}^z$-quantum number defined as

$$\hat{S}^z = \frac{1}{2}\sum_{j=1}^{L} \hat{c}^\dagger_{j\alpha}\sigma^z_{\alpha\beta}\hat{c}_{j\beta}. \tag{4.7}$$

Note that we do not explicitly take the total spin quantum number originating from $\hat{S}^2$ into account, since implementing $SU(2)$-symmetries in the code is highly nontrivial.

In order for numerical simulations using MPS methods to efficiently capture physical processes, it is important to include these quantum numbers [123]. Quantum number conservation imposes a block-sparse-structure on the tensors of the state representation and only subspaces of the Hilbert-space corresponding to the symmetry sectors the initial state vector resides in are considered in the time evolution.

In ITensor, the quantum number information is added to the respective indices with a flux direction and tracked during all operations. In this framework, operators $\hat{A}$ that commute with all symmetry generators have a total flux of 0. An initial MPS therefore always remains in its original sector of the block-sparse matrix product state manifold under operations with $\hat{A}$. It can only change its sector when applying an operator with finite flux. Respecting this quantum number flux attribute in matrix product operations for large systems naturally restricts the MPS manifold to the initial symmetry sector without needing to explore the entire exponentially large Hilbert space in order to select states characterized by a certain set of quantum numbers. Note that only indices with opposite flux direction can be contracted.

Ground state search with DMRG

We usually initialize the cavity mode to be empty at the beginning and set the atoms-cavity coupling to 0. To this initial state, that has low mixing, we apply a standard ground state search algorithm for closed systems called "Density-Matrix-Renormalization-Group" (DMRG) that is based on variational principles. It returns, if converged, the ground state of the Fermi-Hubbard Model. This is the usual starting point for experiments that cool their atomic system as much as possible before starting switching on the pump beam that couples the atomic system to the cavity mode. Since one of the later introduced time evolution algorithms also hinges on an analogous variational algorithm we want to provide some more detail on the DMRG method. Reformulating the variational method in the matrix-product state formalism allows to find efficient algorithms to study correlated systems in one dimension [121–124].

The ground state of a system is defined by $|\psi\rangle$ that minimizes the energy

$$E_{\text{GS}} = \min\left[\frac{\langle\psi|\,\hat{H}\,|\psi\rangle}{\langle\psi|\psi\rangle}\right]. \tag{4.8}$$

This can be cast to an optimization problem with Lagrange multiplier λ

$$\langle\psi|\,\hat{H}\,|\psi\rangle - \lambda\,\langle\psi|\psi\rangle\,. \tag{4.9}$$

Solving the equation with variational methods $|\psi\rangle$ is the approximate ground state of the system with ground state energy λ.

In the matrix-product state representation $|\psi\rangle = \sum_{\sigma_1..\sigma_L} \sum_{a_1..a_{L-1}} M^{\sigma_1}_{1,a_1} M^{\sigma_2}_{a_1,a_2} ... M^{\sigma_L}_{a_{L-1},1} |\vec{\sigma}\rangle$, the local tensors $M^{\sigma_i}_{a_{i-1},a_i}$ correspond to the variational parameters of the problem. The Hamiltonian is represented as a matrix-product operator (MPO)

$$\hat{H} = \sum_{\sigma_1,\sigma_1'..\sigma_L\sigma_L'} \sum_{b_1..b_{L-1}} W^{\sigma_1,\sigma_1'}_{1,b_1} W^{\sigma_2,\sigma_2'}_{b_1,b_2} ... W^{\sigma_L,\sigma_L'}_{b_{L-1},1} |\vec{\sigma}\rangle \langle\vec{\sigma}'| .$$

Since the minimization is highly non-linear, one typically iteratively minimizes the expression. One sweep consists of fixing all but one or two of the variational matrices, optimize and shift the variable $M^{\sigma_i}_{a_{i-1},a_i}$ through the full system. Repeating these sweeps to right and left are until convergence is reached one obtains a minimum in the energy up to a specified accuracy.

Going through the algorithm in more detail, one starts by bringing the MPS to mixed canonical form with orthogonality center at site i. In this representation, the derivation of $\partial \langle\psi|\psi\rangle / \partial M^{\sigma_i *}_{a_{i-1},a_i}$ is given by $M^{\sigma_i}_{a_{i-1},a_i}$. This transforms the optimization problem to

$$\frac{\partial \langle\psi| \hat{H} |\psi\rangle}{\partial M^{\sigma_i *}_{a_{i-1},a_i}} - \lambda \frac{\partial \langle\psi|\psi\rangle}{\partial M^{\sigma_i *}_{a_{i-1},a_i}} = 0 \tag{4.10}$$

$$\sum_{\sigma_i'} \sum_{a_{i-1},a_{i-1}'} \sum_{b_{i-1},b_i} L^{a_{i-1},a_{i-1}'}_{b_{i-1}} W^{\sigma_i,\sigma_i'}_{b_{i-1},b_i} R^{a_i,a_i'}_{b_i} M^{\sigma_i'}_{a_{i-1}',a_i'} - \lambda M^{\sigma_i}_{a_{i-1},a_i} = 0 \tag{4.11}$$

where $M^{\sigma_i}_{a_{i-1},a_i}$ is the variable tensor and L and R are the contracted block states of the left (right) normalized part of the state.

$$L^{a_{i-1},a_{i-1}'}_{b_{i-1}} = \sum_{a_l,a_l',b_l} \sum_{l<i-1} \left(\sum_{\sigma_1\sigma_1'} A^{\sigma_1 *}_{1,a_1} W^{\sigma_1,\sigma_1'}_{1,b_1} A^{\sigma_1'}_{1,a_1'} \right) ... \left(\sum_{\sigma_{i-1}\sigma_{i-1'}} A^{\sigma_{i-1} *}_{a_{i-2},a_{i-1}} W^{\sigma_{i-1},\sigma_{i-1'}}_{b_{i-2},b_{i-1}} A^{\sigma'_{i-1}}_{a'_{i-2},a'_{i-1}} \right)$$

$$R^{a_i,a_i'}_{b_i} = \sum_{a_l,a_l',b_l} \sum_{l>i} \left(\sum_{\sigma_{i+1}\sigma_{i+1}'} B^{\sigma_{i+1} *}_{a_i,a_{i+1}} W^{\sigma_{i+1},\sigma_L'}_{b_i,b_{i+1}} B^{\sigma'_{i+1}}_{a_i',a'_{i+1}} \right) ... \left(\sum_{\sigma_L\sigma_L'} B^{\sigma_L *}_{a_{L-1},1} W^{\sigma_L,\sigma_L'}_{b_{L-1},1} B^{\sigma_L'}_{a'_{L-1},1} \right)$$

Eq. (4.11) is solved for the respective vector $M^{\sigma_i}_{a_{i-1},a_i}$ with iterative eigensolvers like Lanczos or Jacobi-Davidson algorithm [178] since the tensors are usually too large to diagonalize them exactly. The local vector within the MPS $|\psi\rangle$ is then updated with the optimized $\tilde{M}^{\sigma_i}_{a_{i-1},a_i}$ at lower energy-eigenvalue, yielding the new state $|\tilde{\psi}\rangle$ with $\tilde{E}$. Next, the position of the variable element is shifted one site to the left or right, depending on the direction of the sweep and the procedure is repeated with the new variable tensor. Note that one needs to be careful as the procedure might get stuck in a local minimum. To prevent this it is possible to test various initial states, add a noise term and include good quantum numbers.

Additionally, using two-site optimization is also expected to converge faster and is less likely to get stuck in local minima. One of the main advantages of keeping two neighbouring site tensors variable instead of a single one is the adjustable maximal bond dimension D of the system. As the entanglement of the state might grow as it approaches the ground state, the fixed bond dimension in the single-site optimization algorithm might lead to severe truncation errors. Optimizing the two-site tensor however allows to truncate at an arbitrary, potentially higher bond dimension in the singular value decomposition of the varied two-site tensor after the optimization step to restore the original MPS form. The algorithm is now presented in some more detail. In order to optimize two sites simultaneously one introduces the two-site MPS tensor N and respective MPO tensor P

$$N^{\sigma_i\sigma_{i+1}}_{a_{i-1},a_{i+1}} = \sum_{a_i} M^{\sigma_i}_{a_{i-1},a_i} M^{\sigma_{i+1}}_{a_i,a_{i+1}}, \qquad P^{\sigma_i\sigma_{i+1}\sigma_i'\sigma'_{i+1}}_{b_{i-1},b_{i+1}} = \sum_{b_i} W^{\sigma_i\sigma_i'}_{b_{i-1},b_i} W^{\sigma_{i+1}\sigma'_{i+1}}_{b_i,b_{i+1}}. \tag{4.12}$$

Eq. (4.11) can the be extended to

$$\sum_{\sigma_i'\sigma'_{i+1}} \sum_{a'_{i-1},a'_{i+1}} \sum_{b_{i-1},b_{i+1}} L^{a_{i-1},a'_{i-1}}_{b_{i-1}} P^{\sigma_i\sigma_{i+1}\sigma_i'\sigma'_{i+1}}_{b_{i-1},b_{i+1}} R^{a_{i+1},a'_{i+1}}_{b_{i+1}} N^{\sigma_i'\sigma'_{i+1}}_{a_{i-1},a_{i+1}} - \lambda N^{\sigma_i\sigma_{i+1}}_{a_{i-1},a_{i+1}} = 0. \tag{4.13}$$

The optimization can then be performed using the same algorithms as for the single-site case. A graphical representation for the algorithm is given in Fig. 4.1.

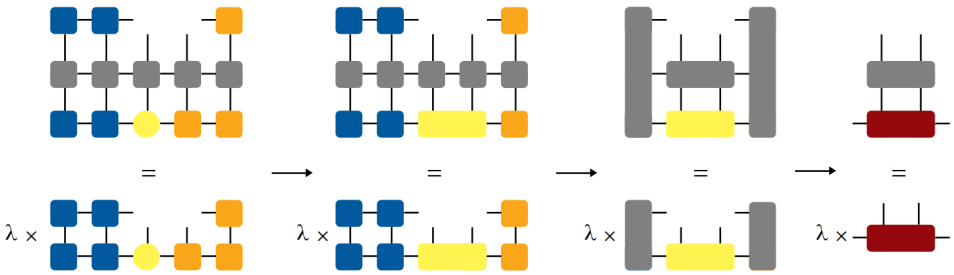

Fig. 4.1: Graphical representation of the two-site optimization DMRG algorithm. The MPS is brought to a mixed canonical form with left (blue) and right (orange) normalized tensors. The two variable MPS tensors that are to be optimized are contracted (yellow bar) to a two-site tensor. Contracting the left and right edge tensors (grey bars) efficiently allows to rewrite the optimization to an effective eigenvalue problem with an effective Hamiltonian and eigenmatrix (red).

Finally, after variational optimization the resulting two-site tensor $N^{\sigma_i \sigma_{i+1}}_{a_{i-1},a_{i+1}}$ needs to be transformed back into single site tensors $\tilde{M}^{\sigma_i}_{a_{i-1},a_i}$ and $\tilde{M}^{\sigma_{i+1}}_{a_i,a_{i+1}}$. This is done by performing a truncated singular value decomposition, restoring the initial MPS form. In this step, the bond dimension of the index connecting sites l and $l+1$, which during the optimization step is potentially increased to dD as compared to D in the original MPS, can be reduced back to D, taking only the most influential contributions into account.

For a sweep to the right (left), the diagonal singular-value tensor is contracted with the right(left)-hand factor tensor.

This operation is then, similarly to the single-site case, iteratively shifted to the right and left through the MPS in subsequent sweeps until the convergence criteria put on the algorithm are fulfilled. Because of the beneficial properties formerly mentioned, this two site-optimization is the algorithm of choice for any DMRG calculations performed in this work. Note that this method is most efficient for open boundary conditions (OBC), which are also used in the quasi-exact numerical tMPS code developed in this work, because the computational costs for the algorithm scale linearly with the system size. Open boundary conditions introduce stronger edge effects than periodic boundary conditions (PBC), but are often more natural in physical systems. Using PBC drastically increases the computational costs of the DMRG algorithm, requiring to keep D^2 instead of D states at each singular value decomposition to reach the same accuracy.

Time evolution algorithm

Now that the initial state is prepared, we describe the various time evolution methods used to progress the MPS representation of a wave function in time.

4.2.3 Trotter-Suzuki time evolution and application of swap gates

We begin by introducing the well known Trotter-Suzuki decomposition of the time evolution operator to perform a unitary time evolution on the closed part of our quantum state [125, 126]. It is combined with a sequence of swap-gate applications, newly developed in our group [102], that allow us to decompose the global range photon-mediated interaction into repeated applications of short-range operators. This will be part of the full time evolution algorithm for open Markovian quantum systems in Sec. 4.2.5 and Sec. 4.2.6. Suppose we have a closed quantum system with a time-independent Hamiltonian $\hat{H}$. Starting from an initial state at $t=0$, the time evolution is defined by the Schroedinger equation

$$|\psi(t)\rangle = e^{-\frac{it}{\hbar}\hat{H}} |\psi(t=0)\rangle = \mathcal{U}(t) |\psi(t=0)\rangle . \tag{4.14}$$

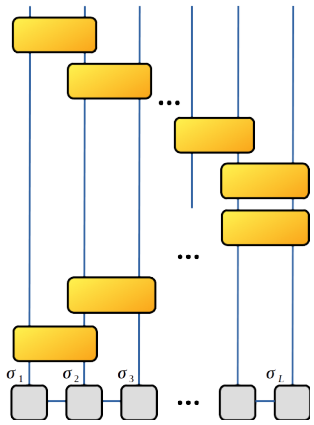

Fig. 4.2: Scheme of the gate application to an MPS in the Trotter-Suzuki algorithm. The gates are represented by yellow boxes. The gates are applied by a sweep from left to right and subsequently from right to left.

Numerically, we cannot continuously solve the time evolution but rather need to discretize it into N_t small finite time steps τ until reaching the desired final time t_{end}. The full operator is factorized to $\mathcal{U}(t) = \mathcal{U}(\tau)^{N_t}$. Assuming the system Hamiltonian only includes short range interactions, which is the case for many popular models for one-dimensional quantum systems, it can be split into local terms. If it i.e. only couples neighboring sites the decomposition is done as

$$\hat{H} = \sum_{j=1}^{L-1} \hat{h}_{j,j+1} = \underbrace{\sum_{j\text{odd}} \hat{h}_{j,j+1}}_{\hat{H}_{\text{odd}}} + \underbrace{\sum_{j\text{even}} \hat{h}_{j,j+1}}_{\hat{H}_{\text{even}}} \tag{4.15}$$

with $\left[\hat{H}_{\text{odd}}, \hat{H}_{\text{even}}\right] \neq 0$, but all terms within the two sums commute with each other. Using this property for small τ the time step operator can be approximated by the Trotter-Suzuki decomposition. This results in

$$\mathcal{U}(\tau) = e^{-\frac{i\tau}{\hbar}\hat{H}} = \prod_{j=1}^{L-1} e^{-\frac{i\tau}{2\hbar}\hat{h}_{j,j+1}} \prod_{j=L-1}^{1} e^{-\frac{i\tau}{2\hbar}\hat{h}_{j,j+1}}. \tag{4.16}$$

A finite time step τ leads to a systematic error of order $\mathcal{O}(L\tau^3)$, also called "Trotter error", where L is the number of sites of the MPS. This error accumulates, leading to an overall error of order $\mathcal{O}(L\tau^2 t_{\text{end}})$ at the defined final time. The exponentiation of the operators on the small subspace of the Hilbert-space can be done efficiently. In the matrix product state representation, individual factors can be represented by gate tensors acting on the neighboring MPS sites $j, j+1$.

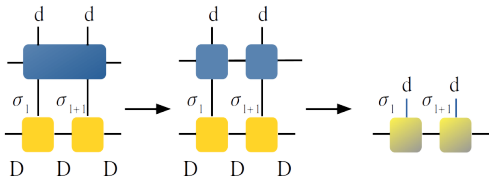

Here, the dimension of the bond index connecting sites $(j, j+1)$ grows at every gate application. To limit the computational costs one subsequently performs a SVD compression that introduces a second error in the time evolution step. After contracting the adjacent MPS site tensors with a gate tensor, the bond dimension is truncated to a maximal dimension m in the decomposition. By keeping only m contributing states with the largest singular values, one introduces a truncation error ϵ which is the combined weight of all discarded states. An in-depth discussion of the different error sources will we provided in Sec. 4.3.1. Repeatedly contracting the two-site tensors with the MPS in the right order time evolves the initial state until the final time t_{end} is reached. This right- and left sweeping algorithm in diagram representation is shown in Fig. 4.2.

The global range coupling between the cavity mode and all the atomic sites makes the use of the tMPS implementation based on the Trotter-Suzuki decomposition, which is based on short-range Hamiltonians, impossible. Thus,

in order to take both the global coupling between photons and atoms and the short range interaction of the atoms into account, we develop a variant of the tMPS based on the dynamical deformation of the MPS structure. The dynamical deformation allows one to alter the order of the sites as needed using swap gates [140, 174, 175]. This implementation can efficiently deal with interacting spinful fermionic models globally coupled to the dissipative photonic field.

In detail looking at the dynamics of the individual quantum trajectories, a time step is done as follows. The trajectory is represented as a matrix product state. Here, the first site is initially representing the single-mode cavity field. One needs to be careful in all operator application since we have both a bosonic site for the field as well as fermionic sites for the atomic chain. The in principal arbitrary large dimension of the Hilbert space of the photonic mode is dealt with by dynamically truncating it during the time evolution, as introduced in Sec. 4.2.7. Then, the time step operation is based on the second order Trotter-Suzuki decomposition of the time evolution propagator, combined with swap gates. The Hamiltonian is split in an atomic part $\hat{H}_{\text{FH}}$, which only contains atomic operators, and the remaining terms involving the cavity field.

$$e^{-\frac{i\tau}{\hbar}\hat{H}_{\text{eff}}} \sim e^{-\frac{i\tau}{2\hbar}\hat{H}_{\text{FH}}} e^{-\frac{i\tau}{\hbar}(\hat{H}_{\text{ac}}+\hat{H}_{\text{cav}}-\frac{i\hbar}{2}\Gamma\hat{a}^\dagger\hat{a})} e^{-\frac{i\tau}{2\hbar}\hat{H}_{\text{FH}}} \tag{4.17}$$

While evolving with $\hat{H}_{\text{FH}}$ is possible using the standard Trotter-Suzuki-algorithm, one needs to consider how to implement the global coupling to the cavity field more carefully. For $e^{-\frac{i\tau}{\hbar}(\hat{H}_{\text{ac}}+\hat{H}_{\text{cav}}-\frac{i\hbar}{2}\Gamma\hat{a}^\dagger\hat{a})}$, one can decompose the coupling $\hat{H}_{\text{ac}}$ into terms that each only act on two sites [150]

$$\begin{aligned} e^{-\frac{i\tau}{\hbar}(\hat{H}_{\text{ac}}+\hat{H}_{\text{cav}}-\frac{i\hbar}{2}\Gamma\hat{a}^\dagger\hat{a})} = &\prod_{j=1}^{L-1} e^{-\frac{i\tau}{2}\left[\frac{g}{\sqrt{L}}(\hat{a}^\dagger+\hat{a})(-1)^j\hat{n}_j+\frac{1}{L}(\delta-\frac{i}{2}\Gamma)\hat{a}^\dagger\hat{a}\right]} \\ &\times \prod_{j=L-1}^{1} e^{-\frac{i\tau}{2}\left[\frac{g}{\sqrt{L}}(\hat{a}^\dagger+\hat{a})(-1)^j\hat{n}_j+\frac{1}{L}(\delta-\frac{i}{2}\Gamma)\hat{a}^\dagger\hat{a}\right]} + \mathcal{O}(L\tau^3). \end{aligned} \tag{4.18}$$

Note that these are not only adjacent but connect each site with all of the others individually.

Since most of the resulting two-site operators do not act on two neighboring sites in the initial MPS structure of the quantum state, we resolve to modifying the structure of the MPS. Before applying the two site operators, the site information is virtually swapped such that the indices targeted by the coupling operator are neighboring each other in the MPS structure. This is realized via application of swap gates S_{s,σ_j} that exchange the order of physical indices (s, σ_j) of a state $|\sigma_1, \sigma_2, ...\sigma_s, \sigma_j, ...\sigma_L\rangle$ in MPS representation.

$$\begin{aligned} S_{s,\sigma_j}\left(M^{\sigma_1}_{a_1}...M^{s}_{a_{j-1}a_j}M^{\sigma_j}_{a_j a_{j+1}}..M^{\sigma_L}_{a_{L-1}}\right) &= S_{s,\sigma_j}\left(M^{\sigma_1}_{a_1}...(MM)^{s,\sigma_j}_{a_{j-1}a_{j+1}}..M^{\sigma_L}_{a_{L-1}}\right) \\ &= M^{\sigma_1}_{a_1}...(MM)^{\sigma_j,s}_{a_{j-1}a_{j+1}}..M^{\sigma_L}_{a_{L-1}} \\ &= M^{\sigma_1}_{a_1}...M^{\sigma_j}_{a_{j-1}a_j}M^{s}_{a_j a_{j+1}}..M^{\sigma_L}_{a_{L-1}} \end{aligned} \tag{4.19}$$

The swap basically consists of a combination of two Kronecker-deltas $\delta(s, s')$ and $\delta(\sigma, \sigma')$ with exchanged site information. The swapping procedure is done as follows:

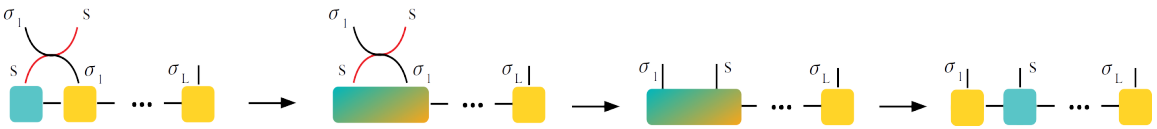

One starts with the two MPS sites that correspond to the cavity site, with physical index s, the adjacent atomic site with index σ and the swap gate with matching indices $(s; \sigma)$ as well as the new indices with exchanged site information $(\sigma'; s')$. In order to apply the gate, the sites with indices s, σ are contracted through the connecting bond index. Then the resulting 2-site tensor can be contracted with the swap-gate tensor, which results in a 2-site tensor with physical indices $(\sigma'; s')$. It is split into two one-site tensors via SVD, renaming the physical indices $(\sigma'; s') \to (\sigma; s)$. Note that besides the SVD truncation error this procedure is exact.

The full time step is concluded by applying all two-site tensors and swap gates following an specific order shown in Fig. 4.3.

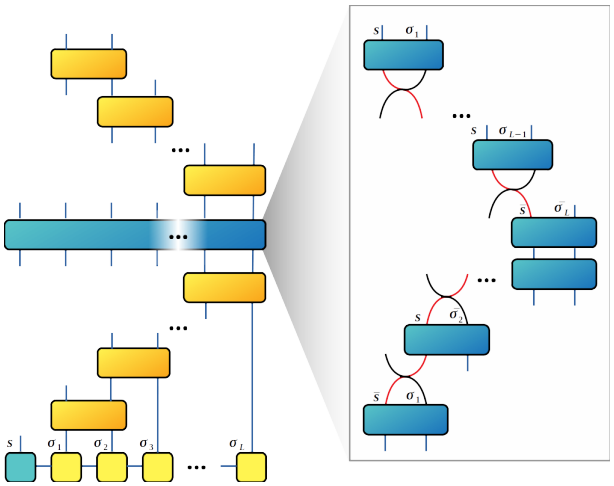

Fig. 4.3: Scheme of a single time step of the individual trajectories in the Monte-Carlo-Wavefunction algorithm. Yellow boxes represent the two-site Trotter gates, the blue bar the global coupling of the fermionic system to the cavity mode (blue MPS site). The gray box on the right shows the decomposition of the global coupling into two site gates combined with swap gates.

4.2.4 Time Dependent Variational Principle (TDVP) with optional local basis extension

In this section we will introduce an alternative time evolution algorithm, the time-dependent variational principle (TDVP) [179, 180] that has many similarities to time dependent Density Matrix Renormalization Group methods (tDMRG) [115, 131]. We implement the method in order to confirm our algorithm works and eventually benchmark against the Lie-Trotter decomposition introduced in the previous section. Since it does not rely on the lattice deformation with swap gates, an agreement between the methods can serve as a justification for this approach. Additionally, depending on the specific parameter regime, one or the other time evolution method might be favorable from a point of computational costs.

The TDVP algorithm is based on the DMRG algorithm introduced in Sec. 4.2.2, that applies the variational principle to matrix product states. The method was adapted for MPS applications [127–130] to obtain flexible and efficient variational algorithms that allow us to study one dimensional correlated quantum systems with excellent precision. As in DMRG methods the integration scheme is typically based on the single-site variant or the two-site variant.

Due to the symplectic structure, as in classical approaches, probabilities, energy as well as other integrals of motion are conserved if the state does not leave the manifold under the corresponding symmetry transformation. Contrarily most other time-dependent MPS methods do not automatically conserve energy and probabilities because they include a truncation step necessary to allow for an efficient MPS representation of the time evolved state. Note, that TDVP methods, similar to DMRG, can fail uncontrollably by getting stuck in local minima. Generally, one needs to be careful since time evolution with TDVP optimizes the systems total energy. This can be at the cost of convergence in arbitrary observables that are not explicitly contained in the Hamiltonian. For integrable models even global observables included in the Hamiltonian might suffer from numerical convergence issues because the TDVP algorithm does not explicitly conserve non-local conserved quantities that result from the integrability [181].

We will begin by discussing the single-site method. This variant does not violate unitarity or energy conservation at the drawback of the fixed MPS bond dimension that is unable to adapt to an increasing entanglement. A product state, independent of the Hamiltonian, will always stay in a product state. The unitary part of the time evolution of a quantum state is determined by the Schroedinger equation. The TDVP algorithm relies on the derivation of a series of local time-dependent Schroedinger-equations (TDSE). For the single-site variant, in a time step, the action of the Hamiltonian is projected into the tangent space to the specific manifold of matrix-product states corresponding to the initial bond dimension. The resulting TDSE are then solved within this manifold, which defines a simultaneous update for all tensors of the MPS. Independent of the system Hamiltonian, this ensures the evolution to never leave the manifold of the initial MPS. For real time evolution, the constraint of the fixed bond dimension can be interpreted analogous to a classical motion under a constraint.

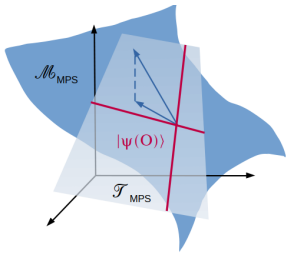

Fig. 4.4: Sketch of the MPS manifold $\mathcal{M}_{\text{MPS}}$ at fixed bond dimension and single-site tangent space $\mathcal{T}_{\text{MPS}}$

We define the single-site tangent space $\mathcal{T}_{\text{MPS}}$ which is spanned by varying a single MPS tensor, as sketched in Fig. 4.4. The representation of the projection operator onto the tangent space $\hat{P}_{\mathcal{T}_{\text{MPS}}}$ in MPS representation is derived for an arbitrary state by minimizing the norm squared of its deviation from an arbitrary tangent state. This results in the definition [182]

$$\hat{P}_{\mathcal{T}_{\text{MPS}}} = \sum_j \hat{P}_{j-1}^{L,|\psi\rangle} \otimes \hat{\mathbb{1}} \otimes \hat{P}_{j+1}^{R,|\psi\rangle} - \sum_j \hat{P}_j^{L,|\psi\rangle} \otimes \hat{P}_{j+1}^{R,|\psi\rangle}, \tag{4.20}$$

where the projectors $\hat{P}_j^{L(R),|\psi\rangle}$ use the gauge-fixed left-(right-)normalized MPS tensors

$$\hat{P}^{L,|\psi\rangle}_{j:\bar{\sigma}_1,\ldots,\bar{\sigma}_j,\sigma_1,\ldots,\sigma_j} = \sum_{a_j} \bar{\psi}^{L;\bar{\sigma}_1,\ldots\bar{\sigma}_j}_{j;a_j} \otimes \psi^{L;\sigma_1,\ldots\sigma_j}_{j;a_j} \tag{4.21a}$$

$$\hat{P}^{R,|\psi\rangle}_{j:\bar{\sigma}_j,\ldots,\bar{\sigma}_L,\sigma_j,\ldots,\sigma_L} = \sum_{a_{j-1}} \bar{\psi}^{R;\bar{\sigma}_j,\ldots\bar{\sigma}_L}_{j;a_{j-1}} \otimes \psi^{R;\sigma_j,\ldots\sigma_L}_{j;a_{j-1}}. \tag{4.21b}$$

The individual tangent vectors are constructed by replacing any orthogonality center tensor M_j of the MPS by another tensor M'_j which satisfies $M_j \cdot \bar{M}'_j = 0$. Using Eq. (4.20) the projected TDSE can be written as

$$i\frac{\partial}{\partial t}|\psi(t)\rangle = \hat{P}_{\mathcal{T}_{\text{MPS}}}\hat{H}|\psi\rangle, \tag{4.22}$$

which is approximately solvable by considering a set of L forward- and $L-1$ backward-evolving equations and solving them individually.

$$i\frac{\partial}{\partial t}|\psi(t)\rangle = \hat{P}_{j-1}^{L,|\psi\rangle} \otimes \hat{\mathbb{1}}_j \otimes \hat{P}_{j+1}^{R,|\psi\rangle}\hat{H}|\psi\rangle \tag{4.23a}$$

$$i\frac{\partial}{\partial t}|\psi(t)\rangle = -\hat{P}_j^{L,|\psi\rangle} \otimes \hat{P}_{j+1}^{R,|\psi\rangle}\hat{H}|\psi\rangle \tag{4.23b}$$

with the single-site map $\bar{\psi}^L_{j-1} \otimes \bar{\psi}^R_{j+1}$ or the center-bond map $\bar{\psi}^L_j \otimes \bar{\psi}^R_{j+1}$, one retrieves local time-dependent Schroedinger-equations for each effective center matrix or single-site tensor

$$\frac{\partial}{\partial t}M_j = -i\hat{H}_j^{\text{eff}}M_j, \qquad \frac{\partial}{\partial t}C_j = -i\hat{H}_j^{\text{eff}}C_j. \tag{4.24}$$

The straight-forward integration of these equations often suffers from numerical instability. Thus, an alternative integration scheme based on a Lie-Trotter decomposition of the tangent space projector was proposed and implemented [183] and is used as the standard. The computational costs are typically of the order $\mathcal{O}(D^3)$, as described in Sec. 4.2.2. Starting from a right orthogonal MPS at site $j=1$ one iterates through all sites repeating the following steps:

- Evolve the variational parameters M_j as defined in Eq. (4.24) for a time step τ.
- Factorize the new parameter matrix at time $t+\tau$ to $M'_j = A'_j C_j$.
- Evolve the center bond matrix C_j backwards in time $t+\tau \to t$ and absorb it into site $j+1$, creating $M'_{j+1} = C_j B'_{j+1}$.

This algorithm differs from one-site DMRG described in Sec. 4.2.2 by replacing the optimization step for M_j with the evolution step. Additionally, the backwards time evolution step for C_j is performed before absorbing it at the next site. A full left-to-right sweep captures the action of a first-order integrator, producing an updated state at time $t+\tau/2$, $|\psi(t+\tau/2)\rangle$ introducing a local integration error ($\mathcal{O}(\tau^2)$). Subsequently sweeping from right-to-left composes this integrator with its adjoint. The full sweeps result in a second-order symmetric method we define as a single integration step. The new evolved state at time $t+\tau$ is obtained with a time step error of order $\mathcal{O}(\tau^3)$. Note that the finite time step error is calculated with respect to the exact solution of the TDVP differential equation. Additionally, an error with respect to the original Schroedinger-equation stems from the discrepancy between the TDVP evolution and the Schroedinger evolution and contributes to the overall error. It is determined by

$$\left\|(\hat{\mathbf{1}} - \hat{P}_{\mathcal{T}_{\text{MPS}}})\hat{H}\,|\psi(A(t))\rangle\right\|. \tag{4.25}$$

We now comment on the two-site scheme, that will be predominantly used for our purposes due to the flexibility to increase the tensor dimensions that is able to accommodate the build up of entanglement we typically see in our system. Additionally it is less likely to get stuck in local minima. Changing the bond dimension of the MPS sites, corresponds to leaving the manifold. Thus, a smooth evolution captured by a differential equation is not possible. However, since the one-site algorithm is implemented for a finite time step, one can construct an analogous two-site algorithm. In this algorithm variant two neighboring sites $(j, j+1)$ are optimized and updated simultaneously, again similar to the two-site DMRG method Eq. (4.13). In the process they are treated as a block $M_{j,j+1}$ that is later factorized back to individual tensors using SVD. Here one defines a cutoff error ϵ [see Eq. (4.3)] and/or maximal bond dimension m to which the state is truncated to in the decomposition step.

The convergence of the algorithm depends on the initial MPS (starting from a state with sufficiently large bond dimension). There have been proposals to quickly enlarge the bond dimension of the manifold during the first few time steps by performing a local basis extension [129] or to introduce a controlled bond expansion [130] to the single-site TDVP. We typically avoid these steps by running a DMRG algorithm on our initial state and consequently start the time evolution with an MPS that usually already has some entanglement. Further parameters that influence the time step τ, number of sweeps in the optimization and, if the two-site method is used, the truncation error ϵ and/or maximal bond dimension M to be kept in the SVD step. Typically, the TDVP allows for larger time steps than the Trotter-Suzuki time evolution algorithm.

Lindblad dynamics

So far we only considered unitary dynamics, of the quantum many-body system with global coupling to the cavity mode, neglecting the dissipation the light field is subjected to. To be able to capture the dissipative nature of a system following the Lindblad dynamics it is necessary to evolve the full density matrix of a mixed state rather than single pure states. We now aim to tackle this by using two vastly different methods. We begin by implementing the Monte-Carlo-Wavefunctions algorithm in the following Sec. 4.2.5, which relies on stochastic sampling. This is contrasted with the approach using purification of the density matrix and subsequently time evolving the resulting super-vector in time [see Sec. 4.2.6]. Since this method was introduced in detail in Ref. [184], we will restrict to a brief overview here.

4.2.5 Monte-Carlo-Wavefunctions (MCWF)

To imitate Lindbladian dynamics, one can use the stochastic unraveling of the Lindblad master equation using quantum trajectories. The evolution of the systems density matrix is modeled by means of Monte-Carlo averages over the time-evolution of many different trajectories in phase space, which has been used to simulate non-equilibrium dynamics repeatedly [135, 136, 142]. This method has the advantage of simulating the time evolution of individual wavefunctions instead of density matrices, which typically cuts the computational cost of evolving individual trajectories drastically. However, it requires stochastic sampling, introducing an additional stochastic error to the results that needs to be tracked carefully. Efficiently combining the stochastic nature of the time evolution with matrix product state methods taking quantum number conservation into account has relatively recently been implemented by a few groups, e.g. [137–141, 143–145]. As stated above, we conserve atomic quantum numbers in this approach as well. To simulate the stochastic unraveling of the master equation, many pure trajectories are

evolved in time, with random initial states drawn corresponding to their probability weights in the initial density matrix. Results are then obtained by averaging over them [102, 149].

We describe the stochastic time-evolution performed for the individual trajectory in the following steps.

- We draw a random number r from the interval $[0; 1)$.
- Each trajectory is evolved by a time step τ via application of the non-unitary time evolution operator $\exp\left(-\frac{i}{\hbar}\hat{H}_{\text{eff}}\tau\right)$, where the effective Hamiltonian is $\hat{H}_{\text{eff}} = \hat{H} - \frac{i\hbar}{2}\Gamma\hat{a}^\dagger\hat{a}$. Here, $\hat{H}$ is the Hamiltonian describing the full closed atoms-cavity coupled system.
- Due to the non-hermitian Hamiltonian, the norm of the state decays in time. These deterministic time steps are repeated until the norm falls below r, which serves as a threshold.
- Once the threshold is reached, the jump operator $\hat{a}$ is applied to the wavefunction to simulate a quantum jump. The state is subsequently normalized.

These steps are repeated until reaching the final time. It was shown [185, 186] that averaging over the stochastically sampled quantum trajectories, the average time evolution reproduces the Lindblad dynamics correctly up to $\mathcal{O}(\tau)$ in the chosen time step. Note that is is crucial to choose the time step, such that the probability of more than one jump in the cavity field is low, since the stochastic application of the jump operator can only occur once per time step.

4.2.6 Purification

Alternatively we implemented the time evolution using a purification ansatz [132–134, 175] to capture the Lindbladian dynamics. This method was mainly developed during my master thesis [184]. The idea is to vectorize the system's density-matrix by enlarging the physical Hilbert space with an auxiliary Hilbert space. Once the Liouvillian $\mathcal{L}$ is projected onto the enlarged Hilbert space, the vectorized density matrix can be evolved with the super-Liouvillian $\mathbb{L}$ analogously to the unitary time evolution with the Schroedinger-equation on a closed system.

A mixed state described by the density matrix $\hat{\rho}$ on the physical Hilbert space $\mathcal{H}_{\text{phys}}$ is mapped to a pure state $|\rho\rangle\!\rangle$ on an enlarged Hilbert space $\mathcal{H}_{\text{phys}} \otimes \mathcal{H}_{\text{aux}}$. It is common practice to choose a copy of $\mathcal{H}_{\text{phys}}$ as auxiliary Hilbert space $\mathcal{H}_{\text{aux}}$. Note, that this mapping drastically increases the scaling of the Hilbert space, from d^L in the pure state representation to d^{2L} for the purified density matrix. Here, d is the local dimension of the atomic Hilbert spaces and L the size of the physical system. From now, elements defined on the enlarged space are written with doubled angular parentheses $|\rangle\!\rangle$ and described with the prefix "super-".

$$\hat{\rho} = \sum_{\vec{\sigma},\vec{\sigma'}} \rho_{\vec{\sigma},\vec{\sigma'}} \left|\vec{\sigma}\right\rangle_{\text{phys}} \left\langle\vec{\sigma'}\right|_{\text{phys}} \quad \rightarrow \quad |\hat{\rho}\rangle\!\rangle = \sum_{\vec{\sigma},\vec{\sigma'}} \rho_{\vec{\sigma},\vec{\sigma'}} \left|\vec{\sigma}\right\rangle_{\text{phys}} \otimes \left|\vec{\sigma'}\right\rangle_{\text{aux}}$$

The ordering of the new basis can be chosen freely. For our purposes the auxiliary site-tensors are ordered to alternate with the physical ones representing the same position. For our specific system this would result in an MPS geometry where the system density matrix MPO (left) with two physical indices, i.e. $\{\sigma_j, \sigma_{j+1}\}$ is mapped to an MPS with one physical indices per site and doubled length.

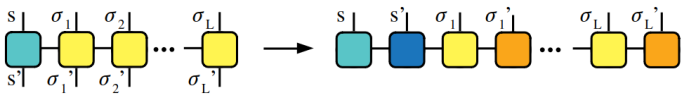

Note that in the purified form, the cavity mode is represented by two bosonic cavity sites. The time evolution defined in Eq. (2.12), taking the initial density matrix as a starting point is performed by mapping the Lindbladian to a superoperator on the same enlarged Hilbert space.

$$\frac{d}{dt}|\hat{\rho}\rangle\!\rangle = \Big[-\frac{i}{\hbar}\hat{H}\otimes\mathbb{1} + \frac{i}{\hbar}\mathbb{1}\otimes\hat{H}^T + \frac{\Gamma}{2}\Big(2\hat{L}_j\otimes\left(\hat{L}_j^\dagger\right)^T - \hat{L}_j^\dagger\hat{L}_j\otimes\mathbb{1} - \mathbb{1}\otimes\left(\hat{L}_j^\dagger\hat{L}_j\right)^T\Big)\Big]|\hat{\rho}\rangle\!\rangle \tag{4.26}$$

This now unitary time evolution operator can be decomposed in an analogous way to the Trotter-Suzuki algorithm introduced in Sec. 4.2.3. Due to the doubling of the sites, in order to reach the same accuracy in the decomposition

one needs to apply "4-site-gates" in both the atomic time evolution step and the swap gate application that act on neighboring physical and auxiliary sites.

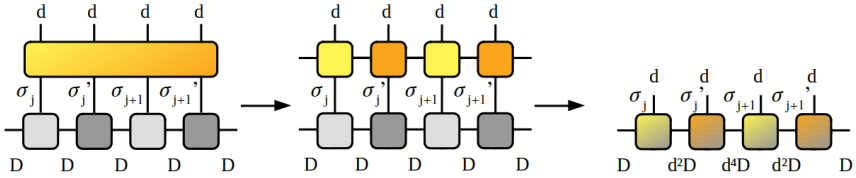

In principal the physical density matrix can be restored by tracing over the auxiliary degrees of freedom

$$\hat{\rho} = \mathrm{Tr}_{\mathrm{aux}}\left[|\rho\rangle\rangle\langle\langle\rho|\right] = \sum_{\vec{\sigma},\vec{\sigma'}} \rho_{\vec{\sigma},\vec{\sigma'}} \, |\vec{\sigma}\rangle_{\mathrm{phys}} \, \langle\vec{\sigma'}|_{\mathrm{phys}} \, . \tag{4.27}$$

However, one typically resorts to measure observables. The expectation value is obtained with the help of the purified un-normalized infinite temperature state $|\mathbb{I}\rangle\rangle$ [145]

$$\langle\hat{A}\rangle = \mathrm{Tr}\left(\hat{\rho}\hat{A}\right) = \langle\langle\mathbb{I}|\,\hat{A}\,|\rho\rangle\rangle \quad \text{with} \quad |\mathbb{I}\rangle\rangle = \bigotimes_{j=1}^{L} \sum_{\sigma_j} |\sigma_l\rangle_{\mathrm{phys}} \otimes |\sigma_l\rangle_{\mathrm{aux}} \, . \tag{4.28}$$

Since $|\mathbb{I}\rangle\rangle$ spans over all symmetry blocks of the Lindbladian our restriction to a certain quantum number sector in the time evolution would require a manual selection of basis states fulfilling the condition. However, since the auxiliary space states are traced out when measuring physical observables, the measurement results are invariant to a gauge transformation with respect to the auxiliary the constituents of the density-vector. We choose the transformation $\mathcal{U} = \bigotimes_{j=1}^{L} (\mathbb{1} \otimes U)$ such that

$$\mathcal{U}\,|\mathbb{I}\rangle\rangle = \bigotimes_{j=1}^{L} \sum_{\sigma_j} |\sigma_l\rangle_{\mathrm{phys}} \otimes U\,|\sigma_l\rangle_{\mathrm{aux}} \equiv \bigotimes_{j=1}^{L} \sum_{\sigma_j} |\sigma_l\rangle_{\mathrm{phys}} \otimes |\tilde{\sigma}_l\rangle_{\mathrm{aux}} \, ,$$

where the specific choice of U ensures that the respective quantum number of the full initial state is equally distributed to the local pairs of physical and auxiliary states and thus restricts the trace-generating infinite temperature state to the initial symmetry sector. The initial state and Lindbladian are transformed correspondingly $\mathcal{L} \to \mathcal{U}^\dagger \mathcal{L} \mathcal{U}$.

For local operator acting on site j this is graphically depicted by:

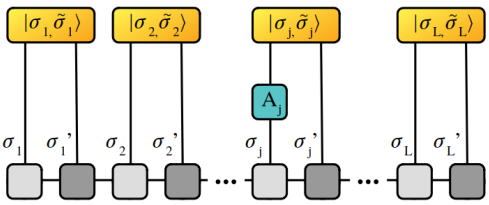

The purification method has the advantage that the full system information (up to numerical losses) is retained and it does not introduce a statistic error. However, the enlarged Hilbert space leads to huge computational costs of a single simulation run. A detailed analysis of the numerical convergence of the algorithm is presented in Sec. 4.3.1.

4.2.7 Dynamic truncation of the photonic Hilbert space

The Hilbert space of the photonic cavity mode in principle has infinite dimension. In order to efficiently calculate the time evolution numerically, it is necessary to truncate it at a maximal dimension M, restricting the cavity mode to a maximal photon number occupation of $N_{\mathrm{pho,max}}$. In the time evolution the photon number often varies a lot. In our system, turning on the atoms-cavity coupling, we often observe an initial steep increase in the measured photon number until it eventually evolves towards a much lower steady state value. Therefore, at short times a

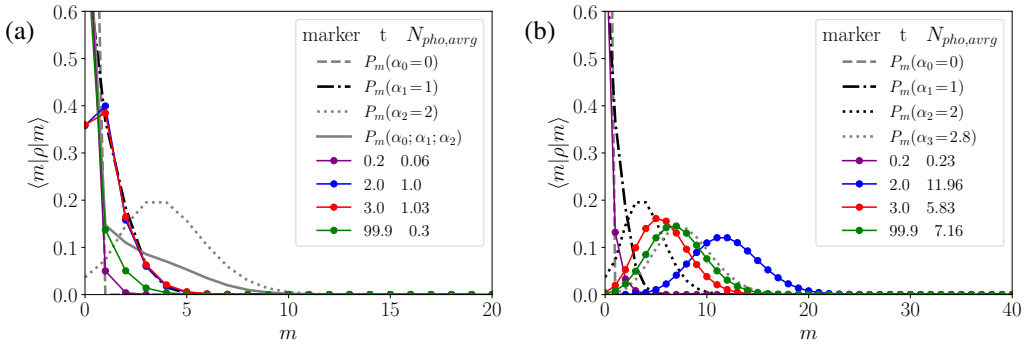

Fig. 4.5: Photon number distribution $P_m = \mathrm{Tr}\left[\langle m|\,\hat{\rho}\,|m\rangle\right]$ in Fock-states $|m\rangle$ (a) at the phase transition ($\hbar g/J=2$) and (b) above the phase transition ($\hbar g/J=4$) at different points during the time evolution towards the steady state that is already reached at $tJ/\hbar=100$. The inset in a) is the number distribution in log-scale. Parameters used are $L=8$, quarter filling, $\hbar\Gamma/J=3$, $\hbar\delta/J=2$, $U/J=2$ and a fixed cutoff dimension of the local photonic Hilbert space $M=40(60)$.

much higher local dimension is needed in order to capture the system dynamics correctly, while for later times one could drastically reduce the maximally allowed photon number and still obtain converged results. Similar scenarios are thinkable where the photon number slowly grows or is subjected to long-time periodic strong oscillations. To optimize the algorithm, we introduce a dynamical adaptation of the cutoff dimension depending on the photon number distribution of the current state in the time evolution. This procedure was developed by Catalin-Mihai Halati in Ref. [149] and is here adapted to the fermionic many-body system as well as for applications on the purified states that features an auxiliary cavity site.

To determine the optimal procedure, the photon number distribution over the different Fock-states $|m\rangle$ is measured by tracing over the atomic sector and projecting out the respective photon number state

$$P_m = \mathrm{Tr}\left[\langle m|\,\rho\,|m\rangle\right]. \tag{4.29}$$

The distribution over the number states helps to determine where to truncate the site dimension.

Dimension adaptation algorithm

We show the evolution of the photon number distribution in Fig. 4.5. Coherent state distributions at a few values of α are plotted as gray lines for comparison. Below or very close to the self-ordering phase transition P_m decays approximately exponentially with m similar to a Poisson-distribution with small α, which hints towards a coherent state of the photonic field. In contrast to this above the transition the number distribution shows multiple maxima at larger m. At short times, where the system dynamics are fast and far from equilibrium, the occupation shows two peaks. A large contribution comes from the states with small m while a second maximum builds up at photon number states that are significantly higher than the eventual mean photon number of the steady state for the given parameter settings. Towards the steady state, the occupation of the small m states increases again. This contribution stems from the admixture of states without perfect population imbalance in the steady state. The second maximum moves to lower m at long times.

This adaptation is especially sensible in the purification approach to the time evolution [see Sec. 4.2.6] since here instead of a single photonic site we have the additional auxiliary cavity site. Therefore, if the local dimension of the bosonic Hilbert space is chosen too large it can be a bottleneck for the time evolution of the system.

Every few time steps, the photon number distribution P_m is measured up to the current dimension cutoff M' and compared to set threshold values $p_{i/d}$. We distinguish three cases:

1. The contributions of partial states with higher dimensions $M'>M$ are below a set threshold value $P_{M+1}<p_{\mathrm{d}}$, the contribution from these states in negligible and the cutoff dimension can be set to $M+1$. The local dimension of the cavity site are compressed to the new maximal dimension. The gate dimension is adjusted as well and all relevant indices are updated.

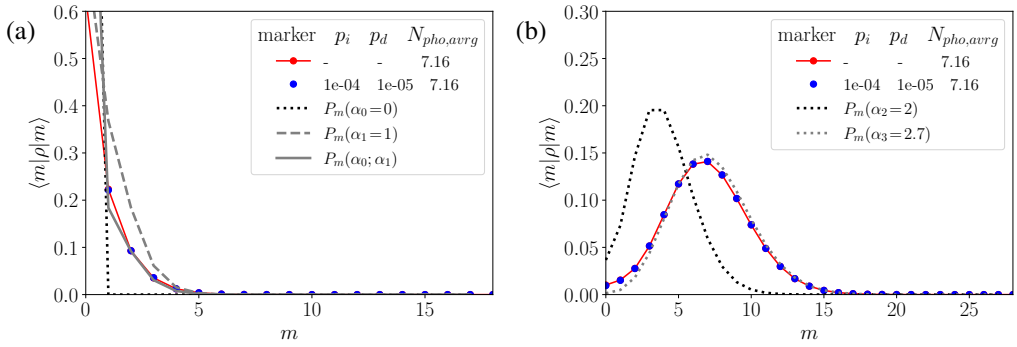

Fig. 4.6: Time evolution of a spin balanced initial state at quarter filling with $L = 8$, comparing observables truncating the local bosonic Hilbert space of the cavity mode at fixed $M=40(60)$ and using the dynamical photon number adaptation. p_d (p_i) set the truncation error thresholds triggering the adaptation of M. (a) Mean photon number $\langle N_\mathrm{pho}\rangle$ and (b) the deviation from the run with fixed local dimension $M=80$ of the local cavity Hilbert space. (c) Atomic density $\langle \hat{n}_{L/2,\uparrow}\rangle$ in the middle of the chain and (d) the deviation from the run with fixed local dimension $M=80$ of the local cavity Hilbert space. The parameters used are $\hbar g/J=2$, $\hbar\Gamma/J=3$, $\hbar\delta/J=10$ and $U/J=40$.

2. The occupation of states at the maximal dimension exceeds a second threshold value $P_{M'} > p_\mathrm{i}$. Then the local dimension of the MPS and gate-tensors representing the cavity mode is raised to $M=M'+1$.
3. Else, the dimension stays the same.

For short times, where the photon number is expected to increase very quickly for our typical choice of the initially empty cavity mode, we start with a fixed cutoff dimension. Then, from a chosen time t_start, the dynamical adjustment starts. Some trajectory averages for a fixed maximal dimension as compared to the run with dynamical cutoff and two different threshold settings for the new convergence parameters p_d and p_i is depicted in Fig. 4.6. For the same parameters the photon number distribution was shown and discussed in the left panel of Fig. 4.5. While the evolution for these setting does not seem fully converged in the initial peak of the mean photon number, they all evolve towards the same steady state. Some theoretical background on the observed photonic states of the cavity field is provided in Appendix A.1. While the benefits of this method might not be decisive for some parameter settings, especially in the highly-dissipative regime where the photon number is mostly flat and does not exhibit any spikes, it is very efficient to apply as the check of the photon number distribution is a local measurement. So while it might not speed up the evolution in these cases, its additional computational costs are negligible compared to the overall costs of a single time step.

Now that we introduced the algorithm that captures the dynamics of our atom-cavity coupled system, we show the validity and numerical convergence of the methods.

4.3 Method Comparisons and Convergence

Since the open system tMPS algorithm to simulate the many-body atomic system coupled globally to the dissipative cavity field is highly complex and uses non-standard methods, we compare simulations using independent numerical algorithms (MCWF with Trotter-Suzuki algorithm, TDVP, Purification) and compare the respective results. These kind of method comparisons and bench-marking of the computational efficiency and convergence are a field of interest by itself that has attracted a lot of research interest for many years and has been performed for different models and methods [114, 145, 187].

Each of the methods we present is suitable to tackle the problem of the time evolution by itself, which allows us to gain knowledge about how the individual methods work for the complicated dissipative many-body system with global interactions at hand. Further the behavior and interplay with the multiple evolution and convergence parameters provide further insight and help us to push the implementations to higher efficiencies and ultimately develop new algorithms. Besides providing insights on the complex tensor-network algorithms themselves, these checks validate the numerical results that will be presented in Chapter 7 by ruling out formal and systematic errors

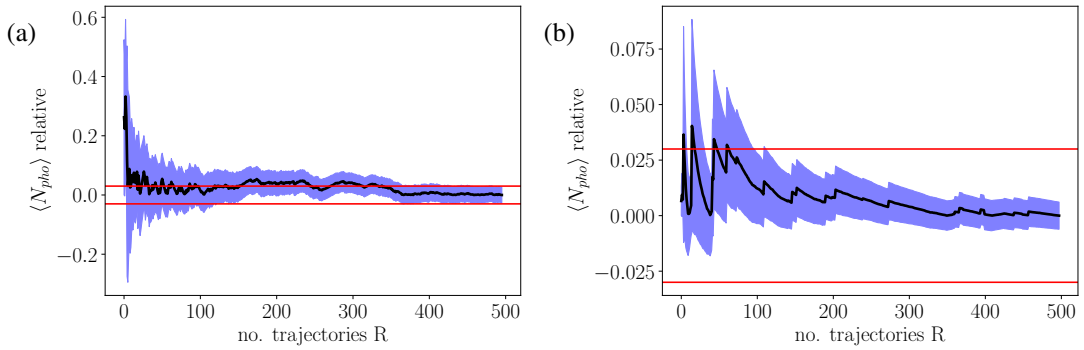

Fig. 4.7: Photon number relative to the average over all trajectories $\langle N_{\text{pho}} \rangle(R) - \langle N_{\text{pho}} \rangle(R=500)$ as a function of the number of trajectories in the Monte-Carlo average, where the blue area is the stochastic error $\sigma(N_{\text{pho}}(\hbar t/J=100)$ [Eq. (4.30)] . Starting with the ground state of the Fermi-Hubbard model at quarter filling with $L=8$, $S_z=0$ and $U/J=2$, the parameters used in the time evolution are $\hbar g/J=2(4)$, $\hbar \Gamma/J=1$, $\hbar \delta/J=2$ and $N_{\text{pho,max}}=40(60)$.

in the implementation.

4.3.1 Convergence of the individual methods

Multiple parameters control the convergence and accuracy of the computed time evolution for both the Purification- and MCWF-method. We provide here a convergence analysis and method comparisons for exemplary parameters in the typical regime we investigate. For all of the presented methods, the von-Neumann entropy $S_{\text{vN,j}}$ is a measure of the computational entanglement present between the subsystems left and right of a specific bond j in either each trajectory (MCWF methods) or the vectorized density matrix (purification). Since the possible compression in the SVD steps of the MPS methods is typically limited by the presence of entanglement, we require $S_{\text{vN,j}}$ to be finite and saturating in time to assume we correctly capture the dynamics of the system.

Monte-Carlo-Wavefunction-method

For the stochastic unraveling of the master equation, the number of trajectories needs to be sufficiently high to sample the density matrix evolution to a sufficient accuracy. The stochastic error from the finite number of quantum trajectories is estimated by computing the standard deviation from the Monte-Carlo average for the measured expectation value of an operator $\hat{A}$

$$\sigma^2(\hat{A}(t)) = \frac{1}{R(R-1)} \sum_{l=1}^{R} \left(\langle \psi_l(t) | \hat{A} | \psi_l(t) \rangle - \bar{A}(t) \right)^2 \tag{4.30}$$

where R is the total number of samples, $|\psi_l(t)\rangle$ the time evolved wavefunction of the trajectory labeled by l, and $\bar{A}(t)$ the statistical average over all quantum trajectories. We want the measured physical observables to have a relative error below 3%, which typically requires about 500 trajectories. This is confirmed by looking at the dependence of the trajectory average of the photon number on the number of trajectories in the Monte-Carlo average relative to the average over all trajectories $\langle N_{\text{pho}} \rangle(R) - \langle N_{\text{pho}} \rangle(R=500)$ [Fig. 4.7]. Typically close to the phase transition or in the large dissipation limit, where fluctuation effects in the atom-cavity coupling are observed to be particularly strong, more trajectories are needed in order to converge the average.

Trotter-Suzuki time evolution algorithm

As described in Sec. 4.2.3, the discrete time step $\tau J/\hbar$ in the time evolution introduces the systematic Trotter-Suzuki-error of order $\mathcal{O}(L\tau^3)$. An additional truncation error ϵ stems from the SVD compression after each application of the time-evolution operator gates.

Another issue might arise, because the bond dimension of the MPS typically increases during the application of a Trotter gate. The representation of the state consequently leaves the variational manifold defined by a set bond dimension. Therefore, one needs to approximate the new time-evolved state by a representative from the manifold

of the initial state. To control the computational costs, after contracting the adjacent MPS site tensors with a gate tensor, the bond dimension is truncated to a maximal dimension m in the decomposition. By keeping only m contributing states with lowest Eigenvalues, one introduces a truncation error ϵ which is the combined weight of all discarded states in the singular value decomposition performed in the time evolution gates and swap gates [see Eq. (4.3)].

Varying the truncation error at fixed maximal bond dimension and assuming we are converged in the time step Trotter error [188], one can observe that the obtained cavity field occupations agree up to $\epsilon \approx 10^{-6}$ for final times around $tJ/\hbar$. For lower truncation errors, the deviations between the trajectory averages are of the same order as the statistical error introduced by the stochastic sampling. We therefore find that a truncation error of $\epsilon \approx 10^{-7}$ captures the nature of the considered states in the matrix product form sufficiently well.

Starting from an initial state with low entanglement and bond dimension significantly lower than the set maximal bond dimension, the bond entropy and correspondingly the bond dimension typically increases as time evolves until it reaches the dimension cutoff m at a certain threshold time. From this point on, the maximal bond dimension no longer suffices to represent the full state as an MPS to the requested truncation accuracy ϵ. At this point in time one would observe that two time evolution calculations for different values of m but otherwise identical parameter sets begin to deviate.

The time step error [see Fig. 4.8] typically accumulates as the system evolves. While larger time steps might yield acceptable results at short times the observables diverge from the measurement obtained from a simulation with smaller time step as time progresses. Note, that one needs to consider that by decreasing the time step the number of truncation steps needed to reach a fixed final time increases and so does the influence of the SVD compression truncation error. The two errors introduced in the time step lead to a balance that needs to be considered carefully. Decreasing the time step reduces the Trotter-Suzuki error at the cost of more gate applications, which increases the truncation error [Fig. 4.8(c)]. Therefore, an intermediate time step size is expected to yield the optimal results.

However, in the complex open system we simulate here, the dependence of the numerical convergence on the time step is more involved. Not only the Trotter error, but also the convergence of the stochastic sampling process depends on $\tau J/\hbar$. The way the jump operator application is implemented in the time step only allows for a single jump within the discrete time steps. Therefore, if the time step is chosen too large, the cavity field occupation will stay below the time step converged photon number at a given time. This can be seen in Fig. 4.8 since here the simulation run at the larger time step fails to capture the initial steep rise of the cavity photon number.

We want to now move on to the alternative time evolution scheme that is based on variational methods.

Time Dependent Variational Principle Algorithm

For the Time Dependent Variational Principle Algorithm, as described in Sec. 4.2.4, the convergence of the individual trajectories depends on the number of sweeps in the optimization and, if the two-site method is used, the truncation error ϵ and/or maximal bond dimension m to be kept in the SVD compression. Here, instead of the Trotter-Suzuki time step error, a local integration error that amounts to a total time step error of order $\mathcal{O}(\tau^3)$ in sweeping right and left through the chain occurs. The dependence of the convergence on this time step error looks similar to what was discussed in the previous section. As shown in Fig. 4.9 (b), while increasing the time step initially yields good results, the deviations due to the larger time step error quickly grows as the error accumulates with each time step.

Typically, the TDVP allows for larger time steps than the Trotter-Suzuki time evolution algorithm for closed system. However, in the large dissipation regime the application of the jump operator is limiting the time step size, such that in this regime choosing the Trotter-Suzuki algorithm for the unitary part of the time evolution tends to be favorable. In the two-site algorithm containing the SVD compression the truncation error and time step error do not influence the convergence independently. Rather, as for the Trotter algorithm, there typical exists a sweet spot where the numerical errors are minimal while restraining to reasonable computational costs.

Purification

In the purification algorithm, since the time evolution method is based on the Trotter-Suzuki algorithm, the convergence behavior in many ways is similar to what was described for the MCWF method [see Ref. [184] for details].

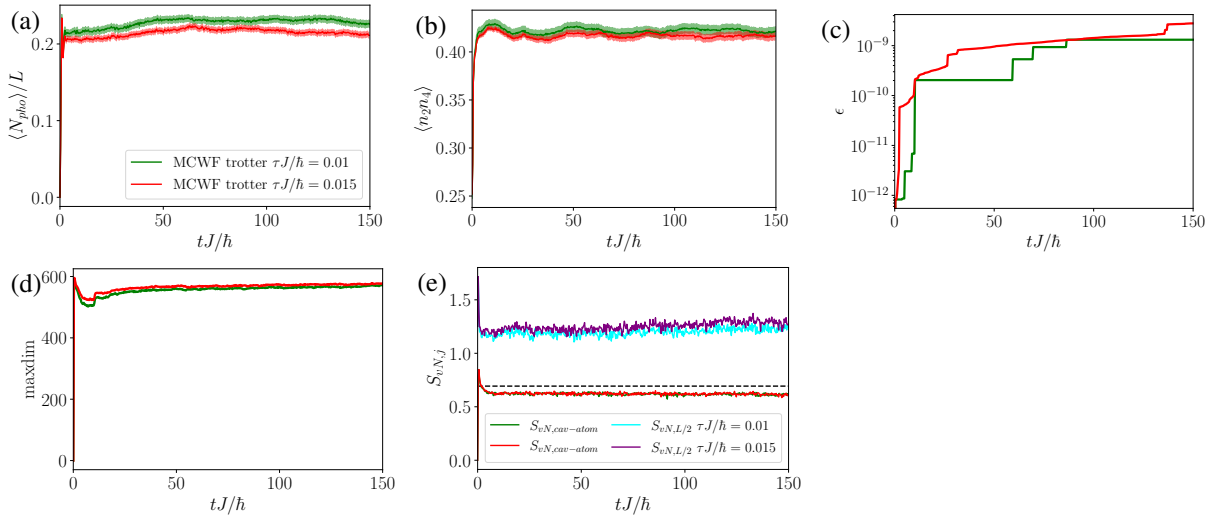

Fig. 4.8: Real time evolution using the Trotter-Suzuki algorithm of the (a) rescaled photon number $\langle N_{\text{pho}} \rangle / L$, (b) atomic density-density correlation at even distance $\langle \hat{n}_2 \hat{n}_4 \rangle$, (c) truncation error ϵ, (d) maximal bond dimension m and (e) von-Neumann bond entropy S_{vN} at the bond connecting the cavity site to the first atomic site and at the center of the atomic chain ;comparing time step sizes $\tau J/\hbar = 0.01,\ 0.015$. Starting with the ground state of the Fermi-Hubbard model at quarter filling with $L = 12$, $S_z = 0$ and $U/J = 40$, the parameters used in the time evolution are $\hbar g/J = 6$, $\hbar \Gamma/J = 3$, $\hbar \delta/J = 5$ and $N_{\text{pho,max}} = 40$, maximal bond dimension $m = 600$.

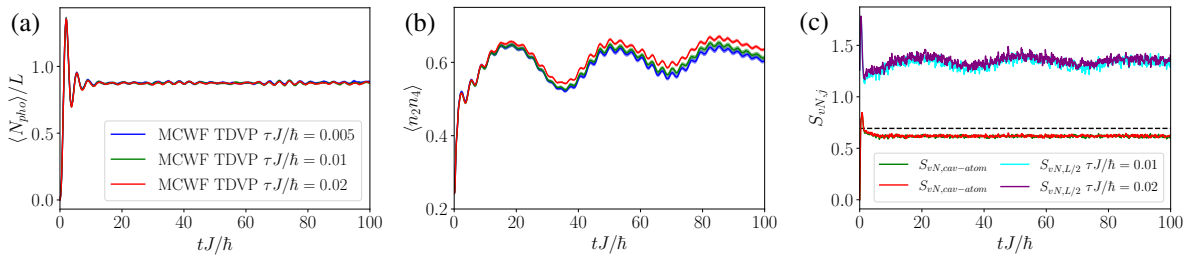

Fig. 4.9: Real time evolution using the TDVP algorithm of the (a) rescaled photon number $\langle N_{\text{pho}} \rangle / L$ and (b) atomic density-density correlation at even distance $\langle \hat{n}_2 \hat{n}_4 \rangle$ and (c) von-Neumann bond entropy S_{vN} at the bond connecting the cavity site to the first atomic site and at the center of the atomic chain comparing time step sizes $\tau J/\hbar = 0.005,\ 0.01,\ 0.02$. Starting with the ground state of the Fermi-Hubbard model at quarter filling with $L = 8$, $S_z = 0$ and $U/J = 2$, the parameters used in the time evolution are $\hbar g/J = 4$, $\hbar \Gamma/J = 1$, $\hbar \delta/J = 2$ and $N_{\text{pho,max}} = 30$, maximal bond dimension $m = 300$, with 3 iterations in the TDVP sweeps.

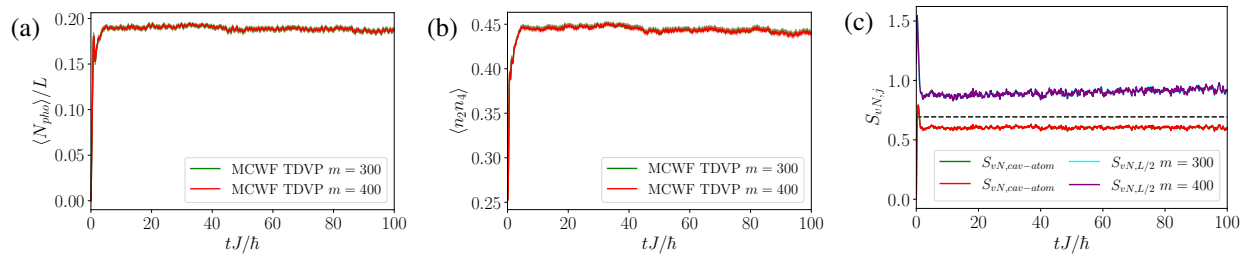

Fig. 4.10: Real time evolution using the TDVP algorithm of the (a) rescaled photon number $\langle N_{\text{pho}} \rangle / L$ and (b) atomic density-density correlation at even distance $\langle \hat{n}_2 \hat{n}_4 \rangle$ and (c) von-Neumann bond entropy S_{vN} at the bond connecting the cavity site to the first atomic site and at the center of the atomic chain comparing maximal bond dimension $m = 300,\ 400$. Starting with the ground state of the Fermi-Hubbard model at quarter filling with $L = 8$, $S_z = 0$ and $U/J = 40$, the parameters used in the time evolution are $\hbar g/J = 5$, $\hbar \Gamma/J = 3$, $\hbar \delta/J = 5$ and $N_{\text{pho,max}} = 10$, time step size $\tau J/\hbar = 0.01$, with 3 iterations in the TDVP sweeps.

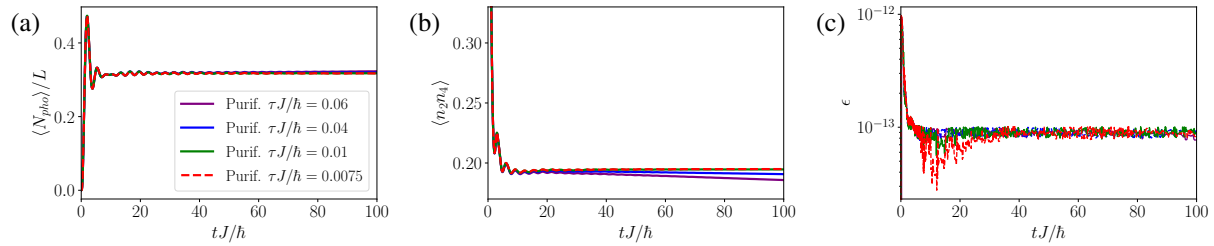

Fig. 4.11: Real time evolution using the purification algorithm of the (a) rescaled photon number $\langle N_{\text{pho}}\rangle$ and (b) atomic density-density correlation at even distance $\langle \hat{n}_2 \hat{n}_4\rangle$ comparing time step size $\tau J/\hbar = 0.06,\ 0.04,\ 0.01,\ 0.0075$. Starting with the Néel state of the Fermi-Hubbard model at quarter filling with $L=4$, $S_z=0$ and $U/J=2$, the parameters used in the time evolution are $\hbar g/J=3$, $\hbar\Gamma/J=1$, $\hbar\delta/J=2$ and $N_{\text{pho,max}}=20$, maximal bond dimension $m=400$.

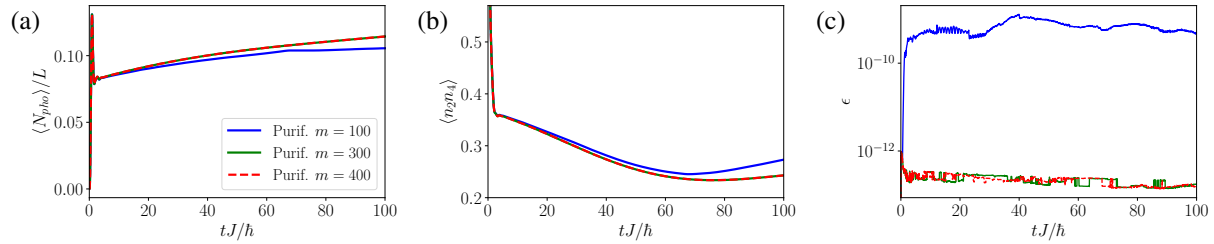

Fig. 4.12: Real time evolution using the purification algorithm of the (a) relative photon number $\langle N_{\text{pho}}\rangle$, (b) atomic density-density correlation at even distance $\langle \hat{n}_2 \hat{n}_4\rangle$and (c) truncation error ϵ comparing maximal bond dimension $m=100,\ 300,\ 400$. Starting with the Néel state of the Fermi-Hubbard model at quarter filling with $L=4$, $S_z=0$ and $U/J=40$, the parameters used in the time evolution are $\hbar g/J=5$, $\hbar\Gamma/J=3$, $\hbar\delta/J=5$ and $N_{\text{pho,max}}=20$, time step size $\tau J/\hbar=0.01$.

A Trotter-error from the finite discrete time steps is introduced as well as a SVD compression error. Variants of the two methods have been compared for other models not including global range interactions in Refs. [139, 145]

However, since here the Lindbladian dynamics is contained in the unitary time evolution operator on the enlarged Hilbert space, the time step convergence is not constrained by the application of the jump operator. However, it might still be limited the dissipation rate in the large-dissipation regime. One could expect a reduced sensitivity on the time step in the limit of large dissipation rates as long as it is not the dominating energy scale in the system. The time step convergence for exemplary values is shown in Fig. 4.11. The system convergence is not limited by the truncation error [Fig. 4.11 (c)] or maximal matrix dimension, but by the time step size and we see the deviations increasing at longer times.

Since the evolution explores an essentially squared Hilbert space and needs to accommodate two high dimensional bosonic sites, the maximal bond dimension needed to represent the time evolved density matrix is approximately squared compared to the individual trajectories in the MCWF algorithm, though this scaling also depends on the entropy of the state representation [Fig. 4.12]. This puts a strong constraint on the realizable system sizes, since the calculation can not easily be parallelized and the run time quickly exceeds reasonable timescales. The global interaction mediated by the cavity field and resulting correlations seems to prevent strong compression in the SVD step.

Bosonic Hilbert Space truncation

Lastly, the cutoff dimension of the bosonic Hilbert space of the cavity mode introduces an error that we control by dynamically adjusting the cutoff to stay below a set weight of the discarded photon number states. This procedure is described in detail in Sec. 4.2.7. Choosing the maximal photon number too low in the low dissipation limit, the time evolution of observables can deviate from the converged run at short times because the cavity field occupation typically shoots up to values far above the eventual expected steady state value. However, even if initially not converged the average might still evolve towards the same steady state [see Figs. 4.13 & 4.14].

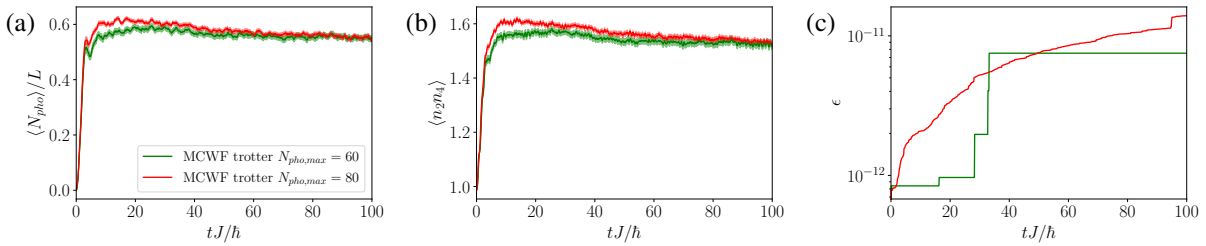

Fig. 4.13: Real time evolution using the Trotter-Suzuki algorithm of the (a) rescaled photon number $\langle N_{\text{pho}} \rangle / L$, (b) atomic density-density correlation at even distance $\langle \hat{n}_2 \hat{n}_4 \rangle$ and (c) truncation error ϵ; comparing maximal photonic Hilbert space dimensions $N_{\text{pho,max}} = 60$, and $N_{\text{pho,max}} = 80$. Starting with the ground state of the Fermi-Hubbard model at half filling with $L = 8$, $S_z = 0$ and $U/J = 2$, the parameters used in the time evolution are $\hbar g/J = 5.65$, $\hbar \Gamma/J = 1$, $\hbar \delta/J = 2$ and time step size $\tau J/\hbar = 0.01$, maximal bond dimension $m = 500$.

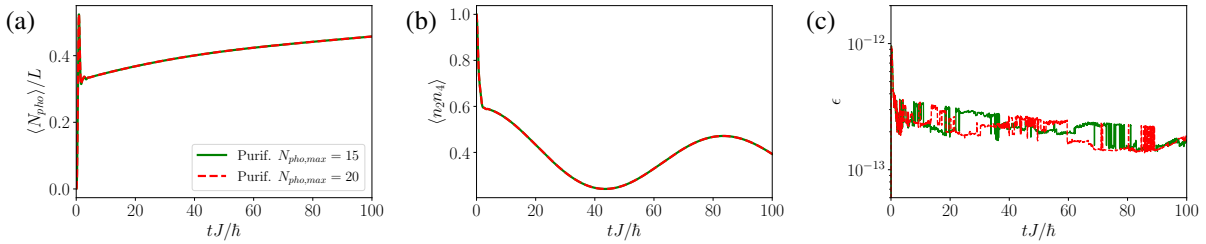

Fig. 4.14: Real time evolution using the purification algorithm of the (a) rescaled photon number $\langle N_{\text{pho}} \rangle / L$, (b) atomic density-density correlation at even distance $\langle \hat{n}_2 \hat{n}_4 \rangle$ and (c) truncation error ϵ; comparing $N_{\text{pho,max}} = 15$ and $N_{\text{pho,max}} = 20$. Starting with the Néel state of the Fermi-Hubbard model at quarter filling with $L = 4$, $S_z = 0$ and $U/J = 2$, the parameters used in the time evolution are $\hbar g/J = 3$, $\hbar \Gamma/J = 1$, $\hbar \delta/J = 2$ and time step size $\tau J/\hbar = 0.01$, maximal bond dimension $m = 500$.

4.3.2 Method comparisons

In this section we want to provide a comparison of the individual tMPS methods and confirm their results agree within the numerical accuracy of the simulation. Note however, that the complex dependence of run time and convergence on multiple parameters makes a quantitative comparison very complex. It should therefore be noted, that the here provided results so far serve as examples and the behavior of the methods is expected to change for different parameter regimes. Our research to benchmark both time evolution algorithms and their performance in different system parameter regions is currently still ongoing.

MCWF methods: Trotter-Suzuki vs TDVP time step

We begin by comparing the algorithms based on Monte-Carlo-Wavefunctions [see Fig. 4.15]. Exemplarily, the quantities chosen to compare the real time evolution are the cavity field occupation $\langle N_{\text{pho}} \rangle$ as well as various atomic properties such as a density-density-correlation later used to characterize the density wave state and average kinetic and interaction energy of the system.

The results using the Trotter-Suzuki time step decomposition are in nice agreement with the TDVP evolution with and without an additional basis-extension step for all shown quantities. Slight deviations appear only at later times. This is a strong support for the credibility of our numerical results. The error of the interaction energy is calculated by binning 25 trajectories at a time and propagating the errors from their deviations from the full average.

In the large dissipation limits, convergence issues arise in the TDVP algorithm and the individual trajectories tend to fail in the optimization step. This observation is to be further investigated.

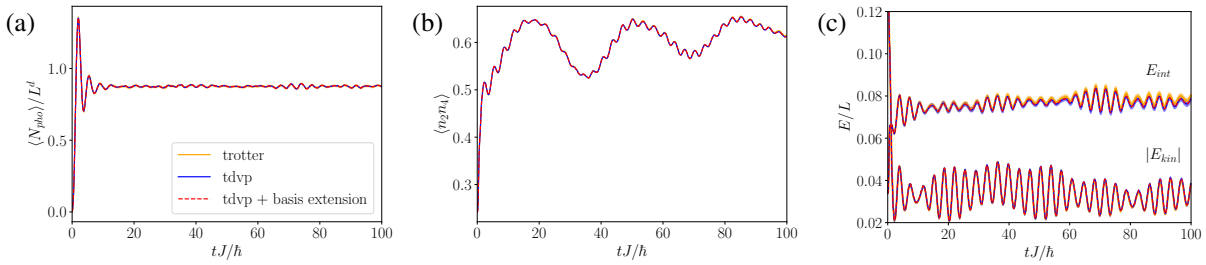

Fig. 4.15: Real time evolution of various observables using different MCWF time evolution methods (a) rescaled photon number $\langle N_{\text{pho}} \rangle$ and (b) atomic density-density correlation at even distance $\langle \hat{n}_2 \hat{n}_4 \rangle$ (c) absolute value of the kinetic energy $E_{\text{kin}}/(L-1)$ and the interaction energy E_{int}/L. Starting with the ground state of the Fermi-Hubbard model at quarter filling with $L=8$, $S_z=0$ and $U/J=2$, the parameters used in the time evolution are $\hbar g/J=4$, $\hbar \Gamma/J=1$, $\hbar \delta/J=2$ and time step size $\tau J/\hbar=0.01$, maximal bond dimension 300, $N_{\text{pho,max}}=30$.

MCWF methods vs purification algorithm

Spin-balanced fermions

We compare the time evolution of spin-balanced ($S_z=0$) fermions obtained with our purification algorithm to the one using the MCWF method with Trotter-Suzuki time evolution for a very small system size of $L=4$. Starting from a pure state with occupations $|\uparrow, 0, \downarrow, 0\rangle$, the dynamics of the photon number and density-density correlation $\langle \hat{n}_2 \hat{n}_4 \rangle$ are shown in Fig. 4.16 (a),(b). Stochastic errors in the MCWF results are included as a colored area around the mean value. We see, that the results from both methods agree in cavity- as well as atomic observables, which serves as further validation for our methods. We show here the time evolution choosing the maximal bond dimension such that the full Hilbert space can be represented. As expected in this case, the matrix-dimension of the un-truncated systems is squared in the purification when compared to the individual trajectories in the MCWF evolution [see Fig. 4.16 (c)].

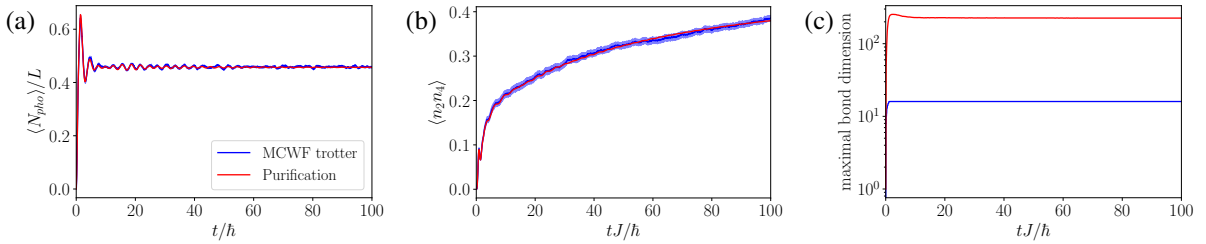

Fig. 4.16: Comparing the dynamics of a system of spinful fermions using purification and using a MCWF algorithm with Trotter-Suzuki time evolution (a) rescaled photon number $\langle N_{\text{pho}} \rangle$ (b) atomic density-density correlation at even distance $\langle \hat{n}_2 \hat{n}_4 \rangle$ and (c) maximal bond dimension m. The systems are at quarter filling ($N=L/2$) with $L=4$, $S_z=0$, $U/J=2.0$, $\hbar g/J=3.0$, $\hbar \Gamma/J=1$ and $\hbar \delta/J=2$. The numerical parameters are for the purification: time step size $\tau J/\hbar=0.01$, maximal bond dimension $m=260$, $N_{\text{pho,max}}=20$ and MCWF: time step size $\tau J/\hbar=0.01$, maximal bond dimension $m=16$ (exact), $N_{\text{pho,max}}=20$, averaging over 500 trajectories.

Spin-polarized fermions vs hard-core bosons

Another powerful method check is provided by comparing the time evolution of a system of spin-polarized fermions to that of hard-core bosons (restricting the maximal on-site occupation of the bosons to 1). Since the considered fermionic model conserves the total spin upon initializing a fully spin-polarized state the dynamics are restricted to the symmetry sector containing a single spin species which immensely reduces the dimensionality of the system. The local dimension of the physical index restricted to 2 since the Pauli blocking prevents the fermions from occupying the same site.

The tMPS code for bosons using MCWF was independently implemented by Catalin-Mihai Halati [149]. A detailed comparison to the Purification method for fermions was already provided in Ref. [184]. Therefore we restrict ourselves to a brief summary here. The comparison of both algorithms in this limiting case is very compelling be-

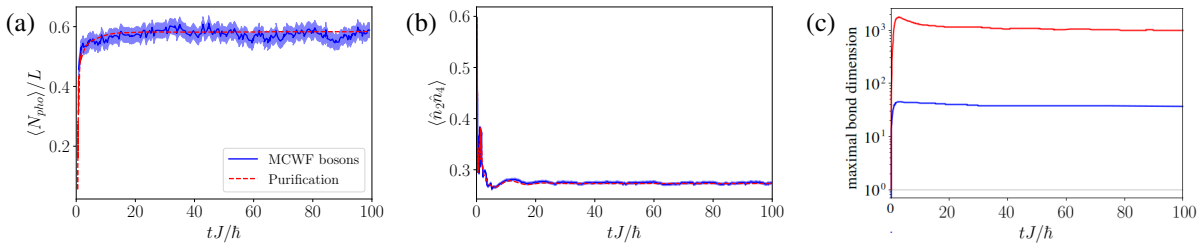

Fig. 4.17: Comparing a system of spin-polarized fermions time evolved using purification and hard-core bosons using a MCWF algorithm (a) rescaled photon number $\langle N_{\text{pho}} \rangle$ (b) atomic density-density correlation at even distance $\langle \hat{n}_2 \hat{n}_4 \rangle$ and (c) maximal bond dimension m. The systems are at quarter filling $N = L/2$ with $L = 8$, $\hbar g/J = 1.5\sqrt{L}$, $\hbar\Gamma/J = 5$ and $\hbar\delta/J = 2$. The numerical parameters are for the purification: time step size $\tau J/\hbar = 0.01$, maximal bond dimension 2000, $N_{\text{pho,max}} = 30$ and MCWF: time step size $\tau J/\hbar = 0.01$, maximal bond dimension 300, $N_{\text{pho,max}} = 30$, averaging over 500 trajectories. Plots taken from my master thesis [184]

cause it allows for checks including dissipation as well as the global range interaction of the cavity mode with the atomic chain. The use of MCWF and purification and the differing Hilbert spaces of hard-core bosons compared to spin polarized fermions assures that the agreement of the data is not a result of a shared error in the implementation of the time evolution. Note, that still in both implementations the sequence of gate applications and swap gates is the same, the results still need to be handled with care. However, the specific lattice architecture (i.e. placing the local tensor representing the cavity field in the center of the chain) was shown not to alter the time evolution [149]. In the special case of spin-polarized fermions and hard-core bosons, agreeing results are expected in the density observables. Note, that this equivalency is not generally expected for arbitrary operators.The fermionic anti-commutation relations require inserting non-local Jordan-Wigner strings [see Sec. 4.2.1] when representing them in terms of bosonic operators. For densities, since the non-local strings in the fermion operators contract to unity, the operators of hard-core bosons and spin-polarized fermions become equal. This is not true e.g. for single particle correlations. Very good agreement is observed [see Fig. 4.17] in both cavity field and atomic observables.

Summary

In the first part of this chapter we introduced our newly developed and implemented algorithm that allows us to time evolve the many-body fermionic system globally coupled to the dissipative cavity field. We showed how we prepare the initial state in the ground state of the Fermi-Hubbard model. The time evolution is based either the Trotter-Suzuki algorithm, where the global range interaction is decomposed into a sequence of two-site operators and swap gates, or the TDVP algorithm. The Lindblad-dynamics are included via the purification of the system, which we first implemented for the many-body atom-cavity system. Alternatively we brought the Monte-Carlo-Wavefunction method over to spinful fermions, that stochastically reproduces the effect of dissipation averaging over many trajectories. Also, we presented an algorithm that dynamically adapts the dimension of the tensor representing the cavity mode in order to save computational costs.

The second part showed the dependence of the convergence of the time evolution on the numerical parameters for the individual methods. We further checked their validity by providing comparisons between the various independently implemented algorithms that show very good agreement within the numerical accuracy.

Chapter 5

Properties of the ionic Hubbard model

In Chapter 3 we have seen that both for the $T=0$ MF limit as well as the many-body adiabatic elimination method [Sec. 3.1] the resulting effective Hamiltonian $\hat{H}_{\text{eff}}$ for the treated atoms-cavity coupled system is an ionic Hubbard model with self-consistently determined potential imbalance. Thus, we want to introduce the ionic Hubbard model in Sec. 5.1 and comment on its ground state phase diagram and dominant excitations to lay a groundwork for further explanations in Sec. 5.2. Further, to support the thermal assumption in our derivation of the adiabatic elimination model [see Sec. 3.1], we analyze the energy level statistics of the ionic Hubbard model to confirm the Gaussian orthonormal ensemble (GOE) statistics and associated breaking of the integrability at finite staggering of the potential in Sec. 5.3. This work was previously published in Ref. [3].

We want to note, that besides the applications in our specific setup, the ionic Hubbard model itself has attracted a lot of interest and has been realized in cold atomic gases using a super-lattice potential [189, 190]. It has been devised in order to study the physics occurring at neutral-ionic phase transitions as they occur in solids for example, ionic to neutral transitions in organic charge-transfer solids [191, 192] and at ferro-electric transitions in perovskites [193]. An alternating local potential is also at the heart of the staggered fermion formulation of massive fermions in quantum field theories on a lattice [194].

5.1 Ionic Hubbard Hamiltonian

The ionic Hubbard Hamiltonian is defined on a bipartite lattice

$$\begin{aligned}\hat{H}_{\text{IH}} = &- J \sum_{\langle j,l\rangle,\sigma} \left(\hat{c}^{\dagger}_{j\sigma}\hat{c}_{l\sigma} + \text{H.c.}\right) + U\sum_{j}\hat{n}_{j\uparrow}\hat{n}_{j\downarrow} \\ &- \eta\Big(\sum_{j\in A,\sigma}\hat{n}_{j\sigma} - \sum_{l\in B,\sigma}\hat{n}_{l\sigma}\Big)\end{aligned} \tag{5.1}$$

where neighboring lattice sites $\langle j,l\rangle$ belong to different sublattices A, B. The ground state of the ionic Hubbard model is governed by the competition between the kinetic energy, the on-site interaction U and the energy offset between lattice sites of the sublattices 2η. This leads to a very involved phase diagram that has been the subject of many theoretical works in both one dimension [195–200], higher dimension [201–204] or at finite temperature [205–207]. Some works have focused on the predicted exotic bond-order wave phase at commensurate filling [208–210], that we will briefly comment on later.

We begin by investigating the influence of the potential staggering on the phases of the *non-interacting* model ($U=0$) with periodic boundary conditions (PBC) in one dimension. However, this could be adapted to higher dimension in a straight forward way. The model can be diagonalized in momentum space on the reduced Brillouin zone with $k\in(-\pi/2,\pi/2]$ by performing a standard Bogoliubov-transformation defined by

$$\hat{c}_{k,\sigma} = u_k\hat{\gamma}_{-,k,\sigma} + v_k\hat{\gamma}_{+,k,\sigma}, \quad \hat{c}_{\pi+k,\sigma} = -v_k\hat{\gamma}_{-,k,\sigma} + u_k\hat{\gamma}_{+,k,\sigma}$$

with $|u_k|^2+|v_k|^2=1$ and the dispersion relation $\epsilon(k)=-2J\cos(k)$. Assuming $u_k^*=u_k$ and $v_k^*=v_k$, the transformation parameters are given by

$$u_k=\sqrt{\frac{1}{2}\Big(1+\frac{\epsilon(k)}{\sqrt{\epsilon(k)^2+\eta^2}}\Big)},\qquad v_k=\sqrt{\frac{1}{2}\Big(1-\frac{\epsilon(k)}{\sqrt{\epsilon(k)^2+\eta^2}}\Big)} \tag{5.2}$$

We use $E(k)=\sqrt{\epsilon(k)^2+\eta^2}$ to obtain the Hamiltonian in momentum space

$$\hat{H}_{\mathrm{IH}}=\sum_{k,\sigma}E(k)(\hat{\gamma}^\dagger_{+,k,\sigma}\hat{\gamma}_{+,k,\sigma}-\hat{\gamma}^\dagger_{-,k,\sigma}\hat{\gamma}_{-,k,\sigma}) \tag{5.3}$$

At finite staggering a band gap $\propto 2\eta$ opens at the edges of the reduced Brillouin zone. The band is consequently split into a low- and high-energy band labeled by $(\hat{\gamma}_{\pm,k,\sigma})$. Calculating the average filling in the transformed basis yields

$$\langle\hat{n}\rangle=\sum_{k,\sigma}(u_k-v_k)^2(\langle\hat{\gamma}^\dagger_{-,k,\sigma}\hat{\gamma}_{-,k,\sigma}\rangle+\langle\hat{\gamma}^\dagger_{+,k,\sigma}\hat{\gamma}_{+,k,\sigma}\rangle). \tag{5.4}$$

The density imbalance between the occupations of the two sublattices is given by

$$\langle\hat{\Delta}\rangle=\sum_{k,\sigma}u_kv_k(\langle\hat{\gamma}^\dagger_{-,k,\sigma}\hat{\gamma}_{-,k,\sigma}\rangle+\langle\hat{\gamma}^\dagger_{+,k,\sigma}\hat{\gamma}_{+,k,\sigma}\rangle) \tag{5.5}$$

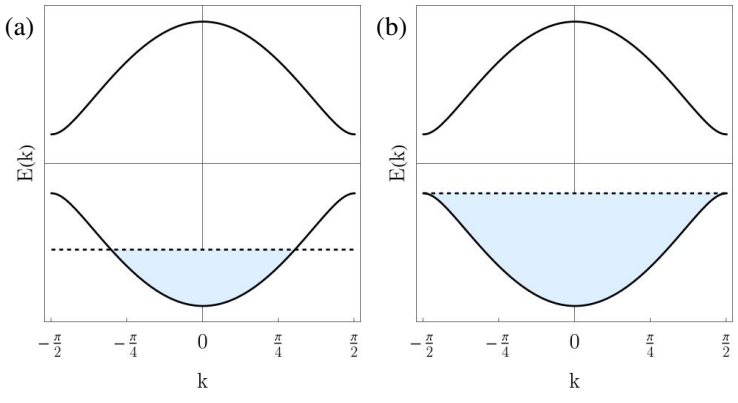

Fig. 5.1: Sketch of the occupied momenta in the low and high energy bands at (a) quarter filling and (b) half filling in the continuous limit $L\to\infty$.

Note, the expectation values $\langle ...\rangle$ are calculated with respect to the respective states of interest, e.g. the ground state at specific filling or a thermal state. In the non-interacting system in the ground-state the N particles on the chain occupy the N lowest momentum values in the lower band [see Fig. 5.1]. Only once it is filled, the high energy band starts to be occupied. The expectation values thus yield $\langle\hat{\gamma}^\dagger_{-,k,\sigma}\hat{\gamma}_{-,k,\sigma}\rangle=1$ for the lowest N momenta and else $\langle\hat{\gamma}^\dagger_{-,k,\sigma}\hat{\gamma}_{-,k,\sigma}\rangle=0$. In the thermal case at inverse temperature β, all momentum states can be occupied at varying probability. The thermal occupation in the non-interacting limit is captured by the Fermi-distribution

$$\langle\hat{\gamma}^\dagger_{-,k,\sigma}\hat{\gamma}_{-,k,\sigma}\rangle_T=\frac{1}{e^{\beta(+E(k,\lambda)-\mu)}+1}\qquad\langle\hat{\gamma}^\dagger_{+,k,\sigma}\hat{\gamma}_{+,k,\sigma}\rangle_T=\frac{1}{e^{\beta(-E(k,\lambda)-\mu)}+1} \tag{5.6}$$

where μ is the chemical potential.

5.2 Ground state phase diagram and excitations in one dimension

We want to discuss the phase diagram and low lying excitations of the one dimensional ionic Hubbard model at quarter filling ($n=N/L=1/2$) and half filling ($n=1$), since the nature of the ground state phases and excitations fundamentally changes depending on the specific filling.

5.2.1 Quarter filling

At quarter filling ($n=1/2$) [211–214] we begin by describing the ground state in the non-interacting limit as well as the dominant excitations. Then we continue to discuss the phases at finite interaction, along with describing the dominant excitations in each of the limits.

The non-interacting model at $U=0$ is given by Eq. (5.3). In the ground state the lower band is half-filled up to momenta $|k|=\pi/4$ [see Fig. 5.1 (a)] since due to the independent spin species each momentum state is doubly occupied. Low-lying excitations within the lower band are gapless and the state thus behaves as a liquid.

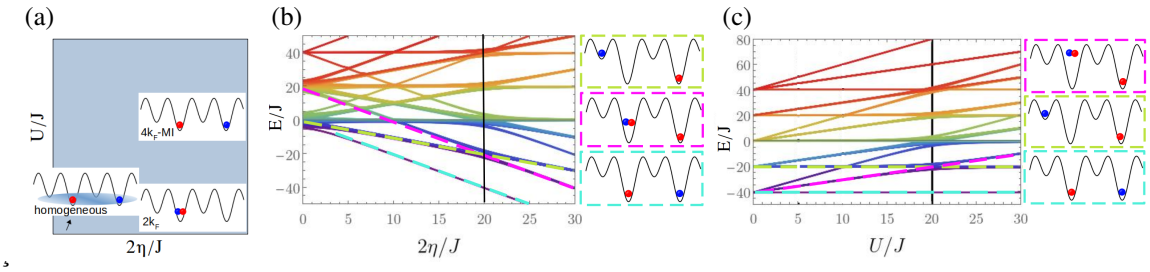

Fig. 5.2: (a) Sketch of the ground state phase diagram for the Ionic Hubbard model at quarter filling, (b),(c) Energy spectra of the Ionic Hubbard model at quarter filling. The parameters used are $L=8$, (b) $U/J=20$, (c) $2\eta/J=20$. We sketch the nature of ground states and excited states crossing around $2\eta\sim U$. Vertical black, solid line at $2\eta=U$.

As the sublattice potential imbalance 2η grows, we move along the low edge of the phase diagram sketched in Fig. 5.2 (a). The band-gap opens in the excited spectrum and clear bands appear in the excitation spectrum, that are separated by $\sim 2\eta/J$.

The phase diagram [Fig. 5.1 (a)] becomes much more involved considering interacting atoms due to the many-body character which has been investigated in numerous works, e.g. [211–214]. Here we want to restrict our explanations to processes that we identified as relevant in the self-ordering transitions and for the fluctuation-induced bistability we observe in our self-consistent model in Sec. 6.1.

The ground state of the quarter-filled one-dimensional Hubbard model is a liquid at finite on-site interactions. Charge excitations are gapped with Δ_c, while spin-excitations remain gapless. At a fixed, finite on-site interaction, increasing the potential imbalance $2\eta/J$ the sublattice density imbalance rises. The gap in the bands at the edges of the reduced Brillouin-zone opens, as can be seen in e.g. the green dashed line of Fig. 5.2 (b). Around $2\eta/J\sim U/J$, marked by the black vertical lines, the nature of the lowest excitation band above the ground state changes from states with a single particle on a high potential sublattice site [light green box] to a state with perfect density imbalance but a doubly occupied low-potential site [magenta box]. This change in the nature of the lowest excitations will be an important for the appearance of the fluctuation-induced bistability we present in Sec. 6.3.

For large $\eta/J\gg U/J,1$ the gap at the band edges is $\sim 2\eta/J$ [cyan and green dashed lines at right edge in Fig. 5.2 (b)]. In this limit, one can approximately restrict to the effectively half-filled lower band. A $4k_F$-periodic potential can be observed, leading to a Mott-insulator with antiferromagnetic alignment of the spins on sites belonging to the low potential sublattice.

Contrarily, in the limit of large interaction strength $U/J\gg 2\eta/J$ [lower right in Fig. 5.2 (a)] the charge gap can be approximated as $\Delta_c\sim U$ since in a simplified picture a charge excitation would correspond to the creation of a single doubly occupied site [see left edge of Fig. 5.2 (b) or right edge in Fig. 5.2 (c) between the cyan and magenta lines]. In the extreme case of $U\to\infty$, the system can approximately be mapped to effectively spinless fermions described by Eq. (5.3), where each momentum state can only be singly occupied. The low band is thus completely filled and behaves like a band-insulator.

The phase diagram has fundamentally different properties at commensurate filling.

5.2.2 Half filling

At half filling ($n=1$) [197, 215–218] the model has an additional particle-hole symmetry.

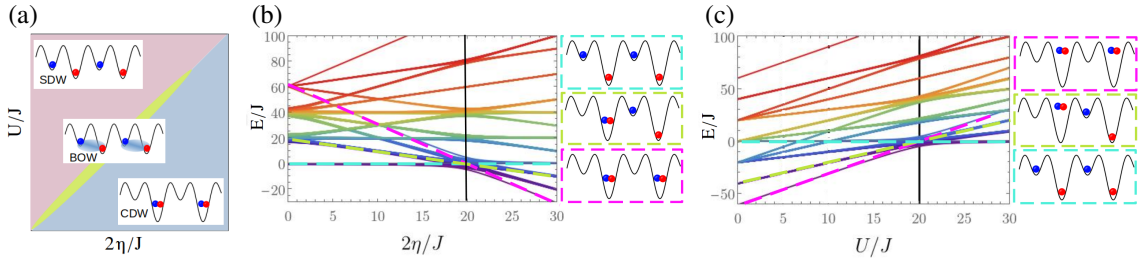

Fig. 5.3: (a) Sketch of the ground state phase diagram for the Ionic Hubbard model at half filling (b),(c) Energy spectra of the Ionic Hubbard model at half filling. The parameters used are $L=6$, (b) $U/J=20$, (c) $2\eta/J=20$. We sketch the nature of ground states and excited states crossing around $2\eta\sim U$. Vertical black, solid line at $2\eta=U$.

For $2\eta-U\gg J$ the system behaves as it is a band insulator (BI) or charge-density wave (CDW) [Fig. 5.3 (a)] due to the band splitting connected to the doubling of the unit cell. Neglecting the on-site interactions in the ground state the lower band in Eq. (5.3) is completely filled [$\langle\hat{\gamma}^\dagger_{-,k,\sigma}\hat{\gamma}_{-,k,\sigma}\rangle=1$ and $\langle\hat{\gamma}^\dagger_{+,k,\sigma}\hat{\gamma}_{+,k,\sigma}\rangle=0$] and separated by a gap from the high band [see Fig. 5.1 (b)]. Spin and charge gaps $\Delta_{c,s}$ are equal and correspond to the transfer of one particle to a high energy site at an energy cost $\sim 2\eta$.

Thus for $J=0$ a single critical point $U_{\mathrm{cr}}(\eta)=2\eta$ with vanishing excitation gap can be found. One expects similar critical behavior with at least one critical point to persist for finite J. This is supported by the vanishing density imbalance between sublattices A and B $\langle\hat{\Delta}\rangle=\sum_{j\in A,\sigma}\hat{n}_{j,\sigma}-\sum_{j\in B,\sigma}\hat{n}_{j,\sigma}$ and average number of double occupancies [Fig. 5.4 (a),(b)]. Note, that at finite temperature, instead of the ground state the system will be in a steady state where typically larger temperatures will increase the probability weight of the admixed higher energy eigenstates. The occupation follows Eq. (5.6). This leads to a broadening of the region where the phase might be ambiguous.

For $U-2\eta\gg J$ at $T=0$, the steady state is a critical Mott insulator (MI) or spin-density wave (SDW) [Fig. 5.3 (a)]. One can typically derive an effective Heisenberg model in this limit [195, 200], with nearest-neighbor exchange constant $J_2=4J^2U/(U^2-4\eta^2)$ to leading order. Each site is singly-occupied with gapless spin excitations $\Delta_s=0$ and finite charge gap $\Delta_c\sim U-2\eta$ corresponding to the creation of one doubly occupied site while changing the sublattice density imbalance by 1 [magenta to green states in Fig. 5.3]. As shown in Fig. 5.4 (a),(b), the atoms almost exclusively doubly occupy the low-potential sublattice sites as the density imbalance and average double occupancy approach their respective maximum values $\langle\hat{\Delta}\rangle/L\approx 1$ and $\langle\hat{n}_{j\uparrow}\hat{n}_{j\downarrow}\rangle\approx 0.5$.

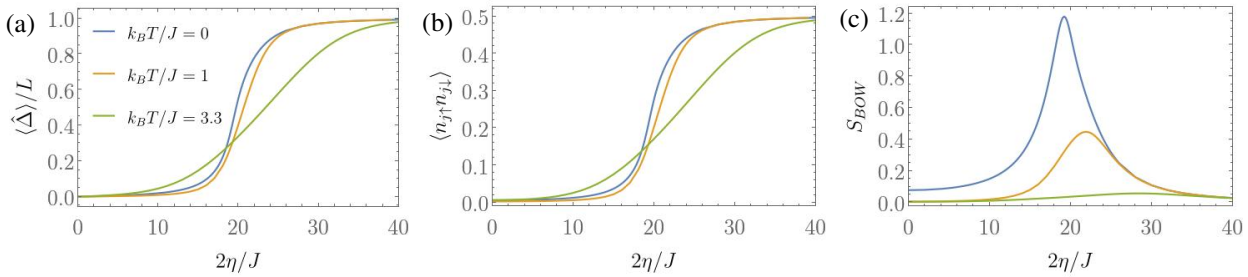

Fig. 5.4: Observables at half filling varying the potential imbalance η across the Mott-insulator (MI) to Band insulator (BI) transition. The colors denote different effective temperatures. (a) Sublattice density imbalance $\langle\hat{\Delta}\rangle/L$, (b) average site-double-occupancy $\langle\hat{n}_{j\uparrow}\hat{n}_{j\downarrow}\rangle$ and (c) Bond-order wave (BOW) phase order parameter S_{BOW} [Eq. (5.7)]. $L=6$, $U/J=20$.

In the regime $U\sim 2\eta$, where the energy scales cross over and the single particle band insulator gap is comparable to the Mott-insulating gap, a bond-order wave phase, is predicted [219–221]. It is characterized by a spontaneous dimerization of the kinetic energy and is bounded by two continuous transitions: a Kosterlitz-Thouless transition at $U_{\mathrm{cr},2}$, characterized by the closing of a spin gap, and a charge transition with vanishing charge gap at $U_{\mathrm{cr},1}<U_{\mathrm{cr},2}$. The dimerized phase is expected to vanish at a multi-critical point in the regime where both $U, 2\eta$ are very large.

However, it is doubtful that this phase will prevail at finite temperature, as supported by Fig. 5.4 (c). The peaked

feature of the order parameter for the bond-order wave phase

$$S_{\mathrm{BOW}} = \frac{1}{L}\sum_{j,l}(-1)^{j-l}\langle \hat{k}_j \hat{k}_l\rangle - \langle \hat{k}_j\rangle^2, \quad \text{with } \hat{k}_j = \sum_{\sigma}(\hat{c}^{\dagger}_{j+1\sigma}\hat{c}_{j\sigma} + \mathrm{H.c.}) \tag{5.7}$$

is very sensitive to finite temperature and is quickly damped and near unidentifiable for $k_B T/J \sim 3$. The steady states are strongly mixed and no dominant bond-order can be established.

5.3 Integrability of the ionic Hubbard model

In this section we want to present the results of our analysis of the level statistics of the ionic Hubbard model published in Ref. [222].This provides a strong argument justifying the assumption of a thermal atomic state for our effective atomic many-body system that we obtained in our approximation of the full driven-dissipative atoms-cavity coupled system [see Sec. 3.1]. Similar work has been done in the group since, considering a dimerized model [see Ref. [223]].

In the past years a significant effort has been devoted to the understanding of the dynamics of quantum systems. In contrast to the equilibrium physics at low temperature which is typically dominated by the low energy properties of a quantum system, the non-equilibrium physics relies often on properties of an arbitrary part of the spectrum. A central question is the determination of the conditions under which an isolated quantum many-body system thermalizes or fails to thermalize [224–228]. In this context it is generally believed that a generic chaotic system is best suited to exhibit thermalization towards a suitable statistical mechanics ensemble [229].

Recent studies have put forward several examples of non-equilibrium phenomena, which provide examples of systems failing to thermalize, such as many-body localization [227, 228, 230–232], and Hilbert space fragmentation [233, 234]. These systems feature a large number of (almost) conserved quantities and are thus not chaotic. The phenomenon of quantum many-body scarring [235–238] highlights that even in overall chaotic systems tiny subspaces can be found, which fail to thermalize. This scenario is especially relevant if the initial conditions lie in this subspace [239].

A powerful probe of the properties of a many-body quantum system in the context of quantum chaos are the universal properties of the level statistics. There exist two cornerstone limits: the Poisson statistics and the statistics stemming from random matrix theory [240]. The random matrix theory statistics is conjectured to hold for generic chaotic systems [241, 242], where the energy levels repel each other.In contrast, the Poisson statistics is found for quantum integrable systems.

In this section, we investigate the spectral properties of the one-dimensional ionic Hubbard model introduced in Sec. 5.1. It is typically assumed that the alternating potential of the ionic model breaks the integrability of the standard one dimensional Hubbard model. Clashing with this belief, a few years ago numerical results that allegedly point to a Poisson statistics of the levels [243] were presented. This controversial statement served as motivation to thoroughly investigate the level statistics of this model, as the integrability of the model would require us to reconsider the thermal ansatz taken in our adiabatic elimination method. Indeed we confirm that after all *symmetries* of the Hamiltonian [see Sec. 5.3.2] are taken into account, the model exhibits the statistics of Gaussian orthogonal ensemble (GOE) in a wide range of parameters considered.

In Sec. 5.3.1 we provide an introduction to the analysis of the level statistics and its interpretation concerning integrable or chaotic character of the respective model. Due to the importance of the consideration of all symmetries of the model to be analyzed to ensure a correct analysis, we then identify and present the symmetries present in the specific case of the ionic Hubbard model Sec. 5.3.2. We determine the eigenenergies of the model via full numerical exact diagonalization after block diagonalizing the Hamiltonian with respect to the identified symmetries. The resulting spectral properties for generic as well as the special case of half filling are finally presented in Sec. 5.3.3.

5.3.1 Introduction to level statistics

In this section we present some properties of the spectra of general quantum many-body models that comprise the ionic Hubbard model. The spectral statistics of quantum integrable systems follow Poisson statistics. In contrast chaotic quantum many-body systems exhibit universal features described by random matrix theory (RMT) for

chaotic quantum systems if all known symmetries are considered [241,242,244,245]. Numerous existing examples show the usefulness of the information obtained from spectral analysis as means to categorize many-body quantum models following their integrable or chaotic nature [232, 246–253]. The level statistics of different many-body quantum systems have been classified as for the Hubbard model [246], which can exhibit Poissonian statistics or statistics of Gaussian orthogonal ensemble (GOE) [254] depending on dimensionality and filling. Variants of the Hubbard model [243], or its bosonic counterpart [250], a kicked-parameter model of spinless fermions [252], or more recently a family of Sachdev-Ye-Kitaev models [253] have also been analyzed.

The distance $\delta_n = E_{n+1} - E_n$ between adjacent many-body eigenvalues $\{E_n\}$ is helpful in order to quantify the spectral properties of a model. One distinguishes the two cases. For integrable models that entail an extensive number of conserved quantities, the distribution of the level spacings typically follow a Poisson distribution

$$P(\delta/\Delta) = \exp\left(-\frac{\delta}{\Delta}\right), \tag{5.8}$$

where Δ is the average of all level spacings.

For a chaotic model the random matrix ensemble describing the universal features is determined by the underlying symmetries. In the case of the here considered ionic Hubbard Hamiltonian [Eq. (5.1)], since exhibits a time-reversal symmetry as well as a rotational symmetry, the correct ensemble is the Gaussian orthogonal ensemble (GOE) in random matrix theory [245]. Therefore we will concentrate on this from here on. The level spacing distribution for a GOE has the Wigner-Dyson form

$$P(\delta/\Delta) = \frac{\pi}{2}\frac{\delta}{\Delta}\exp\left(-\frac{\pi}{4}\frac{\delta^2}{\Delta^2}\right). \tag{5.9}$$

Note that to evaluate the level-statistics with the method presented up to here one needs to compute the density of states, which depending on the individual model is often highly non-trivial. Numerically it would require a procedure for the unfolding of the spectrum, which bears the risk of inaccurate results [255]. Thus one often employs an alternative way in order to characterize the spectral properties by considering the behavior of the gap ratio between consecutive energy levels [249]

$$r_n = \frac{\min(\delta_n, \delta_{n+1})}{\max(\delta_n, \delta_{n+1})}. \tag{5.10}$$

The corresponding probability distribution for Poisson and the GOE statistics [256] is then defined as

$$P_{\text{Poisson}}(r) = \frac{2}{(1+r)^2}, \qquad P_{\text{GOE}}(r) = \frac{27}{4}\frac{r+r^2}{(1+r+r^2)^{5/2}}. \tag{5.11}$$

In the individually considered models one can use either the mean value $\bar{r}$ or the value $P(r=0)$ as a means to quantify the proximity of the distribution of gap ratios to Poisson or GOE. The expected values for the Poisson and GOE distributions are given in Table 5.1.

statistics	$\bar{r}$	$P(r=0)$
Poisson	0.386	2
GOE ($m=1$)	0.536	0
GOE ($m=2$)	0.423	1.408
GOE ($m=3$)	0.403	1.715

Table 5.1: Values of averages $\bar{r}$ and the probability at $r=0$, for statistics following the Poisson distribution and the GOE distribution for m different equally sized symmetry sectors. Values taken from Refs. [256, 257].

Typically the spectral properties of a Hamiltonian are analyzed by block-diagonalizing it with respect to all known symmetries present and consider every symmetry sector individually when comparing their level spacing statistics to the Poissonian or Random Mastrix Theory (RMT) ensembles. However, if the block diagonalization procedure

is computationally challenging or even impossible, or if some symmetries are unknown one can instead adapt the statistics one compares to correspondingly, accounting for situations where additional symmetries are present [257–260].

We want to highlight the work of Giraud and coworkers [257] in this context. They provide analytical results for the case where several independent symmetry blocks with respect to a discrete symmetry remain un-separated and the distributions of random matrices are consequently altered. One can observe that by having multiple symmetry sectors the value $P(r=0)$ becomes finite and increases for larger m (see Table 5.1). By taking a very large number of symmetry sectors, $m \to \infty$, one will recover the Poisson distribution [257]. But already for $m=2$ or 3 blocks of same size that remain un-separated the mean value $\hat{r}$ is already closer to the value one would expect for the Poisson distribution, than the one for the GOE distribution Eqs. (5.11). One thus needs to be careful not to miss symmetries in the numerical analysis of the spectral properties of many body quantum model since this could lead to falsely attributing integrability to a chaotic model .

We demonstrate this explicitly for the half-filled ionic Hubbard model in Sec. 6.2 where we compare the results with an additional particle-hole symmetry to the GOE distribution for $m=2$ or 3 blocks of equal size. The explicit values for $P(r=0)$ and the mean value $\bar{r}$ for various m are given in Table 5.1. Further detail on the derivation as well as the analytical expression of the distributions is provided in Supplementary Material of Ref. [257]. Note that for the results presented in this section we mainly focus on results with m symmetry blocks of equal size for the GOE distributions, due to the nature of the symmetries in our model. In general, one can perform the analysis analogously for blocks containing an unequal number of eigenvalues [257], as we will use for Fig. 5.11 (b) with $m=10$. One can understand the influence of the block sizes by considering the case of $m=2$. Increasing the ratio of the two block sizes from 0 to 1, both $P(r=0)$ and $\bar{r}$ take values on a smooth curve between the expected values for $m=1$ and $m=2$.

5.3.2 Symmetries

It is crucial to identify all discrete symmetries existing in the considered model, here the ionic Hubbard model, in order to correctly analyze the energy level statistics. Here we present a list of the symmetries of the ionic Hubbard model beside the time-reversal symmetry that was already introduced in the previous section. For the analysis we focus on even number of particles N, and consequently integer total spin and periodic boundary conditions in Eq. (5.1), defined by the mapping at the edges $\hat{c}^{(\dagger)}_{L+1,\sigma} \equiv \hat{c}^{(\dagger)}_{1,\sigma}$.

Symmetries of the Ionic Hubbard Model

We identify the corresponding generators that allow to block-diagonalize the full Hamiltonian with respect to the individual symmetries.

Gauge symmetry: The conservation of the particle number N_σ in each spin sector σ and consequently the total particle number $N = N_\uparrow + N_\downarrow$ is a consequence of the global $U(1)$ gauge symmetry generated by

$$\hat{U}\hat{c}_{j,\sigma}\hat{U}^\dagger = e^{i\phi}\hat{c}_{j,\sigma}, \qquad \phi \in \mathbb{R} \tag{5.12}$$

Restricting to the respective set of basis states in the computation one can implement the symmetry directly in the numerical exact diagonalization method.

Spin rotation symmetry: A well known symmetry from the Hubbard model is the $SU(2)$ spin rotation symmetry, which remains present when including an alternating potential in the model. The spin operators that generate the rotations in spin space are defined using the Pauli matrices $\hat{\sigma}^\alpha$:

$$\hat{S}^\alpha = \frac{1}{2}\sum_{j=1}^{L}\sum_{a,b\in\uparrow,\downarrow}^{2} \hat{c}^\dagger_{j,a}(\hat{\sigma}^\alpha)_{a,b}\hat{c}_{j,b}, \quad \alpha \in \{x,y,z\} \tag{5.13}$$

Since the Hamiltonian of the ionic Hubbard model in Eq. (5.1) commutes with all spin operators, $[\hat{H}, \hat{S}^\alpha] = 0$ it is rotationally invariant in spin space. Therefore the total spin S is conserved and the corresponding symmetry sectors can be labeled by a set of quantum numbers $|s, m_z\rangle$. Here $\hat{S}^2 |s, m_z\rangle = s(s+1)|s, m_z\rangle$ and

$\hat{S}^z |s, m_z\rangle = m_z |s, m_z\rangle$, using $\hbar = 1$. While the m_z quantum number is directly implemented in the numerical exact diagonalization method, the absolute spin $\hat{S}$ symmetry sectors are reconstructed after the diagonalization from the numerical results. We provide a detailed description of the procedure in the following paragraph "Implementation for exact diagonalization".

Translational symmetry: The ionic Hubbard model is invariant under translation by a multiple of the two-site unit cell

$$\hat{T}_x \hat{c}_{j,\sigma} \hat{T}_x^\dagger = \hat{c}_{j+2,\sigma}. \tag{5.14}$$

Consequently the eigenvalues $\exp(ik)$ of the generator $\hat{T}_x$ determine the possible values of the conserved (dimensionless) momentum $k = \frac{2\pi}{L/2} j$ with $j = 0, 1, \ldots, \frac{L}{2} - 1$, for a chain with an even number L of sites. From here we label the translational symmetry sectors by the dimensionless momentum k.

Parity (reflection) symmetry: Additionally the ionic Hubbard Hamiltonian is invariant under reflection on any site of the chain (not at bonds as in Ref. [223]). The symmetry transformation choosing the first site of the chain as the reflection center is defined as

$$\hat{P} \hat{c}_{j,\sigma} \hat{P}^\dagger = \hat{c}_{2-j,\sigma}. \tag{5.15}$$

The corresponding eigenvalues are $p = \pm 1$.

Remarkably besides $(\hat{T}_x, \hat{P})$ all the here presented symmetry generators commute. Since the direction of the momentum is inverted by the reflection symmetry, it generally does not commute with the translational symmetry. This is only the case at specific momentum values, namely $k = 0$ or $k = \pi$. Note, that the momentum $k = \pi$ is only a quantum number for $\mod (L/4) = 0$. Therefore, we choose to restrict to these special cases in our computation, using the translation symmetry first and block diagonalizing with respect to the reflection symmetry only for $k = 0, \pi$. The individual symmetry blocks are thus characterized by the combination of all quantum numbers (N, s, m_z, k, p), where the p quantum number is only present for $k = 0, \pi$. If not stated otherwise, the distributions are calculated individually for all computable sectors. Since the level statistics are independent of the respective quantum numbers of the symmetry sectors we decrease the statistical error of the distributions by combining the results from the individual sectors afterwards by averaging over them.

Particle-hole like symmetry: At half filling, the ionic Hubbard model is invariant under an additional symmetry transformation resembling a particle hole symmetry. Here it is defined on the bipartite lattice, i.e. with the transformation

$$\hat{C} \hat{c}_{j,\sigma} \hat{C}^\dagger = (-1)^j \hat{c}_{j+1,\sigma}^\dagger. \tag{5.16}$$

We will comment in detail on the influence of this symmetry on the properties of the obtained level statistics in the result section.

Implementation for exact diagonalization

We want to briefly sketch how we take care of the individual symmetries of the model in the exact diagonalization code. The total particle number conservation 5.3.2 (a), conservation of the spin component 5.3.2 (b), translational symmetry 5.3.2 (c) and reflection symmetry 5.3.2 (d) can be implemented in a straight forward way by constructing the sub-sectors with the corresponding quantum numbers N, m_z, k and p.

However, combining the particle hole-like symmetry with the other symmetries in the existing code involves a great deal of effort. Therefore we decided not implement it. Instead we carefully detect the presence of this symmetry in the level statistics distributions and consider the changes resulting from the not fully separated symmetry sectors in our analysis. Further we explicitly break the particle hole-like symmetry retaining all other symmetries by introducing an alternating Hubbard on-site interaction. This allows us to make the influence of the particle-hole symmetry visible by contrasting it to the explicitly broken setup. For the results presented in the next section Sec. 5.3.3 we are able to diagonalize individual symmetry blocks of sizes up to $\sim 1.27 \times 10^4$. Taking all calculated blocks into account this amounts to up to $\sim 3.84 \times 10^5$ eigenvalues that can be taken into account for the averages.

Note, that of the spin-rotation quantum numbers $|s, m_z\rangle$ only the quantum number of S^z, m_z is directly implemented in our computation but one can make use of the degeneracy of the eigenvalues for different m_z's if the

total spin s is fixed. The individual eigenvectors in the spin-space $|s, m_z\rangle$ and $|s, m_z'\rangle$ sharing the same s quantum number are connected by ladder operators $\hat{S}^+$ and $\hat{S}^-$, changing m_z by ± 1. The eigenvectors $|s, m_z\rangle$ and $|s, m_z'\rangle$ are degenerate since the Hamiltonian commutes with the ladder operators. Therefore, it suffices to know the eigenvalues for different m_z's in order to choose the correct ones in the desired sector belonging to a total spin s. Starting with the symmetry block labeled by the maximum value of m_z, i.e. $m_z = N/2$ for N spin-half particles. Since in this block a unique value $s = m_z$ resides one obtains the solution right away. Moving to the next symmetry sector reducing the quantum number $m_z = s - 1$ one obtains the eigenvalues for both, s and $s - 1$, but because the ones with total spin s agree with the previous sector one can assign all remaining eigenvalues to the new symmetry sector with total spin $s - 1$. Subsequently decreasing the quantum number m_z until one reaches $m_z = 0$ and repeating the described procedure at every step allows to label all eigenvalues with both quantum numbers s and m_z. Note, that the eigenvalue spectrum with positive $m_z' > 0$ quantum number at fixed total spin s can be labeled in parallel to the negative ones since for $-m_z' = |m_z|$ the spectra are degenerate.

5.3.3 Results

In this section we show our results on the spectral properties of the ionic Hubbard model and an extension using alternating interactions. We start discussing the results at quarter filling $N/L = 1/2$ and at filling $N/L = 2/3$ as typical fillings in Sec. 5.3.3. Only the standard symmetries (Sec. 5.3.2 (a)-(d)) are present for this case. We are able to recover the GOE like behavior pointing towards the expected chaotic character of the ionic Hubbard model. Additionally, in Sec. 5.3.3 the case of half filling is discussed. This is a special case due to the presence of an extra particle hole like symmetry [Sec. 5.3.2 (e)]. We proceed to demonstrate that the obtained level distributions are in nice agreement with a GOE like behavior taking into account the non-separated symmetry sectors.

Away from half filling

We start considering the ionic Hubbard model, Eq. (5.1), at quarter filling, i.e. $N/L = 1/2$. We compute the energy levels of the Hamiltonian in each block of the symmetries discussed in Sec. 5.3.2 and consider the level distribution separately within these blocks. The data obtained from different symmetry sectors at quarter filling is then assembled in a single histogram. In the representation of the histograms the chosen size of the bins plays a role. We choose the bin size in order to minimize the statistical fluctuations and still obtain a good representation of the distribution. Since the distributions vary depending on the Hamiltonian parameters, we adapted the bin size correspondingly.

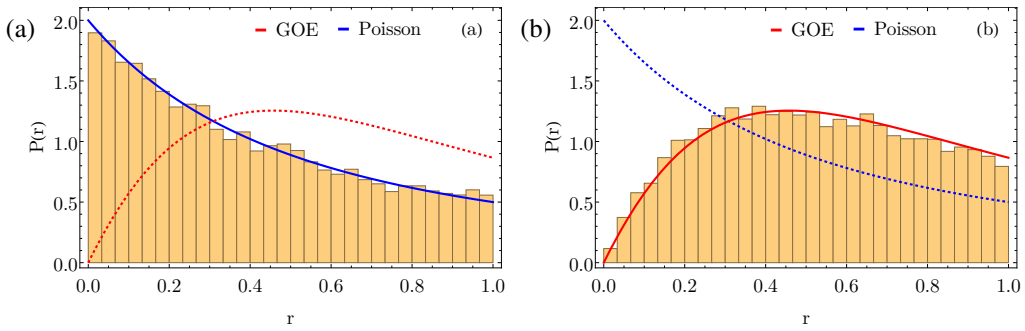

Fig. 5.5: Distribution of the ratios of consecutive level-spacings for (a) the standard Hubbard model ($\eta/J = 0$) and (b) the ionic Hubbard model at $\eta/J = 1$ in a chain with $N = 6$, $L = 12$ at $U/J = 2$ combining all s and k, p symmetry sectors for $m_z = 0$. We use 30 bins to represent the distribution. Adapted from Ref. [3].

In Fig. 5.5 (a) we present the distribution of the ratios of consecutive level-spacings averaged over all symmetry blocks for the standard Hubbard model, i.e. $\eta/J = 0$, as a benchmark of our procedure. For the standard Hubbard model, the ratios of consecutive level-spacings are known to follow Poisson statistics [246]. For the chosen intermediate value of the interaction, $U/J = 2$, we find a distribution which nicely follows the Poisson prediction, as can be seen from the good overall agreement between the numerical histogram and the Poisson prediction for $P(r)$, including the correct limiting behavior as $r \to 0^+$. Furthermore the mean value $\bar{r} = 0.386$ of the numerical data, which does not depend on the number of bins, agrees with the Poisson distribution value in the first three digits.

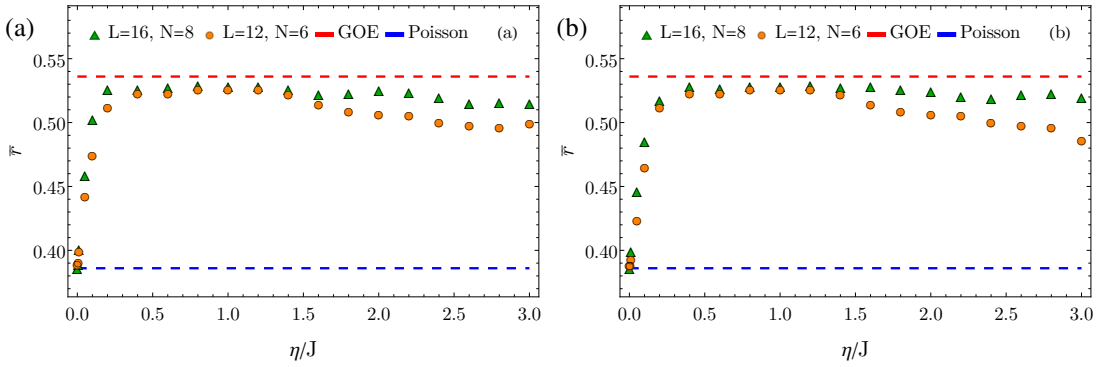

Fig. 5.6: Evolution of the mean value $\bar{r}$ of the ratios of consecutive level-spacings with the strength of the alternating potential η/J for a) $U/J=2$ and b) $U/J=4$. The expected mean value for the Poisson-distribution and the GOE are marked with the horizontal dashed lines. For system size $L=12$ combining all s and k,p symmetry sectors, for $L=16$ combining $s=3,4$ and all k,p for $m_z=0$. Adapted from Ref. [3].

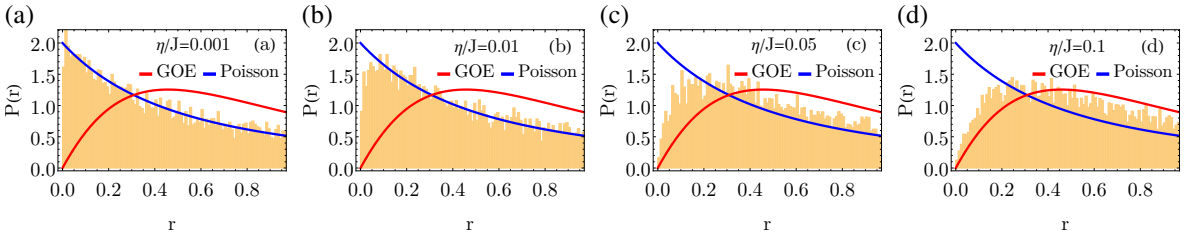

Fig. 5.7: Distribution of the ratios of consecutive level-spacings for $L=12$, $N=6$ for the symmetry sector $m_z=0$ combining $s=0,1$ and all k,p symmetry sectors. The parameters of the system are $U/J=2$ and $\eta/J=0.001, 0.01, 0.05, 0.1$ and 100 bins. The mean values are given by $\bar{r}=0.391, 0.405, 0.450, 0.482$. Adapted from Ref. [3].

Once we switch on the alternating potential of the ionic Hubbard model, the behavior is changed drastically. In Fig. 5.5 (b) the distribution $P(r)$ from the numerical data is shown for a value of the alternating potential of $\eta/J=1$ following closely the distribution expected for the GOE random matrix theory ensemble. The behavior for small r, where $P(r)$ clearly starts at 0 and rises linearly for small values of r, is in stark contrast with the Poisson behavior and is a consequence of the level repulsion of chaotic systems. The mean value $\bar{r}=0.515$ is also rather close to the GOE prediction 0.536.

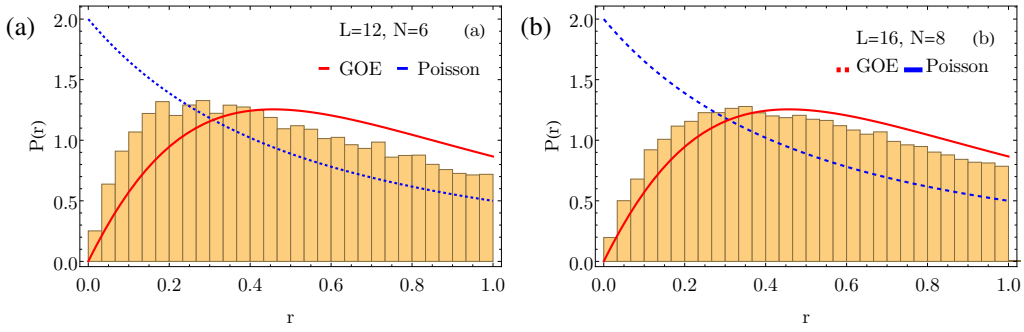

Fig. 5.8: Distribution of the ratios of consecutive level-spacings for $L=12$, $N=6$ and $L=16$, $N=8$. The parameters of the system are $U/J=2$ and $\eta/J=0.1$, 30 bins. The mean value is given by $\bar{r}=0.474,\ 0.502$. For system size $N=6$ combining all s and k,p symmetry sectors, for $N=8$ combining $s=3,4$ and all k,p for $m_z=0$. Adapted from Ref. [3].

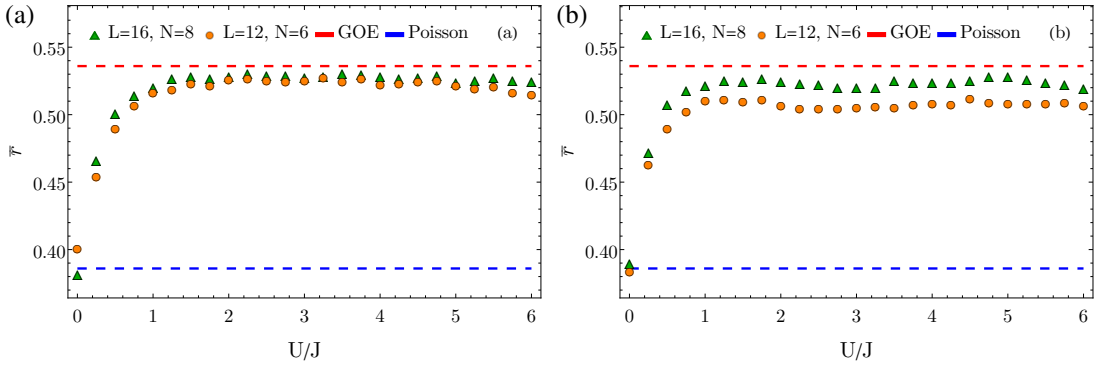

Fig. 5.9: Evolution of the mean value $\bar{r}$ of the ratios of consecutive level-spacings with the interaction strength U/J for a) $\eta/J=1$ and b) $\eta/J=2$. The value of the Poisson distribution and the GOE are marked by horizontal dashed lines. For system size $L=12$, $N=6$ combining all s and k,p symmetry sectors for $m_z=0$ and for $L=16$, $N=8$ combining $s=3,4$ and all k,p for $m_z=0$. The statistical standard error of the weighted mean of r over all computed symmetry sectors was found to be of order 3×10^{-4} or lower for all shown system sizes. This is below the symbol sizes. Adapted from Ref. [3].

In order to investigate in more detail the behavior as a function of the amplitude of the alternating potential η/J and the dependence on U/J, we use the average value of the ratio of the consecutive level-spacings $\bar{r}$. For the Poissonian distribution the mean value of this ratio is given by $\bar{r}_{\mathrm{P}}=0.386$ and for the GOE the mean value is $\bar{r}_{\mathrm{GOE}}=0.536$ (see Table 5.1). The dependence on η/J for fixed U/J is shown in Fig. 5.6 (a)-(c) for different interaction strength $U/J=2,4$. As discussed above, at $\eta=0$ the value of $\bar{r}$ is very close to $\bar{r}_{\mathrm{P}}$ of the Poisson distribution. We observe that for the smallest non-zero values of η we consider and for all considered interactions, the average value of r increases very rapidly to almost the value expected for a GOE ensemble. A very good agreement with the expected value of the GOE is found in particular for $0.5\lesssim\eta/J\lesssim2$.

Since, in principle one expects an infinitesimal value of η in the thermodynamic limit to follow the GOE like distributions, we investigate the transition from the Poisson distribution at $\eta=0$ to the GOE distribution for $\eta>0$ more carefully and study the numerical distributions at very small values of η. Fig. 5.7 shows the distribution of level spacing for four different values of η for a finite system of size $L=12$, at quarter filling for $U/J=2$. The main difference between the Poisson distribution and the GOE like distribution is the finite value arising in the Poisson distribution at $r=0$ and its suppression due to the level repulsion in the GOE like ensemble. This shows that focusing on the manifestation of level repulsion at small values of r is much more sensitive than merely tracking the mean value of r. In order to resolve the steep distributions at low values or r we choose a small bin size to represent the distributions. Already at very small values of $\eta/J=0.001,0.01$ a clear suppression of the value in the first bins is visible for the considered chain length. Whereas for $\eta/J=0.001$ this is only the case for the first bin, at $\eta/J=0.01$ already about a handful of bins contributes to the decrease of the distribution at low values of r due to the level repulsion. For larger values of $\eta/J=0.05$ and $\eta/J=0.1$, the vanishing distribution at $r=0$ is clearly visible and the distribution approaches the GOE distribution.

The GOE distribution is expected for any finite value of the alternating potential ($\eta/J\neq0$) for sufficiently large system sizes. We see in Fig. 5.8 that the suppression of the distribution at low values of r is very sensible to system size. Whereas for $L=12$ still the distribution for low r lies considerably above the GOE distribution, this deviation is already reduced for $L=16$ and the distribution lies much closer to the GOE distribution. This hints that already at small values of the alternating potential the level distribution follows the predictions from the GOE if sufficiently large system sizes are considered.

Also for large values of approximately $\eta/J\gtrsim2$ the numerically found average value of r drops below the value of the GOE ensemble (cf. Fig. 5.6). We attribute the deviations from the expected GOE ensemble to finite size effects as discussed for small values of η/J. This is supported by the results obtained for larger system sizes in Fig. 5.6 moving towards the GOE predictions with increasing system size both at small and large η/J. The deviations between the different system lengths are in particular large for low and large values of the alternating potential, where the GOE expectation is not yet met.

The dependence of the average value of r on the interaction strength is shown in Fig. 5.9 for two different values of η. A drastic rise is clearly seen from the non-interacting integrable case at $U=0$ which lies close to the predictions for the Poisson distribution to a finite interaction strength. Already at interaction strength of about $U/J \approx 1$ an almost steady value is reached for $\eta/J=1$, which agrees well with the predictions for a GOE ensemble even for a smaller system size considered [see Fig. 5.9 (a)]. At larger value of the alternating potential, $\eta/J=2$ similar behavior is observed but a larger system size of $L=16$ is needed to reach the expected GOE value due to finite size effects as discussed above [see Fig. 5.9 (b)]. At large values of the interaction we would expect again that deviations from the GOE ensemble arise due to the large separations occurring in the energy scales.

In order to show that the discussed behavior is generic for different fillings, we show in Fig. 5.10 the dependence of the average value of r on both the alternating potential η and the interaction strength U for $N/L=2/3$. We find that the shown behavior resembles very much the behavior of the quarter filling. The only difference is that the deviations from the GOE value at a larger values of the alternating potential are smaller than for quarter filling.

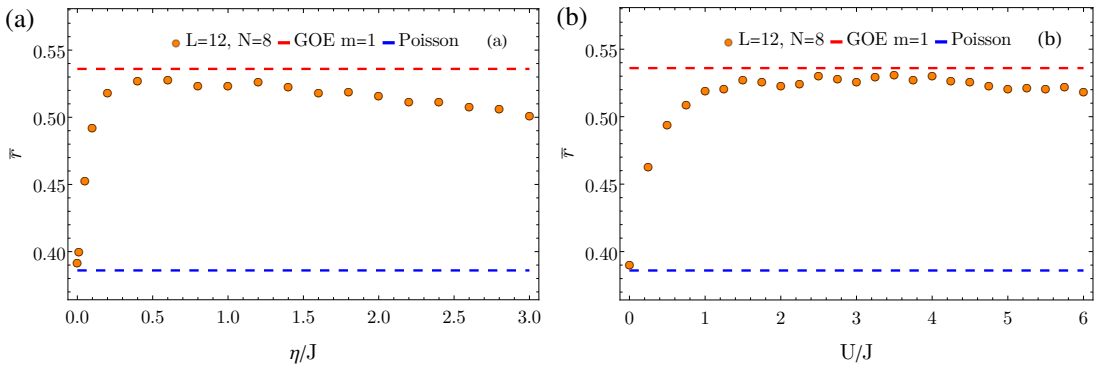

Fig. 5.10: Evolution of the mean value $\bar{r}$ of the ratios of consecutive level-spacings (a) with the alternating potential η/J at $U/J=2$, and (b) with the interaction strength U/J at $\eta/J=1$. The value for the Poissonian distribution and the GOE are marked by horizontal dashed lines. For system size $L=12$, $N=8$ combining $s=2,3,4$ and all k,p for $m_z=0$. Adapted from Ref. [3].

We therefore conclude this section, that the energy spectra of the ionic Hubbard model at a generic filling (here $N/L=1/2$ and $N/L=2/3$) nicely follow the expected behavior of a GOE ensemble and therefore point towards a chaotic nature of the model.

Half filling

At half filling $N/L=1$, the distribution of the level-spacing ratios change drastically compared to the previously described quarter filling [see Fig. 5.11 (a)]. As introduced in Sec. 5.3.2, in the case of half filling the ionic Hubbard model exhibits an additional particle-hole like symmetry, Eq. (5.16). This drastically changes the behavior seen in the spectra as shown in Ref. [257], if the different symmetry blocks are not considered separately when performing the level statistics. Depending on the number of symmetries blocks that remain unseparated in the analysis, the distribution of the consecutive level spacing changes in nature. Starting from the case where every symmetry sector is separated and the distribution follows the GOE, to a more Poisson like distribution when many sectors are treated together [257]. In Fig. 5.11 (a) the distribution of the consecutive level spacings is shown for the case of half filling, where we have separated the spectrum into the blocks of the symmetries, Sec. 5.3.2 (a)-(d), but not into the additional particle hole symmetry, Sec. 5.3.2 (e). Note that resulting distribution neither follows a GOE like distribution nor a Poisson like distribution, but lies somewhere in between. These distributions are genuinely in between GOE and Poissonian, and do not converge to either of them with larger system sizes, unlike the crossover behavior discussed in the previous section. Using the predictions from Ref. [257] we compare the obtained distribution to the ones which correspond to the presence of two ($m=2$) or three ($m=3$) equally sized symmetry blocks (see Sec. 5.3.1). The numerical results lie very close to the results for a GOE RMT with *two* symmetry blocks present, as expected from our symmetry analysis.

In this section, we emphasize how neglecting the separation into the different symmetry sectors the in principle

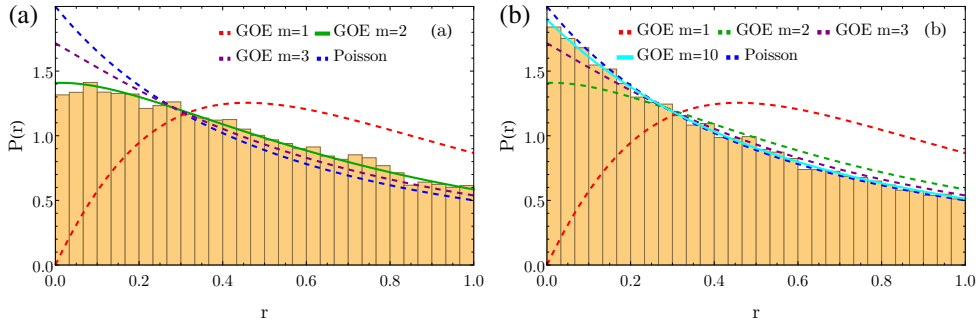

Fig. 5.11: Distribution of the ratios of consecutive level-spacings for $L = 10$, $N = 10$ for the symmetry sector $m_z = 0$ (a) performing the statistics in each symmetry sector (except particle hole) separately and combining all s and k, p symmetry sectors afterwards. The mean value is given by $\bar{r} = 0.426$. (b) *Not* separating for the s quantum number and combining data from all k, p sectors, resulting in $\bar{r} = 0.392$. The parameters of the system are $U/J = 1$ and $\eta/J = 1$. Adapted from Ref. [3].

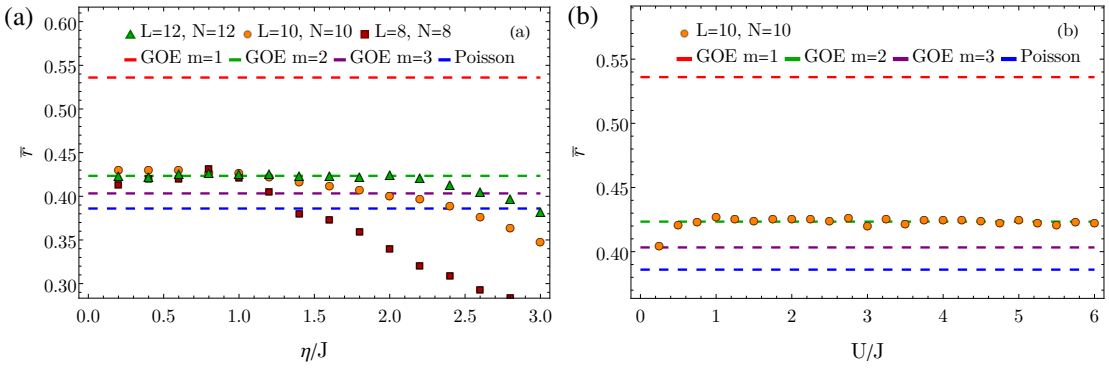

Fig. 5.12: Evolution of the mean value $\bar{r}$ of the ratios of consecutive level-spacings with (a) the alternating potential at $U/J = 1$ and (b) the interaction strength U/J at $\eta/J = 1$ for various system sizes. The value for the Poissonian distribution and the GOE for different m are marked by horizontal dashed lines (see Table 5.1). Adapted from Ref. [3].

GOE like distribution of the consecutive level spacings approaches the Poisson-like distribution. In particular, we focus on half filling, for parameters close to the ones considered in Hosseinzadeh et al. [243] where the Poisson statistics was identified.

To emphasize the effects of the separation into the different symmetry sectors, we present in Fig. 5.11 (b) the distribution of the consecutive level spacings at half filling, but only taking a fixed S_z sector, and not a fixed sector of the total spin S. In this case the expected distribution for a chaotic system would be a GOE with $m = 10$ symmetry blocks [257]. The number of blocks results from the five symmetry sectors due to the total spin, which are of unequal size, which should furthermore be split in half due to the particle-hole symmetry present at half filling (see Sec. 6.2). The sizes of the symmetry sectors are: $s = 0$, 3880 states; $s = 1$, 5940 states; $s = 2$, 2475 states; $s = 3$, 385 states; $s = 4$, 20 states. We can notice in Fig. 5.11 (b) that this GOE distribution with $m = 10$ is very close to a Poisson distribution due to the large number of symmetry blocks. Our numerical data is in agreement with this distribution and thus, also lies very close to the Poisson distribution. This again underlines the importance of the separation of the spectra into the different symmetry sectors.

This is further supported considering the mean value of r and its dependence on the value of the alternating potential shown in Fig. 5.12 (a). As for the case of quarter filling, at $L = 12$ intermediate value of $0.5 \lesssim \eta/J \lesssim 2$ lead to an excellent agreement with the predicted value of the one predicted for the distribution GOE $m = 2$. Larger deviations occur at larger values of η. We attribute these again to finite size effects, as we can show that the longer

system sizes considered strongly approach the expected mean value compared to the smaller system sizes. The average value of r for the system size $L=12$ already agrees nicely up to $\eta/J \approx 2$ to the expected value fo the distribution of the GOE with $m=2$.

In Fig. 5.12 (b) the average value and its dependence on different values of U/J is shown. For $U/J > 0.5$, the obtained main value fluctuates very closely around the one predicted for the distribution GOE $m=2$ and is distinct from the one predicted for the distribution with $m=3$ equal symmetry blocks.

Thus, our entire results indicate that the ionic Hubbard model shows similar properties as the GOE like ensemble, if all known symmetries are considered.

Half filling - breaking the particle-hole symmetry

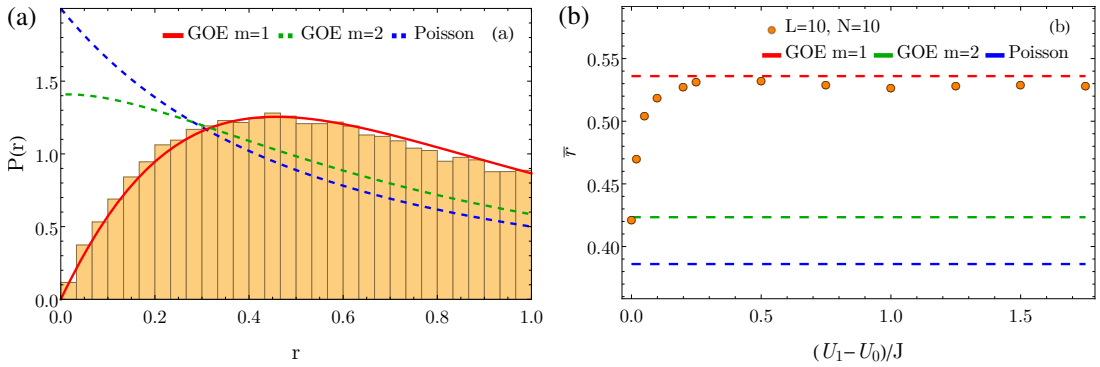

Fig. 5.13: (a) Distribution of the ratios of consecutive level-spacings. The parameters of the system are $U_0/J=1$ $U_1/J=2$ and $\eta/J=1$, and 30 bins. The mean value is given by $\bar{r}=0.527$. (b) Evolution of the mean value $\bar{r}$ of the ratios of consecutive level-spacings with the difference of the interaction strengths $(U_1-U_0)/J$ at $\eta/J=1$, $U_0/J=1$. The horizontal dashed lines mark the expected values for the Poisson distribution and for the GOE with different m (see Table 5.1). System size $L=10$, $N=10$ considered symmetry sector $m_z=0$ combining all s and k,p symmetry sectors. Adapted from Ref. [3].

We want to further substantiate our finding of the importance of considering all symmetries of the considered model, by explicitly breaking it and compare the resulting statistics. We achieve this by introducing an additional term in the ionic Hubbard Hamiltonian, explicitly breaking the particle-hole symmetry present at half filling. In this concrete case the homogeneous on-site interaction is substituted with an alternating interaction

$$\hat{H}_{\text{int}} = U_0 \sum_{j=1}^{L/2} \hat{n}_{2j,\uparrow}\hat{n}_{2j,\downarrow} + U_1 \sum_{j=1}^{L/2} \hat{n}_{2j+1,\uparrow}\hat{n}_{2j+1,\downarrow} \tag{5.17}$$

It is suitable for our analysis since this term only breaks the particle-hole like symmetry,leaving all other identified symmetries (a)-(d) unaffected. As shown in Fig. 5.13 (a) the symmetry-breaking term restores a distribution very clearly following the GOE distribution expected for a *single* symmetry block $m=1$.

To investigate these findings more thoroughly we show $\bar{r}$ with the symmetry breaking term in Fig. 5.13 (b). The average value of r steeply rises at small amplitudes of the symmetry breaking term, approaching and stabilizing around the expected value of the GOE $m=1$ ensemble for $(U_1-U_0)/J \approx 0.2$. As discussed in the previous sections, we expect that the finite slope of $\bar{r}$ as $(U_1-U_0)/J \to 0$ can be associated with finite size effects. In the thermodynamic limit we would expect an abrupt switch of the behavior from the $m=2$ ensemble in the presence of the particle-hole like symmetry to the $m=1$ GOE distribution when the symmetry is explicitly broken.

Summary

In this chapter, we have given a brief overview of the properties of the ionic Hubbard model in one dimension. We considered the ground state phase diagram at quarter and half filling and commented on the dominant excitations.

This description will serve as a basis for our discussion of the adiabatic elimination results for the cavity-atoms coupled many-body system Chapter 6.

Further we investigated the energy level statistics of the ionic Hubbard model. We find that in general the ionic Hubbard model and its generalization show, when all known symmetries are considered, the spectral features of a GOE ensemble. This finding of a chaotic behavior of the level statistics of the ionic Hubbard model is in agreement with the general belief that the ionic Hubbard model is non-integrable for generic parameters with finite potential staggering. This provides support for the validity of our assumption made in Sec. 3.1 that the steady state of atomic many-body system in our full driven-dissipative is well approximated by a thermal state.

Chapter 6

Cooling effects and fluctuation-induced bistability in the steady state phase diagrams

In this chapter we analyze the nature of the steady state for spinful fermionic atoms confined to optical lattices and coupled to the dissipative field of an optical cavity via transverse pumping. These type of systems usually exhibit a phase transition between a normal phase with an empty cavity and a self-organized phase [152]. Here we will provide a detailed analysis of the steady states across the self-ordering transition for the cases of quarter filling [see Sec. 6.1] or half filling [see Sec. 6.2]. We present our main findings regarding the effect of resonances in the complex quantum system, leading to both *cavity cooling* [see Sec. 6.1.2] and *many-body-cooling* effects [see Sec. 6.1.3]. The observations from explicitly solving the systems of equations for finite size [Eqs. (3.3) & (3.14)] and in the thermodynamic low-hopping limit [Eqs. (3.25)] are complemented by several analytical approximations, shining light on the physical processes happening around the self-ordering transition as well as deep in the self-ordered regime.

We will also put special focus on a novel mechanism appearing at quarter filling, which we refer to as *fluctuation-induced bistability* in Sec. 6.3, in which bistability occurs in a *dissipative quantum* system, *only* if quantum fluctuations around a mean-field solution are taken into account. Part of the results presented in this section was published in Ref. [1]. We provide a detailed analysis of the bistability and distinguish it from the case at half-filling where a bistability of fundamentally different nature is present at the self-ordering transition [Sec. 6.2.1].

We include the fluctuations in the atoms-cavity coupling on top of the mean-field solution resulting from the adiabatic elimination of the cavity field as introduced in Sec. 3.1. The thermalization process induced by the fluctuations results in steady states that are characterized by a self-consistently determined temperature. In the strong atoms-cavity coupling regime two (several) different self-organized states exist, which differ in their effective self-consistently determined temperatures. Whereas the dominant contribution is the same in both bistable solutions, the nature of the admixed excited states change. In particular, in the second steady solution, excited states with double occupied sites become crucial, with a cooling mechanism emerging due to resonant photon-assisted transitions between states with double occupancies and other atomic excitations. Thus, we pinpoint the origin of the multi-stability in the interplay between the *short-range* atomic interactions and the *global-range* coupling via the cavity-induced self-consistent potential. It is remarkable, that the presence of fluctuations around the mean-field solution it crucial for the presence of this bistability, since typically mean-field methods show to be valid for for long-range couplings and in many cases fluctuations would lead to the destruction of bistabilities.

As a reminder, as derived in Sec. 3.1 we obtain results by simultaneously fulfilling the self-consistency condition Eq. (3.3) and the steady state condition of the energy transfer equation Eq. (3.14). In parameter regions where the hopping is small compared to the other system parameters we complete our discussion with results from the thermodynamic limit in the weak tunneling perturbation [Sec. 3.2]. In the following, we investigate the case of balanced spin configurations $S^z = 0$. We do not explicitly consider the total spin symmetry sectors, however, we confirmed that we obtain agreeing effective temperatures in all typical spin sectors [see Sec. 3.4].

6.1 Phase diagram at quarter filling

In this section we present our observations and results for the steady state phase diagram at quarter filling ($n = N/L = 1/2$). We identify the dominant processes driving the self-ordering transition, cavity cooling mechanisms as well as many-body-cooling transitions over a wide range of system parameters. Further the appearing fluctuation-induced bistability is characterized. Details on this surprising finding are provided in Sec. 6.3.

6.1.1 Self-ordering phase transition

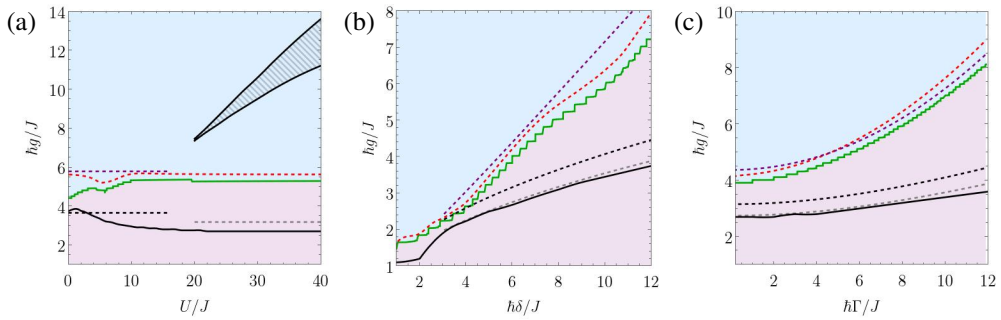

Fig. 6.1: Simplified phase diagrams over a range of atom-cavity coupling $\hbar g/J$ and (a) the on-site interaction U/J at $\hbar\delta/J = 8$, $\hbar\Gamma/J = 1$; (b) the pump-cavity detuning $\hbar\delta/J$ at $U/J = 8$, $\hbar\Gamma/J = 1$; (c) the dissipation rate $\hbar\Gamma/J$ at $\hbar\delta/J = 6$, $U/J = 8$ of a finite size system $L = 8$ at quarter filling. We mark the transition between normal [purple region] and self-organized phase [blue region] determined by solving Eqs. (3.3) & (3.14) with ED [green line]. Analytical approximations are calculated from Eq. (6.1) using the self-consistently determined β in the limit $U/J \to \infty$ [red dashed line in (b),(c)] and replacing each occurrence of β is by the large temperature limit Eq. (6.8) before solving [purple dashed line]. The critical coupling $\hbar g_{\text{cr}}^{\text{MF}}$ in the $T = 0$ MF approach solving Eq. (3.3) via ED [black solid line] is compared to the approximate analytical result for $g_{\text{cr}}^{\text{MF}}$ in Eq. (6.2) for $U = 0$ [black dashed line] and $U \to \infty$ [gray dashed line].

The driven-dissipative coupled atoms-cavity system exhibits a self-ordering transition [78, 152]. In the context of *dissipative phase transitions*, phase transitions occurring in systems away from thermal equilibrium are characterized [40]. Systems that interact with an environment via dissipation while being driven by an external coherent source are typically driven to a steady state which depends on both the system and environment parameters. The self-ordering transition is marked by a sudden change in the system properties at a specific parameter configuration. By increasing the strength of the transversal pump laser while keeping the other system parameters fixed the effective coupling between the atoms and the photons is growing. The system transitions from a normal phase (purple region in Fig. 6.1), which is characterized by a vanishing occupation of the cavity field and vanishing atomic sublattice density imbalance, to a self-ordered phase (blue region in Fig. 6.1), exhibiting a finite occupation of the cavity field and emerging density imbalance. For the here considered system of spin-$1/2$ fermions confined to an external optical lattice such a self-organization transition occurs. We begin by presenting and discussing our findings in the parameter regime around the self-ordering transition at $g \sim g_{\text{cr}}$. The observables we typically present are the sublattice density imbalance $\langle\hat{\Delta}\rangle/L^d$ as well as the inverse temperature β. The temperature $k_B T = 1/\beta$ takes values that are typically large compared to the energy gaps between the lowest eigenstates of the effective mode for the parameter regimes explored in this work. The excited states in the Hamiltonian spectrum thus contribute significantly and can be expected to result in a nature of the steady state which is very different from the results at the $T = 0$ mean-field level where the atoms are in the ground state of the effective Hamiltonian Eq. (3.4).

We want to note that in the normal phase below the self-ordering transition, the atoms still couple to the cavity field fluctuations despite the vanishing average density imbalance, which determines an effective finite temperature. However, one should be careful in using the thermal state ansatz in this regime.

Starting from the normal phases expected for the Fermi-Hubbard model, the system enters into the self-ordered phase as we increase the atoms-cavity coupling above $\hbar g_{\text{cr}}/J$. The transition is signaled by a simultaneous increase of the cavity field occupation and the sublattice imbalance, e.g. see the behavior of $\langle\hat{\Delta}\rangle/L^d$ around $\hbar g_{\text{cr}}/J \approx 5$ in Fig. 6.2 (a),(d). The blue points are obtained via exact diagonalization of the $\hat{H}_{\text{eff}}$ when solving Eqs. (3.3) & (3.14)

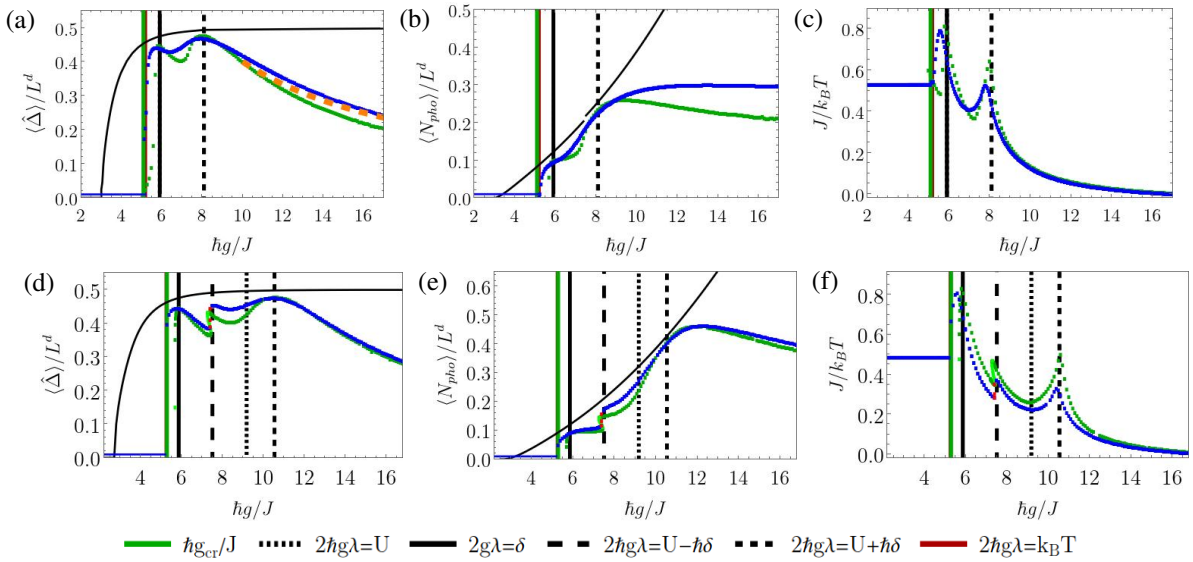

Fig. 6.2: Cuts of the (a),(d) sublattice imbalance $\hat{\Delta}/L$, (b),(e) scaled photon number N_{pho}/L^d and (c),(f) inverse temperature β as a function of atom-cavity-coupling $\hbar g/J$ at (a)-(c) $U/J=8$ and (d)-(f) $U/J=20$; at quarter filling. Results using ED solving Eqs. (3.3) & (3.14) for a finite system size $L=8$ (blue points), and taking the thermodynamic limit in the weak tunneling perturbation, solving Eq. (3.25) numerically (green points). The other parameters used are $\hbar\delta/J=8$, $\hbar\Gamma/J=1$. Lines denote resonances in the atomic limit. The red solid line is underneath the green solid line in (d)-(f).

for a finite system size while the green points are from taking the thermodynamic limit in the weak tunneling perturbation, solving Eq. (3.25) numerically. For both of the methods, the critical coupling shown in the results is the value where the self-consistently determined cavity-field order parameter λ surpasses the set accuracy of 10^{-6}. As expected, the thermodynamic limit in the weak tunneling perturbation fits better for the higher value of the on-site interaction $U/J=20$ in Fig. 6.2 (d)-(f). For $U=8$, while it fits reasonably well at intermediate couplings the weak tunneling limit fails at larger couplings.

In our adiabatic elimination method and the perturbative approximation, the atomic state is given by a thermal state Eq. (3.13), the self-consistently obtained inverse temperature β [see for example Fig. 6.2 (b),(d)] determines the weights of the excited states contributing in the steady state. In the self-ordered regime close to the transition, the inverse temperature [see Fig. 6.2 (b),(e)] rapidly increases until it reaches a maximum and subsequently starts to decrease around the coupling marked by the solid black vertical line. This line represents the resonance condition $2g\lambda=\delta$ in the atomic limit and coincides for the here shown parameters with the maximum in the density imbalance [see Fig. 6.2 (a),(d)]. We will comment on the physical nature of dominant processes around the resonances in Sec. 6.1.2.

In Fig. 6.3 we show how the behavior of the $\langle\hat{\Delta}\rangle/L^d$, the inverse temperature βJ and the average number of double occupancies $\sum\langle\hat{n}_{j\uparrow}\hat{n}_{j\downarrow}\rangle/L$ depends on the on-site interaction U/J. The normal phase at low atoms-cavity couplings, corresponding to $\langle\hat{\Delta}\rangle=0$, is shown as a deep blue region in Fig. 6.3 (a). The transition is clearly seen around the green solid line, when the blue color changes to a lighter white/yellow color. We find that the critical coupling $\hbar g_{\text{cr}}/J$ is slightly decreased for small values of the interaction strength U/J. However in the limit of large atomic interactions, starting from $U/J\gtrsim\hbar\delta/J=10$, the critical coupling only very weakly depends on U/J [see Fig. 6.1 (a) and Fig. 6.3 (a)]. We attribute this to the low filling. The ground state and the lowest excited states of $\hat{H}_{\text{eff}}$ that dominantly contribute to the steady state have mostly singly occupied sites [see sketch Fig. 5.2 (b) for $U/J>20$]. Excited states which include double occupancies are present only at large energies and does have low weight close to the phase transition, which results in the overall really low average number of double occupancies at finite interaction strength [see Fig. 6.3 (c)].

Since already at the $T=0$ mean-field level a self-ordering transition can be observed [78, 152], we want to show a comparison to the results from the many-body adiabatic elimination method (AE) we developed [Sec. 3.1] to

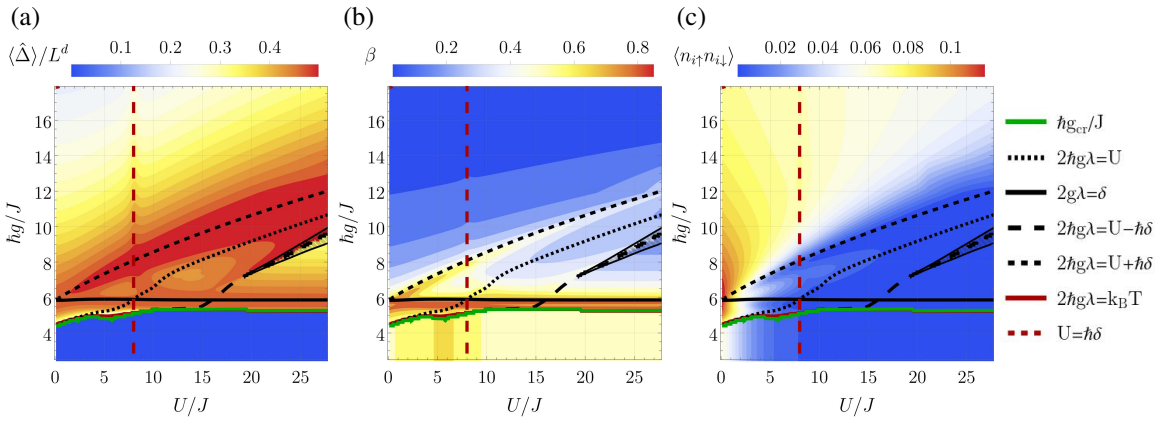

Fig. 6.3: (a) Sublattice imbalance $\hat{\Delta}/L$, (b) inverse temperature β and (c) average number of double occupancies as a function of atom-cavity coupling $\hbar g/J$ and on-site interaction U/J of a finite size system $L=8$ at quarter filling. The other parameters used are $\hbar\delta/J=8$, $\hbar\Gamma/J=1$. The hatched triangular region on the center right marks the fluctuation-induced bistability region within the self-organized phase. Lines denote parameter resonances in the atomic limit. The red solid line is underneath the green solid line.

emphasize the role of the fluctuations in the atoms-cavity coupling. We want to emphasize the fundamentally different nature of the transition between both methods. At $T=0$ MF, the atoms are described by a pure state, namely the ground state of the effective model, while in the AE approach the atomic state is a mixed state with a self-consistently determined effective finite temperature determined by the fluctuations.

In all considered parameter regimes, the presence of fluctuations shifts the critical coupling strength $\hbar g_{\mathrm{cr}}/J$ to higher values compared to the $T=0$ MF result [see green solid curve vs black solid curve in Fig. 6.1]. Including the fluctuations in the atoms-cavity coupling also can be seen to alter the dependence of $\hbar g_{\mathrm{cr}}/J$ on the on-site interactions in Fig. 6.1. While in the $T=0$ mean-field approach the critical coupling decreases to lower values, the contrary is observed for the many-body adiabatic elimination approach. Besides the different transition point, the behavior of the observables when increasing the coupling strength above the transition is also changed. Fixing the on-site interactions, the increase of the cavity field occupation is much more abrupt for the self-consistent finite temperature approach [Fig. 6.2 (b),(e)]. The differences to the $T=0$ MF and finite temperature nature of the atomic state are supported by the temperature has a value of $k_BT/J\approx 2$ obtained close to the transition in Fig. 6.2 (f). The finite temperature leads to a decreased coherence in the atomic system. The thermal fluctuations therefore push the critical coupling strength to higher values. Our observations are consistent with those obtained for a previously investigated system of interacting bosonic atoms coupled to a dissipative cavity in Ref. [164].

Analytical approximations of the critical atom-cavity coupling

We want to discuss the behavior of the critical coupling strength on the system parameters like cavity detuning $\hbar\delta$ and the dissipation strength $\hbar\Gamma$ beyond mere empirical observations. To this end we derive approximate analytical expressions that hold in certain regimes and ultimately compare them to our exact solution [see Fig. 6.1]. Note, that the here shown expressions for g_{cr} are derived for incommensurate values of the filling, assume the cavity field, λ, to be continuous at the phase transition. The values of the cavity order parameter λ are therefore small at the edge of the self-ordered regime. As we will discuss in Sec. 6.2 for a commensurate filling the system this assumption is not valid since the system exhibits a bistability between the normal and the self-organized states.

Here we consider two limits, namely the solvable non-interacting limit ($U=0$) and the $U\to\infty$-limit where the system at low fillings can be approximated by effectively spinless fermions. Similar approaches were derived for non-interacting fermionic gases [261, 262] (no underlying optical lattice) and bosonic gases [30, 263] at the mean-field level. We want to provide expressions that include finite temperature effects.

For both cases, we can start from the Hamiltonian in momentum space derived in Eq. (5.3), where the energy bands are determined by $E(k)=\sqrt{\epsilon(k)^2+(\hbar g\lambda)^2}$. The equations were derived for periodic boundary conditions although the self-consistently determined solutions using ED are typically obtained for open boundary conditions.

However, since we are mainly interested in the scaling of g_{cr} with the system parameters and generally in the self-ordered phase edge effects tend to be suppressed we still expect good agreement. We insert the expression for the sublattice imbalance Eq. (5.5) into the self-consistency equation Eq. (3.3). This results an implicit equation for λ besides the trivial solution $\lambda = 0$

$$\frac{\delta^2 + (\Gamma/2)^2}{2g_{\mathrm{cr}}^2 \delta/L} = \sum_k \frac{\hbar}{E(k,\lambda)} (\langle \hat{\gamma}^\dagger_{-,k,\sigma} \hat{\gamma}_{-,k,\sigma} \rangle + \langle \hat{\gamma}^\dagger_{+,k,\sigma} \hat{\gamma}_{+,k,\sigma} \rangle). \tag{6.1}$$

Calculating the expectation values we distinguish between the $T = 0$ mean field method and the many-body adiabatic elimination method.

In the $T = 0$ *mean field method*, the expectation value on the right-hand-side of the equation has to be evaluated with respect to the ground state of $\hat{H}_{\mathrm{eff}}$. At quarter filling ($n = N/L = 1/2$) and $U/J = 0$, lower band is half-filled up to momenta $|k| = \pi/4$ and the upper band is empty. Due to the independent spin species each momentum state can be doubly occupied [see Fig. 5.1 (a)]. Contrarily for $U/J \to \infty$, approximating the system with a model of spinless fermions, each momentum state can only be singly occupied and the lower band is filled completely [see Fig. 5.1 (b)]. In the atomic limit this results in a band insulator state with an insulating gap $\propto 2\hbar g\lambda$. The critical value of the coupling g_{cr}, is obtained by solving the self-consistency condition Eq. (6.1) for g under the condition of vanishing $\lambda \to 0^+$. This results in solving

$$\frac{\delta^2 + (\Gamma/2)^2}{2g_{\mathrm{cr}}^2 \delta/L} = \sum_k \frac{\hbar}{E(k, \lambda = 0)} \tag{6.2}$$

We evaluate the discrete sum for finite size systems and show the results for both a non-interacting system [black dashed line in Fig. 6.1] as well as for $U \to \infty$ [gray dashed line]. In the thermodynamic limit if only the lowest band is filled and $U = 0$, we can consider continuous momenta $\sum_k \to \frac{L}{2\pi} \int_{-n\pi/2}^{n\pi/2} dk$ and derive an analytic expression for $g_{\mathrm{cr}}^{\mathrm{MF}}$ and the behavior of λ close to the transition.

$$g_{\mathrm{cr}}^{\mathrm{MF}} = \sqrt{\frac{J\pi\left(\delta^2 + (\Gamma/2)^2\right)}{\hbar\delta \mathrm{F}(n\pi/2|\,1)}} \tag{6.3}$$

where $\mathrm{F}(\phi|m) = \int_0^\phi (1 - m\sin^2(\theta))^{-1/2} d\theta$ is the elliptic integral of the first kind. For $U \to \infty$ since every momentum state can only be singly occupied so one needs to integrate $[-\pi n, \pi n]$. The here shown resulting equations are derived in one dimension, but the corresponding expressions for higher dimensional systems can be obtained analogously.

To obtain an approximate scaling of the cavity field order parameter λ close to the transition we expand Eq. (6.2) in λ, which yields

$$\lambda \propto J (g_{\mathrm{cr}}^{\mathrm{MF}})^{3/2} \sqrt{g - g_{\mathrm{cr}}^{\mathrm{MF}}}. \tag{6.4}$$

This result agrees with the one derived for the Dicke model $\alpha \propto (g' - g'_{\mathrm{cr}})^{1/2}$ [38, 263–265] with g' the respective coupling strength and $\alpha = \langle \hat{a} \rangle$ the cavity order parameter. The scaling exponent $1/2$ is obtained both in- and out of equilibrium. The self-ordering transition of an ensemble of non-interacting fermions [261, 262] shows the same scaling in a mean field approach. However note that in Ginzburg-Landau type theories a switch in the scaling to $1/4$ at a tricritical point is derived for low pump-cavity detuning [49].

In the framework of *many-body adiabatic elimination* however, we perform the calculation considering the occupations of higher energy momentum states. The occupation of the momentum states in Eq. (5.5) is captured by the Fermi-distribution in the non-interacting case. This results in Eq. (5.6), defined as

$$\langle \hat{\gamma}^\dagger_{\pm,k,\sigma} \hat{\gamma}_{\pm,k,\sigma} \rangle_T = \frac{1}{e^{\beta(\mp E(k,\lambda) - \mu)} + 1}.$$

The chemical potential is fixed by the particle density Eq. (5.4). Evaluating the expectation values with respect to the thermal states this results in

$$n = \sum_{k,\sigma} \left(1 - \frac{\hbar g \lambda}{E(k,\lambda)}\right) \left[\frac{1}{e^{\beta(E(k,\lambda)-\mu)} + 1} + \frac{1}{e^{\beta(-E(k,\lambda)-\mu)} + 1}\right]$$

The condition for the critical coupling within the many-body adiabatic elimination approach Eq. (6.1) becomes

$$\frac{\delta^2+(\Gamma/2)^2}{2g_{\mathrm{cr}}^2\delta/L}=\sum_k\frac{\hbar}{E(k,\lambda=0)}\left[\frac{1}{e^{\beta(E(k)-\mu)}+1}+\frac{1}{e^{\beta(-E(k)-\mu)}+1}\right] \tag{6.5}$$

At this point we evaluate the discrete sum using the self-consistently determined values of β [red dashed line in Fig. 6.1] to get an intuition for our approximations up to now, without restricting to specific temperature regimes.

As before taking the thermodynamic limit the momentum values become continuous and the sum can be replaced by an integral. Here one needs to integrate over the full reduced Brillouin-zone $\sum_k \to \frac{L}{2\pi}\int_{-\pi/2}^{\pi/2}dk$ since all momentum states are thermally occupied. Note that for this expression β still depends on the system parameters and needs to be solved together with Eq. (3.14) ($\partial\langle\hat{H}_{\mathrm{eff}}\rangle/\partial t=0$).

We will find analytic expressions for g_{cr} for $U=\infty$ (purple dashed line Fig. 6.1) and $U=0$ [blue dashed line in Fig. 6.1 (a)] in the large temperature limit.

In the *large temperature limit* $\Gamma, \Gamma^2/\delta \gg J/\hbar, g\lambda$ or $\delta \gg J/\hbar, g\lambda$ we saw in Sec. 3.1 that the inverse temperature takes the approximate form Eq. (3.16) given by

$$\beta \approx \frac{4\delta/\hbar}{\delta^2+(\Gamma/2)^2}$$

If the large-temperature approximation $\langle\hat{\Delta}\rangle/L \propto \hbar g\lambda\beta$, which will be derived in the paragraph following Eq. (6.8), is valid close to the self-ordering transition, using the self-consistency condition Eq. (3.3) the critical coupling scales as

$$g_{\mathrm{cr}}(\beta\ll 1) \propto \frac{\delta^2+(\Gamma/2)^2}{\delta} \tag{6.6}$$

in both interaction limits $U=0$ and $U=\infty$.

Comparing the analytical critical atom-cavity coupling to the phase diagram

In a next step the analytical findings can be compared to our calculated phase diagrams in more detail. A simplified phase diagram comparing the transition lines from solving the full effective model via ED with the analytical approximations at both with and without fluctuations are shown in Fig. 6.1. Further some measured observables are shown for parameter regions varying the coupling strength on the vertical axis and either the pump-cavity detuning δ [Fig. 6.4] or the dissipation rate Γ [Fig. 6.8] on the horizontal axis.

For low couplings $g < g_{\mathrm{cr}}$ the system is in the normal phase of the Fermi-Hubbard model at finite temperature, characterized by a homogeneous density distribution over all sites, which is depicted as the blue region in density imbalance plots. Fixing δ or Γ respectively while increasing the coupling strength, the system transitions to the self-ordered phase. At large detuning $\delta \gg \Gamma$, the critical coupling strength increases approximately linearly with the detuning $g_{\mathrm{cr}} \sim \delta$. This consistent with the analytic approximation obtained in the high temperature limit [Eq. (6.6)]. Note that in order to ensure this limit is valid Γ typically still needs to be sufficiently high. For an equivalent system with bosonic atoms, a similar dependence on the detuning was obtained [164]. Comparing $T=0$ MF and the many body adiabatic elimination results, the shift of the critical coupling between both methods increases with the detuning. Without fluctuations Eq. (6.3) can be simplified in the large detuning limit, resulting in $\hbar g_{\mathrm{cr}}^{\mathrm{MF}}/J \sim \sqrt{\hbar\delta/J}$, while in the presence of fluctuations the critical coupling behaves as $\hbar g_{\mathrm{cr}}/J \sim \hbar\delta/J$ [see Fig. 6.1 (b)]. A larger pump detuning reduces the effective long-range cavity-mediated coupling. In order to reach the same effective atom-cavity coupling, the large detuning needs to be compensated by increasing the amplitude of the pump field correspondingly. Additionally a large detuning δ typically leads to an increase in the effective temperature around the self-ordering transition. This also contributes to the shift of the transition towards higher couplings when including fluctuations, while this effect is not present at $T=0$, leading to a scaling difference between the methods.

We now turn to the dependence on the dissipation strength Γ [Fig. 6.1 (c)]. Here, as supported by Eq. (6.6), the self-ordering threshold increases approximately quadratically with Γ. In a parallel to the large detuning limit, increasing Γ also typically leads to a growing effective temperature close to the self-ordering transition. As a result we obtain a weaker scaling of the critical coupling with the dissipation strength (linear instead of quadratic) at the

$T=0$ MF level, as predicted by Eq. (6.3) in the limit $\Gamma \gg \delta$. As can be seen in Fig. 6.7, increasing the dissipation rates while keeping the other parameters fixed the decoherence of the atoms increases until the system transitions to the normal phase at the critical coupling.

After looking at the dependence of the critical coupling on the system parameters, we now investigate the nature of the steady state obtained within the self-ordered phase.

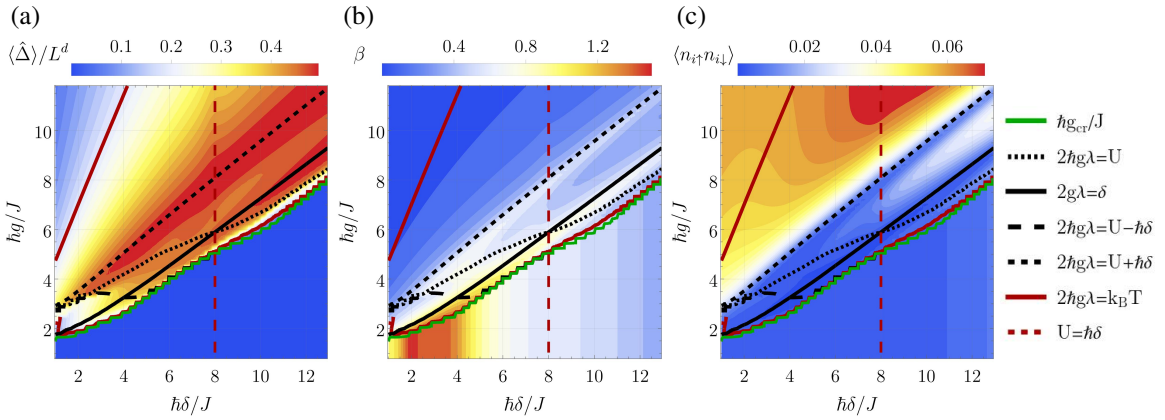

Fig. 6.4: (a) Sublattice imbalance $\hat{\Delta}/L$, (b) inverse temperature β and (c) average number of double occupancies as a function of atom-cavity coupling $\hbar g/J$ and detuning $\hbar\delta/J$ of a finite size system $L=8$ at quarter filling. The other parameters used are $U/J=8$, $\hbar\Gamma/J=1$. Lines denote the parameter resonances in the atomic limit.

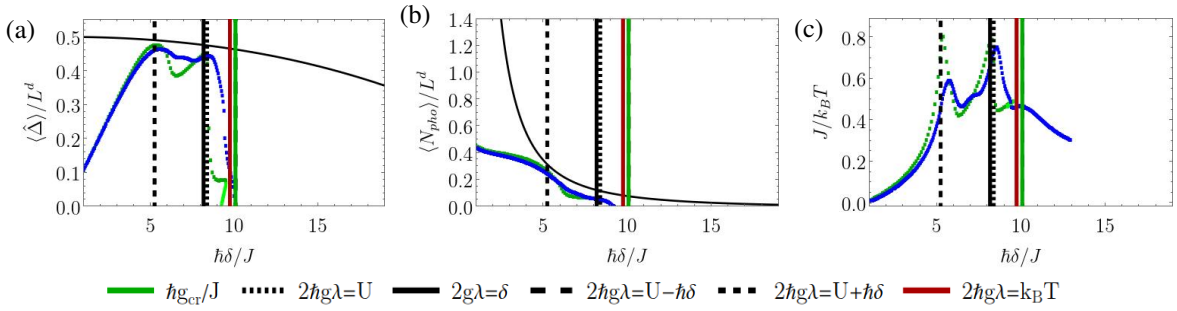

Fig. 6.5: Cuts of the (a) sublattice imbalance $\hat{\Delta}/L$, (b) scaled photon number N_{pho}/L^d and (c) inverse temperature β as a function of $\hbar\delta/J$ at $\hbar g/J=6$ at $\hbar\delta/J=8$; at quarter filling. Results are obtained using ED solving Eqs. (3.3) & (3.14) for a finite system size $L=8$ (blue points), and taking the thermodynamic limit in the weak tunneling perturbation, solving Eq. (3.25) numerically (green points). The other parameters used are $U/J=8$, $\hbar\Gamma/J=1$. Vertical lines denote the resonances in the atomic limit.

6.1.2 Fluctuation-effects in the ordered phase

In this section, we discuss the nature of the steady states within the self-ordered phase. In our considerations we focus on effects that arise due to the influence of the fluctuations in the atoms-cavity coupling.

Cavity cooling process

In the sublattice imbalance $\langle\hat{\Delta}\rangle$ determined using the many-body adiabatic elimination, a non-monotonic behavior emerges varying the coupling strength within the self-ordered phase [see Fig. 6.2 (a),(d) and Fig. 6.5 (a)]. This is closely connected to the values of the self-consistently determined effective temperature [see Fig. 6.2 (c),(f) and Fig. 6.5 (c)]. At the phase transition, the imbalance shows a steep increase to a maximum, followed by a decrease for both shown interaction strengths. In the inverse temperature we identify a corresponding behavior that signals a minimum in the effective temperature and thus a cooling of the atomic system through the coupling to the cavity

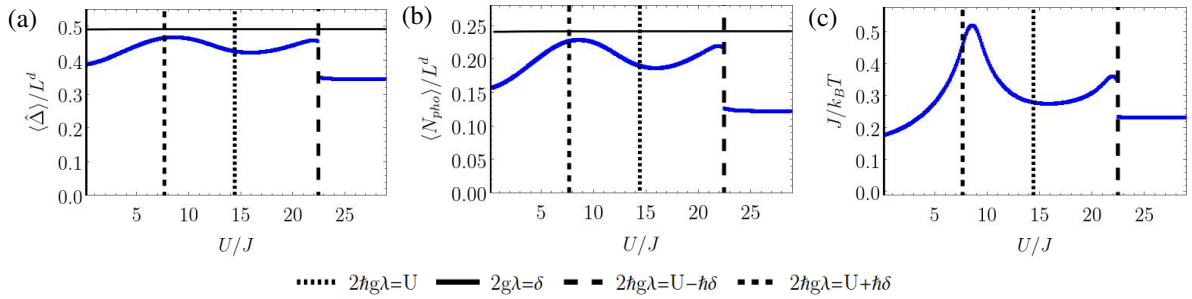

Fig. 6.6: Cuts of the (a) sublattice imbalance $\hat{\Delta}/L$, (b) scaled photon number N_{pho}/L^d and (c) inverse temperature β as a function of U/J at $\hbar g/J=8$; of a finite size system $L=8$ at quarter filling The other parameters used are $\hbar\delta/J=8$, $\hbar\Gamma/J=1$. Vertical lines denote the resonances in the atomic limit.

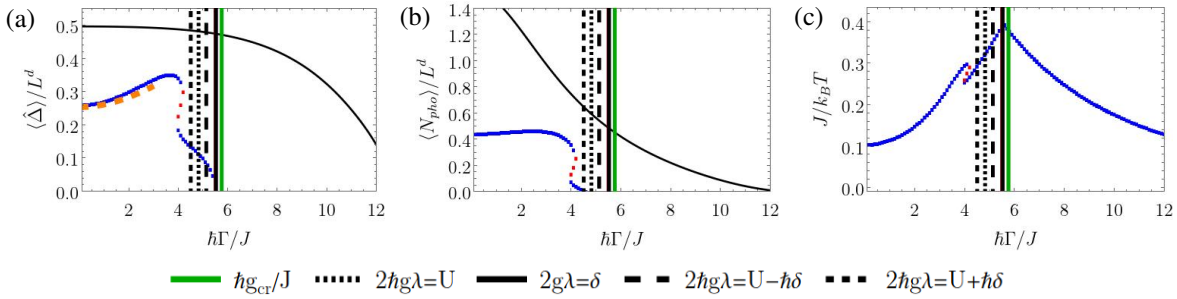

Fig. 6.7: Cuts of the (a) sublattice imbalance $\hat{\Delta}/L$, (b) scaled photon number N_{pho}/L^d and (c) inverse temperature β as a function of $\hbar\Gamma/J$ at $\hbar g/J=5$; of a finite size system $L=8$ at quarter filling showing stable (blue points) and unstable (red points) solutions. The other parameters used are $U/J=8$, $\hbar\delta/J=2$. Vertical lines denote the parameter resonances in the atomic limit.

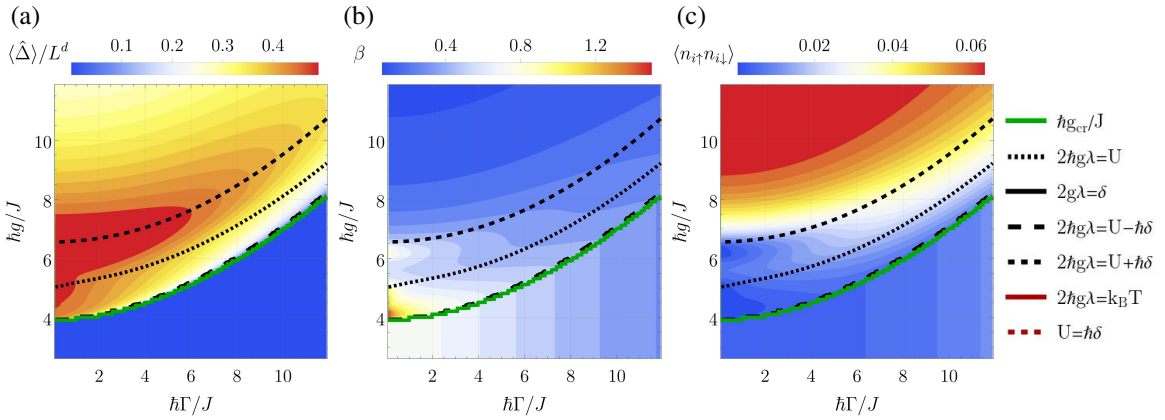

Fig. 6.8: (a) Sublattice imbalance $\hat{\Delta}/L$, (b) inverse temperature β and (c) average number of double occupancies as a function of atom-cavity coupling $\hbar g/J$ and dissipation $\hbar\Gamma/J$ of a finite size system $L=8$ at quarter filling. The other parameters used are $U/J=8$, $\hbar\delta/J=6$.The contour lines denote the parameter resonances in the atomic limit.

field. This cooling process occurs approximately around the coupling value where $2g\lambda \approx \delta$ is fulfilled, which we confirmed by looking at the system varying both the atoms-cavity coupling g and the detuning δ. We include this condition as solid black lines in the density plots Figs. 6.3 & 6.4 and vertical black lines in the corresponding cuts. It can be seen that the line seems to follow the general behavior of the phase transition over a wide parameter range varying both U and δ.

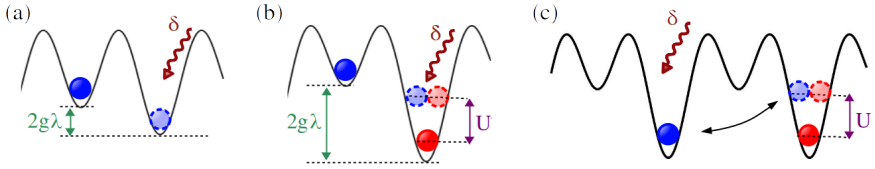

Fig. 6.9: Sketches of the energy transfer transitions in the atomic limit captured by Eq. (3.25a). (a) First line in Eq. (3.25a): hopping from a high- to an empty neighboring low potential sublattice site, adding a photon to/removing a photon from the cavity field $\Delta E_{nm} = \pm(2\hbar g\lambda \pm \hbar\delta)$. (b) Second line in Eq. (3.25a) with $p = 1$: hopping from a high- to a neighboring low potential sublattice site, creating a double occupancy and adding/removing a photon to the cavity field $\Delta E_{nm} = \pm(2\hbar g\lambda - U \pm \hbar\delta)$. (c) Next neighbor hopping process resonant at $\Delta E_{nm} = \pm(U - \hbar\delta)$

This so-called *cavity cooling* process has been identified for single atoms [74] and non-interacting gases [76, 78, 266]. For our system, the $T = 0$ mean-field approach does not capture this effect. The key ingredients are the fluctuations in the atom-cavity coupling which lead to a finite effective temperature. In our case we want to provide a physical interpretation of the resonance condition $2g\lambda = \delta$ obtained in the limit of vanishing tunneling amplitude (atomic limit). It marks an energy degeneracy between states where an atom hops from a singly occupied high-potential sublattice site to a neighboring empty site. Looking at the ionic Hubbard model ground state that is isolated from its environment, the conservation of the system's total energy suppresses these kinds of (de-) excitations. In contrast, for the Hubbard model coupled to the cavity, even at vanishing dissipation rates the cavity field is able to facilitate transitions, as sketched in Fig. 6.9 (a). The change in energy from excitations is compensated by the coupled field by while adding/removing a photon in the cavity mode. This results in an efficient transfer process where the energy is removed from the atomic system as the number of defects to the perfect density order is decreased. Simultaneously the energy is added to the cavity field, leading to an increase in the photon number. While the process can occur in both directions, the system eventually stabilizes at a minimal steady state temperature. Typically the position of the maximum in the imbalance slightly deviates from the resonance condition $2g\lambda = \delta$ which we account to deviations from the finite tunneling rate [see Fig. 6.5 (c)]. Our approximation taking the thermodynamic limit in the weak tunneling perturbation is also able to capture this resonance, which manifests in the denominators of the first line of Eq. (3.25a). One can interpret the contributions in the upper line of Eq. (3.25a) as originating from eigenstates of $\hat{H}_{\text{eff}}$, which differ by a single particle being on the lower potential or upper potential sub-lattice [sketched in Fig. 6.9 (a)] i.e. $E_n - E_m \approx 2\hbar g\lambda$ corresponds to transitions between the ground state and an excited state of the effective ionic Hubbard model (see Fig. 5.2).

A similar cooling process manifests for the case of many-body resonances. We will provide some details on the corresponding processes in the next section.

6.1.3 Many-body cooling processes

Beyond the cavity cooling processes that also appear in non-interacting systems, the many-body character of our system also causes non-trivial effects to emerge. In this section, we present the cooling processes and corresponding minima in the effective temperature that originate from the many body resonances. A match between the energy gaps in the spectrum of the many-body effective Hamiltonian and the cavity detuning a cooling mechanism emerges, leading to lower self-consistently determined effective temperatures of the atomic states. The presence of these resonances, similar to the cavity cooling process, explains the non-monotonic behavior of the density imbalance and inverse temperature appearing at intermediate coupling strength in the self-organized phase, e.g. Fig. 6.2 (d),(f) around $\hbar g/J \sim 7 - 11$ and also varying the on-site interaction in Fig. 6.6 (a),(c) around $U/J \sim 6 - 24$. The many-body cooling processes will also prove to be a crucial ingredient for the emergence of the fluctuation-induced bistability analyzed in detail in Sec. 6.3.

It is important to note that the cooling effects can only arise due to the fact that in our method the temperature

is self-consistently determined from the perturbative effect of the fluctuations [see Sec. 3.1]. Such dynamical phenomena would not be captured by imposing a fixed temperature for the atomic state as we show in Fig. 6.20. Here, the self-consistency equation Eq. (3.3) is solved for a thermal atomic state at fixed inverse temperature β. Consequently, the cavity occupation rises monotonically for each value of the temperature.

In order to understand the nature of the steady states of the coupled atoms-cavity system, it is useful to briefly revisit the energy gaps of the effective Hamiltonian at quarter filling (discussed in Sec. 5.2.1). The weight of the terms that capture the transition between eigenstates $|n\rangle$ and $|m\rangle$ in Eq. (3.14), namely

$$\frac{\partial}{\partial t}\langle \hat{H}_{\text{eff}}\rangle_T \propto \sum_{n,m} |\Delta_{nm}|^2 \frac{e^{-\beta E_m}(E_n - E_m)\Gamma}{(E_n - E_m + \hbar\delta)^2 + (\hbar\Gamma/2)^2} \stackrel{!}{=} 0$$

is strongly influenced by resonances $E_n - E_m$, with E_n the energy of the eigenstate $|n\rangle$ of $\hat{H}_{\text{eff}}$ [see Eq. (3.4)] and $\Delta_{nm} = \langle n|\,\hat{\Delta}\,|m\rangle$ [150, 164].

By looking at the energy transfer equation derived in the weak tunneling limit, Eq. (3.25a), atomic processes which take take place during the exchange of energy between the atoms and cavity can be connected with resonances in the limit of vanishing tunneling rates. Small deviations can be expected for the finite J results. These resonances will be the focus of our following discussion. Whether a process is of heating or cooling nature in the self-consistent dynamics driving the system to its steady state is determined by the sign of the individual terms in Eq. (3.25a). In the steady state all processes are balanced [164].

The many-body cooling resonances occur when transitions between two excited states involving the interaction energy are resonant with the cavity mode, i.e. around the couplings where $2\hbar g\lambda = U \pm \hbar\delta$ is fulfilled. This is expressed in the lower lines of Eq. (3.25a), which originate from transitions the sublattice density imbalance and number of double occupancies is changed simultaneously. The energy in the atomic subsystem changes by i.e. $E_n - E_m \approx 2\hbar g\lambda \mp U$, which is compensated by the corresponding change in the cavity field energy by $\pm\hbar\delta$. We depict this process in Fig. 6.9 (b). As with the cavity cooling around these resonances energy can be transferred from the atomic subsystem to the cavity field in an efficient way, which causes the steady state to stabilize at a minimum of the effective temperature with increased density sublattice imbalance. The resonance conditions $2g\lambda_2 = U/\hbar \pm \delta$ are marked by black, long(-)/short(+)-dashed lines, e.g. in Fig. 6.3 and Fig. 6.4, or as vertical lines in the cuts varying the coupling [Fig. 6.2 and Fig. 6.21] or the on-site interaction [Fig. 6.6].

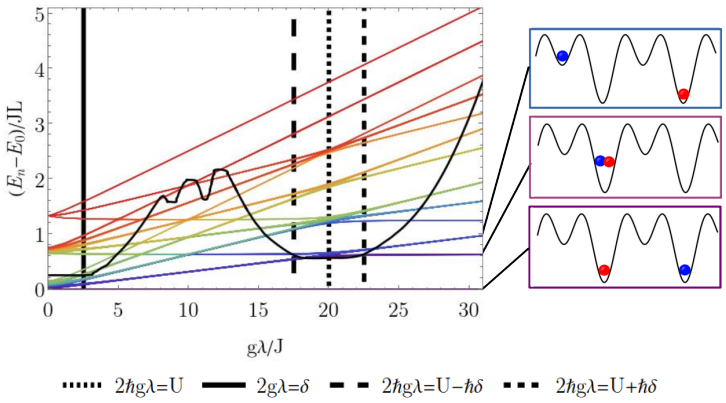

Fig. 6.10: We show the eigenenergy spectrum of the effective atomic Hamiltonian $\hat{H}_{\text{eff}}$ and effective temperature (black line) as a function of the effective coupling $\hbar g\lambda/J$ at finite size $L = 8$ and quarter filling. The other parameters used are $U/J = 40$, $\hbar\delta/J = 5$, $\hbar\Gamma/J = 3$. Vertical lines denote resonances in the atomic limit.

To further illustrate the energy level crossing and behavior of the temperature, we present the relative atomic energy spectrum $(E_n - E_0)/L$ obtained via ED of a system of size $L = 8$ as a function of the effective atom-cavity coupling $\hbar g\lambda/J$ and compare it to the self-consistently determined temperature $k_B T/J$ (black line) in Fig. 6.10. Note, that here we do not distinguish between stable and unstable results. We identify the region bordered by the two vertical purple dashed lines that mark the cooling resonances $2g\lambda_2 = U/\hbar \pm \delta$. In between, the temperature lies below the excitation gap, resulting in a steady state that is close to the ground state. The resonances involving

doubly occupied sites are also important within the emerging fluctuation-induced bistable regime that exhibits a bistability between two ordered states with different effective temperatures [1]. This is marked by the hatched region in the phase diagram shown in Fig. 6.1 (a) & 6.3 and will be discussed in detail in Sec. 6.3.

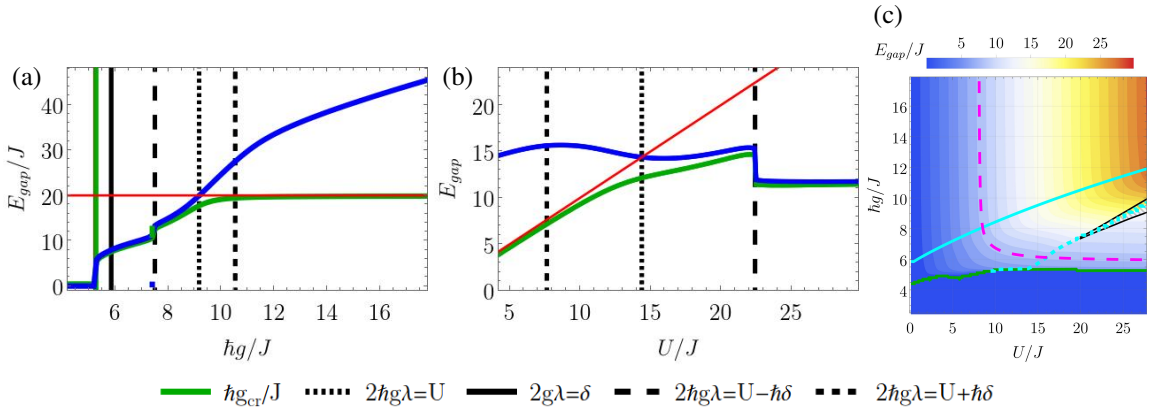

Fig. 6.11: Energy excitation gap [green line] between eigenstates with $\langle\hat{\Delta}\rangle = N$ and $\langle\hat{n}_{j\uparrow}\hat{n}_{j\downarrow}\rangle = 0$ and the lowest energy states differing in either of the quantities in the eigenspectrum of the effective atomic model $\hat{H}_{\text{eff}}$. We show it (a) as a function of atom-cavity-coupling $\hbar g/J$ at $U/J = 20$ and (b) as a function of the on-site interaction strength U/J at $\hbar g/J = 8$; The effective sublattice potential imbalance $2\hbar g\lambda/J$ is plotted in blue, the on-site interaction U/J in red. Vertical lines denote parameter resonances in the atomic limit. (c) Energy excitation gap varying atoms-cavity coupling and on-site interaction. Contour lines mark: $E_{\text{gap}} > 0$ (green), $E_{\text{gap}} = \hbar\delta$ (magenta dashed), $E_{\text{gap}} = U - \hbar\delta$ (cyan dashed) and $E_{\text{gap}} = 2\hbar g\lambda - \hbar\delta$ (cyan). For all plots: $L = 8$ at quarter filling with $\hbar\delta/J = 8$, $\hbar\Gamma/J = 1$.

As our results show the importance of including the excited states of the effective model $\hat{H}_{\text{eff}}$ in the steady state density matrix and the resonance condition matching the cavity energy and gap in the atomic spectrum, it is important to understand the nature of the excited states and the behavior of the gaps. We investigate the excitation gap in the energy spectrum E_{gap} that is obtained from the eigenspectrum of $\hat{H}_{\text{eff}}$. Since we are interested in many-body processes, the excitation gap we show here is the gap between bands of eigenstates that are characterized by the same total density imbalance $\langle\hat{\Delta}\rangle$ and number of double occupancies $\sum_j\langle\hat{n}_{j\uparrow}\hat{n}_{j\downarrow}\rangle$. With this assumption we neglect the individual particle configurations because they would only lead to small changes in the eigenenergies within each band due to finite size effects and higher order hopping processes. As shown in Fig. 6.11 (a), the excitation gap [green line] starts to grow from the phase transition approximately following $2\hbar g\lambda/J$ [blue line]. This corresponds to a band-insulating behavior. Further increasing the coupling strength as one reaches the regime where $2\hbar g\lambda/J \gg U$ the energy gap approaches U/J and the nature of the excitations change to a Mott insulator on the low-potential sublattice sites. This can correspondingly be seen in Fig. 6.11 (b). Increasing the on-site interaction one can observe a smooth change from Mott-insulating to band insulating behavior of the low-lying excitations. We want to note, that for large dissipation strength, since the spectral peaks are broadened, it becomes increasingly difficult to observe the cooling resonances. In Fig. 6.7 this can be seen, as presumably the broadened peaks of various resonances overlap and no separated peaks can be observed.

Another cooling effect that does not involve a change in the density imbalance is emerging around the resonance condition $\hbar\delta \sim U$. Here the dynamics towards the steady state is influenced significantly by transitions of higher order in the tunneling, like the one depicted in Fig. 6.9 (c). We observe in our results that when the condition $\hbar\delta \sim U$ is satisfied as for the other cooling resonances the value of the effective temperature is reduced and the sublattice imbalance exhibits a maximum. This effect can be followed over a large parameter range varying both the interaction strength U, Fig. 6.3, or the detuning δ, Fig. 6.4, where it is marked by the red dashed lines. Note that an equivalent resonant cooling effect was identified for the case of interacting bosonic atoms in Ref. [164].

The $U \approx \hbar\delta$ resonance can be understood in more detail by considering its effect on the imaginary part of the retarded susceptibility defined in Eq. (3.15). The function exhibits a main peak at $\hbar\omega = \pm 2g\lambda$ with secondary peaks around $\hbar\omega = \pm U$. Generally, the secondary peaks are suppressed by a factor of $J^2/\hbar g\lambda$ due to their dependence on second order hopping processes. This changes at the resonance $U/J \sim \hbar\delta/J$, that increases the transition

rates between the states and compensates the higher hopping order. At this specific parameter configuration, the dominant cooling terms are those at energies $\hbar\omega \sim -U$, which corresponds to the processes decreasing the number of double occupancies by 1 while adding a photon to the cavity field. Contrarily, the heating is dominated by the peaks at $\hbar\omega \sim U$, where a double occupancy is created.

We can view the $U \approx \hbar\delta$ resonance more generally as an instance in which the energy of the cavity field matches the gap between the ground state and the first excited state of the effective Hamiltonian $E_{\text{gap}} = \hbar\delta$. We can exemplify this comparing Fig. 6.11 (c) to Fig. 6.3. The magenta dashed curve that marks $E_{\text{gap}} = \hbar\delta$ in Fig. 6.11 (c) matches the $U \approx \hbar\delta$ line in Fig. 6.3 for the $\hbar g/J \gtrsim 9$ regime. Increasing the on-site interaction, the magenta line instead approaches the condition $2g\lambda = \delta$, marked by the black solid curve Fig. 6.3. This further allows us to understand maxima in the sublattice density imbalance away from regimes where the nature of the eigenstates of $\hat{H}_{\text{eff}}$ can be easily identified, as for example around $U/J \approx 9.8$, $\hbar g/J \approx 6.8$ in Fig. 6.3. They are caused by the smooth change from Mott- to band insulating behavior as the on-site interaction increases above the energy scale determined by $2\hbar g\lambda$.

Large atom-cavity coupling limit and saturation of the cavity occupation

To conclude our discussion of the quarter-filled phase diagram we consider the large atoms-cavity coupling limit. In the $T = 0$ mean-field approach one would expect to see a saturation of the density imbalance to its maximal value that represents perfect order as the coupling is increased. As determined from the steady state solution of the cavity field in Eq. (3.2) the corresponding photon number increases quadratically with the coupling [see black curve in Fig. 6.2 (b)]. However, the behavior observed in the results including fluctuations in the atoms-cavity coupling and thus a self-consistently determined finite temperature is drastically changed [164]. Within our many-body adiabatic elimination method the imbalance is seen to decrease at intermediate to larger coupling strengths for the shown parameter regimes [see blue curves in Fig. 6.2 (b),(e)]. While in the $T = 0$ limit the large coupling regime would lead to a larger effective potential shift between neighboring sites, including fluctuations this effect is competing with a rapid increase of the value of the effective temperature of the atomic state [see Fig. 6.2 (c),(f)]. When the energy scale given by the effective potential offset $2\hbar g\lambda/J$ is surpassed by the thermal energy $k_B T/J$, the excitation rate of atoms to the lattice sites corresponding to a higher potential is strongly increased. This consequently leads to a decreased sublattice imbalance in the steady state and a corresponding saturation in the cavity field occupation. This scale is $\hbar g/J \gtrsim 10$ for the parameters shown in Fig. 6.2 (b) where the photon number saturation appears. Due to the larger on-site interaction $U/J = 20$, in Fig. 6.2 (e) the saturation is not yet visible at the maximal shown coupling strength.

We will provide an approximate analytical framework in the following paragraphs that captures the described effect of including fluctuations in the atoms-cavity coupling. Eventually we identify a scaling behavior of the imbalance with the coupling $\langle\hat{\Delta}\rangle \propto g^{-1}$, while the photon number saturates at a value independent of g in the limit of large coupling strengths.

Deep in the self-ordered regime, $\hbar g\lambda \gg U, \hbar\delta, J$, at quarter filling all low potential sublattice sites are singly occupied in the ground state of the effective Hamiltonian $\hat{H}_{\text{eff}}$, Eq. (3.4). Here we neglect the influence of spin-correlations since at the large temperatures that cause the saturation, spin-coherence is typically lost. The relevant processes starting from the ground state are first-order hopping events, changing the energy in the atomic subsystem by $\hbar\omega = \pm 2g\lambda$. Processes of higher order in the hopping that include the on-site interaction $\hbar\omega \sim \pm U$ are suppressed by a factor of $\sim J^2/\hbar g\lambda$. Restricting to the dominant processes we simplify the system of equations derived in Sec. 3.2. The resulting approximation of the steady state condition of the energy transfer, Eq. (3.25a), holds for both the non-interacting $U/J = 0$ and the $U/J \to \infty$ limit and is given by

$$\frac{-e^{\beta\hbar g\lambda}}{(2g\lambda+\delta)^2+(\Gamma/2)^2} + \frac{e^{-\beta\hbar g\lambda}}{(2g\lambda-\delta)^2+(\Gamma/2)^2} = 0.$$

we obtain

$$e^{\beta\hbar g\lambda} = \sqrt{\frac{(\Gamma/2)^2+(\delta+2g\lambda)^2}{(\Gamma/2)^2+(\delta-2g\lambda)^2}} \tag{6.7}$$

Note that the same equation can alternatively be derived by neglecting the λ-dependence of the chemical potential and and going to the limit of large on-site interaction $e^{\beta U} \gg 1$ (see Appendix B, published in Ref. [1] Supplemental).

For $\beta\hbar g\lambda \ll 1$ and $\hbar g\lambda \to \infty]$ we can approximate Eq. (6.7) and solve for the effective inverse temperature

$$\beta \approx \frac{\delta}{\hbar(g\lambda)^2} \tag{6.8}$$

and find the scaling of the temperature with the effective potential imbalance $g\lambda$ to be quadratic.

We continue the approximation of the system of equations to determine μ and λ, now distinguishing between the two interaction limits $U/J=0$ and $U/J\to\infty$. In the following, we first consider the $U/J\to\infty$ limit. The particle conservation condition Eq. (3.25b) results in the expression

$$e^{\beta\mu} = \frac{(2-4n)\cosh(\beta\hbar g\lambda) + \sqrt{2(1-2n)^2\cosh(2\beta\hbar g\lambda) - 8(n-1)n + 2}}{8(n-1)}.$$

We only confirmed the validity of this result for $N/L \leq 0.5$, since the approximation breaks down as one approaches half filling as the chemical potential diverges with U and can no longer assumed to be finite. These results are inserted into the self-consistency condition Eq. (3.25c) at $U/J\to\infty$ and using $\hbar g\lambda \gg \hbar\delta, \hbar\Gamma$ it results in

$$\lambda(U\to\infty) = \sqrt{\frac{2\delta^2(1-n)n}{(\Gamma/2)^2+\delta^2}}. \tag{6.9}$$

From the expression of the cavity field we can obtain the inverse temperature, imbalance and photon number in the strong coupling regime

$$\beta \approx \frac{(\Gamma/2)^2+\delta^2}{2\hbar\delta g^2 n(1-n)}, \qquad \frac{\langle\hat{\Delta}\rangle}{L} = \frac{\sqrt{(1-n)n((\Gamma/2)^2+\delta^2)}}{\sqrt{2}g}, \qquad \frac{\langle\hat{a}^\dagger\hat{a}\rangle}{L} \approx \frac{n}{2}(1-n). \tag{6.10}$$

These results slightly change when considering the non-interacting limit $U/J=0$. The spin species can occupy the states independently. Consequently one can block diagonalize the Hamiltonian, resulting in independent system of equations for each of the spin species. This yields for the self-consistency condition Eq. (3.25c)

$$\lambda(U=0) = \sqrt{\frac{\delta^2(2-n)n}{(\Gamma/2)^2+\delta^2}}. \tag{6.11}$$

Using this result combined with Eq. (6.8) we obtain the inverse temperature, imbalance and photon number in the non-interacting strong coupling regime

$$\beta J \approx \frac{(\Gamma/2)^2+\delta^2}{g^2 n(2-n)}, \qquad \frac{\langle\hat{\Delta}\rangle}{L} = \frac{\sqrt{(2-n)n((\Gamma/2)^2+\delta^2)}}{2g} \qquad , \frac{\langle\hat{a}^\dagger\hat{a}\rangle}{L} \approx \frac{n}{4}(2-n). \tag{6.12}$$

Here we are not as restricted in the filling except approaching fully filled bands $N/L\sim 2$. It can be assumed to hold for the largest fillings we consider in this work which is $N/L=1$. Both expressions derived in Eqs. (6.10) & (6.12) strongly deviate from the behavior at the $T=0$ mean-field level where, as stated in the introduction of this section, one would obtain that the photon number scales quadratically with the coupling strength, $\propto \frac{g^2}{\delta^2+(\Gamma/2)^2}n^2$.

The resulting scaling of the photon number with the filling for spinful fermions we obtain here is differing from the one derived for an equivalent Bose-Hubbard system in Ref. [164]. There, the photon number is found to scale as $n(n+1)$ with the filling.

We observe in our results both the scaling of the inverse temperature, $\beta \propto g^{-2}$, and the imbalance, $\langle\hat{\Delta}\rangle \propto g^{-1}$, as we increase the coupling strength, for example in Figs. 6.2 (a),(c) & 6.21 (b),(c). Additionally we confirm the correct scaling of our expression with the dissipation strength in the low dissipation limit in Fig. 6.7.

Further confirmations of the derived scalings will be provided for the steady-state phase diagram at half-filling in the next section. We finally want to remark, that the high temperature that typically appears in the large coupling limit at sufficiently high dissipation and detuning also causes an increased occupation of the excited states that feature doubly occupied sites, leading to a growing average double occupancy [Figs. 6.3 & 6.4 (c)]. However, since the overall average remains low at quarter filling and it does not directly influence the density imbalance or cavity field occupation we omitted this observation in the previous discussion. The situation is different at half filling, which we will present in the next section.

6.2 Phase diagram at half filling

In this section we discuss the special case of commensurate or half filling ($N/L = 1$) for the atomic many-body system.

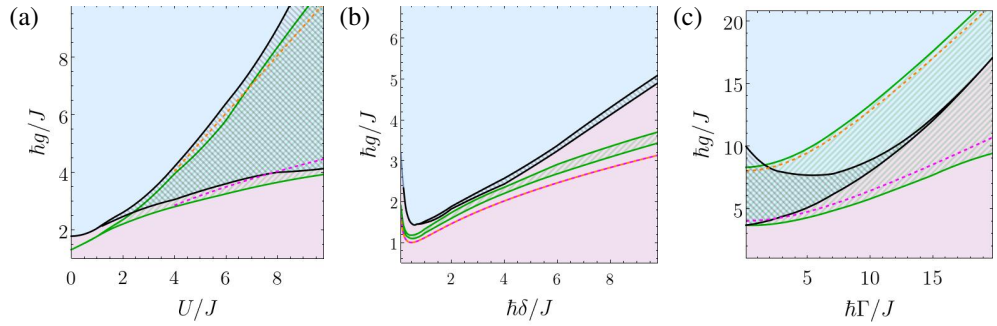

Fig. 6.12: Simplified phase diagrams varying the atom-cavity coupling $\hbar g/J$ and (a) the on-site interaction U/J at $\hbar\delta/J = 4$, $\hbar\Gamma/J = 1$; (b) the pump-cavity detuning $\hbar\delta/J$ at $U/J = 2$, $\hbar\Gamma/J = 1$; (c) the dissipation rate $\hbar\Gamma/J$ at $\hbar\delta/J = 4$, $U/J = 8$ of a finite size system $L = 6$ at half filling. The lower black line marks the transition between normal [purple region] and the high-λ solution in the self-organized phase [blue region] determined by solving Eqs. (3.3) & (3.14) with ED. The lower green line marks the critical coupling $\hbar g_{\mathrm{cr}}^{\mathrm{MF}}$ obtained for the $T = 0$ MF approach. The dashed lines are approximations critical couplings $g_{\mathrm{cr}}^{\mathrm{MF}}$ Eq. (6.13).

In the absence of the pump the atomic system is captured by the Fermi-Hubbard model at half filling, which, depending on the interaction strength, can be in a Mott insulating or liquid phase [267]. Increasing the atoms-cavity coupling, the ordering of the atomic system that leads to an effective potential imbalance between the sublattices is forcibly accompanied by an increase in the density of doubly-occupied sites on the low potential sublattice in the classical limit [see Sec. 5.3.3 for details]. We expect that across the self-ordering transition an initial Mott-insulating state is destroyed and the character of the fermionic state changes to a state with finite density imbalance in the steady state. In both the $T = 0$ MF method and when taking fluctuations into account we find a bistability at the self-ordering phase transition. It can by characterized as a region of coupling strengths that supports two stable steady states that differ in their average photon number as well as the atomic many-body state. We mark the corresponding regions as hatched regions in Fig. 6.12, where for the $T = 0$ MF method it is bordered by the green lines and the bistability in the many-body adiabatic elimination approach is black. We want to emphasize the fundamentally different the nature of this bistability at half filling when compared to the fluctuation-induced bistability we identified in Sec. 6.1 and will analyze in detail in Sec. 6.3. Here the nature of the ground state of the effective model, changes its character due to a closing of the gap to the lowest excitations from a Mott insulator to a charge density wave. While at lower filling the eigenenergy of the ground state contribution in the mixed steady state does not show any level-crossings within the bistability region and the bistable behavior is determined within the excited eigenspectrum of $\hat{H}_{\mathrm{eff}}$, at the commensurate filling considered here the crossing appears in the ground state eigenenergy. This behavior has an important impact on the coupled cavity-atoms system, as already in the $T = 0$ MF approach the transition shows a strong bistable behavior at large interaction strength.

In past works, similar bistable behaviors have been observed around dissipative quantum phase transitions. Their appearance was typically attributed to the spontaneous breaking of a weak-symmetry [14, 32, 78, 91–96, 98, 99, 268], or the first order characteristics of the phase transition [18, 40, 82, 83, 86–90, 269, 270]. In first order transitions a hysteresis behavior can typically be observed within a mean-field approach. Depending on the nature of the initially prepared state, the system takes either of the competing phases. Taking quantum fluctuations around the mean-field solutions into account, the competing states usually resolve to metastable states [92, 101, 102, 271]. The mean-field bistable states admix and a unique steady state is recovered. Note that this is in contrast to the multiple stable steady states present in case of a strong symmetry of the system [103–106].

6.2.1 Self-ordering transition and bistable solutions

As for the quarter filled case we begin by considering the behavior of the steady state close to the self-ordering phase transition. We start by discussing the simpler $T = 0$ MF method and then proceed to identify changes caused

by the presence of fluctuations.

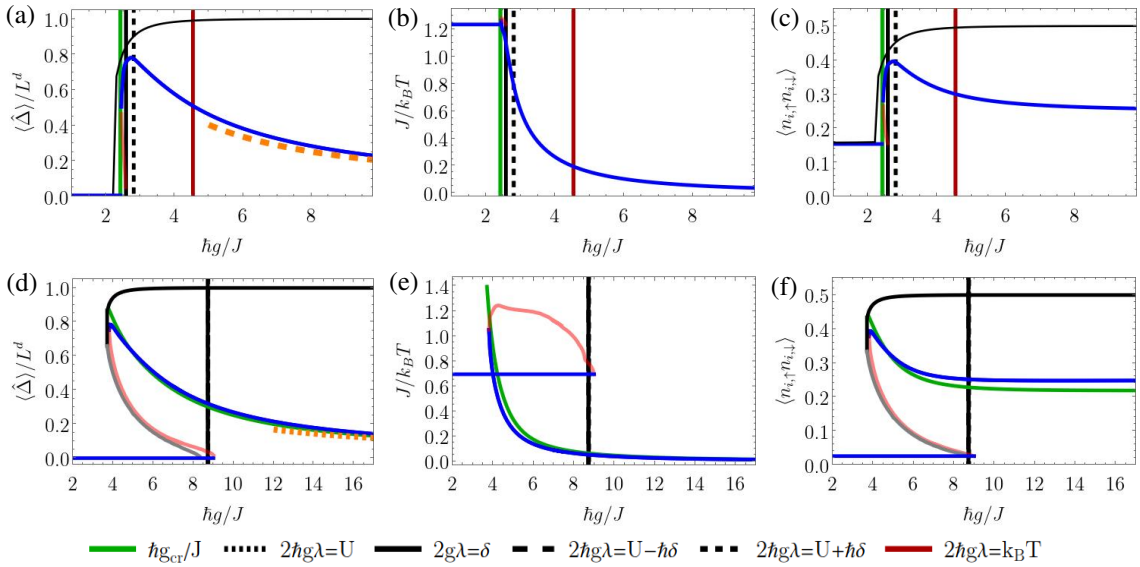

Fig. 6.13: Cuts of the (a),(d) sublattice imbalance $\hat{\Delta}/L$, (b),(e) inverse temperature β and (c),(f) average number of double occupancies as a function of atom-cavity-coupling $\hbar g/J$ at $\hbar\delta/J=4$; at half filling. We show the results from AE: stable (blue) and unstable (red); and the $T=0$ MF results: stable (black) and unstable (gray) for a finite system size $L=6$ and results in the thermodynamic limit in the weak tunneling perturbation (green points). The other parameters used are $U/J=8$, $\hbar\Gamma/J=1$. The orange dashed lines are the scaling from the analytical approximations for $U=0$ Eqs. (6.12) where a universal scaled photon number is expected.

Phase transition at $T=0$ mean field level

As expected the photon number, sublattice density imbalance and the average number of double occupancies take large values right above the transition to the self-ordered phase, that coincides with the onset of the bistability for sufficiently large on-site interactions. This is shown for intermediate interaction strength $U/J=2$ as well as larger interaction strength $U/J=8$ in Fig. 6.13. The result of the $T=0$ mean-field method is shown as a black line. Since at commensurate filling an ordering of the atoms coincides with the increase in the number of double-occupancies on the low-potential sublattice, both observables show similar behavior [see Fig. 6.13 (a),(c) or (d),(f)]. Both the sublattice imbalance and the average double occupancy approach their maximal value and the photon number rises very steeply with the coupling strength.

At the larger value of the on-site interaction strength, $U/J=8$, the bistable behavior appears above a critical coupling $g_{\mathrm{cr}}^{\mathrm{MF}}$, which can be seen in Fig. 6.13 (d)-(f) for $T=0$ MF. The two stable solutions are a trivial solution with homogeneous density distribution and empty cavity field (i.e. the Fermi-Hubbard model) and a solution with a self-ordered atomic state and finite occupation of the cavity mode (black points). Both are connected by a third, unstable solution (gray points). For the parameters shown in the plot, parts of the gray line are covered by the red line. In contrast to this we only observe a very narrow range of couplings where two stable solutions exist for interaction strength $U/J=2$ [see Fig. 6.13 (a)-(c)]. Lowering the on-site interaction further, bistable region continues to narrow until it becomes numerically difficult to detect. This can be seen in Fig. 6.12 (a), where the edges of the bistability are shown as a function of the on-site interaction U/J and atom-cavity coupling $\hbar g/J$. The $T=0$ mean field results are marked by the green hatched region. Contrarily, at large interaction strength the width of the bistable region increases. The onset of the bistability marks the self-ordering transition. This behavior can be connected to a change of the ground state of the effective ionic Hubbard model (introduced in Sec. 5.3.3). The nature goes from a Mott-insulating state at vanishing potential imbalance to a charge density wave in the self-ordered phase. Analogous to the ionic Hubbard model we expect this to occur around $2\hbar g\lambda\approx U$ for $U,\hbar g\lambda\gg J$, where λ is the stable self-ordered solution, that we will mostly concentrate on. The self-consistency

condition assuming maximal density imbalance $\langle\hat{\Delta}\rangle/L = N/L = n$ is given by

$$\frac{U}{2\hbar g} \sim \frac{2g\delta}{\delta^2 + (\Gamma/2)^2} n.$$

Resulting in a scaling of the critical coupling in the atomic limit of

$$g_{\text{cr}}^{\text{MF}} \approx \sqrt{\frac{U}{4n} \frac{\delta^2 + (\Gamma/2)^2}{\delta}}. \tag{6.13}$$

This approximation is shown as magenta dashed lines in Fig. 6.12 and fits the critical coupling obtained with ED reasonably well. While the scaling with the detuning and the dissipation agree with the ones determined at lower fillings [c.f. Eq.(6.3)], here an additional scaling with the interaction $\sqrt{U}$ is introduced.

Alternatively the bistability region can be determined using the stability condition derived in Eq. (3.33). Here, under the assumption that the branch connecting the two stable solution is generally unstable, the zero crossings of the stability condition roughly marks the edges of the bistability. This approach was evaluated numerically and agrees with our results obtained from solving Eq. (3.3) via ED up to some small deviations.

Influence of fluctuations in the atoms-cavity coupling on the phase transition

We continue to discuss the observed changes appearing around the self-ordering transition and bistable region when allowing for fluctuations in the atoms-cavity coupling and consequently the self-consistently determined finite temperature. More specifically, we identify similarities as well as new effects introduced by the fluctuations that drastically change the behavior in certain parameter regions.

The sublattice density imbalance behaves similar to the $T = 0$ MF one just above the self-ordering transition, that again coincides with the onset of the bistability at higher on-site interactions. At the critical coupling g_{cr} it steeply rises for $U/J = 2$ [see Fig. 6.13 (a)]. At larger interactions, $U/J = 8$, the bistable behavior emerges around $\hbar g/J \approx 3.8$, where a non-trivial stable steady state characterized by finite cavity field occupation and density imbalance appears [see Fig. 6.13 (d)]. At the bistability edge, the imbalance takes large values slightly below the one obtained for $T = 0$. We show the results obtained from solving Eq. (3.3) & (3.14) using ED for a finite size system. The stability of the solutions is the determined using Eq. (3.32), resulting in two stable solutions (blue points) connected by an unstable one (red points). We further include results obtained in the thermodynamic limit of the weak tunneling perturbation (see Sec. 3.2). To increase readability, we only show the non-trivial stable solution (dark green points) and omit the unstable solution connecting it to the normal phase. As demonstrated in Appendix A.2 the perturbative results hold also for higher dimensions of the external atomic sublattice. The bistability clearly prevails in both the finite size ED results and the perturbative limit. Its behavior looks similar to observations of so-called *dissipative first order* phase transitions [40].

While the close to the transition the fluctuations seem to only weakly alter the steady state, which is dominated by the contribution of the ground state of the effective Hamiltonian, their influence is still crucial for the description of the physical state. In the limit of vanishing cavity occupation, an effective finite temperature $k_B T \approx J$ induced by the coupling can be obtained [see Figs. 6.13 (b),(e)]. Consequently the system is in a mixed steady state, where contributions from states with below-maximal density ordering lower the expected density imbalance below the value obtained at $T = 0$. Comparing systems of equal size, the fluctuations in the atoms-cavity coupling shift the self-ordering transition to a slightly increased coupling strength at moderate detuning and low dissipation [compare green and black hatched regions in Fig.6.12 (a)]. The upper edge of the bistability is shifted in a similar way. Intuitively, one can understand this effect by considering that small density orderings are destroyed by the finite temperature and therefore can not be amplified by an emerging cavity field. This prevents the self-ordering transition for a range of couplings $g_{\text{cr}}^{\text{MF}} \leq g \leq g_{\text{cr}}$.

We complete our discussion of the phase transition by looking at the dependence of the critical couplings and width of the bistability region on the systems parameters, namely the on-site interaction strength U/J, the pump-cavity detuning $\hbar\delta/J$ as well as the dissipative losses $\hbar\Gamma/J$.

In Fig. 6.12 (a)] we show how the onset of the bistability behaves with the interaction strength. The critical couplings and scaling of the bistability width with U/J shows to be qualitatively the same for both the $T = 0$ mean field method and the many-body adiabatic elimination approach [see Fig. 6.12 (a)]. Therefore, the critical

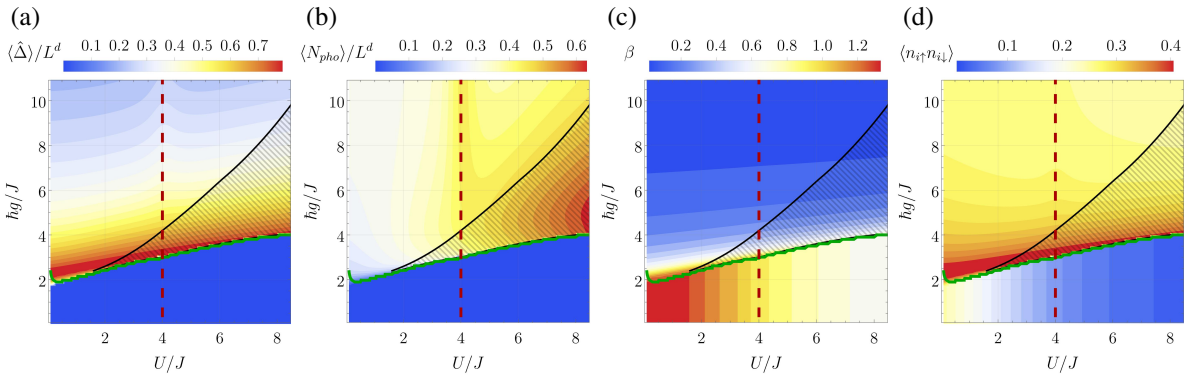

Fig. 6.14: (a) Sublattice imbalance $\hat{\Delta}/L$, (b) Scaled photon number N_{pho}/L^d, (c) inverse temperature β and (d) average number of double occupancies as a function of atom-cavity coupling $\hbar g/J$ and on-site interaction U/J of a finite size system $L=6$ at half filling. The other parameters used are $\hbar\delta/J=4$, $\hbar\Gamma/J=1$. The hatched region marks the fluctuation-induced bistability region at the transition to the self-organized phase.

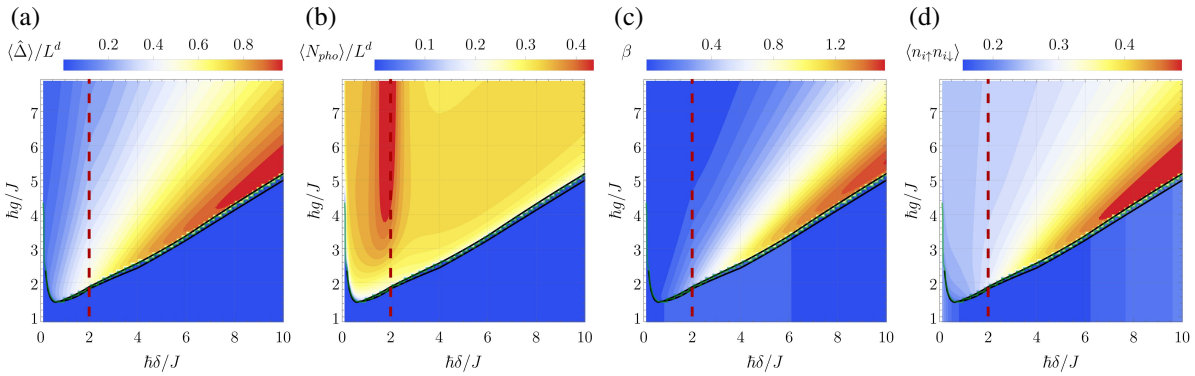

Fig. 6.15: (a) Sublattice imbalance $\hat{\Delta}/L$, (b) Scaled photon number N_{pho}/L^d, (c) inverse temperature β and (d) average number of double occupancies as a function of atom-cavity coupling $\hbar g/J$ and detuning $\hbar\delta/J$ of a finite size system $L=6$ at half filling. The other parameters used are $U/J=2$, $\hbar\Gamma/J=1$. The hatched region marks the fluctuation-induced bistability region at the transition to the self-organized phase.

coupling derived in Eq. (6.13), which scales with $\hbar g_{\text{cr}} \propto \sqrt{U}$ in the limit of large interactions matches both regions reasonably well. This observation is in contrast to the case of lower fillings, where the self-ordering transition only showed very weak dependence on the interaction strength [see Sec. 6.1.1].

At half filling, the self-ordering transition is forcibly accompanied by the creation of doubly occupied sites in order to form a charge density wave, underlining the importance of the many-body character of our system at the phase transition. For the self-organization process the system needs to overcome the interaction energy. Therefore, the critical coupling strength increases with U/J. The increase of the region with two stable solutions, the normal phase and phase with finite sublattice density imbalance grows on faster than on a linear scale [as seen in Fig. 6.12 (a)]. In this sense it is not surprising that we observe a significant increase in the width of the bistability with U/J. In the opposite limit, we can identify a critical interaction strength U_{cr}/J below which the width of the bistability becomes smaller than our numerical accuracy of 10^{-5} in the coupling. These features are nicely visible in Fig. 6.14 (a),(d), where we show the density imbalance and average number of double occupancies across the phase diagram, varying U/J and $\hbar g/J$. For all presented density plots we show the non-trivial self-ordered solution in the bistable region that is marked as a hatched region.

We continue by considering the dependence of the critical coupling g_{cr} and the bistability width on the pump-cavity detuning $\hbar\delta/J$ [Fig. 6.12 (b)]. As for the on-site interaction strength, the critical coupling g_{cr} increases as δ rises. However, the underlying processes are fundamentally different, as we directly see from the difference in the scaling with and without considering fluctuations in the coupling. The critical coupling derived in Eq. (6.13)

nicely captures the observed transition in the $T=0$ mean-field method. At large detuning δ it is seen to rise as $\sqrt{\delta}$, with the upper edge of the bistability exhibiting the same scaling. The bistability region retains an approximately constant width varying δ. The scaling with the detuning changes when including the fluctuations. A faster increase of the critical coupling with $\hbar\delta/J$ is observed. In parameter regimes where $\hbar\delta/J$, becomes the largest energy scale in the system, the critical coupling strength grows almost linearly with $\hbar\delta/J$ similar to the scaling found at lower fillings. This consequently leads to an growing shift $\left|g_{\mathrm{cr}}-g_{\mathrm{cr}}^{\mathrm{MF}}\right|$ between the critical couplings obtained in the two approaches at large $\hbar\delta/J$. We accredit this effect to a large self-consistently temperature approaching the normal phase $\lambda\to 0$ [see Figs. 6.13 (b),(e) & 6.15 (c)]. These observations further validate the necessity to go beyond the standard mean field approach to describe the atoms-cavity coupled system. We refrain from discussing the limit of small detuning since our method assumes a coherent steady state cavity field, which might not be fulfilled in this regime.

The dissipation strength Γ also influences both the critical coupling and width of the bistability. In the limit of vanishing $\hbar\Gamma/J$, the onset of the bistabilities in mean field and adiabatic elimination results agrees up to a small shift [black and green hatched region in Fig. 6.12 (c)]. The self-consistently determined temperature in this regime is typically small compared to the excitation gap, which scales as U/J and thus only weakly influences the transition point.

Increasing the dissipation the extension of the bistability in direction of the coupling slightly increases for the $T=0$ MF result. Contrarily, including the fluctuations a larger value of Γ causes a drastic decrease in the width of the bistability region [Fig. 6.12 (c)]. This opposite behavior can be connected to the observed rise in the effective temperature in the limit of large dissipation Γ and increasing disorder in the atomic system [see blue points in Fig. 6.17 (c)]. This leads to a growth of g_{cr} at a faster rate than in the $T=0$. The same does not apply to the coupling that marks the upper edge of the bistability. Here, both methods show a similar behavior in the limit of large dissipation. Therefore, the width of the bistability in the AE approach continues to decrease until at around $\hbar\Gamma_{\mathrm{cr}}/J\sim 18.3$ within numerical accuracy no bistability can be detected anymore. This behavior shows similarities to observations made in Ref. [270] for a different model. They claim to identify an ordering phase transition with first-order characteristics which becomes continuous at a critical point in the large dissipation limit.

After this extensive discussion of the self-ordering transition and the bistability, we conclude this section by looking at effects that are caused by the fluctuations within the ordered phase.

Influence of fluctuations in the atoms-cavity coupling within the self-ordered phase

At the $T=0$ MF level, as the coupling strength increases $g\geq g_{\mathrm{cr}}^{\mathrm{MF}}$, the imbalance and double occupancy saturate at their respective maximal value, while the photon number increases quadratically [see black curves in Fig. 6.13]. Varying the coupling strength above the self-ordering transition using the any-body adiabatic elimination method, the density imbalance develops a small maximum which is followed by a decrease at large coupling strength and strong interactions [see Fig. 6.13 (d)]. Looking at a smaller value of the on-site interaction, the maximum is shifted further away from the self-ordering transition [see Fig. 6.13 (a)]. The double occupancy behaves correspondingly. We can understand this analogous to the previously discussed lower filling (Sec. 6.1.1). Just above the critical coupling g_{cr} the finite cavity field solution stabilizes at a minimum of the effective temperature [see Figs. 6.13 (b),(e)]. This leads to an increase in the atomic order. The minimum is followed by a quick rise in the effective temperature. The heating results in the reduced sublattice imbalance at larger coupling strength. The same behavior prevails over a large parameter range. The maximum in sublattice density imbalance and double occupancies close to the self-ordering transition and minimum in the effective temperature around the same parameters can be seen in Fig.6.14 & 6.15. The largest value reached when following the maximum increases with δ, which is directly connected to the minimum in the temperature that decreases with δ [see Figs.6.15 (a),(c)]. In the photon number no maximum can develop due to its strong increase with the coupling which prevents the decrease of the cavity field until much larger temperatures are reached [see Figs.6.15 (b)].

Similar to lower fillings a saturation of the photon number at large couplings $\hbar g/J$ in the high temperature regime can be observed. Its matches the general behavior predicted for $U/J=0$, derived in Eq. (6.12). The equations obtained for $U/J\to\infty$ do not hold at half filling since the bands would be completely filled and no dynamics would be possible. We thus show the corresponding scaling for $U/J=0$ of $\langle\hat{\Delta}\rangle\propto g^{-1}$ [orange dashed line in Fig. 6.13 (a),(d)], $\langle\hat{\Delta}\rangle\propto\delta$ [Fig. 6.16 (a),(e)] as well as the scaling with Γ [Fig. 6.17 (a)]. Here we explicitly show the scaling, not the absolute values given by Eq. (6.12), since the finite value of U/J leads to an altered prefactor

of the curve for $U \gg \hbar\delta, \hbar\Gamma$. This however seems to leave the scaling unchanged.

Finally, we want to point out the cooling resonance $U = \hbar\delta$. Its effect is especially striking in the photon number, where a clear maximum appears [dashed red line in Fig. 6.14 and Fig. 6.14]. An explanation of the effect was provided in Sec. 6.1.3.

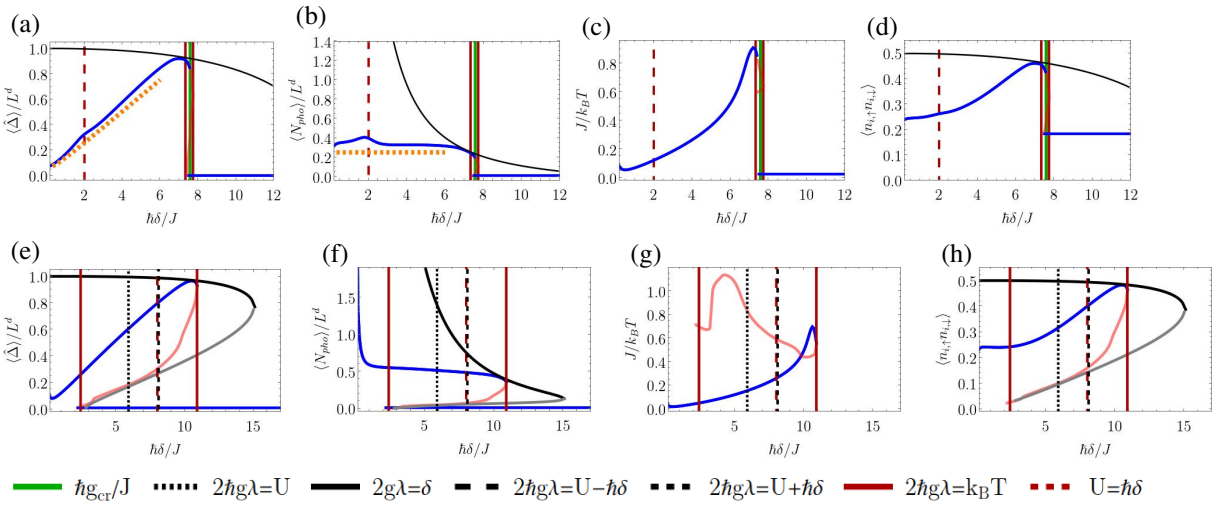

Fig. 6.16: Cuts of (a),(e) sublattice imbalance $\hat{\Delta}/L$, (b),(f) scaled photon number N_{pho}/L^d, (c),(g) inverse temperature β and (d),(h) average number of double occupancies as a function of $\hbar\delta/J$ of a finite size system $L = 6$ at half filling. We show the results from AE: stable (blue) and unstable (red); and the $T = 0$ MF results: stable (black) and unstable (gray). The other parameters used are $\hbar\Gamma/J = 1$ and (a)-(d): $U/J = 2$, $\hbar g/J = 4$; (e)-(h): $U/J = 8$, $\hbar g/J = 7$. Vertical lines denote resonances in the atomic limit. The orange dashed lines are the scaling from the analytical approximations for $U = 0$ Eqs. (6.12) where a universal scaled photon number is expected.

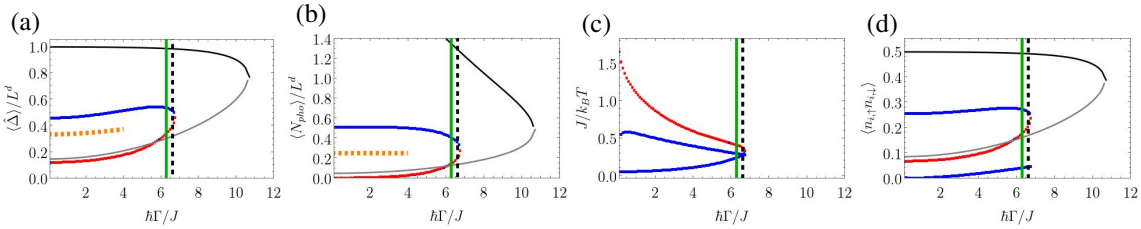

Fig. 6.17: Cuts of the (a) sublattice imbalance $\hat{\Delta}/L$, (b) scaled photon number N_{pho}/L^d, (c) inverse temperature β and (d) average number of double occupancies as a function of $\hbar\Gamma/J$ at $\hbar g/J = 6$ of a finite size system $L = 6$ at half filling. We show the results from AE: stable (blue) and unstable (red); and the $T = 0$ MF results: stable (black) and unstable (gray). The other parameters used are $U/J = 8$, $\hbar\delta/J = 4$. Vertical lines denote resonances in the atomic limit. The orange dashed lines are the scaling from the analytical approximations for $U = 0$ Eqs. (6.12) where a universal scaled photon number is expected.

In the ionic Hubbard model an interesting phase is the bond-order phase expected for the parameter regime $2\eta \sim U$. However, in our case this parameters correspond to the parameter regime $2\hbar g\lambda \sim U$, which is typically within the unstable solution determined by the self-consistency condition. Furthermore, due to the finite self-consistent temperatures we obtain here, which broaden the features in the observables used for the detection of the phase, e.g. $k_B T/J \sim 3$, we cannot distinguish it for the system sizes we consider [see Fig. 5.4].

Until here, we provided an extensive discussion of the phase diagrams at both quarter-and half filling where in the latter we focused on the bistability at the self-ordering transition. As mentioned, at lower fillings a bistability can also be found *within* the self-ordered phase, that has a fundamentally different nature. We want to provide a detailed analysis of this novel mechanism in the following section.

6.3 Fluctuation-induced bistability

In this section we present and analyze a novel mechanism, we call the *fluctuation-induced bistability* and first described in Ref. [1]. We encounter this phenomenon within the self-ordered phase of our *dissipative* quantum many-body system when considering fluctuations around a $T=0$ mean-field solution. Note that the here presented system of spinful interacting fermions confined to optical lattices and transversely coupled to a dissipative cavity field can be seen as a paradigmatic example. We believe that the observations made for this open system can be generalized to a large class of atoms-cavity models with comparable atomic and photonic energy scales. As an argument towards the generality of the mechanism, we provide proof the fluctuation-induced bistability exists independent of the dimensionality of the atomic gas. Further we show its presence in an equivalent system with bosonic atoms, which will be discussed in Sec. 6.3.1].

To start we provide some context on bistabilities that are a fascinating effect that has attracted great research interest for many years. The emergence of a bistability of a system i.e. that it can reach two stable steady states, has been observed under a multitude of circumstances in nature. Which state the system evolves to might be influenced by multiple factors like the previous dynamics or the preparation of the initial state. The resulting high sensitivity of the system dynamics to the initial conditions and external perturbations can cause profound changes in the overall behavior of the system. A well known bistability in cavity systems is the optical bistability [81], that is characterized by the emergence of two stable states with different light intensities. For fermionic atoms in optical cavities optomechanical interactions of the cold atomic gas coupled to an optical cavity field [78] can induce a non-linearity to appear around the BEC-BCS crossover [24, 44]. Bistable behaviors emerging in the vicinity of a dissipative phase transition are typically ascribed to the first order character of the transition [18, 40, 82–87, 90], or to the spontaneous breaking of a weak-symmetry [14, 32, 91, 95, 98, 99]. If it behaves as a first order transition often a hysteresis behavior in the dynamics across the phase transition is observed. The transition point between the two competing phases depends on the initially prepared state and parameter protocol.

In most of these cases the bistability is only obtained within a mean-field approach. Considering quantum fluctuations around the mean-field solutions the competing bistable states resolve to meta-stable states [92, 100–102] that are admixed in the density matrix, leading to a unique steady state in the dissipative quantum dynamics. This partly matches our observations of the bistability at the self-ordering transition that appears in our system at half filling [see Sec. 6.2] that narrows as the dissipation becomes large.

This is to be differentiated from multiple stable steady states observed within each symmetry sector in the presence of a strong symmetry of the dissipative system [103–106]. For instance fluctuations don't always counteract bistability. There are cases where fluctuations have been shown to change the nature of a phase transition from second-order to a first-order character. This has been observed in equilibrium, for classical setups or systems that can be described by Ginzburg-Landau type theories like superconductors or magnets [107–111].

Here we want to present the novel mechanism that not only prevails when including the fluctuations in the atom-cavity coupling, but fundamentally depends on them and thus is not present at the $T=0$ MF level. It is therefore fundamentally different from the ones observed in $T=0$ MF methods, which rely on a change in the ground state of the respective model. Contrarily the fluctuation-induced bistability is solely determined by the excited eigenstate spectrum of the effective Hamiltonian.

Solving the system for the steady states using the many-body adiabatic elimination approach at quarter filling ($n=1/2$) we obtain a very rich steady state phase diagram. Many of the intriguing effects entering due to the mixed state character of the steady state, like cavity cooling as well as many-body cooling effects have already been discussed in Sec. 6.1.

We start with a general look at the development of the cavity field occupation with the coupling strength at large on-site interaction $U/J=40$ [see Fig. 6.18]. At low pump power g the system is in the normal phase, with a vanishing photon number. Above a critical value g_{cr} the transition to the self-organized phase occurs, signaled by the emergence of a finite cavity field as the atoms partly order on the low-potential sublattice. Increasing the coupling strength further, well inside the self-ordered phase a novel type of bistability occurs, the *fluctuation-induced bistability* [1].

Within a region of the atoms-cavity coupling $g \in (g_{\text{bi},1}, g_{\text{bi},2})$ (blue hatched region), two stable solutions are found solving the system of Eqs.(3.3) & (3.14). They are characterized by different finite values of the cavity order

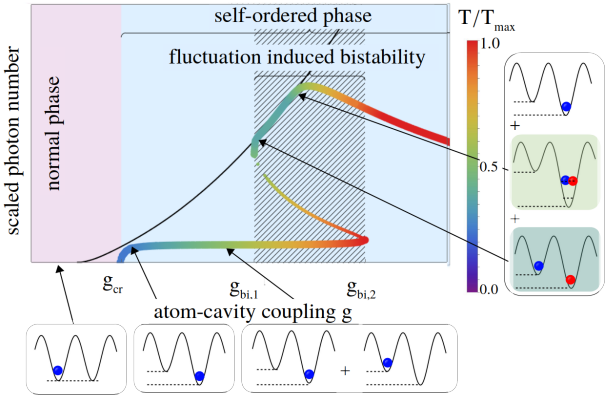

Fig. 6.18: Scaled photon number N_{pho} as a function of atom-cavity coupling g. The color of the points represents the effective self-consistently determined temperature T/T_{max}. The black line is the atom-cavity mean-field result ($T=0$ MF). The sketches highlight the dominant occupations contributing to the different steady states. The the sketches show the ground state and dominant excited state admixed by the self-consistent effective temperature on a unit cell. ©2025 Phys. Rev. Lett. [1].

parameter and a corresponding self-consistently determined temperature. The two stable solutions are connected by a third unstable one that we include with smaller dots in Fig. 6.18. As stated above, the bistable behavior can not be observed at the $T=0$ mean-field level (black line, Fig. 6.18), where a unique solution prevails throughout the self-ordered phase.

To emphasize the varying effect of fluctuations and the resulting effective temperature on the two stable solutions within the bistability region, we include the respectively obtained temperature as a color scale of the points. It is scaled with respect to the maximal obtained temperature in the shown parameter region. From this it becomes apparent, that the solution at higher cavity field occupation has the lower effective temperature at equal coupling strength. Since the two solutions are characterized by the pair of parameters (λ_1,β_1) and (λ_2,β_2), it is sensible to assume that the bistability relies on the determination of the effective temperature by considering the energy flow between the atoms and the cavity. This is confirmed by fixing the temperature externally to various different values and solving the self-consistency condition Eq. (3.3) with respect to the set thermal state. As expected a single stable solution is obtained for all shown constant temperatures, the bistability is not present [see in Fig. 6.20].

In each solution of the fluctuation-induced bistability, the emerging cooling mechanisms play a significant role for the weight of the individual eigenstates of the effective Hamiltonian in the steady state. The two stable solution have different physical properties that are determined by the excitation spectrum of $\hat{H}_{\text{eff}}$. More specifically, the competition between the global range interaction mediated by the cavity field and atomic on-site interactions is of importance for the emergence of the bistability. The solution that captures the emerging cavity field from the self-ordering transition is determined by (λ_1,β_1) and has the lower scaled photon number of the two stable steady states. The self-consistent dissipative dynamics towards the steady state are dominantly driven by transitions between eigenstates of $\hat{H}_{\text{eff}}$, that are connected by single-particle hopping processes as sketched in Fig. 6.9 (a), generally accompanied by a change in the cavity field occupation. An atom hops from a singly-occupied site to a neighboring empty lattice site, resulting in an energy change of $E_n - E_m \approx 2\hbar g\lambda_1$ in the atomic subsystem. The cavity cooling resonance introduced in Sec. 6.1.2 can typically also be found in this solution. Within this first solution, the temperature rises quickly with the coupling strength, resulting in the observed saturation of the photon number to a constant value. Contrarily the second solution (λ_2,β_2) that appears at the lower edge of the bistability $g_{\text{bi,1}}$ we observe a higher occupation of the cavity field and lower effective temperature. In this solution the processes with the largest contributions to the balance in the steady state stem from transitions in the excited spectrum between states with a change in the number of double occupancies [see Fig. 6.9 (b)]. An atom hops i.e. from a singly occupied site on the high-potential sublattice to a neighboring site that is already occupied by a fermion of opposite spin, creating a double-occupancy on the low potential sublattice. This causes an energy change in the atomic subsystem of $E_n - E_m \approx 2\hbar g\lambda_2 - U$ that can be compensated by the cavity field. Therefore the many-body nature of our interacting system is crucial for the appearance of this high-cavity field solution. The relatively low temperature around the onset can be understood when considering the many-body cooling

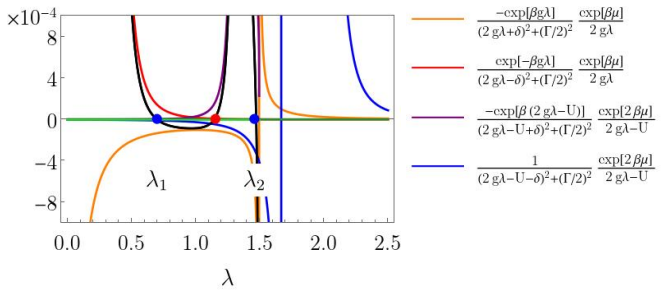

Fig. 6.19: Individual terms of Eq. (3.25a) and full equation [black line] at $\hbar g/J = 12$, $U/J = 40$, $\hbar\delta/J = 8$, $\hbar\Gamma/J = 1$ in the thermodynamic limit at quarter filling. The system of equations has two stable [blue points, $\lambda_{1(2)}$] and one unstable [red point] solutions at the zero crossings of the black line.

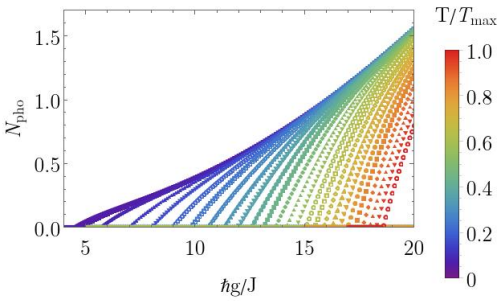

Fig. 6.20: Solution of the system of equations Eqs. (3.25) with fixed values of $k_B T = 1/\beta$ varying $\hbar g/J$ at $U/J = 40$, $\hbar\delta/J = 8$, $\hbar\Gamma/J = 1$, $k_B T_{\mathrm{max}}/J = 25$ in the thermodynamic limit at quarter filling. ©2025 Phys. Rev. Lett. [1] Supplemental

resonances [see Sec. 6.1.3 for details] that are typically occurring within the bistable region for the here considered parameters. The efficient transfer of energy from the atoms to the cavity mode drives the atoms to a steady state with a much lower temperature.

´

Now we present some more quantitative observables obtained for a small one-dimensional system $L = 8$ at quarter filling that can be solved using exact diagonalization to determine the eigenspectrum of $\hat{H}_{\mathrm{eff}}$ and self-consistently solve Eqs. (3.3) & (3.14). The two stable solutions, which we label by their cavity field order parameter $\lambda_{1(2)}$ with lower (higher) cavity field are depicted with blue points in Fig. 6.21. The connecting unstable branch, that usually exhibits a decrease in the cavity occupation when increasing the coupling, is shown in red. One however needs to be careful when determining the stability since the decrease of N_{pho} with larger couplings can also stem from temperature effects. Therefore, one needs to employ the stability criterion derived for thermal steady states given in Eq. (3.32).

As can be seen in the unstable branch in Fig. 6.21, finite size effects that arise in the small exactly solvable systems can lead to added solutions within the bistability region. This stems from energy shifts in the states involved in the resonant transitions from finite size effects and higher order hopping processes. The spectrum can no longer be separated into clean bands, but rather the individual bands are broadening and begin to overlap. This interpretation is supported by the observed strong system size dependence of the additional solutions and the fact, that they are not present in the thermodynamic limit in the weak tunneling perturbation [darker green (stable) and green (unstable) points in Fig. 6.21]. In this limit, all state configurations with the same overall density imbalance and number of doubly occupied sites are degenerate in energy. Since we are mostly interested in the stable solutions, we will not get into more detail of this observation here. For the stable steady states, both the finite size systems and thermodynamic limit in the weak tunneling perturbation show the same qualitative behavior, including the emergence of a multi-stable region caused by resonances with the excited spectrum of the effective Hamiltonian, which provides a strong argument that the fluctuation-induced bistability is not a feature of the perturbative approach.

From here we want to focus on the thermodynamic limit solution, as described in Sec. 3.2, since the energy spectrum is cleaner and allows for an easier interpretation of the resonances in the atomic limit. Further we can identify the dominant heating/cooling terms that contribute to the dynamics towards the respective steady state in each of the stable solutions. The weak tunneling perturbation typically holds in the parameter region where the fluctuation-induced bistability appears. Further, since the obtained solutions are valid for higher lattice dimensions, it permits us to generalize our findings beyond one dimensional atomic systems. Since similar equations of motion could be derived for a larger class of models within this perturbation theory, which we show exemplarily for interacting bosonic atoms coupled to the cavity field in Sec. 6.3.1, it can be implied that the bistability we observe is an effect that is not only a particularity of our model.

As a reminder, the steady state condition of the energy transfer equation in the approximation, Eq. (3.25) was given

by

$$\frac{\partial}{\partial t}\langle \hat{H}_{\text{eff}}\rangle \propto J^2\Bigg[\left(\frac{-\exp(\beta\hbar g\lambda)}{(2\hbar g\lambda+\hbar\delta)^2+(\hbar\Gamma/2)^2}+\frac{\exp(-\beta\hbar g\lambda)}{(2\hbar g\lambda-\hbar\delta)^2+(\hbar\Gamma/2)^2}\right)\frac{e^{\beta\mu}+e^{\beta(3\mu-U)}}{2\hbar g\lambda}$$
$$+\left(\frac{-\exp[\beta(2\hbar g\lambda-U)]}{(2\hbar g\lambda-U+\hbar\delta)^2+(\hbar\Gamma/2)^2}+\frac{1}{(2\hbar g\lambda-U-\hbar\delta)^2+(\hbar\Gamma/2)^2}\right)\frac{e^{2\beta\mu}}{2\hbar g\lambda-U}$$
$$+\left(\frac{-\exp[\beta(2\hbar g\lambda+U)]}{(2\hbar g\lambda+U+\hbar\delta)^2+(\hbar\Gamma/2)^2}+\frac{1}{(2\hbar g\lambda+U-\hbar\delta)^2+(\hbar\Gamma/2)^2}\right)\frac{e^{2\beta\mu}}{2\hbar g\lambda+U}\Bigg]\overset{!}{=}0$$

We plot the left hand side of this equation as well as the individual terms as a function of λ for fixed values of the parameters within the bistable region in Fig. 6.19. Here we used some approximations for the particle number equation Eq. (3.25b) that we empirically confirm to be valid for the here presented parameters [see Appendix B.1.1 or Supplemental of [1]]. We find an expression for the chemical potential $\mu \approx \log(1/2)/\beta$ and use the expression for the temperature Eq. (6.8). This allows us to show the energy transfer Eq. (3.25) as a function of the cavity field order parameter λ. The steady state solutions are approximately given by the λ for which the energy transfer function has a zero crossing [black line]. In Fig. 6.19 this expectedly results in the two stable solutions $\lambda_{1(2)}$ (blue points) with one unstable solution (red point) in between. This allows us to get an intuition which terms in the energy transfer equation dominantly contribute and are the most important in determining the solutions.

In the plot we can nicely identify the most relevant terms and corresponding processes at each of the solutions. For the λ_1-solution with the lower cavity field the dynamics toward the self-consistent steady state is mostly captured by the first line terms in Eq. (3.25a). These describe processes between states with single site occupations on the lower or upper potential sub-lattice, that do-not include double occupancies. In this parameter region, on-site interactions are high in energy compared to the single particle excitations to the high-potential sublattice. Consequently, they can be effectively eliminated from the system dynamics by reducing the description to the low-energy sector or taking the limit $U \to \infty$. More specifically, the dominant heating process is described by $\propto 1/((2g\lambda-\delta)^2+(\Gamma/2)^2)$ [dark orange line in Fig. 6.19] while the main cooling process can be accounted to the term $\propto 1/((2g\lambda+\delta)^2+(\Gamma/2)^2)$ [light orange line]. The other terms are vanishing around λ_1. For the λ_1-solution the heating and cooling balances at a relatively high temperature $k_B T_1/J > 8z$. Here, the lattice coordination number z permits to adapt the scaling to higher dimensions. The high temperature matches our observations in Fig. 6.21 (b). The inverse temperature $\beta_1 J$ quickly decreases from the self-ordering transition until the λ_1-solution disappears. Due to the high temperature and reduced density imbalance in the relevant excitations, the λ_1 solution quickly saturates to an almost constant value when increasing the coupling strength within the bistability region. This behavior is nicely described by the universal scaled photon number derived for the $U \to \infty$-limit in Eq. (6.9), including the corresponding scaling of the imbalance given in Eq. (6.10) with $\langle \hat{\Delta}\rangle \propto g^{-1}$ [orange dashed lines in Fig. 6.21 (a),(c)]. All of these observations match the previous interpretation of the finite-size system.

We now want to repeat these considerations for the second stable solution λ_2. Here, in contrast to the previous case, states with either two neighboring singly occupied sites or a double occupancy on the low-potential sublattice are crucial in the dynamics towards the steady state. They are described in the second line of Eq. (3.25a) $\propto 1/((2g\lambda\text{–}U\pm\delta)^2+(\Gamma/2)^2)$ [purple/blue line in Fig. 6.19]. Contributions from states that feature a double occupancy in the high potential sublattice however remain high energy states throughout the considered parameter region and thus have vanishing weight in the sum. This concerns the terms $\propto 1/((2g\lambda+U\pm\delta)^2+(\Gamma/2)^2)$, which are described in the third line of Eq. (3.25a) [light/dark green line in Fig. 6.19]. In contrast to the λ_1-solution, where typically $2\hbar g\lambda_1 \ll U$ is fulfilled, the cavity-induced density-order, which can be seen in Fig. 6.21 (c), and the effective sublattice potential are of order U. Therefore, in this regime, we are close to a resonant energy transfer between the atoms and cavity that involves the many-body character of the atomic system. The described processes drive the atoms to a steady state with a much lower self-consistently determined temperature $1/\beta_2$ compared to the one obtained in the first solution. We partly account this to the many-body cooling mechanism that we described in Sec. 6.1.3. The many-body resonances that enable an efficient transfer of energy from the atoms to the cavity mode, while increasing the atomic occupation of the low-potential sublattice. Within the fluctuation-induced bistability, the resonance conditions, that are given by $2g\lambda_2 = U\pm\delta$ in the atomic limit, are typically fulfilled in the λ_2-solution. Further, the energy gap between the ground state and low lying-excited states in the atomic spectrum is increasing in $g\lambda$ and consequently in the λ_2 solution the overall weight of atomic state configurations besides the ground state of $\hat{H}_{\text{eff}}$ in the steady state are suppressed compared to the λ_1-solution.

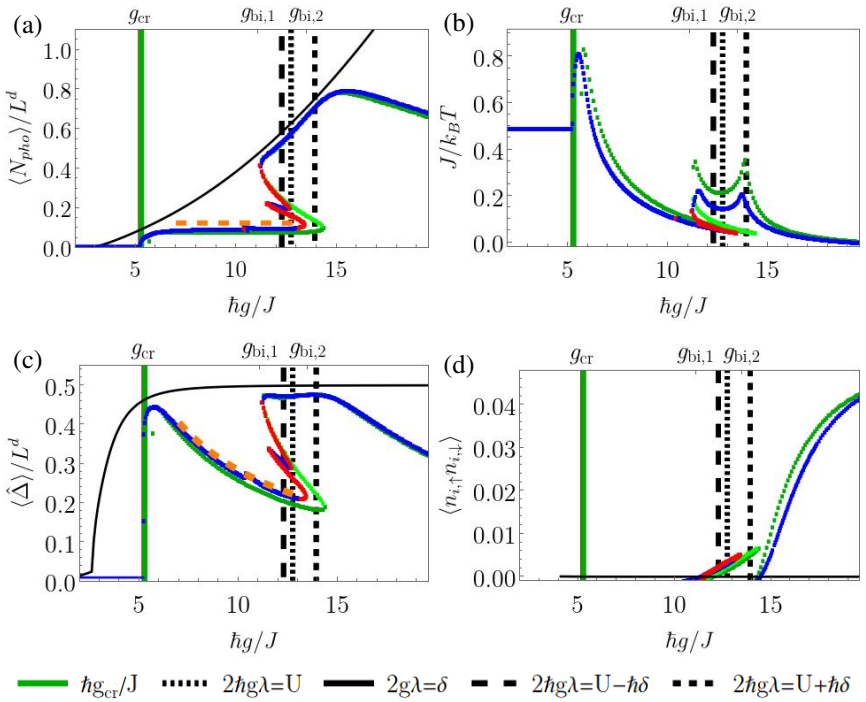

Fig. 6.21: Cuts of the scaled photon number, inverse temperature β, sublattice imbalance $\hat{\Delta}/L$ and average double-occupancy as a function of atom-cavity-coupling $\hbar g/J$ at $U/J = 40$; of a finite size system $L = 8$ stable (blue) and unstable (red); in the thermodynamic limit at low hopping Eqs. (3.25) stable (dark green) and unstable (green) at quarter filling. The other parameters used are $\hbar\delta/J = 8$, $\hbar\Gamma/J = 1$. Lines denote parameter resonances in the atomic limit. The orange dashed lines are the analytical approximations for $U \to \infty$ Eqs. (6.10) where a universal scaled photon number is expected.

As the coupling strength is increased further, the low λ_1-solution becomes unstable and the bistability disappears, with only the λ_2-solution prevailing [around $\hbar g_{\mathrm{bi},2}/J = 13.5$ in Fig. 6.21].

The emergence of the fluctuation-induced bistability and width of the region where it is present depend in different ways on the external system parameters U/J, $\hbar\delta/J$ and $\hbar\Gamma/J$. We show this dependence in the simplified phase diagrams in Fig. 6.22. Note, that a detailed discussion of the dependence of the critical couplings $\hbar g_{\mathrm{cr}}/J$, which is marked by the green line separating the purple and blue regions, on the parameters was provided in Sec. 6.1.1.

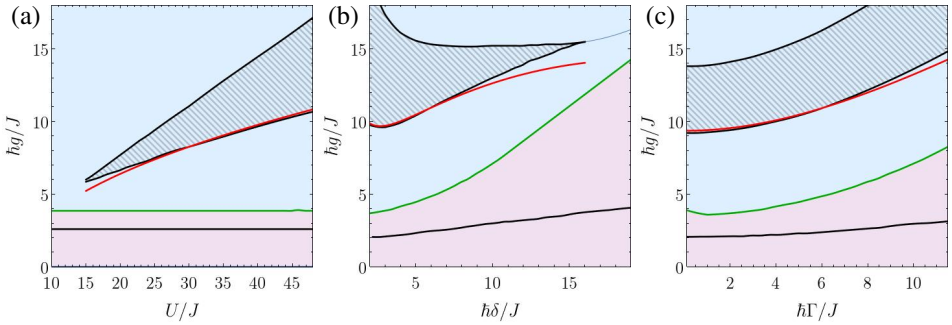

Fig. 6.22: Simplified phase diagrams varying the atom-cavity coupling $\hbar g/J$ and (a) the on-site interaction U/J at $\hbar\delta/J = 5$, $\hbar\Gamma/J = 3$; (b) the pump-cavity detuning $\hbar\delta/J$ at $U/J = 40$, $\hbar\Gamma/J = 5$; (c) the dissipation rate $\hbar\Gamma/J$ at $\hbar\delta/J = 5$, $U/J = 40$ in the thermodynamic low hopping limit $L \to \infty$ at quarter filling. The red line marks the onset of the bistability approximated by Eq. (6.14), derived in Appendix B.1.1. The lower black line in the purple region marks the critical coupling $\hbar g_{\mathrm{cr}}^{\mathrm{MF}}$ obtained for the $T = 0$ MF approach. (a),(b) adapted from [1].

The bistability region shows a width that grows with the on-site interaction U/J [Fig. 6.1 (a)]. Fixing the detuning $\hbar\delta/J$ the couplings at which the cooling resonances appear are determined by U/J, which directly influences the appearance of the bistability. In the limit of large U/J we derive an approximate expression for lower onset of the bistability $g_{\mathrm{bi},1}$ from Eq. (3.25) [see Appendix B.1.1 or Supplemental of Ref. [1]]. The chemical potential is observed to scale approximately as $\mu \approx -\log(2) k_B T$, independent of the cavity field parameter λ. Replacing μ in the self-consistency equation with the found expression, it can be solved for the temperature. Inserting both into the energy-transfer equation Eq. (3.25a) and performing some further approximations we finally obtain an approximation of the coupling marking the onset of the bistability [red line in Fig. 6.22]

$$g_{\mathrm{bi},1} = \sqrt{(U/\hbar - \delta)\left[(\Gamma/2)^2 + \delta^2\right]/(2\delta)}. \tag{6.14}$$

The obtained scaling with $\sim \sqrt{U}$ in the large interaction limit emphasizes the different nature of the processes that cause the bistability from those that induce the self-ordering transition. The critical coupling g_{cr} is almost U/J-independent throughout the interaction range where the bistability is observed. The upper edge of the bistable region $g_{\mathrm{bi},2}$ increases approximately linearly with U/J, resulting in a growth of the width of bistable region with the on-site interactions.

If we instead consider the dependence on the detuning [see Fig. 6.1 (b)], increasing δ leads to a narrowing of the bistability region, until it ultimately vanishes as its width gets beneath the numerical accuracy in the coupling $\sim 10^{-5}$. The scaling of the lower edge $g_{\mathrm{bi},1}$ with δ agrees approximately with that of the self-organization transition. In contrast the upper edge is observed to be almost independent of the detuning for large δ.

Varying the dissipation [Fig. 6.8 6.1 (c)] in the regime where $U \gg \hbar\Gamma$, both coupling strengths $g_{\mathrm{bi},1(2)}$ marking the edges of the bistability increase with a similar scaling as the critical coupling strength. It looks to follow an approximately quadratic scaling for intermediate dissipation. Since the dissipation is observed to affect both edges in a similar way, the extension of the bistability region is almost independent of Γ.

Our observations in the simplified phase diagram are complemented by quantitative measurements of a few observables that characterize the physical state of the system varying the on-site interaction and the coupling [see Fig. 6.23]. Note, that within the hatched bistability region the observable measurements corresponding to the large cavity-field λ_2-solution are shown. Here we further demonstrate the good agreement of the results obtained in the thermodynamic low hopping limit with the exact diagonalization results for finite system size $L = 8$. While the shown measurements for $U/J \leq 8$, where the perturbation in kinetic energy will not hold, are calculated from

solving Eqs. (3.3) & (3.14) for large U/J we instead use Eqs. (3.25). The two regimes are separated by the double black vertical lines in the plots. While some of the resonance lines and the self-ordering transition are lightly shifted overall the qualitative behavior remains consistent switching from one method to the other. We expect even better agreement going to very large U/J, as i.e. in Figs. 6.21. The largest mismatch between the perturbative result and the full effective model appears in the double occupancies Fig. 6.21 (d). While this effect might appear the most prominent in this observable due to the overall very low density of doubly-occupied sites, going to the low hopping seems to overestimate the number of double-occupancies. This can be understood from the slightly lower temperature and negligence of higher order hopping processes (i.e. hopping of one of the atoms on a doubly occupied site to an empty next-nearest neighbor site on the low potential sublattice).

Fig. 6.23: (a) Sublattice imbalance $\hat{\Delta}/L$, (b) Scaled photon number N_{pho}/L^d, (c) inverse temperature β and (d) average number of double occupancies as a function of atom-cavity coupling $\hbar g/J$ and on-site interaction U/J of a finite size system $L=8$ at quarter filling left of the vertical double-line and in the thermodynamic-limit in the weak tunneling perturbation right of it. The other parameters used are $\hbar\delta/J=5$, $\hbar\Gamma/J=3$. The hatched region marks the fluctuation-induced bistability region within the self-organized phase. Contour lines denote resonances in the atomic limit.

We identify the cavity cooling resonance $2g\lambda_1=\delta$ discussed in Sec. 6.1.2 marked by the approximately horizontal solid black line in the region where only the λ_1-solution is present. Throughout the large U/J region it follows mostly in parallel to the self-ordering transition since it almost independent of U/J in the low hopping limit. The associated minimum in the temperature and corresponding maximum in β is confirmed in Fig. 6.23 (c). As one approaches low on-site interactions, the resonance joins and vanished within the steep slope in λ at the self-ordering transition, since here the on-site interaction considerably influences the critical coupling and generally all processes around the self-ordering transition. The many-body cooling [see Sec. 6.1.3] is also observed, as marked by the dashed black lines at $2g\lambda_2=U\pm\delta$. Both lines follow approximately parallel to the onset of the bistability in the λ_2-solution. Consequently, due to the efficient cooling of the atomic system around these resonances, the maximal density imbalance Fig. 6.23 (a) also follows the bistability edge. The reduced effective temperature in the large cavity field solution close to the onset of the bistability also reflects in the behavior of the double-occupancies [Fig. 6.23 (d)]. Although in this regime the dominant exited states contributing to the steady state in the λ_2-solution contain doubly occupied sites, its value does not immediately rise as one crosses over into the bistability region [also visible in Fig. 6.21 (d)] because the low temperature, that remains below the excitation gap around the cooling resonances, suppresses any excitations [see Fig. 6.10].

We have also verified the dependence of the bistability on the atomic filling and find that at lower fillings a similar behavior is found. However, for $n>1/2$, the situation is substantially different as discussed in Sec. 6.2.

6.3.1 Fluctuation-induced bistability for bosons

In this section, we show that the fluctuation-induced bistability we identified and analyzed for the fermionic system in Sec. 6.3 is also present in a bosonic many-body system. This is especially interesting, since experimental setups of atomic many-body systems within a cavity that are subjected to an external optical lattice are more advanced for bosons [10, 21, 272, 273] than for fermions. Further, the presence for bosons reveals a more general character of the fluctuation-induced bistability that we expect to also appear in similar models that also exhibit a competition of energy scales within a self-ordered phase. We are further able to highlight the importance of on-site interactions for its existence by going to higher on-site occupations. The adiabatic elimination model at finite system sizes can be adapted for spinless bosons straight away by replacing the fermionic operators by their bosonic equivalent, removing the spin degree of freedom and solving the system of equations Eqs. (3.3) & (3.14) via exact diagonalization.

The model treated here was derived and analyzed in Refs. [31, 149, 152, 164] with the Hamiltonian defined as

$$\begin{aligned}\hat{H} &= \hat{H}_{\text{BH}} + \hat{H}_{\text{cav}} + \hat{H}_{\text{ac}}, \\ \hat{H}_{\text{BH}} &= -J\sum_{\langle j,l\rangle}\left(\hat{b}_j^\dagger \hat{b}_l + \text{H.c.}\right) + \frac{U}{2}\sum_j \hat{n}_j(\hat{n}_j - 1), \\ \hat{H}_{\text{cav}} &= \hbar\delta\hat{a}^\dagger\hat{a}, \\ \hat{H}_{\text{ac}} &= -\frac{\hbar g}{\sqrt{L^d}}(\hat{a} + \hat{a}^\dagger)\hat{\Delta},\ \hat{\Delta} = \sum_{j\in A}\hat{n}_j - \sum_{l\in B}\hat{n}_l.\end{aligned} \tag{6.15}$$

Note here the density operator is $\hat{n}_j = \hat{b}_j^\dagger \hat{b}_j$ with bosonic creation/annihilation operators $\hat{b}_j^\dagger$, $\hat{b}_j$. The corresponding self-consistency equation is given by

$$\lambda \equiv \frac{1}{\sqrt{L^d}}\langle \hat{a} + \hat{a}^\dagger\rangle = \frac{2g\delta}{\delta^2 + (\Gamma/2)^2}\frac{\langle\hat{\Delta}\rangle}{L^d}. \tag{6.16}$$

Analogous to the fermionic case, the energy transfer in Lehmann-representation can be rewritten as a function of the retarded susceptibility $\chi_T(\omega)$ [164].

$$\frac{\partial}{\partial t}\langle \hat{H}_{\text{eff}}\rangle_T = \frac{2\hbar g^2}{L^d Z_{1\text{D}}}\int d\omega \frac{\hbar\omega}{1 - e^{-\beta\hbar\omega}}\,\text{Im}\left[\chi_T(\omega)\right]\frac{\Gamma/(2\pi)}{(\omega+\delta)^2 + (\Gamma/2)^2}, \tag{6.17}$$

where $\chi_T(\omega) = -\frac{i}{\hbar}\int_0^\infty dt e^{i(\omega+i\epsilon)t}\left\langle\left[\hat{\Delta}(t), \hat{\Delta}(0)\right]\right\rangle_T$ We solve this energy transfer equation together with the self-consistency condition using exact diagonalization for finite system sizes. From these equations we also derive a perturbation in low hopping rates that allows us to go to the thermodynamic limit. This permits us to estimate finite size effects and facilitates the identification of relevant physical processes. The aim is to obtain a system of equations equivalent to Eqs. (3.25) for the fermions.

Perturbation theory in kinetic terms for bosons

Following the steps described in Sec. 3.2, we do a perturbation in the kinetic energy for bosonic atoms. The thermodynamic limit we take allows us to go beyond the system sizes that can be solved via exact diagonalization and yields an estimate for the finite size effects present in the exact diagonalization results. A more detailed calculation is given in the Appendix C. In this sense, we split the effective bosonic Hamiltonian obtained from Eq. (6.15) by replacing $(\hat{a} + \hat{a}^\dagger)/\sqrt{L} \to \lambda$ into a part $\hat{H}_0$ containing only density terms and the perturbative kinetic part $\hat{H}_{\text{kin}}$

$$\begin{aligned}\hat{H}_{\text{eff}} = \hat{H}_0 + \hat{H}_{\text{kin}} \quad \text{with} \quad \hat{H}_0 &= \frac{U}{2}\sum_j \hat{n}_j(\hat{n}_j - 1) - \hbar g\lambda\hat{\Delta} - \mu\sum_j \hat{n}_j \\ \hat{H}_{\text{kin}} &= -J\sum_{\langle j,l\rangle}\left(\hat{b}_j^\dagger\hat{b}_l + \text{h.c.}\right).\end{aligned} \tag{6.18}$$

As for fermions we rewrite the susceptibility $\chi_T(\omega)$ in terms of the perturbation $\hat{H}_{\text{kin}}$.

$$\chi_T(\omega) = -\frac{i}{\hbar^3\omega^2}\int_0^\infty dt e^{i(\omega+i\epsilon)t}\left\langle\left[\left[\hat{H}_{\text{kin}}, \hat{\Delta}\right](t), \left[\hat{H}_{\text{kin}}, \hat{\Delta}\right](0)\right]\right\rangle_T \tag{6.19}$$

This agrees with the result for fermions, replacing all fermionic operators with the respective bosonic ones. By computing the expectation values with respect to the unperturbed Hamiltonian $\hat{H}_0$, defined as $\langle ...\rangle = \text{Tr}\{e^{-\beta\hat{H}_0}...\}$, we obtain perturbative result in the kinetic terms on the order of $\mathcal{O}(J^2)$. The explicit calculation of the commutators and expectation value results in the following

$$\big[\hat{H}_{\text{kin}},\hat{\Delta}\big](0) = -J\sum_{\langle j,l\rangle,m}(-1)^m\big[\hat{b}_j^\dagger\hat{b}_l+\hat{b}_l^\dagger\hat{b}_j,\hat{b}_m^\dagger\hat{b}_m\big] = -2J\sum_{\langle j,l\rangle}\text{sgn}(l-j)\hat{b}_j^\dagger\hat{b}_l$$

$$\big[\hat{H}_{\text{kin}},\hat{\Delta}\big](t) = e^{i\hat{H}_0t/\hbar}\big[\hat{H}_{\text{kin}},\hat{\Delta}\big](0)e^{-i\hat{H}_0t/\hbar} = -2J\Big(\sum_{\langle j,l\rangle}\text{sgn}(l-j)\hat{b}_j^\dagger(t)\hat{b}_l(t)\Big) \tag{6.20}$$

where $\hat{b}_l^\dagger \equiv \hat{b}_l^\dagger(0)$. For simplicity, we restrict to one-dimensional systems from here on, but since it is a low hopping approach higher dimensional lattices can be expected to yield equivalent results. We showed that for fermions the calculated equations hold for arbitrary dimension [see Sec. 3.2].

$$\begin{aligned}\Big\langle\big[\big[\hat{H}_{\text{kin}},\hat{\Delta}\big](t),\big[\hat{H}_{\text{kin}},\hat{\Delta}\big](0)\big]\Big\rangle_T &= -4J^2\sum_{j,l}(-1)^{j+l}\Big(\Big\langle\big[\hat{b}_j^\dagger(t)\hat{b}_{j+1}(t),\hat{b}_{l+1}^\dagger\hat{b}_l\big]\Big\rangle+\Big\langle\big[\hat{b}_{j+1}^\dagger(t)\hat{b}_j(t),\hat{b}_l^\dagger\hat{b}_{l+1}\big]\Big\rangle\Big)\\ &= -\frac{4J^2}{\text{Tr}\Big[\prod_m e^{-\beta\hat{H}_m}\Big]}\sum_{j,l}(-1)^{j+l}\Bigg(\text{Tr}\Bigg[\prod_m e^{-\beta\hat{H}_m}\big[\hat{b}_j^\dagger(t)\hat{b}_{j+1}(t),\hat{b}_{l+1}^\dagger\hat{b}_l\big]\Bigg]\\ &\qquad+\text{Tr}\Bigg[\prod_m e^{-\beta\hat{H}_m}\big[\hat{b}_{j+1}^\dagger(t)\hat{b}_j(t),\hat{b}_l^\dagger\hat{b}_{l+1}\big]\Bigg]\Bigg)\end{aligned}$$

In the low hopping limit to $\mathcal{O}(J^2)$, we restrict to local two-site unit cells with the local basis states

$$\{|0\rangle_j,|1\rangle_j,|2\rangle_j,...,|n_{\text{max}}\rangle_j\}$$

where for the non-truncated local Hilbert spaces $n_{\text{max}}=N$. The diagonal entries in the two-site number basis are thus

$$\begin{aligned}&\langle n_j,n_{j+1}|[[\hat{H}_{\text{kin}}^{j,j+1},\hat{\Delta}^{j,j+1}](t),[\hat{H}_{\text{kin}}^{j,j+1},\hat{\Delta}^{j,j+1}](0)]\,|n_j,n_{j+1}\rangle =\\ &\quad-4J^2\Big(\langle n_j,n_{j+1}|\,\big[\hat{b}_j^\dagger(t)\hat{b}_{j+1}(t),\hat{b}_{j+1}^\dagger\hat{b}_j\big]\,|n_j,n_{j+1}\rangle+\langle n_j,n_{j+1}|\,\big[\hat{b}_{j+1}^\dagger(t)\hat{b}_j(t),\hat{b}_j^\dagger\hat{b}_{j+1}\big]\,|n_j,n_{j+1}\rangle\Big)\end{aligned}$$

where we introduced the notation $\hat{\Delta}^{j,j+1}=|\hat{n}_j-\hat{n}_{j+1}|$ and $\hat{H}_{\text{kin}}^{j,j+1}=-J(\hat{b}_j^\dagger\hat{b}_{j+1}+\text{H.c.})$. Evaluating the expectation values on the two-site unit cell yields

$$\begin{aligned}&\big\langle\big[\big[\hat{H}_{\text{kin}},\hat{\Delta}\big](t),\big[\hat{H}_{\text{kin}},\hat{\Delta}\big](0)\big]\big\rangle_T\\ &\quad=-\frac{4iJ^2}{Z}\Big(\sum_{n,m=0}^{n_{\text{max}}-1}e^{-\beta(\frac{U}{2}(n(n-1)+m(m-1))-\mu(n+m))}\\ &\quad\times\Big[e^{\beta\eta/2(n-m)}\big(n(m+1)\sin(t(U(m-n+1)+\eta))-(n+1)m\sin(t(U(m-n-1)+\eta))\big)\\ &\qquad+e^{-\beta\eta/2(n-m)}\big(n(m+1)\sin(t(U(m-n+1)-\eta))-(n+1)m\sin(t(U(m-n-1)-\eta))\big)\Big]\\ &\quad-2\sum_{n=0}^{n_{\text{max}}-1}e^{-\beta(\frac{U}{2}(n(n-1)+n_{\text{max}}(n_{\text{max}}-1))-\mu(n+n_{\text{max}}))}\times\Big[e^{\beta\eta/2(n-n_{\text{max}})}(n+1)n_{\text{max}}\sin(t(U(n_{\text{max}}-n-1)+\eta))\\ &\qquad+e^{-\beta\eta/2(n-n_{\text{max}})}(n+1)n_{\text{max}}\sin(t(U(n_{\text{max}}-n-1)-\eta))\Big]\Big).\end{aligned}$$

Inserting this in Eq. (6.19) and using the expression obtained after explicitly integrating over ω in Eq. (6.17), we arrive at the equation for the energy transfer

$$\frac{\partial}{\partial t}\langle\hat{H}_{\text{eff}}\rangle_T = -\frac{2\Gamma g^2 J^2}{L^d Z}\sum_{n,m=0}^{n_{\max}-1} e^{-\beta(\frac{U}{2}(n(n-1)+m(m-1))-\mu(n+m))} \tag{6.21}$$

$$\times\Bigg[-\frac{e^{\beta g\lambda(n-m)}n(m+1)}{U(m-n+1)+2g\lambda}\left[\frac{\left(1-e^{\beta(U(m-n+1)+2g\lambda)}\right)^{-1}}{(U(m-n+1)+2g\lambda-\delta)^2+(\Gamma/2)^2}+\frac{\left(1-e^{-\beta(U(m-n+1)+2g\lambda)}\right)^{-1}}{(U(m-n+1)+2g\lambda+\delta)^2+(\Gamma/2)^2}\right]$$

$$+\frac{e^{\beta g\lambda(n-m)}(n+1)m}{U(m-n-1)+2g\lambda}\left[\frac{\left(1-e^{\beta(U(m-n-1)+2g\lambda)}\right)^{-1}}{(U(m-n-1)+2g\lambda-\delta)^2+(\Gamma/2)^2}+\frac{\left(1-e^{-\beta(U(m-n-1)+2g\lambda)}\right)^{-1}}{(U(m-n-1)+2g\lambda+\delta)^2+(\Gamma/2)^2}\right]$$

$$-\frac{e^{-\beta g\lambda(n-m)}n(m+1)}{U(m-n+1)-2g\lambda}\left[\frac{\left(1-e^{\beta(U(m-n+1)-2g\lambda)}\right)^{-1}}{(U(m-n+1)-2g\lambda-\delta)^2+(\Gamma/2)^2}+\frac{\left(1-e^{-\beta(U(m-n+1)-2g\lambda)}\right)^{-1}}{(U(m-n+1)-2g\lambda+\delta)^2+(\Gamma/2)^2}\right]$$

$$+\frac{e^{-\beta g\lambda(n-m)}(n+1)m}{U(m-n-1)-2g\lambda}\left[\frac{\left(1-e^{\beta(U(m-n-1)-2g\lambda)}\right)^{-1}}{(U(m-n-1)-2g\lambda-\delta)^2+(\Gamma/2)^2}+\frac{\left(1-e^{-\beta(U(m-n-1)-2g\lambda)}\right)^{-1}}{(U(m-n-1)-2g\lambda+\delta)^2+(\Gamma/2)^2}\right]\Bigg]$$

$$+\frac{4\Gamma g^2 J^2}{L^d Z}\sum_{n=0}^{n_{\max}-1} e^{-\beta(\frac{U}{2}(n(n-1)+n_{\max}(n_{\max}-1))-\mu(n+n_{\max}))}(n+1)n_{\max}$$

$$\times\Bigg[\frac{e^{\beta g\lambda(n-n_{\max})}}{U(n_{\max}-n-1)+2g\lambda}\left[\frac{\left(1-e^{\beta(U(n_{\max}-n-1)+2g\lambda)}\right)^{-1}}{(U(n_{\max}-n-1)+2g\lambda-\delta)^2+(\Gamma/2)^2}+\frac{\left(1-e^{-\beta(U(n_{\max}-n-1)+2g\lambda)}\right)^{-1}}{(U(n_{\max}-n-1)+2g\lambda+\delta)^2+(\Gamma/2)^2}\right]$$

$$+\frac{e^{-\beta g\lambda(n-n_{\max})}}{U(n_{\max}-n-1)-2g\lambda}\left[\frac{\left(1-e^{\beta(U(n_{\max}-n-1)-2g\lambda)}\right)^{-1}}{(U(n_{\max}-n-1)-2g\lambda-\delta)^2+(\Gamma/2)^2}+\frac{\left(1-e^{-\beta(U(n_{\max}-n-1)-2g\lambda)}\right)^{-1}}{(U(n_{\max}-n-1)-2g\lambda+\delta)^2+(\Gamma/2)^2}\right]\Bigg]$$

The scaled partition sum on the two-site unit cell is given by

$$Z = \mathrm{Tr}\Big[\exp\Big(-\beta\hat{H}_{j,j+1}\Big)\Big] = \sum_{n,m=0}^{n_{\max}} e^{-\beta(\frac{U}{2}(n(n-1)+m(m-1))-\mu(n+m))}\cosh(\beta g\lambda(n-m)) \tag{6.22}$$

and the equation fixing the average number of particles per site is derived correspondingly

$$\begin{aligned}\langle\hat{n}\rangle_T &= \frac{1}{2Z}\,\mathrm{Tr}\Big[\exp\Big(-\beta\hat{H}_{j,j+1}\Big)(\hat{n}_j+\hat{n}_{j+1})\Big] \\ &= \frac{1}{Z}\sum_{n,m=0}^{n_{\max}} e^{-\beta(\frac{U}{2}(n(n-1)+m(m-1))-\mu(n+m))}\cosh(\beta g\lambda(n-m))(n+m)\end{aligned} \tag{6.23}$$

The self-consistency equation can be calculated as

$$\begin{aligned}\lambda &= \frac{2g\delta}{\delta^2+(\Gamma/2)^2}\frac{\langle\hat{\Delta}\rangle_T}{L^d} \\ &= \frac{1}{Z}\frac{2g\delta}{\delta^2+(\Gamma/2)^2}\sum_{n,m=0}^{n_{\max}} e^{-\beta(\frac{U}{2}(n(n-1)+m(m-1))-\mu(n+m))}\sinh(\beta g\lambda(n-m))(n-m)\end{aligned} \tag{6.24}$$

In order to compare the system of equations to the fermionic case we write the explicit expressions for low local densities, restricting $n_{\max}=2$.

$$\frac{\partial}{\partial t}\langle \hat{H}_{\text{eff}}\rangle_T \propto \frac{1}{2g\lambda}\Bigg(\frac{e^{\beta g\lambda}}{(2g\lambda+\delta)^2+(\Gamma/2)^2}\left[2e^{\beta\mu}+\frac{2e^{\beta(3\mu-U)}}{1-e^{-2\beta g\lambda}}\left(3e^{2\beta g\lambda}-4\right)\right] - \frac{e^{-\beta g\lambda}}{(2g\lambda-\delta)^2+(\Gamma/2)^2}\left[2e^{\beta\mu}+\frac{2e^{\beta(3\mu-U)}}{e^{2\beta g\lambda}-1}\left(3-4e^{-2\beta g\lambda}\right)\right]\Bigg) + \frac{4e^{2\beta\mu}}{2g\lambda-U}\left(\frac{1}{(2g\lambda-U-\delta)^2+(\Gamma/2)^2}-\frac{e^{\beta(2g\lambda-U)}}{(2g\lambda-U+\delta)^2+(\Gamma/2)^2}\right) + \frac{4e^{2\beta\mu}}{2g\lambda+U}\left(-\frac{1}{(2g\lambda+U-\delta)^2+(\Gamma/2)^2}+\frac{e^{-\beta(2g\lambda+U)}}{(2g\lambda+U+\delta)^2+(\Gamma/2)^2}\right)$$

For comparison we remind ourselves of the equation obtained for fermions Eq. (3.25a).

$$\frac{\partial}{\partial t}\langle \hat{H}_{\text{eff}}\rangle_T \propto \frac{e^{\beta\mu}+e^{\beta(3\mu-U)}}{2g\lambda}\left(\frac{-e^{\beta g\lambda}}{(2g\lambda+\delta)^2+(\Gamma/2)^2}+\frac{e^{-\beta g\lambda}}{(2g\lambda-\delta)^2+(\Gamma/2)^2}\right) + \frac{e^{2\beta\mu}}{2g\lambda-U}\left(\frac{1}{(2g\lambda-U-\delta)^2+(\Gamma/2)^2}-\frac{e^{\beta(2g\lambda-U)}}{(2g\lambda-U+\delta)^2+(\Gamma/2)^2}\right) + \frac{e^{2\beta\mu}}{2g\lambda+U}\left(-\frac{1}{(2g\lambda+U-\hbar\delta)^2+(\Gamma/2)^2}+\frac{e^{-\beta(2g\lambda+U)}}{(2g\lambda+U+\delta)^2+(\Gamma/2)^2}\right) \tag{6.25}$$

Both equations have the same structure when projecting out occupations of 3 or more atoms per site for the bosonic system, a state that would be prevented by Pauli blocking for the fermionic spin-$1/2$ model. However the most striking difference is in the terms that do involve singly occupied sites. Since the bosons lack the spin degree of freedom, the energetically degenerate unit cell basis states obtained from mapping $\uparrow\leftrightarrow\downarrow$ in the fermionic system are replaced by a single basis state $|0,\uparrow\rangle, |0,\downarrow\rangle \rightarrow |0,1\rangle$. The same is true for $|\uparrow\downarrow,\uparrow\rangle, |\uparrow\downarrow,\downarrow\rangle \rightarrow |2,1\rangle$ etc. This results in a shift in the relative weights of the contributing terms.

Nevertheless the behavior remains qualitatively similar. This will be discussed in the following section.

Results

We present here some results solving the system of equations via exact diagonalization (ED) of the full effective Hamiltonian for small systems and numerically solving the thermodynamic limit equations derived in Sec. 6.3.1. The obtained results look qualitatively similar to what we calculated for the fermions [see Fig. 6.24 (a),(b)]. Already at system sizes of $L=8$, $N=4$ the ED results (red points) agree nicely with the solution of the thermodynamic limit equations (blue points).

As for the fermions, the atomic system initially self-orders around a critical coupling $\hbar g_{\text{cr}}/J \approx 6.8$ for the parameters shown in the figure ($U/J=40$, $\hbar\Gamma/J=3$, $\hbar\delta/J=10$). After an initial steep increase in the photon field order parameter λ, passing the resonant cooling transition around $2g\lambda=\delta$, it saturates as one increases the coupling further due to the rise of the effective temperature, causing disorder in the atomic system. For a detailed discussion of the resonant cooling and temperature effects refer to Sec. 6.1.2 & 6.1.3 or Ref. [1]. The fluctuation-induced bistability appears in the same way as for the fermions, in shape of a second stable solution characterized by the self-consistently determined (β_2,λ_2) that satisfy $\beta_2>\beta_1$ and $\lambda_2>\lambda_1$.

The more striking differences that support our interpretation of the observed phenomena appear at even higher couplings. Because generally the maximal on-site occupation n_{max} is not constrained as for fermionic systems, we can observe multiple bistable regions at even higher couplings within the self-ordered regime. These correspond to resonances in the atoms-cavity system involving on-site interactions with $3,4,5...N$ bosonic particles occupying the same site. When truncating the local Hilbert spaces to allow a maximum of n_{max} bosons per site one nicely observes that for $n_{\text{max}}=1$, where no double occupancies are possible and, as seen for fermions in the limit $U\rightarrow\infty$, no bistability within the self-ordered phase exists. [green line in Fig. 6.24 (c),(d)]. The importance of the on-site interaction energy U/J can be seen when allowing $n_{\text{max}}=2$. Here the level crossings in the excited spectrum as identified for the fermions, occur in within the ordered phase. In particular, the efficient transfer of energy from the atoms to the cavity mode due to the resonances between excited states and the photonic energy $\hbar\delta$ leads to a cooling mechanism, driving the atoms to a steady state with a much lower temperature in the bistable region.

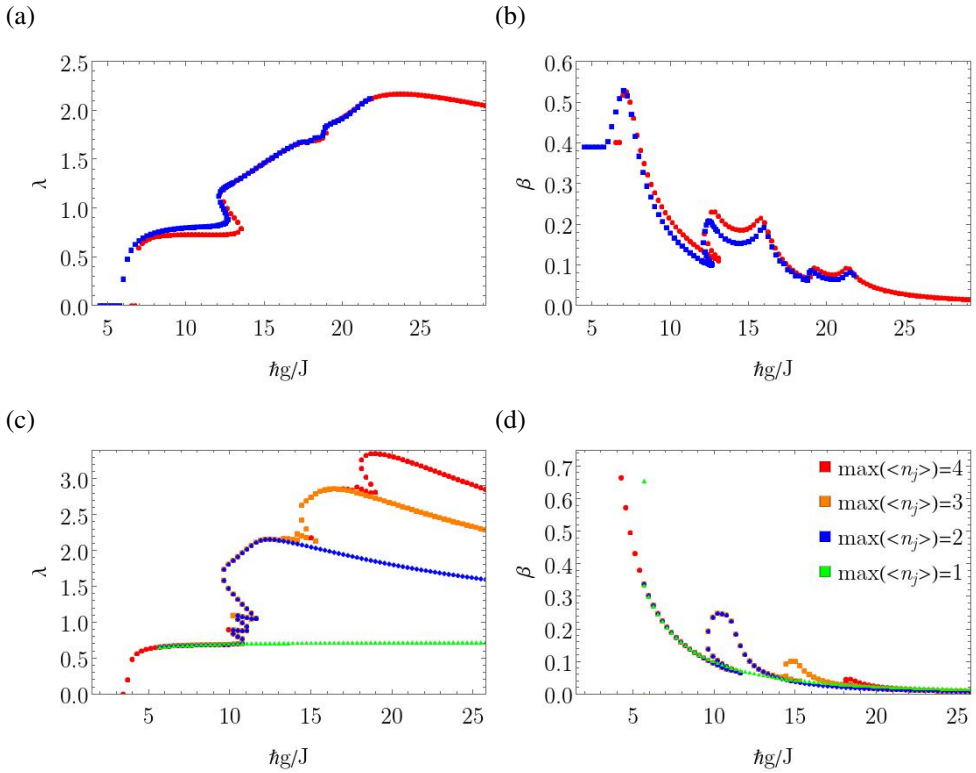

Fig. 6.24: (a) λ, (b) β comparison finite size $L=8$ (red) and thermodynamic limit (blue), for $n_{\max}=3$, $\hbar\delta/J=10$, (c) λ, (d) β comparison of truncated local Hilbert-spaces, allowing for a maximal site-occupation max($\langle\hat{n}_j\rangle$),at $\hbar\delta/J=5$. Parameters for all plots are $U/J=40$, $\hbar\Gamma/J=3$.

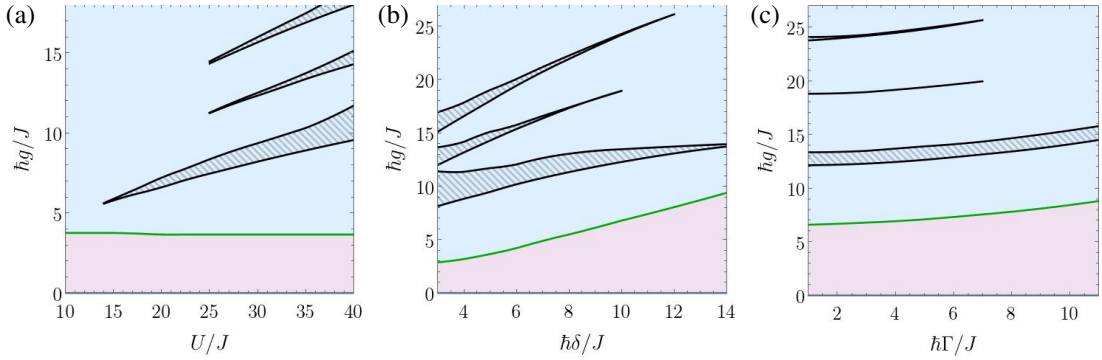

Fig. 6.25: Simplified phase diagrams varying the atom-cavity coupling $\hbar g/J$ and (a) the on-site interaction U/J at $\hbar\delta/J=5$, $\hbar\Gamma/J=3$; (b) the pump-cavity detuning $\hbar\delta/J$ at $U/J=40$, $\hbar\Gamma/J=3$; (c) the dissipation rate $\hbar\Gamma/J$ at $\hbar\delta/J=4$, $U/J=8$ of a finite size bosonic system $L=8$, $N=4$. The green line marks the transition between normal [purple region] and self-organized phase [blue region] determined by solving Eqs. (6.16) & (6.17) with ED. The fluctuation-induced bistability region are the hatched regions.

As mentioned, interesting deviations between fermionic and bosonic many-body systems that are particular to the higher site-occupations possible for bosons are seen at higher couplings. In general, $n_{\text{max}}-1$ energy-level crossings that cause multi-stabilities are observed [see Fig. 6.25 (a),(b)]. These correspond to resonances in the atomic energy levels $E_n-E_m=\{2\hbar g\lambda-U;2\hbar g\lambda-2U;...;2\hbar g\lambda-U(n_{\text{max}}-1)\}$. While lowering the on-site interaction, the width of each of the bistability regions decreases until one can observe a continuous transition between the unique solutions with the properties of $\lambda_{1,2}$ within the reached numerical accuracy. Note, that for the parameter set shown here, while there is a large shift between the critical points where the first and second bistability regions acquire a width $g_{\text{bi},2}-g_{\text{bi},1}\geq 10^{-5}$ respectively, the same can not be observed for the higher on-site occupation bistabilities. This is likely due to the large effective temperatures at the high couplings necessary for them to appear. As one increases the pump-cavity detuning $\hbar\delta/J$ at fixed on-site interaction and dissipation, the individual regions become narrower as well, as it was also observed in the fermionic system. While the first bistability dominantly involving the transition rates between singly and doubly occupied sites prevails the longest, the higher bistability regions that are located at higher coupling strengths seem to be more sensitive to the detuning.

To conclude we obtained a rich steady state phase diagram for the bosonic system that shows multiple fluctuation-induced bistability regions. These are connected to the higher on-site occupations possible for bosonic atoms as opposed to spin-$1/2$ fermions. With this, we confirm one one hand the importance of the many-body character of the system and the presence of fluctuations for the bistability to emerge. On the other hand, it provides arguments that this sort of fluctuation-induced bistability is generic for systems where the cavity energy can probe the many-body energy of the atoms.

Summary

In this chapter, we have investigated the steady state phase diagrams of fermionic atoms in optical lattices coupled to an optical cavity at both quarter filling and half filling. We take fluctuations beyond the mean-field decoupling into account and find a transition between a normal and a self-organized phase, which is shifted from the ground-state transition, and for which we derive approximate analytical expressions in various limits. We identify cavity cooling processes as well as many-body cooling processes and track the corresponding resonances in the effective model over a wide range of parameters. Deep in the self-ordered phase, a saturation in the cavity field occupation is observed and analytically approximated.

At quarter filling and below we surprisingly find the occurrence of a fluctuation induced bistability region, which does not exist in the zero-temperature mean-field solution. The self-consistent determination of the effective temperature was shown to be crucial for its emergence. We attribute the existence of bistable steady states to the facilitated energy transfer between excited eigenstates of the atomic system to the photonic mode in the vicinity of resonances. The quantum fluctuations in the atoms-cavity coupling determine the importance of these resonances in the calculation of the steady states, thus, we label the effect fluctuation induced bistability. We presented the

dependence of the bistability varying the system parameters and identify the dominant transition processes in the stable solutions. We expect that the emergence of the fluctuation induced bistability to be a generic feature of hybrid atoms-cavity systems in which one can control independently the coupling to the cavity and the atomic energies. As in our equations of motion we mainly use the spectrum of effective atomic Hamiltonian, the bistability should emerge for coupled systems where the resonances between the atomic levels and photonic excitations can be obtained. We demonstrated their presence for the weak tunneling perturbation in the thermodynamic limit for arbitrary dimension of the atomic system and confirmed the applicability to bosonic many-body systems.

Many questions remain open, in particular on the dissipative dynamics of such systems, which might show non-thermal behavior in their approach towards the steady state, caused by the importance of the cooling resonances and bistable behavior. We take steps towards answering these questions in the following chapter where we present the quasi-exact numerical time evolution of the full Lindbladian model.

Chapter 7

Tensor Network dissipative dynamics

In this chapter, we present results obtained using the method of the newly developed quasi-exact numerical real time simulations. These are intriguing since we are able to observe interesting dynamics, identify time scales and scaling behavior. Further,the numerical model evolve in time still contains all higher order correlations and thus provides the possibility to see whether this alters the long time limit when compared to the analytical methods where high order correlations were neglected in the mean field step. Details of the various algorithms based on tensor network methods have previously been introduced in Sec. 4.2 and convergence checks and algorithm comparisons are shown in Sec. 4.3.1. The numerical evolution allows us to treat the atoms-cavity coupling exactly and look at the real time ordering dynamics for a broad range of parameters. As already predicted by the thermal mean field steady state analysis [Sec. 3.1] the admixture of higher energy eigenstates on top of the ground state of the effective model [defined in Sec. 3.1] play a crucial role in the physics that govern the system dynamics.

Here we focus on the time evolution of the individual quantum trajectories as well as the averages obtained in the numerical simulation. The individual trajectories would correspond to a single measurement run in experiments. Since the detection of leakage photons through the cavity mirrors allow for a non-destructive real time detection of the state of the cavity field, this is especially interesting as it yields the possibility of comparisons between theory and experiment.

If not stated otherwise, the simulations start from an initial state that is the ground state of the spin-balanced Fermi-Hubbard model with the given on-site interaction U/J. We obtain this via DMRG [see Sec. 4.2.2 for details on the algorithm]. At time $tJ/\hbar = 0$, the coupling to the cavity field $\hbar g/J$ is suddenly quenched to the final value. Some analysis considering a time dependent ramp of the coupling strength is presented in Sec. 7.3.

Finally we extract the long-time average observable values in order to see how they compare to the steady state observables calculated in the adiabatic elimination approach. These results will be presented in Sec. 7.4. The focus is on pinpointing how the fluctuations-induced bistability we obtained in the analytic method manifests in the long time behavior of the full Lindbladian system.

So far in the analytic approaches the atomic ordering process was mostly characterized by the sublattice density imbalance $\langle\hat{\Delta}\rangle = \sum_{j\in A}\hat{n}_j - \sum_{j\in B}\hat{n}_j$, where $A(B)$ denote site-indices belonging to the respective sublattice. This was possible since we arbitrarily chose one of the lattice configurations in the spontaneous $\mathbb{Z}_2$ symmetry breaking at the self-ordering transition, choosing one of the sectors characterized by $(\hat{a}, \hat{\Delta}), (-\hat{a}, -\hat{\Delta})$. However, in the time evolution of the finite size full Lindbladian model, this symmetry is not broken and the measured local densities will always show a symmetric superposition of both lattice configurations with the atoms preferably on even or odd sites of the chain. Therefore the ordering process will average out in the measuring process and is not measurable through the local densities. In order to quantify the atomic many body ordering and emerging staggered density wave one can instead look at the density-density correlations at even vs odd distances. This serves as a measure for the charge density wave state. To minimize edge effects and obtain a quantity that can more easily be used to compare to other parameter configurations, we also consider the average difference between even/odd distance correlations over the whole system

$$c(t) = \sum_j \sum_{d=1} (\langle n_j n_{j+2d} \rangle(t)/(N_1) - \langle n_j n_{j+(2d-1)} \rangle(t)/(N_2))/2. \tag{7.1}$$

Here $N_{1(2)}$ are the respective number of terms in the sum, according to the system size. We will in the following refer to this quantity as density-density correlation contrast or simply contrast.

We start by discussing the system dynamics at quarter filling.

7.1 Self-ordering dynamics at quarter filling

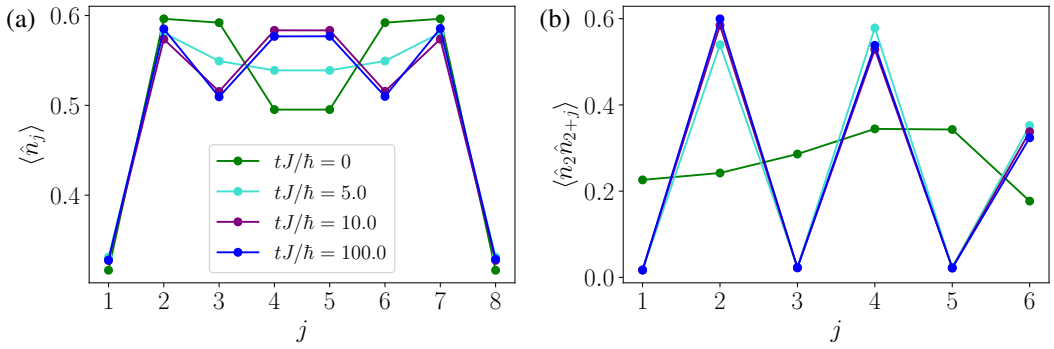

Fig. 7.1: Site resolved (a) local densities $\langle \hat{n}_j \rangle$ and (b) density-density correlations $\langle \hat{n}_2 \hat{n}_{2+j} \rangle$. Starting with the ground state of the Fermi-Hubbard model at $tJ/\hbar = 0$ at quarter filling with $L = 8$, $S_z = 0$, $U/J = 2$, $\hbar g/J = 4$, $\hbar\Gamma/J = 1$, $\hbar\delta/J = 2$. The parameters used in the time evolution of 500 trajectories with Trotter-Suzuki algorithm are the maximal bond dimension $m = 500$, $N_{\text{pho,max}} = 60$, time step size $\tau J/\hbar = 0.01$. The average value of all trajectories is marked in red.

As shown in Fig. 7.1, the atoms self-order as the coupling is switched on to a finite value $\hbar g/J = 4.0$ above the self-ordering transition and the observables evolve to long-time values as the system approaches the steady state. The on-site interaction is $U/J = 2$, the detuning is $\hbar\delta/J = 5.0$ and the dissipation rate $\hbar\Gamma/J = 1.0$. As stated above since the $\mathbb{Z}_2$ symmetry is not broken the local density distribution [Fig. 7.1 (a)] remains symmetric with respect to the center bond. Since the atoms order at equal probability on either even or odd sites of the lattice the staggering is clearly visible in the non-local density-density correlations as a function of the distance [Fig. 7.1 (b)].

We show the time evolution of various observables at these parameters in Fig. 7.2. In the photon number Fig. 7.2 (a) after an initial steep rise following the quench of the coupling strength to its finite value within the self-ordered phase, atoms order and the average photon number of all trajectories (red dashed line) saturates to a finite value. Looking at the individual trajectories, it is apparent, that they seem to saturate to different values. We identify them with the field occupations corresponding to the mean-field value at a certain density imbalance subspaces with $\Delta \in \{N, N-2, N-4, ...\}$.

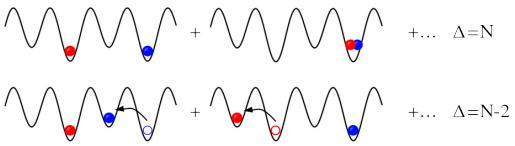

In the limit of vanishing hopping $J \to 0$ the atomic part of the Liouvillian that captures the system dynamics as introduced in Eq. (2.12) is diagonal in the position basis.In the atomic limit we obtain sectors of the Lindbladian that are characterized by the density distribution of the atoms $\{n_j\}$, which results in states in the dissipation free subspace of the Liouvillian of $\hat{\rho}_0 = |\alpha(\langle\hat{\Delta}\rangle), \{n_j\}\rangle\langle\alpha(\langle\hat{\Delta}'\rangle), \{n'_j\}|$ [147]. The corresponding eigenvalues are

$$\lambda(\langle\hat{\Delta}\rangle, u, \langle\hat{\Delta}'\rangle, u') = -\frac{\hbar}{2L}\frac{g^2\Gamma}{\delta^2 + (\Gamma/2)^2}(\langle\hat{\Delta}\rangle - \langle\hat{\Delta}'\rangle) + i\Big[\frac{\hbar}{L}\frac{g^2\delta}{\delta^2 + (\Gamma/2)^2}(\langle\hat{\Delta}\rangle^2 - \langle\hat{\Delta}'\rangle^2) - (u - u')\Big]$$

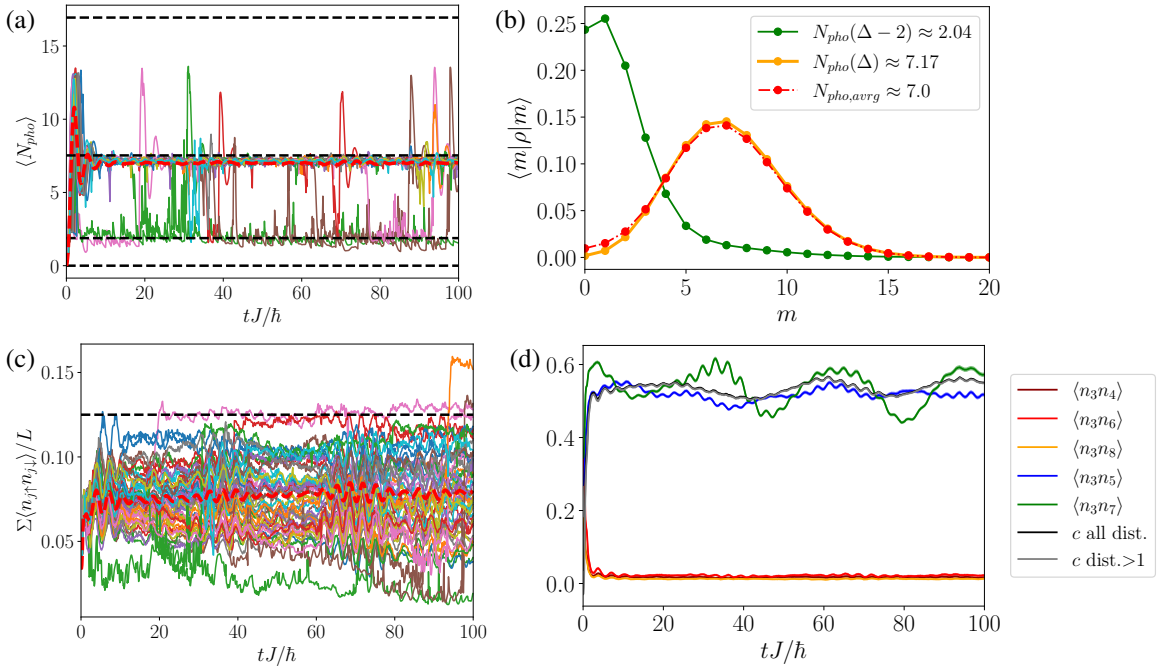

Fig. 7.2: Real time evolution of the (a) photon number $\langle N_{\text{pho}} \rangle$ trajectories and full average (red dashed line) with (b) the corresponding photon number distribution of the individual trajectory bundles and full average at the final time, compared to the coherent state prediction in the density-imbalance subspaces, (c) average number of double occupancies $\langle \hat{n}_{j\uparrow} \hat{n}_{j\downarrow} \rangle$ in individual trajectories as well as the full average (red dashed line) and (d) atomic density-density correlation $\langle \hat{n}_3 \hat{n}_{3+j} \rangle$ at distance j and contrast c between even and odd distance correlations. Quarter filling with $L = 8$, $S_z = 0$, $U/J = 2$, $\hbar g/J = 4$, $\hbar \Gamma/J = 1$, $\hbar \delta/J = 2$. The parameters used in the time evolution of 500 trajectories with Trotter-Suzuki algorithm are the maximal bond dimension $m = 500$, $N_{\text{pho,max}} = 60$, time step size $\tau J/\hbar = 0.01$. The average value of all trajectories is marked in red.

From this follows that whether the eigenvalues are purely real or imaginary depends on the difference in density imbalance and interaction energy $u = U\sum_j \langle \hat{n}_{j,\uparrow}\hat{n}_{j,\downarrow}\rangle$. Coherences stemming from states with agreeing density imbalance and interaction energy have $\lambda_0 = 0$ and vanishing trace. Since they do not decay, they can prevail in the steady state.

In Ref. [147], these were connected to persistent oscillations [104,146] in certain parameter regimes between states within one density imbalance subspace with differing occupations (i.e. different average double occupancy). The frequency of these oscillations was determined to be connected to the on-site interaction U, with a weak damping at the tunneling rate J. For the here presented system we also encounter long-lived oscillations [see Fig. 7.3], though a thorough analytical analysis of the behavior with the system parameters is still work in progress.

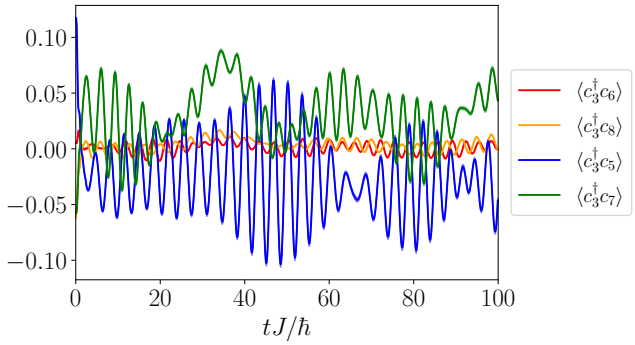

Fig. 7.3: Real time evolution of the average single particle correlations $\langle \hat{c}_3^\dagger \hat{c}_j\rangle$ for a system at quarter filling with $L = 8$, $S_z = 0$, $U/J = 2$, $\hbar g/J = 4$, $\hbar\Gamma/J = 1$, $\hbar\delta/J = 2$. The parameters used in the time evolution of 500 trajectories with Trotter-Suzuki algorithm are $m = 500$, $N_{\text{pho,max}} = 60$, $\tau J/\hbar = 0.01$

The corresponding cavity field occupation within the imbalance subspaces is given by $\frac{g^2}{\delta^2+(\Gamma/2)^2}(\Delta)^2$. The trajectories mostly reside in either of the subspaces with infrequent transitions between them. We will in the following refer to all trajectories within a specific subspace as "bundle". We see a stochastic probability for a trajectory to be found in the individual subspaces that can be related to the behavior at a finite temperature we see in our analytical approach Sec. 3.1. We want to stress, that these separated trajectories do *not* correspond to different multi-stable steady states as identified in Sec. 6.3, but rather the contributions of various states admixed in the steady state. Since in the bistability observed in the analytic mean field approaches both stable steady states are mixed states at different finite temperature it is highly non-trivial to assign the individual trajectories to either one or the other and thus identify the bistability taking the full fluctuation and coupling dynamics into account. Though clear signs of something happening around the parameter region where the bistability was observed can be identified [see Sec. 7.4].

In Fig. 7.2 (b) we show the number state distribution of the cavity field at the final time $tJ/\hbar = 100$ for the full trajectory average $N_{\text{pho,avrg}}$ (red), as well as the separated averages of the trajectories in each of the imbalance subspaces, $N_{\text{pho}}(\Delta = N)$, $N_{\text{pho}}(\Delta = N-2)$ and $N_{\text{pho}}(\Delta = N-4)$. We see that the trajectories are distributed between the subspaces with $\Delta = N$ and $\Delta = N-2$ with a majority residing within the subspace with maximal imbalance. The overall photon number is a superposition of the coherent states in each subspace. The average number of doubly occupied sites [Fig. 7.2 (c)], that is a measure for the interaction energy of the system, shows a broad distribution of the individual trajectories around the average value. They move between on average zero and one double occupancy at this low filling, with persistent oscillations with U/J that also reflect in the trajectory average. Note that at the quarter filling considered here, the number of doubly occupied sites does not have a direct influence on the density imbalance and thus the cavity field. To complement the discussion on how the self-ordering reflects in the density-density correlations, we show the time evolution of the trajectory averages for correlations $\langle \hat{n}_3\hat{n}_{3+j}\rangle$ for various distances j within the chain.The correlations $\langle \hat{n}_j\hat{n}_{j+d}\rangle$ are increased at even distances d (blue/green lines) and suppressed at odd distances (red/orange lines) and the cavity field builds up simultaneously. The even-distance correlations move around the value N/L expected for maximal imbalance with on average one particle per two sites. To minimize edge effects and obtain a quantity that can more easily be used to compare to other parameter configurations, we also consider the contrast defined by Eq. (7.1) (black/gray lines). The density-density correlations, much like the most atomic observables, exhibit long-lived oscillations,

that do not vanish until the final time of the simulation is reached. A slow oscillation increases in amplitude as the correlations become more distant. All of them are modulated by a faster oscillation of the same frequency as the oscillations with U/J seen in the double occupancies.

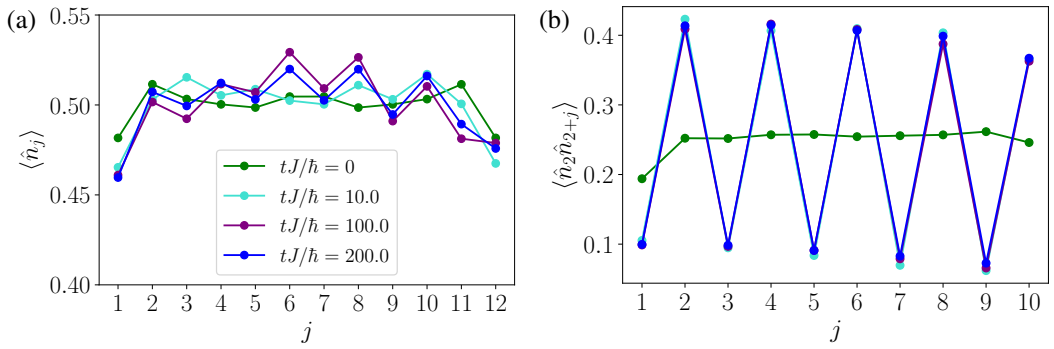

Fig. 7.4: Site resolved (a) local densities $\langle \hat{n}_j \rangle$ and (b) density-density correlations $\langle \hat{n}_2 \hat{n}_{2+j} \rangle$. Starting with the ground state of the Fermi-Hubbard model at $tJ/\hbar = 0$ at quarter filling with $L = 12$, $S_z = 0$, $U/J = 40$, $\hbar g/J = 7$, $\hbar \Gamma/J = 3$, $\hbar \delta/J = 5$. The parameters used in the time evolution of 500 trajectories with Trotter-Suzuki algorithm are the maximal bond dimension $m = 600$, $N_{\text{pho,max}} = 35$, time step size $\tau J/\hbar = 0.01$.

We want to see how the behavior of the system changes in the regime of large on-site interactions $U/J = 40.0$ and moderate coupling strength $\hbar g/J = 7.0$ within the self-ordered phase. The other parameters are $\hbar \delta/J = 5$ and $\hbar \Gamma/J = 3$. In the site resolved densities Fig. 7.4 (a), compared to the previously shown moderate interactions, the suppression of the occupation of the edges of the chain is a lot weaker, leading to an overall mostly homogeneous density distribution throughout the chain. However since due to the large on-site interaction hopping dynamics within the atomic system are suppressed. The density profile is not fully symmetric at the final reached time $tJ/\hbar = 200$ due to its sensitivity to the numerical parameters, which scales strongly with the system size. Nevertheless, the quick self-ordering of the atomic ensemble after the initial quench of the coupling to the cavity field can be seen in the density-density correlation at varying distances [see Fig. 7.4 (b)]. We show the time evolution of various observables in Fig. 7.5 (a)-(d) and compare the observations to a setup with larger coupling strength $\hbar g/J = 16$ but otherwise same parameters shown in Fig. 7.5 (e)-(h). The photon number for both couplings Fig. 7.5 (a),(e) initially quickly rises to an average occupation above the eventual long time expectation value following the quench of the coupling strength to its finite value. The photon number obtained from the average of all trajectories (red dashed line) saturates to a finite value in the long-time limit. The individual trajectories reside in the subspaces that can be associated with specific atomic density imbalances. In Fig. 7.5 (b) we show the number state distribution of the cavity field for the full trajectory average $N_{\text{pho,avrg}}$, as well as the separated averages of the trajectories in each of the imbalance subspaces, $N_{\text{pho}}(\Delta = N)$, $N_{\text{pho}}(\Delta = N-2)$ and $N_{\text{pho}}(\Delta = N-4)$. We observe here a higher mixing of the atomic states than for the previously discussed state at moderate on-site interactions. This partly stems from an interplay of the higher dissipation rate and coupling strength. As the dissipation rate is increased, the system is expected to further approach a fully mixed state. This implies a higher probability for subspaces that have higher dimension. An increasing weight of states with lower imbalance is typically also observed when increasing the atoms-cavity coupling, although here it does not reach the fully mixed state [see Fig. 7.5 (f)]. For the shown parameters, the distribution of trajectories is mostly among the largest subspaces $\Delta = N-2$ and $\Delta = N-4$. The splitting between the respective photon numbers is large, leading to a clearly visible double peak structure in the number state distribution of the full average, that stems from the superposition of the two dominantly contributing coherent states.

In the average number of double-occupancies shown in Fig. 7.5 (c) we see that at the low filling the probability of double occupations is strongly suppressed due to the high on-site interaction and moderate coupling strength. The average value is very small. Therefore, for this parameter set the kinetic energy is dominating over the interaction energy. This is not the case when one goes very deep into the self-ordered phase [Fig. 7.5 (g)]. Here, a relevant fraction of the trajectories resides around the value of on average one double occupancy on the chain, $\sum_j \langle \hat{n}_{j\uparrow} \hat{n}_{j\downarrow} \rangle / L = 1/L$ due to the higher mixing of the steady state. Notably, the time scale for the atoms to reach a steady state is really long, since the long-range correlations only slowly follow the rearranging of the distribution. One observes, besides the sudden switches between the two trajectory bundles, a few trajectories

slowly propagating towards the states with finite double occupancies, which leads to a steady increase in the average that does not stagnate within the measured time span. This can also be observed in the interaction energy that strongly dominates over the kinetic energy at very large couplings.

The self-ordering of the atoms is also confirmed by the non-local density-density correlations shown in Fig. 7.5 (d). We show the correlations $\langle \hat{n}_3 \hat{n}_{3+d} \rangle$ at even distances d (blue/green lines) and odd distances (red/orange lines). The average contrast in the density-density correlations at even and odd distances is shown for comparison (black/gray lines). Comparing to the evolution at larger coupling shown in Fig. 7.5 (h) we observe that the larger mixing and increased weight of states with $\Delta < N$ at large $\hbar g/J$ as expected also reflects in a reduced density-density-correlation contrast that still slowly increases in time. An explanation could be, that in the initial quench we excite various modes, some of which can be very long-lived and prevent the system from reaching the steady state within the computable timescales. An idea to address this issue would be to introduce alternative parameter protocols. We explore the effect of parameter ramps in the following Sec. 7.3.

We stay in the large on-site interaction limit $U/J = 40$ and consider how larger dissipation rates influence the time evolution. On one hand, it introduces more stochastic noise to the system. On the other hand the overlap of the coherent subspaces depends on the effective coupling strength that scales with Γ. Both of these effects alter the rate of jumps in the Lindbladian dynamics, which typically increases with the dissipation rate.

The chosen parameters are $\hbar\delta/J = 5$ and $\hbar\Gamma/J = 25$. As shown in Fig. 7.6 (a), transitions between the cavity occupation bundles corresponding to the different average imbalances with $\Delta < N$ are much more frequent than at lower dissipation. The average over all trajectories (red dashed line) initially quickly shoots up to the value expected for $\Delta = N - 2$, followed by a close to exponential decay approaching the value for $\Delta = N - 4$ in the long time limit. Though a notable number of trajectories also resides in the subspace without order $\Delta = 0$. This also shows correspondingly in the photon number state distribution presented in Fig. 7.6 (b). The large dissipation rate leads to decoherence in the atomic system and counteracts the self-ordering processes. This can be thought of as a high effective temperature of the atomic ensemble, even approaching an infinite temperature state in the limit of very large dissipation that grows faster than the coupling strength.

At the same time, the mixed character with high probability of occupations of states with $\Delta < N$, also shows in the atomic observables. This leads to an increased number of double occupancies since the temperature gets to energies surpassing the energy gain from the creation of a double occupancy [see Fig. 7.6 (c)]. Also, ordering of the atoms is effectively destroyed, leading to a vanishing density-density correlation contrast. A separation of $\langle \hat{n}_j \hat{n}_{j+d} \rangle$ at even and odd distances can not be observed [see Fig. 7.6 (d)] as the influence of edge effects and the varying distance of the correlation dominates over eventual remaining ordering.

To conclude our discussion of the quarter filled case we want to consider the phase indicating parameters for the charge-and spin density wave in momentum space to get a clearer idea of the physical states obtained in the long time limit of the previously presented time evolution. We concentrate on the Fourier transform of the order parameters for the charge density wave defined by $m_{\text{CDW}} = \sum_{j \neq k} (-1)^{j-k} \hat{n}_j \hat{n}_k$ and spin-density wave $m_{\text{SDW}} = \sum_{j \neq k} (-1)^{j-k} \hat{S}^z_j \hat{S}^z_k$ to momentum space. We compare both parameters to the behavior in the normal phase of the corresponding Fermi-Hubbard model that serves as the initial state for the numerical time evolution (depicted by black dashed lines in Figs. 7.7 & 7.8). For the moderate on-site interaction where all of the system parameters are around the same order $U/J = 2$, $\hbar\delta/J = 2$ and $\hbar\Gamma/J = 1$, the self-ordering transition occurs slightly below $\hbar g/J = 2$. The behavior of m_{CDW} and m_{SDW} is analyzed at the final time of the evolution $tJ\hbar = 100$ and shown in Figs. 7.7 for values of the coupling $\hbar g/J = 0, 2, 4$. In the normal phase the charge-density wave parameter shows pronounced peaks at the center and edges of the full Brillouin-zone $q = \{-2\pi, 0, 2\pi\}$. The non-flat behavior in between the peaks can be attributed to finite size effects. Increasing the coupling parameter to a value within the self-ordered phase, the emergence of secondary peaks around momenta $q = \pm\pi$ in the order parameter of the charge density wave $m_{\text{CDW}}(q)$ can be observed. This is due to the doubling of the unit cell by the effective staggering of the confining optical lattice, leading to a reduced Brillouin-zone of $q \in (-\pi, \pi]$. Close to the ordering transition, their amplitude is still considerably lower than the main peaks from the normal phase. This is due to defects in the ordering since the energy scales of the effectively created potential imbalance is not well separated from other processes in the system. Increasing the coupling to $\hbar g/J = 4$, moving further into the self-ordered phase, the amplitude of the peaks around $q = \pm\pi$ reaches approximately the same height as the other peaks, hinting towards a near-complete charge ordering on the even-distant lattice sites. In the spin-density wave parameter, that corresponds to the staggered spin-spin correlations, shows minima at $q = \{-2\pi, 0, 2\pi\}$, where it takes negative

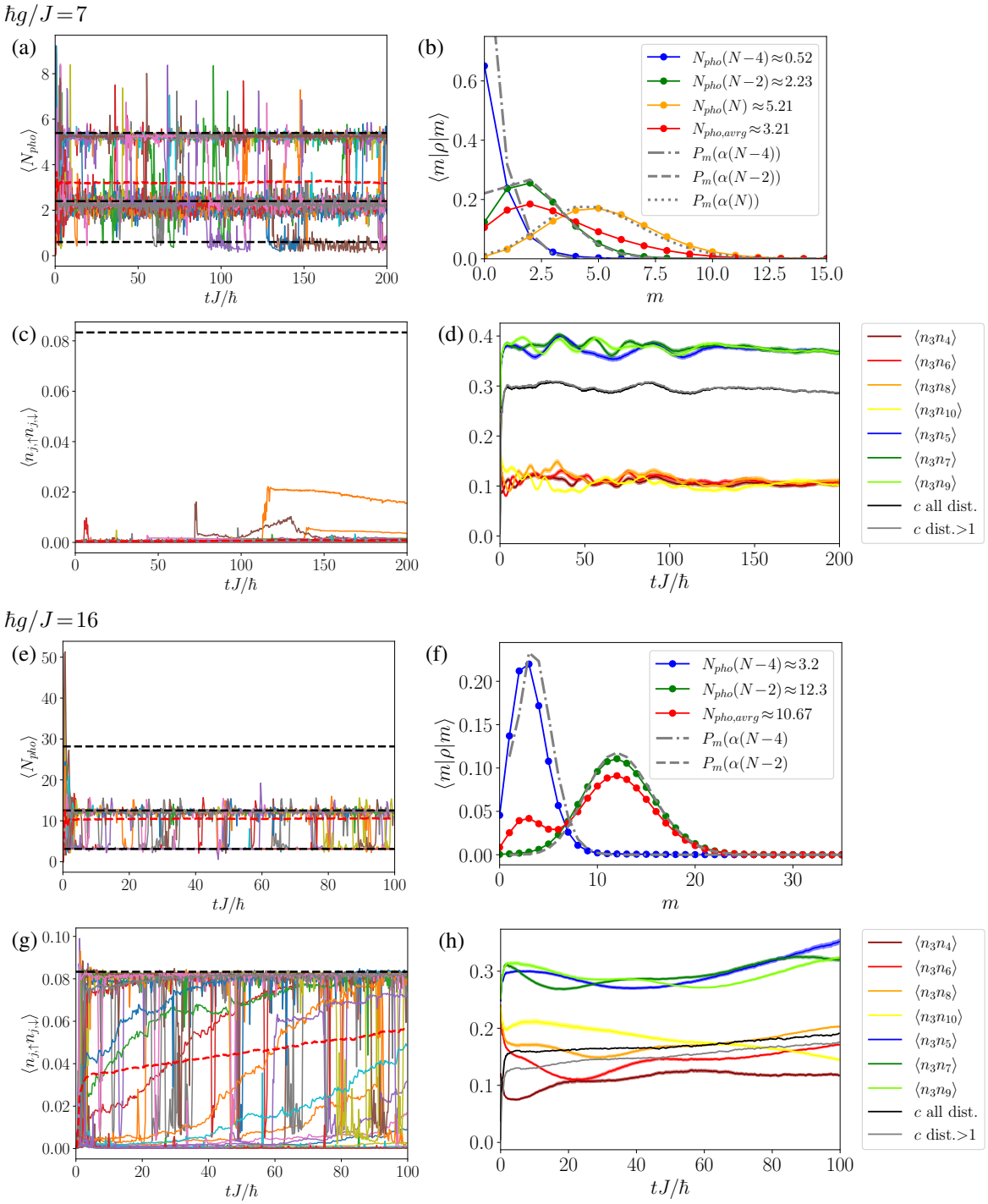

Fig. 7.5: Real time evolution of the (a),(e) photon number $\langle N_{\text{pho}} \rangle$ trajectories with (b),(f) the corresponding photon number distribution of the individual trajectory bundles and full average at the final time $tJ/\hbar = 100$, compared to the coherent state prediction in the density-imbalance subspaces, (c),(g) average number of double occupancies $\langle \hat{n}_{j\uparrow}\hat{n}_{j\downarrow} \rangle$ and (d),(h) atomic density-density correlation $\langle \hat{n}_3\hat{n}_{3+j} \rangle$ at distance j and contrast c between even and odd distance correlations. Quarter filling with $L = 12$, $S_z = 0$, $U/J = 40$, (a)-(d) $\hbar g/J = 7$,(a)-(d) $\hbar g/J = 16$, $\hbar\Gamma/J = 3$, $\hbar\delta/J = 5$. The parameters used in the time evolution of 500 trajectories with Trotter-Suzuki algorithm are (a)-(d) the maximal bond dimension $m = 600$, $N_{\text{pho,max}} = 35$, time step size $\tau J/\hbar = 0.01$ and (e)-(h) $m = 650$, $N_{\text{pho,max}} = 90$, $\tau J/\hbar = 0.0075$. In (a),(c),(e),(g) The average value of all trajectories is marked in red.

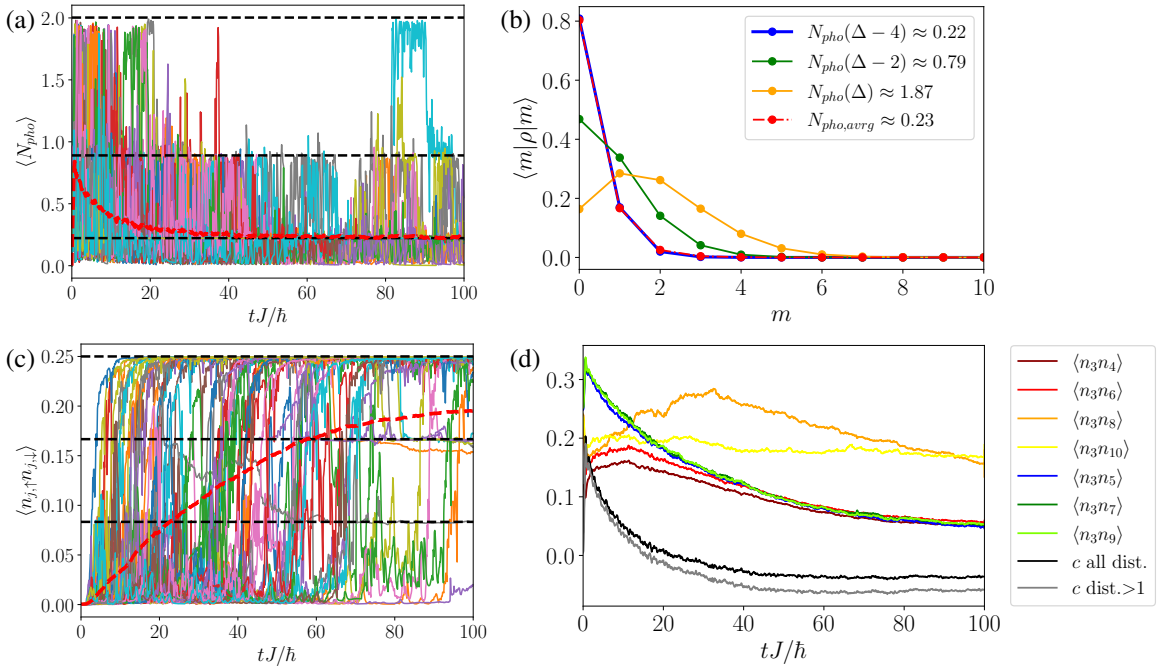

Fig. 7.6: Real time evolution of the (a) photon number $\langle N_{\text{pho}} \rangle$ trajectories and full average (red dashed line) with (b) the corresponding photon number distribution of the individual trajectory bundles and full average at the final time,(c) average number of double occupancies $\langle \hat{n}_{j\uparrow} \hat{n}_{j\downarrow} \rangle$ in individual trajectories as well as the full average (red dashed line) and (d) atomic density-density correlation $\langle \hat{n}_3 \hat{n}_{3+j} \rangle$ at distance j and contrast c between even and odd distance correlations. Quarter filling with $L = 12$, $S_z = 0$, $U/J = 40$, $\hbar g/J = 11$, $\hbar\Gamma/J = 25$, $\hbar\delta/J = 5$. The parameters used in the time evolution of 500 trajectories with Trotter-Suzuki algorithm are the maximal bond dimension $m = 600$, $N_{\text{pho,max}} = 30$, time step size $\tau J/\hbar = 0.005$. The average value of all trajectories is marked in red.

values. This is in agreement with the antiferromagnetic spin ordering expected for the Fermi-Hubbard model at quarter filling [211, 274, 275]

For strong repulsive on-site interaction one can approximately map our case with the self-consistently ordered system at quarter filling to a half-filled system on the even-distance sites. At half filling for strong repulsive on-site interaction the excitations of the Hubbard model are approximately those of an antiferromagnetic Heisenberg chain [276, 277]. We correspondingly see the build up of additional minima around $q = \pm\pi$ crossing over into the self-ordered region.

Some differences from this case can be observed in the limit of strong on-site interactions. As can be seen in Fig. 7.8 (a), a coupling $\hbar g/J$ above the critical value marking the self-ordering transition also goes along with the emergence of secondary peaks around momenta $q = \pm\pi$ in the order parameter of the charge density wave m_{CDW} in momentum space. As one goes to higher coupling, the effective temperature of the thermal state that best approximates the atomic many-body system was observed to rise in our adiabatic elimination approach as described in Sec. 3.1. This is in accordance with the observations made in the shown time evolution far in the self-ordered regime [compare Fig. 7.5], where the atomic order decreased due to a higher number of trajectories in subspaces with $\Delta < N$. In the charge-density wave order parameter, this results in a broadening and reduced peak amplitude increasing $\hbar g/J$ above 7.0.

In Fig. 7.8 (b) the spin-density wave order parameter, the Fourier transform of m_{SDW} is shown for various couplings. Here a similar influence of the admixture of states with reduced order in the large coupling limit is observed in the overall reduction of the order parameter amplitude. The spin-ordering is a lot more sensitive to the effective large temperatures of the atomic system and the main minima around $q = \{-2\pi, 0, 2\pi\}$ are also reduced in amplitude.

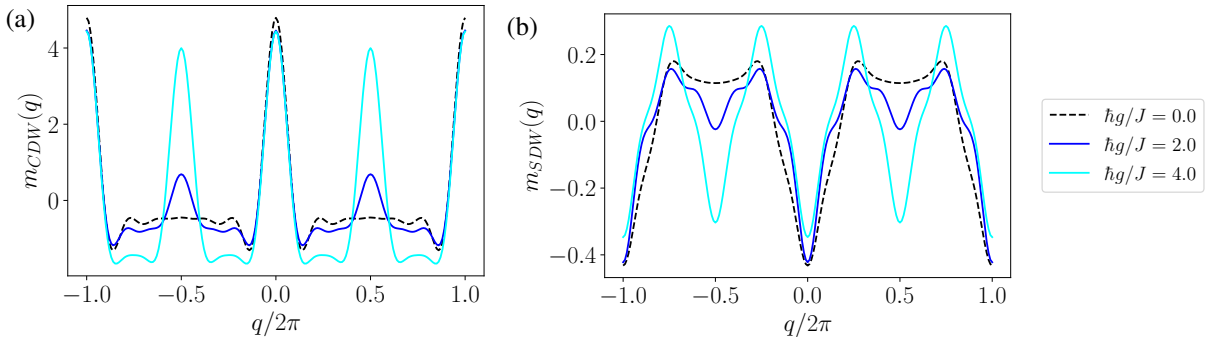

Fig. 7.7: Fourier transform of (a) $m_{\text{CDW}} = \sum_{j \neq k} (-1)^{j-k} \hat{n}_j \hat{n}_k$ and (b) $m_{\text{SDW}} = \sum_{j \neq k} (-1)^{j-k} \hat{S}^z_j \hat{S}^z_k$. Starting with the ground state of the Fermi-Hubbard model at $tJ/\hbar = 0$ at quarter filling with $L = 8$, $S_z = 0$, $U/J = 2$, $\hbar g/J = \{0.0, 2.0, 4.0\}$, $\hbar\Gamma/J = 1$, $\hbar\delta/J = 2$.

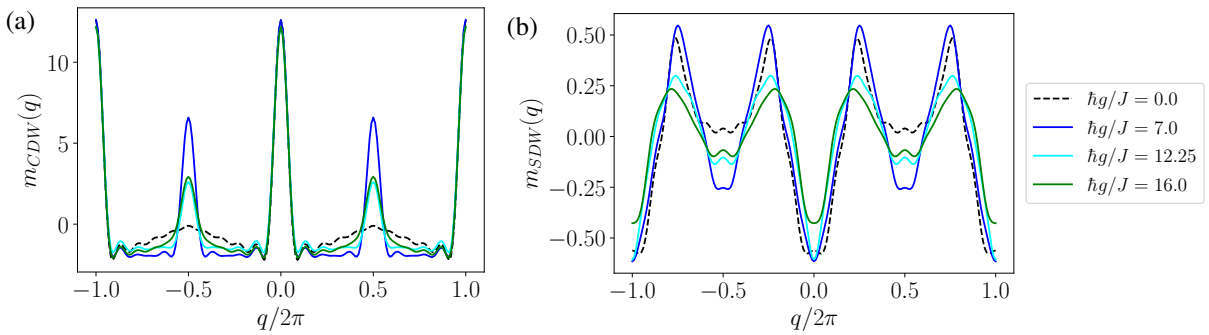

Fig. 7.8: Fourier transform of (a) $m_{\text{CDW}} = \sum_{j \neq k} (-1)^{j-k} \hat{n}_j \hat{n}_k$ and (b) $m_{\text{SDW}} = \sum_{j \neq k} (-1)^{j-k} \hat{S}^z_j \hat{S}^z_k$. Starting with the ground state of the Fermi-Hubbard model at $tJ/\hbar = 0$ at quarter filling with $L = 12$, $S_z = 0$, $U/J = 40$, $\hbar g/J = \{0.0, 7.0, 12.25, 16.0\}$, $\hbar\Gamma/J = 3$, $\hbar\delta/J = 5$.

Here we have taken some first promising steps in analyzing the complex open system dynamics. And provided a solid grounds for our ongoing in-depth analysis. One of our main focuses is to see if we can clearly identify and characterize the fluctuations-induced bistabilities obtained in the analytic many-body adiabatic elimination approach. A first comparison in the relevant parameter regime in provided in Sec. 7.4.

7.2 Self-ordering dynamics at half filling

At the case of commensurate or half-filling ($L=N$) in the ground state of the Fermi-Hubbard model each atom is localized on one site in the semi-classical limit dressed by quantum fluctuations. Higher order hopping processes influence the spin configuration of the particles. This corresponds to a Mott-insulator. However, due to the high mixing the energy in the atomic ensemble is expected we typically don't see coherence in the spin sector. We therefore do not expect to see a signature of spin-phases. As we observed in the adiabatic elimination approach there one would expect a transition from a state where the low lying excitation gap is dominated by the on-site interactions to an insulator that is dominated by the bad gap opening at the edges of the reduced Brillouin-zone [see Sec. 5.1].

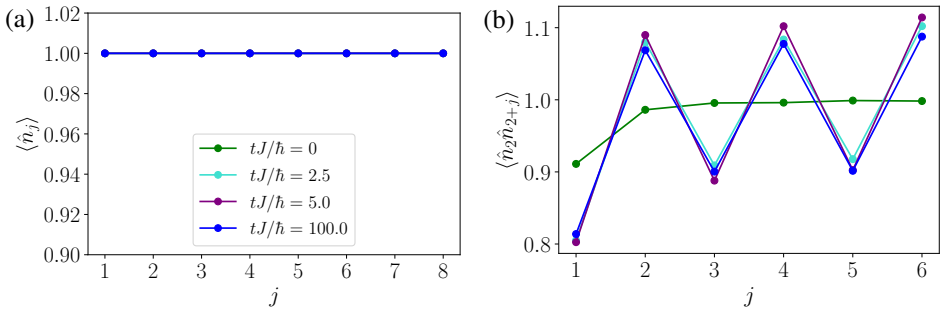

Fig. 7.9: Site resolved (a) local densities $\langle \hat{n}_j \rangle$ and (b) density-density correlations $\langle \hat{n}_2 \hat{n}_{2+j} \rangle$. Starting with the ground state of the Fermi-Hubbard model at $tJ/\hbar = 0$ at half filling with $L = 8$, $S_z = 0$, $U/J = 2$, $\hbar g/J = 1.5$, $\hbar\Gamma/J = 1$, $\hbar\delta/J = 2$. The parameters used in the time evolution of 500 trajectories with Trotter-Suzuki algorithm are the maximal bond dimension $m = 500$, $N_{\text{pho,max}} = 60$, time step size $\tau J/\hbar = 0.005$.

We show in Fig. 7.9 the site resolved density distribution within the chain and the density-density correlations $\langle \hat{n}_2 \hat{n}_{2+j} \rangle$ at varying distance j. For the displayed parameters just above to the self-ordering transition $U/J = 2$, $\hbar\delta/J = 2$, $\hbar\Gamma/J = 1$ and $\hbar g/J = 1.5$, the density density profile is symmetric and homogeneous throughout the system, while clear signs of the self-ordering process are already visible in the correlations. The density-density correlations at even distances are enhanced while those at odd distances are suppressed.

At this commensurate filling, the self-ordering transition is forcibly accompanied by the creation of double occupancies [see Fig. 7.10 (c)]. For a finite potential staggering the lowest energy state is the non-degenerate state with all low-potential sublattice sites doubly occupied in the limit of vanishing hopping, which we schematically depict here

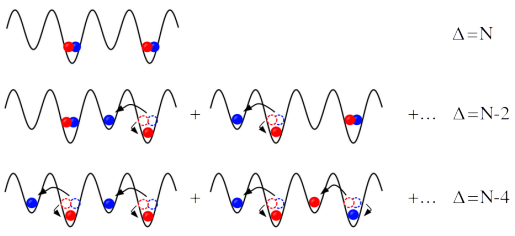

The fluctuations in the coupling as well finite temperature effects lead to increased contribution of states with imbalances $\Delta < N$. At this filling as well as higher fillings, any density distribution varying from the lowest energy state reduce the coupling to the cavity field. Since the the trajectories are always in a superposition of the configurations of the intact $\mathbb{Z}_2$ symmetry and therefore the low energy sites in the schemes are arbitrarily chosen to be on even sites of the chain.

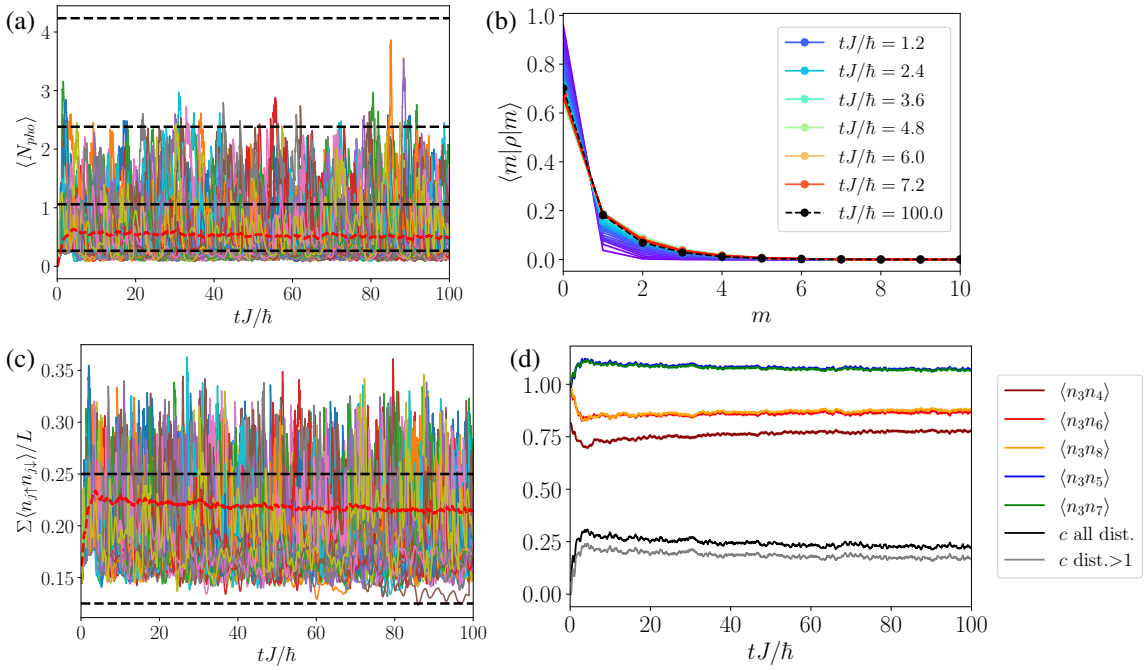

Fig. 7.10: Real time evolution of the (a) photon number $\langle N_{\text{pho}} \rangle$ trajectories and full average (red dashed line) with (b) the corresponding photon number distribution at varying time, (c) average number of double occupancies $\langle \hat{n}_{j\uparrow} \hat{n}_{j\downarrow} \rangle$ in individual trajectories as well as the full average (red dashed line) and (d) atomic density-density correlation $\langle \hat{n}_3 \hat{n}_{3+j} \rangle$ at distance j and contrast c between even and odd distance correlations. Starting with the ground state of the Fermi-Hubbard model at $tJ/\hbar = 0$ at half filling with $L = 8$, $S_z = 0$, $U/J = 2$, $\hbar g/J = 1.5$, $\hbar\Gamma/J = 1$, $\hbar\delta/J = 2$. The parameters used in the time evolution of 500 trajectories with Trotter-Suzuki algorithm are the maximal bond dimension $m = 500$, $N_{\text{pho,max}} = 60$, time step size $\tau J/\hbar = 0.005$. The average value of all trajectories is marked in red.

Above the self-ordering transition, one observes again the emergence of a finite cavity field occupation N_{pho} [see Fig. 7.10 (a)]. For the parameters shown here, since the effective coupling is rather small the trajectories in the individual imbalance configurations are not well separated. Additionally since it is still in the vicinity of the critical coupling that marks the self-ordering transition, the influence of quantum fluctuations in the coupling is particularly strong. Therefore, instead of the separated average photon number distribution, we here show the full average photon number distribution at various times in Fig. 7.10 (b).

As stated above at half filling the ordering and corresponding build-up of the finite cavity field is directly connected to the average number of doubly occupied sites shown in Fig. 7.10 (c). Initially it shows a steep increase as the atomic ensemble orders, followed by a slow decrease that still prevails at the here shown final time of $tJ/\hbar = 100$. The same behavior reflects in the density-density correlations, here exemplarily shown for $\langle \hat{n}_3 \hat{n}_{3+j} \rangle$ in Fig. 7.10 (c). Starting from an average value of 1 for all $j \geq 2$, even distance correlations are enhanced while odd distance correlations are suppressed. The steep splitting is followed by a slow dynamics reducing the contrast.

7.3 Dynamics of the self-ordering transition in the experimental limit

In this section we consider the dynamics of the ordering process across the phase transition. This is of special interest, since in out-of-equilibrium physics, the speed at which the order parameter grows upon crossing a phase transition is observed to grow exponentially. We investigate the ordering dynamics in fermions that are confined to a one-dimensional external lattice as introduced in Sec. 2.1 with a combination of our theoretical methods.This was done in collaboration with Zwettler et. al. Ref. [2] in order to investigate if their experimental findings for a three dimensional unitary Fermi-gas coupled to a cavity remain valid for other systems as well. We will begin by briefly summarizing the experimental findings and interpretation of the ordering dynamics after a quench in the

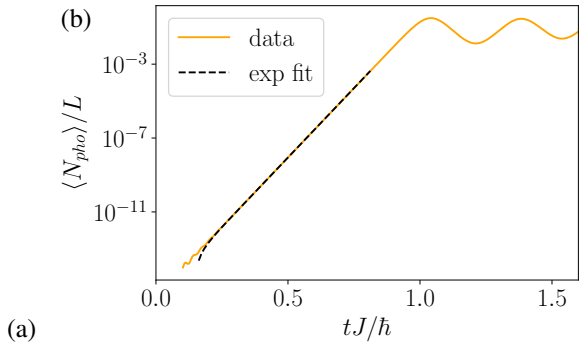

Fig. 7.11: Rescaled photon number after a quench in the atoms-cavity coupling to a value within the self-ordered phase. (a) considering full Lindblad dynamics of the coupled system of $L=8$, $N=8$ with $\hbar g/J=2$, $\hbar\delta/J=1$, $\hbar\Gamma=1$. $m=500$, and $\hbar\tau/J=0.01$. The increase is mostly algebraic and fitted to a quadratic function $\propto t^2$, modulated by strong fluctuations at frequency determined by $\hbar\delta/J$ (b) mean field ansatz in coupling, including the full atomic dynamics at $L=48$, $N=18$, $g/g_{\text{cr}}=25$,$\hbar\delta/J=200$, $\hbar\Gamma=7.5$. $m=600$, and $\hbar\tau/J=0.005$ the increase is obtained to be exponential. The extracted growth rates at various parameters are shown in Fig. 7.12.

atom-cavity coupling strength and then present the results of our numerical simulation and argue picture of the ordering dynamics remains valid also in one dimensional systems on an external optical lattice [Sec. 7.3.1]. Then we complement these results with the systems reaction to a continuous increase in the coupling until reaching a set value above the critical coupling that marks the self-ordering transition in Sec. 7.3.2.

7.3.1 Quenches

At strong long-range interactions, in the experiment an exponential growth in the atomic order parameter was directly observed. It prevails over a wide range of microscopic parameters in the Fermi gas as well as an extended time scale. Such behavior is seen as the hallmark of a dynamical instability [278]. The cavity-mediated global range interactions enable collective processes and introduce universal properties. As an example here the growth rate of the order parameter is observed to exceed the Fermi energy by over an order of magnitude in Ref. [2]. Contrarily in many-body systems where the dynamics is only driven by contact-interactions, it saturates at scaled determined by the Fermi-time [279], since in a Fermi gas, it represents the fastest microscopic timescale.

Generally for the full dynamics we expect a complex interplay of the energy scales at the beginning of the self ordering process, that can not necessarily be time resolved in experiments. Quenching the coupling strength, we expect a "seeding" of the self-ordering process [52] where the atom correlations are mapped to fluctuations in the cavity field. In this regime, oscillations at a frequency determined by the pump-cavity detuning δ^{-1} can be expected, and the photon field occupation grows algebraically. As time progresses, a coupled atom-photon dynamics emerges, as the cavity field approaches a state that can be approximated by a coherent classical field as we saw in our adiabatic elimination approach. The weight of the initial fluctuations decreases with the system size $N_{\text{pho}} \sim \langle\hat{\Delta}^2\rangle$. For our one-dimensional system, evolving the full Lindbladian model as presented e.g. in Sec. 7.1, we are typically restricted to system sizes where the initial rise in the photon number is still dominated by the algebraic behavior of the fluctuations in 1D. As shown in Fig. 7.11 (a), the photon number rises approximately quadratically at short times after the quench. In order to reach larger system sizes beyond what is possible taking the full cavity dynamics into account we employ a mean field decoupling similar to the one described in Sec. 3.1. We neglect the fluctuations in the atom-cavity coupling [152, 164, 166]. By this we implicitly assume that cavity field is described by a single coherent state. With this method, we aim to extract the growth rate over a wide range of coupling strengths.

Thus, we consider the following Hamiltonian for the coupled atom-cavity system [78, 152], as derived here for spinful fermions in Eq. (3.4).

$$\hat{H}_{\text{eff}} = \hat{H}_{\text{FH}} - \hbar g\lambda(\Delta)\hat{\Delta} \quad \text{with} \quad \hat{H}_{\text{FH}} = -J\sum_{\langle j,l\rangle,\sigma}\left(\hat{c}^{\dagger}_{j\sigma}\hat{c}_{l\sigma} + \text{h.c.}\right) + U\sum_{j}\hat{n}_{j\uparrow}\hat{n}_{j\downarrow} - \mu\sum_{j,\sigma}\hat{n}_{j,\sigma}.$$

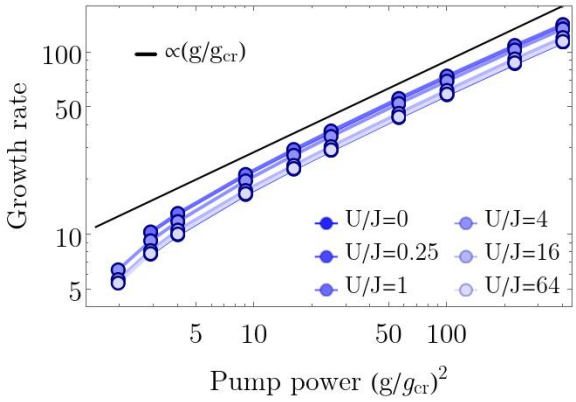

Fig. 7.12: Growth rate across the self-ordering transition after a quench in the atoms-cavity coupling to $\hbar g/J$ relative to the critical coupling where the phase transition occurs in the steady state $\hbar g_{\mathrm{cr}}/J$. We show various on-site interaction strengths with $N=48$, $\hbar\delta/J=200$, $\hbar\Gamma=7.5$.

This is the same model we used in the adiabatic elimination approach. As presented in Chapter 6, the cavity-induced global-range interactions introduced via the transversal pump beam induces a phase transition of the steady states to a density-wave-ordered state above a critical coupling strength [1, 29]. However, here we do not concentrate on steady state but rather recover the short-time dynamics of interest, which was done in collaboration with Catalin-Mihai Halati. Although the cavity field is treated with the mean field approach, the atomic short-range dynamics contain all correlations and are evolved in a numerically exact way. An adapted time-dependent matrix product state (tMPS) algorithm is applied to the Hamiltonian given in Eq. (3.4). Simultaneously, the equation of motion for the cavity field

$$\frac{\partial}{\partial t}\langle\hat{a}\rangle = i\frac{g}{\sqrt{L^d}}\langle\hat{\Delta}\rangle - \left(i\delta + \frac{\Gamma}{2}\right)\langle\hat{a}\rangle$$

is numerically integrated to determine $\lambda = \langle\hat{a}+\hat{a}^\dagger\rangle/\sqrt{L}$. When starting the evolution, the cavity field is initially empty, $\lambda(t=0)=0$, while the atoms are in the ground state of the resulting Fermi-Hubbard model. As shown in Sec. 4.2.2, this is achieved using the DMRG-algorithm [175, 280].

At short times, the photon number $N_{\mathrm{pho}}=|\alpha|^2$ is observed to grow exponentially [see Fig. 7.11 (b)]. Remarkably, this observation holds for the entire range of system parameters we consider and for atomic systems obeying both fermionic and bosonic statistics. The exponential growth rate is determined as a function of the atom-cavity coupling $\hbar g/J$ for various fixed values of the atomic on-site interaction U/J, as shown in Fig. 7.12. The parameters are chosen such that we obtain a scale separation comparable to the experiment. We scale the coupling with the critical value $\hbar g_{\mathrm{cr}}/J$ that marks the self-ordering transition. This transition point at the mean field level is obtained by self-consistently solving the mean-field steady state condition defined in Eq. (3.3) with respect to the ground state of the Hamiltonian, Eq. (3.4). Interestingly, the growth rate is mainly dependent of the atoms-cavity coupling, while at the parameters considered the on-site interaction ranging from the non-interacting to strongly repulsive regime only has a weak affect on the growth rate Fig. 7.12. We obtain the same behavior and even similar quantitative results for both fermionic and bosonic atomic ensembles throughout the entire parameter range we investigate. In accordance to what was obtained experimentally for the 3D Fermi gas, this result suggests that the self-ordering to a density wave state is dominantly driven by the cavity-mediated long range interactions, while the microscopic details of the atomic systems only constitute a weak influence.

The agreement among systems featuring different atom-systems strengthens that the exponential increase of the growth rate will likely hold for systems featuring similar energy-scale competitions.

Here we provided an example for the complex open system dynamics at commensurate filling, putting into perspective our ongoing in-depth analysis. Special interest lies in the dynamics, as the Mott-insulating Fermi-Hubbard state is destroyed when the atoms order.

7.3.2 Linear parameter ramps

We now focus on the behavior of the system as the global-range coupling strength is linearly ramped up across the critical point at which self-ordering occurs. In the experiment, the universality of the growth in the order is also apparent these ramp protocols. The ordering dynamics are in accordance with the Kibble-Zurek scenario [281], i.e. the defect dynamics (here defects to perfect atomic order) exhibit a power-law behavior of the intrinsic length- and time scales of the system. In the experimental setup, they were able to observe that during the ramp the order parameter grows in accordance with a dynamical scaling ansatz relying on the instantaneous instability rate, which has been as obtained from experimental runs where the coupling was quenched. It follows, that the response of the system to linear ramps is fully determined by its reaction to quenches rather than its behavior at criticality. The observed behavior is in accord with the generic behavior in the unstable regime at early times [278].

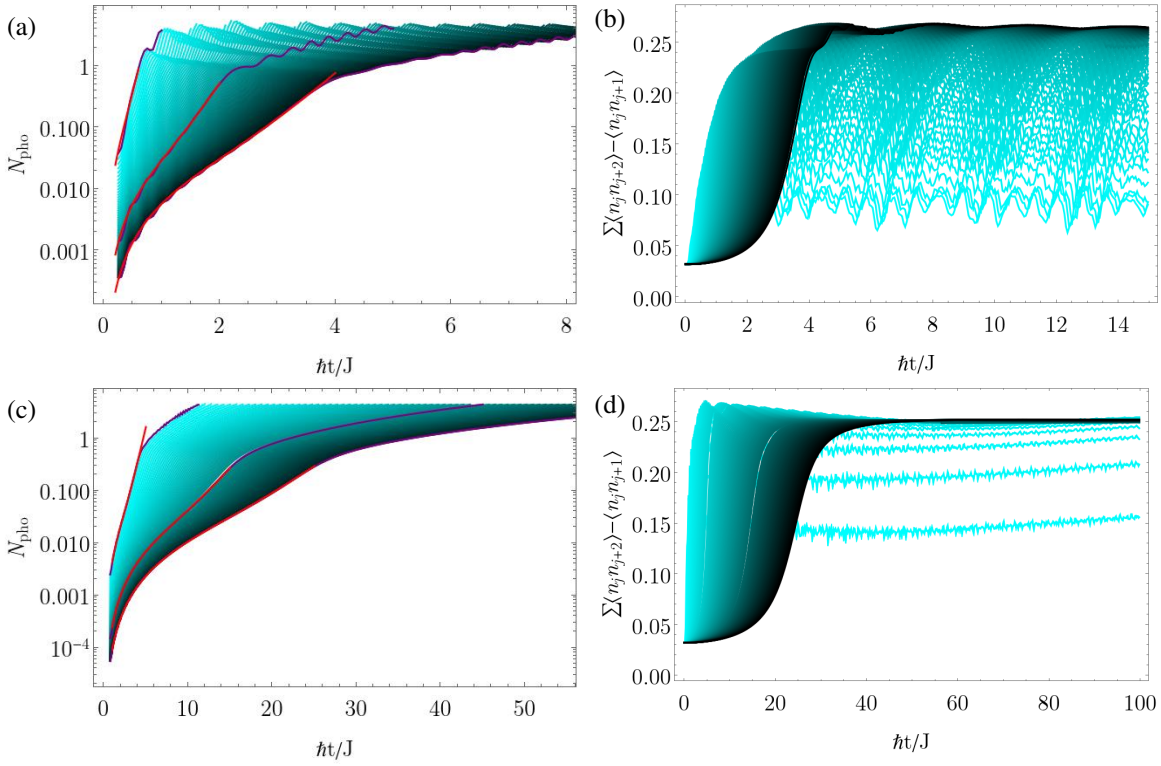

Fig. 7.13: (a),(c) Photon number $\langle N_{\text{pho}}\rangle$ evolution for varying linear ramp time (a) $\hbar\tau_{\text{ramp}}/J \in [1, 10]$ in steps of 0.1 (c) $\hbar\tau_{\text{ramp}}/J \in [1, 100]$ in steps of 0.75 with short-time nonlinear fits [red lines]. (b),(d) average density-density correlation contrast at distances 2 and 1. Starting with the ground state of the Fermi-Hubbard model with $L = 16$, $N_{\text{part}} = 6$, $S_z = 0$ and $U/J = 2$, the parameters used in the time evolution are $\hbar g_{\text{final}}/J = 7$, $\hbar\Gamma/J = 0$, $\hbar\delta/J = 20$, $m = 300$, $N_p = 25$ and $\hbar\tau/J = 0.005$.

Strikingly, running the experiment at three values of the detuning, the growth rate can be collapsed to one curve, which helps to identify the long-range interaction strength as the relevant parameter in the setup that determines the growth rate of the order across the phase transition.

These results motivate us to study the full dynamics and compare the behavior of our system to the ordering dynamics seen in the experiment. In agreement with the experimental observations, we obtain an exponential ordering dynamics at early times, whose growth rate is mainly influenced by the strength of the long-range interactions [see Fig. 7.13]. We show the number of photons in the cavity field as a function of time for various linear ramps. We neglect here the dissipation of the cavity field, setting $\hbar\Gamma/J = 0$. For a system at low filling $L = 16$, $N = 6$, moderate on-site interaction $U/J = 0$ and large detuning $\hbar\delta/J = 20$, in each of the ramps, starting at time $tJ/\hbar = 0$, the coupling is linearly increased until it reaches the final value $\hbar g_{\text{final}}/J$, at the specific ramp time $\tau_{\text{ramp}} J/\hbar$. We show both short ramp times [Fig. 7.13 (a)] and long ramp times [Fig. 7.13 (c)]. One can clearly identify a region in time within the ramp where the photon number shows exponential growth. We account the non-exponential

growth at very short below times $tJ/\hbar \sim 1$ to the influence of the detuning or the influence of fluctuations that are not considered in the determination of the exponential scaling law, but very well influence our system dynamics. In the slowest ramps we can observe a thermalization while the coupling increases, and no oscillation in the average cavity field occupation can be observed. In the contrast [Fig. 7.13 (b),(d)] we see a clear reduction of the ordering for faster ramps within the times we show. The atoms are not able to follow the ramp dynamics and a larger amount of defects to the fully ordered state remain during the phase transition.

We show these quantities in a density plot [Fig. 7.14], where in (a) the fringes from the short-time oscillations in the photon number can clearly be seen at short ramp times. Especially at low couplings around the phase transition $\hbar g/J \sim 1$ we see that if the ramp times are too short, i.e. $\tau_{\text{ramp}}/J \leq 4$ the ordering process is not able to follow the increase of the coupling and order correspondingly but rather delays and the cavity field thus emerges at later times after the ramp is complete.

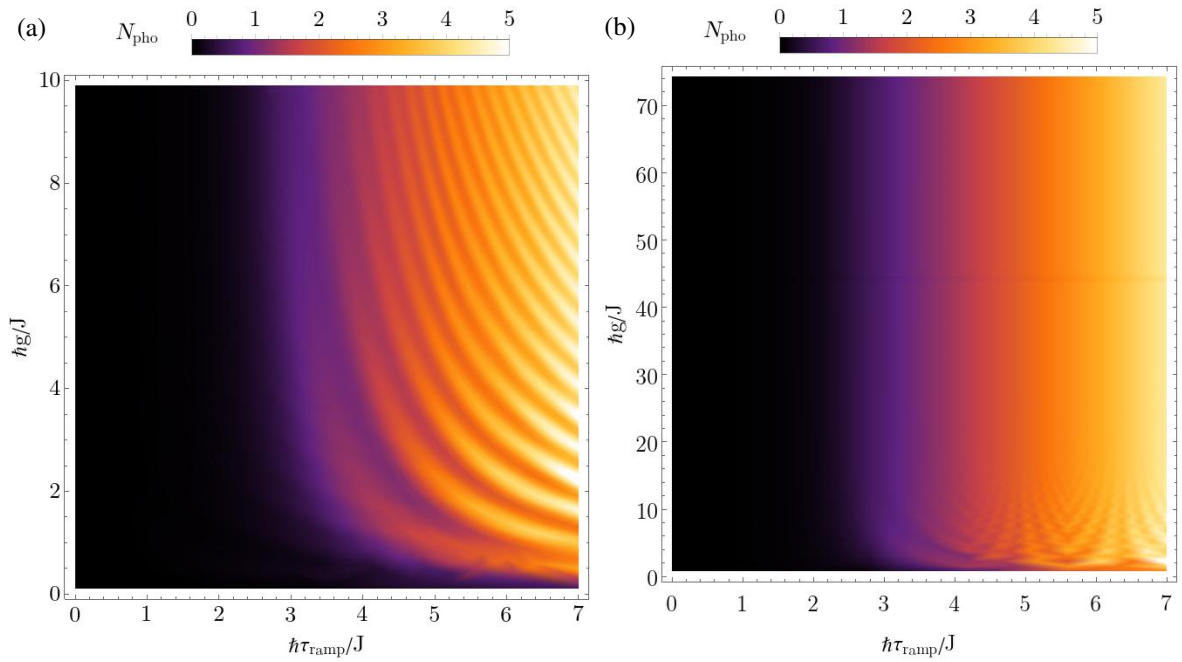

Fig. 7.14: Photon number $\langle N_{\text{pho}} \rangle$ varying linear ramp time $\hbar\tau_{\text{ramp}}/J$ and atoms-cavity coupling $\hbar g/J$. Starting with the ground state of the Fermi-Hubbard model with $L = 16$, $N_{\text{part}} = 6$, $S_z = 0$ and $U/J = 2$, the parameters used in the time evolution are $\hbar g_{\text{final}}/J = 7$, $\hbar\Gamma/J = 0$, $\hbar\delta/J = 20$, $m = 300$, $N_p = 25$ and $\hbar\tau/J = 0.005$.

The implementation of parameter ramps bears further intriguing possibilities for detailed future investigations. On one hand, when comparing to experimental results, one often encounters the issue that in the experiment an instantaneous quench the coupling strength is not necessarily realistic or desired. Therefore, including flexible parameter protocols beyond the quench surely will be beneficial for future collaborations. But it can also open interesting opportunities for numerical exploration of new phenomena in the system dynamics by itself. A near-adiabatic increase of the parameter can reduce the steep increase in the photon number to values way above the eventually obtained long-time limit, which permits us to reduce the dimension of the photonic Hilbert space. Additionally, we might be able to use the quantum Mpemba-effect [282–284], that has recently been predicted for quantum non-equilibrium dynamics, to our advantage. It describes the process that under specific conditions a system relaxes to equilibrium more quickly if it is initially further away from equilibrium. More complex coupling protocols during the early time evolution might allow us to directly cause the excitation of high energy but short-lived modes that quickly decay to the steady state, while avoiding the occupation of long lived excited states.

7.4 Comparison of long-time MPS results to analytic steady state results

In this section we want to present some results comparing numerical results obtained with tensor-network methods [see Sec. 7.1 & 7.2] to the steady state values from our analytic approximation using adiabatic elimination of the

cavity degrees of freedom, going beyond standard mean field models by including fluctuations in the atoms-cavity coupling [see Chapter 6].

From the real time evolution of the stochastically sampled quantum trajectories (Monte-Carlo Wavefunctions) the expectation value of several system-characterizing observables is extracted in the long-time limit. We want to stress, that the results we show give us a hint at interesting effects happening. However, depending on the specific parameter regime dynamics towards the steady state slow down especially in the long-range correlations and are not yet steady within the computationally reachable time range. However, already the extracted results at finite time yield useful information about the system. In the region where two steady state solutions appear in the analytic treatment like at the edges of the bistabilities or around the self-ordering phase transition at commensurate filling, the system dynamics and thus convergence towards the steady state is seen to slow down [113]. In other system, this was related to a gap closing in the Liouvillian spectrum [40, 285]. The difficulties to reach a steady state are especially prevalent in the fermionic system in one dimension due to the strong effects of Fermi-correlations [286] that further slow the thermalization processes.

One thus needs to be careful with statements about the numerically determined steady state as it might as well be a long-lived meta-stable state. In long range systems, often long-lived meta-stable states exist that are difficult to differentiate from the steady state within the computable time scales. We will in the following discussion instead refer to the numerical results as "long time values". Nevertheless even the observed slowing of the dynamics might reveal information about the systems state.

To compare the different methods we choose observables that characterize both the cavity field and the ordering of the atomic subsystem. These are the number of photons on the cavity field N_{pho} as well as the difference of density-density correlations at even and odd distances Eq. (7.1) which captures the ordering of the atoms on either even or odd sites of the atomic chain in one dimension. This choice was justified in Sec. 7.1.

Note, that while we identified and discussed a regime in the analytic adiabatic elimination approach where the fluctuations induce a bistability within the self-ordered phase [see Sec. 6.3 for details] it is not straightforward to identify this phenomenon in the trajectories. The full Lindbladian time evolution generally converges to a unique steady state at finite system size in the absence of strong symmetries [40]. This raises the question if and how the bistabilities from mean field methods can be observed [101]. The density matrix is here reconstructed from the average over the sampled trajectories, individual trajectories thus do not yield full information about the ordering and excitations contributing to the steady state. While the trajectories do bundle around values of the photon number associated with atomic orderings with a specific number of defects, they can not be attributed to different steady states. Instead the system always results in a specific steady state that might consist of a mixture of superposition of the different stable solutions predicted by the analytic results. Rather, if the bistability is visible in the full numerical evolution, it may manifest in meta-stable states or change in behavior depending on the history of the system. This could for instance mean that after suddenly turning on the atoms-cavity coupling strength $\hbar g/J$ to a value within the bistable regime in the analytic mean-field steady-state solution at finite effective temperature, the system is more likely to evolve towards the lower photon number solution due to the large energy deposit in the system and connected disorder of the atoms. Without the presence of specific cooling effects it might take a long time for this excessive energy to dissipate from the system, which would lead to a higher probability of the more ordered high-photon number solution.

We present a comparison of the number of photons and atomic even-odd density-density correlation in Fig. 7.15 for a system at quarter filling ($N = L/2$) with large on-site interaction $U/J = 40$. Here the adiabatic elimination results are calculated both via exact diagonalization of the effective Hamiltonian for a system size $L = 8$ solving Eqs. (3.3) & (3.14) [blue (stable) and green (unstable) points] and in the weak tunneling perturbation in the thermodynamic limit solving Eqs. (3.25) [red/purple (stable) points, unstable solutions not shown]. The stability against linear variation of the cavity field quadrature is again determined with the stability conditions derived in Sec. 3.3. For comparison, the $T = 0$ MF results are included as a black line. Vertical lines denote parameter resonances in the atomic limit. As identified in Sec. 6.1.2 & 6.1.3 these can allow for an efficient energy transfer from the atomic subsystem to the cavity field.

The MPS runs start from the ground state of the corresponding Fermi-Hubbard model with $U/J = 40$ and chain length $L = 12$, suddenly switching on the coupling at time $tJ/\hbar = 0$. The plotted values are extracted at the longest reachable time for the specific parameter set. This reduces as the coupling increases due to the higher dimensions of the cavity mode Hilbert space needed to capture the field dynamics and typically larger bond dimensions to

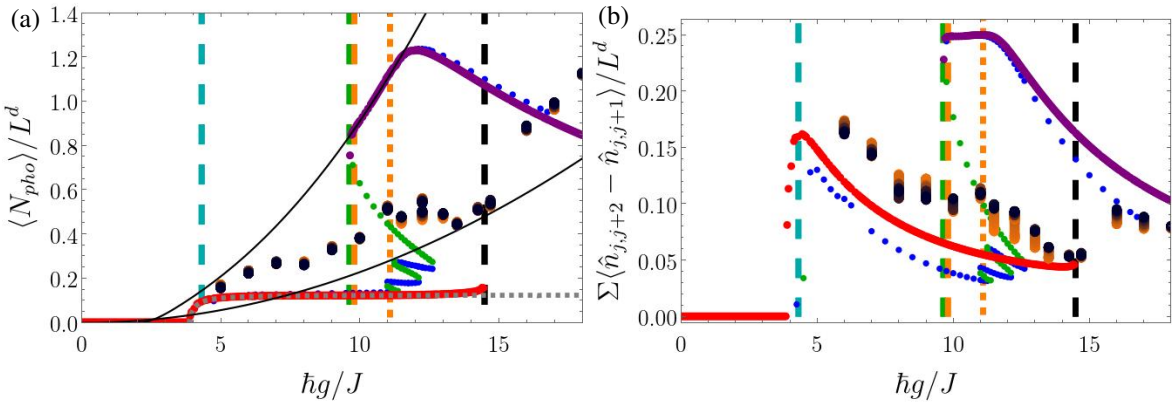

Fig. 7.15: Comparing the steady state results obtained from the thermal mean field method to the long time limit of the real time evolution using MPS algorithms. We show (a) the relative photon number $\langle N_{\text{pho}}\rangle$ and (b) atomic density-density correlation contrast $\sum_{j=1}^{L-2}\langle\hat{n}_j\hat{n}_{j,j+2}\rangle/(L-2)-\sum_{j=1}^{L-1}\langle\hat{n}_j\hat{n}_{j,j+1}\rangle/(L-1)$. The parameters used are $S_z=0$, $U/J=40$, $\hbar\Gamma/J=3$ and $\hbar\delta/J=5$. The lines can be identified as follows: for the analytic results in the thermodynamic limit,$L\to\infty$ for $U/J\gg1$ stable solutions 1 (red) and 2 (purple); for $L=8$ the solution stable (blue), unstable (green); $L=8$, within the $T=0$ MF approximation (black). The MPS runs start from the ground state of the corresponding Fermi-Hubbard model (suddenly switching on the coupling at time $tJ/\hbar=0$) at quarter filling with $L=12$. The long time values extracted from the trajectory averages are plotted as orange points that get darker as the time progresses. The points are obtained at individual convergence parameters and reachable final times. The corresponding values are given in Appendix D.1.

accommodate the photonic Hilbert space that approximately grows with $\sim g^2$.

Comparing the methods, we observe an initial increase as the system self-orders. The long-time values of the photon number from the numerical runs reside between the value predicted from the $T=0$ MF and adiabatic elimination. This could have multiple causes, i.e finite size effects that are expected to be underestimated by the analytic approaches due to the mean field assumption in the derivation. Also the approximations could lead to a shift in the phase diagram or an under/over estimation of the effective temperature depending on the specific parameter regime. We will thus refrain from quantitative comparisons between the two fundamentally different methods and try to concentrate on qualitative behavior changes. Around the coupling strengths where the fluctuations-induced bistability appears, we can indeed observe a slight plateau in the photon number for $\hbar g/J\approx\{11,15\}$. This reflects in the decreasing density-density correlation contrast in the same region.

To conclude, while these results do not suffice to make precise statements on how the fluctuations-induced bistability manifests in the quasi-exact numerical long-time results yet, we are able to identify a region with counter-intuitive plateau-like behavior that differs from the phase diagram regions where the bistability is not present in the adiabatic-elimination approach. This motivates future in-depth analysis of the full Lindbladian steady state behavior in the parameter regime at hand. However it might be favorable to concentrate on the case of bosonic atomic systems where we also identified the bistability [see Sec. 6.3.1] since here, though also challenging, the convergence of the numerical time evolution toward the steady state does not suffer from Pauli blocking and requires lower bond dimensions due to the absence of Fermi-correlations [286].

Summary

In this chapter we presented promising results for the dynamics of the atom-cavity coupled system at both quarter filling and half filling. We are able to observe the self-ordering process, identify time scales and scaling behavior. We show how, while the density profile remains symmetric, the atomic ordering appears in the non-local density-density correlation contrast as well as the charge-and spin-density wave order parameters. At half filling, we confirm the self-ordering process is accompanied by the creation of doubly occupied sites. The quantum trajectories are seen to bundle in subspaces we identify with different imbalances in the atomic density, with transitions

between them. In the photon number state, we see that the cavity field is in a superposition of coherent states expected for the respective imbalance subspaces. In a regime where the system parameters are of similar order, long-lived oscillations occur that are especially pronounced in the single-particle correlations at even distance. We observe how an increased pump strength within the self-ordered phase typically increases the cavity occupation but leads to a larger disorder in the atoms which reduces the density contrast. The disorder also increases at large dissipation, where the system decoheres and approaches a fully mixed state.

Further the dynamics of the self-ordering transition was investigated in the experimental limit, looking at both quenches and linear ramps in the coupling parameter. For quenches, we extract an exponential growth rate of the self-ordering order parameter as the system crosses the phase transition. This is only dependent on the coupling parameter and not the on-site interaction strength. With linear ramps, we demonstrate how slow ramps allow for a near-adiabatic transition to the self-ordered phase, reaching close to maximal ordering at the final ramp time. The faster the ramp crosses the critical coupling parameter, the more defects are introduced in the transition.

Finally, we provided first results comparing the obtained long time results from the numerically exact time evolution of the full Lindbladian model to the steady state results determined with our analytic adiabatic-elimination method. We showed a counter-intuitive plateau-like behavior in the region where one would expect the fluctuation-induced bistability to manifest in the analytical approach.

Chapter 8

Conclusion

In this work we provided a detailed picture of both the steady state and dynamic properties of a complex quantum many-body system with global coupling to a bosonic mode. We put our focus on a quantum-many body system of spinful fermions globally coupled to a dissipative cavity field by a transverse drive. The intricate interplay of short- and long-range atomic interactions as well as kinetic processes generates complex quantum phases that can be accessed through external perturbations. Balancing driving and dissipation present in the system further yields the possibility to stabilize out-of equilibrium phases with certain desired properties, which makes it a perfect platform to study out-of equilibrium phase transitions.

While most explicit results are obtained for a spinful fermionic ensemble of atoms, we occasionally extend our methods to bosons for comparative purposes and to substantiate further the generality of the described phenomena beyond our specific model. To start with the system Hamiltonian in second quantization as well as the corresponding Lindbladian differential equation that determines the dynamics of the full atoms-cavity coupled system towards its steady state was derived.

We further introduced multiple newly developed and applied methods that allow us to gain a broad understanding of the intricate steady state phase diagrams beyond the mean-field level. Our *many-body adiabatic elimination* approach considers fluctuations in the coupling to the photonic mode. The fluctuations cause the system to thermalize towards steady states with a self-consistently determined effective temperature. The method was complemented by various limit considerations, notably a weak tunneling perturbation going to the thermodynamic limit, that proves to be valid in a regime of the steady state phase diagrams that exhibits intriguing fluctuation-induced bistability at low fillings. Notably the results in this limit can be generalized for higher dimensions. The stability of the obtained solutions in the mean field approach is evaluated using a stability condition we derived for thermal systems. With this we presented a variety of analytical tools that allowed us to efficiently compute the steady state behavior of the effective driven dissipative atoms-cavity coupled system. We showed that within the many-body adiabatic elimination approach our complex effective model takes the form of a ionic Hubbard model, where the potential staggering in to be determined self-consistently. A general summary of some properties of the standard ionic Hubbard model was provided in order to facilitate the description of phases and physical processes observed in the effective model. Additionally we confirmed the chaotic nature of the ionic Hubbard Hamiltonian through a thorough analysis of the energy level statistics (Ref. [3]). These properties of the ionic model extend to our effective model capturing the atoms-cavity coupled system and solidifies our assumption that the atomic steady state can be well described by a thermal state.

Applying these analytical considerations to the dissipative atoms-cavity coupled system at hand, we presented the obtained steady state results for atomic densities of quarter filling and half (commensurate) filling. These cases exhibited fundamentally different behavior at both the self-ordering transition and within the self-organized´ phase. Special focus is put on the discussion of the *self-ordering transition* where the atoms spontaneously order and a finite cavity field was seen to emerge. We contrasted the mixed nature of the steady states across the phase transition taking into account fluctuations in the coupling with the transition between ground states obtained at the $T = 0$ mean field level. We complemented our observations with analytical approximations for the critical

coupling strength that marks the self-ordering transition in both the non-interacting and atomic limit and identify the respective scaling with the system parameters. Within the self-ordered phase we discussed the influence of atomic resonances on the self-consistently determined temperature of the steady state. We identified parameter regime where *cavity cooling* resonances allow for an efficient energy transfer from the atomic ensemble to the dissipative cavity mode. In our interacting system, we found processes that enable *many-body cooling* effects that are based on resonant photon-assisted transitions between states with and without double occupied sites. Deep in the self-ordered regime a saturation of the cavity field observables with the coupling strength was observed. We provided the derivation of a *universal scaled photon number* in the large temperature limit and confirmed the corresponding scaling of the density imbalance with the system parameters.

Within the self-ordered regime at quarter filling, we identified a region where multiple stable steady state solutions appear. We call this novel mechanism *fluctuation-induced bistability* (Ref. [1]) since it relies on energy level-crossings in the excitation spectrum of the effective dissipative quantum model. Therefore the bistability can not prevail at the $T = 0$ mean field level. This is an astonishing property, since it is widely believed that mean-field methods remain valid for long-range couplings. We provided a detailed analysis of the processes that dominantly cause the emergence of the bistable region and physical properties of the individual stable solutions. In the strong atoms-cavity coupling regime two stable self-organized steady state solutions are obtained, that are characterized by different self-consistently determined temperatures and cavity field order parameters. Throughout the self-ordered phase the dominant (lowest energy) contribution remains the same. The different nature of the two solution is shown to originate from the weight of the admixed excited states. In the steady solution associated with the stronger cavity field, excited states containing double occupancies become crucial and many-body cooling mechanisms are seen to effectively lower the temperature. We were able to attribute the origin of the fluctuation-induced bistability to the interplay between the cavity-photon mediated global-range coupling and the short-range atomic interactions. In the weak hopping perturbation the existence of this bistability was obtained independent of the dimensionality of the atomic gas or fermionic nature of the atoms. We showed equivalent results for a bosonic many-body system coupled to a dissipative cavity mode with a filling of on average one atom for every two lattice sites. Here the bistability repeated for higher numbers of the on-site occupations and therefore strengthened our arguments for the mechanism that causes the bistability to appear. We are therefore confident that the underlying mechanism exists in a large class of atoms-cavity models with equivalent competing photonic and atomic energy scales and the here presented properties can be seen as a paradigmatic example. In contrast to the fluctuation-induced bistability at quarter filling, at commensurate filling a bistable behavior was observed at the self-ordering transition. This however could be connected to a level crossing in the ground state of the effective model.

Further we investigated the out-of equilibrium dynamics of such a driven dissipative many-body atomic system coupled to a cavity mode. We presented the newly developed quasi-exact numerical algorithms based on tensor network methods, which allow to perform an efficient full quantum time evolution of the many-body fermionic system with global photon-mediated interactions captured by the Lindbladian dynamics. We provided an introduction to Matrix Product State methods, followed by an overview of the full algorithm variants and introduced the methods used at each step in the time evolution. These included time evolution with the Trotter-Suzuki-method combined with swap gates that decompose the global interaction to a sequence of short-range interactions or using the Time-Dependent-Variational principle. The dissipative nature was included via either a Purification ansatz or Monte-Carlo-Wavefunctions combined with stochastic sampling. All variants of the algorithm allow to treat a quantum many-body system with competing short- and long- range interaction, coupled to a lossy bosonic mode and can potentially be adapted to a broad range of systems. We provided an analysis of the numerical convergence of our results depending on various parameters for all of the previously presented method variants. The validity of the obtained results was further confirmed by comparing the measured observables from the independently implemented methods in various limits.

With these methods we were able to analyze the features of the dynamics approaching the steady state. We showed the time evolution of various observables for systems at both quarter- and half filling. The self-ordering dynamics were observed in the cavity field as well as atomic density-density correlations. The cavity field was seen to approach a superposition of coherent states that could be associated with specific subspaces with different levels of atomic order. In special parameter regimes, persistent oscillations were observed in the single-particle correlations. Besides instantaneously switching on the atoms-cavity coupling, we showed the time evolution ramping up the coupling strength across the self-ordering transition at various speeds. In Ref. [2] this was investigated for a variety of experimental and theoretical models to determine a scaling law. Finally we connected our analytical insights into the steady state phase diagrams in the framework of adiabatic elimination to the numerically obtained

long-time results and provided a first step towards the interpretation of the steady state of the full Lindbladian model. We focused here on the regime where the fluctuation-induced bistability was observed with the analytical ansatz and pinpointed a counter-intuitive behavior in both the cavity field and atomic ordering. Therefore we are confident, that the bistability manifests also in the statistics of the Monte-Carlo trajectories.

Overall we provided a detailed picture of both the steady state and dynamic properties of the complex quantum many-body system with global coupling to a cavity field. Many of our findings such as the identified many-body cooling resonances that influence the effective temperature and order of the steady state or the fluctuation-induced bistability can likely be generalized to a large class of atoms-cavity models with comparable atomic and photonic energy scales.

Appendix A

Appendix "Analytical Methods"

A.1 Photonic states of the cavity field

In this section we introduce a theoretical description of coherent state light fields that will allow us to deduce the state of the cavity field from the measured observables.

In the adiabatic elimination we assume the cavity field to be in a coherent state $|\alpha\rangle$. Generally, this is written in the Fock-basis $|n\rangle$

$$|\alpha\rangle = e^{-\frac{|\alpha|^2}{2}} \sum_{m=0}^{\infty} \frac{\alpha^m}{\sqrt{m!}} |m\rangle \tag{A.1}$$

Projecting onto the number state $|n\rangle$

$$|\langle n|\alpha\rangle|^2 = \left| e^{-\frac{|\alpha|^2}{2}} \sum_{m=0}^{\infty} \frac{\alpha^m}{\sqrt{m!}} \langle n|m\rangle \right|^2 = e^{-|\alpha|^2} \frac{|\alpha|^{2n}}{n!} \tag{A.2}$$

Note, that this corresponds to a Poisson-distribution.

In our case. the system is invariant under simultaneously inverting cavity field and sublattice imbalance. Generally we write

$$|\alpha\rangle_{CS} = \frac{1}{\sqrt{2}} \big(|\alpha\rangle + e^{i\varphi} |-\alpha\rangle \big) \tag{A.3}$$

The density matrix of a superposition of N coherent states $e^{i\varphi_j} |\alpha_j\rangle$ is given as [287, 288]

$$\hat{\rho} = A \Big[\sum_{j=1}^{N} |\alpha_j\rangle \langle\alpha_j| + \underbrace{\sum_{\substack{j=1 \\ l\neq j}}^{N} e^{i(\varphi_j - \varphi_l)} |\alpha_j\rangle \langle\alpha_l|}_{\text{correlations}} \Big] \tag{A.4}$$

with $A = \Big[N + 2 \sum_{\substack{j,l=1 \\ l<j}}^{N} \exp\big(-\frac{|\alpha_j - \alpha_l|^2}{2} \big) \cos((\varphi_l - \varphi_j) + \alpha_j \otimes \alpha_l) \Big]^{-1}$.

we define the complex $\alpha_j = \alpha_j^x + i\alpha_j^y$ and $\alpha_j \otimes \alpha_l = \alpha_j^x \alpha_l^x - \alpha_j^y \alpha_l^y$.

for $|\varphi_j - \varphi_l| = \pi$, the off-diagonal entries vanish and this represents the statistical mixture of coherent states. This is what we would expect for individual trajectories since we consider a single-mode cavity.

The corresponding Wigner-function is given by

$$W(\alpha';\alpha_1,...,\alpha_N) = A\Big[\sum_{j=1}^{N} W_j(\alpha';\alpha_j) + \underbrace{2\sum_{\substack{j,l=1\\ l<j}}^{N} W_{jl}(\alpha';\alpha_j,\alpha_l)}_{\text{correlations}}\Big] \tag{A.5a}$$

with

$$W_j(\alpha';\alpha_j) = \frac{2}{\pi}\exp\Big(-2|\alpha'-\alpha_j|^2\Big) \tag{A.5b}$$

$$W_{jl}(\alpha';\alpha_j,\alpha_l) = \frac{2}{\pi}\exp\Big(-2\Big|\alpha'-\frac{\alpha_j+\alpha_l}{2}\Big|^2\Big) \times\cos\big(\varphi_l-\varphi_j+2\alpha'\otimes\alpha_j-2\alpha'\otimes\alpha_j+\alpha_l\otimes\alpha_j\big) \tag{A.5c}$$

Note the connection to the Husimi-Q-function via Weierstrass transformation

$$Q(\alpha) = \frac{2}{\pi}\int W(\alpha')e^{-2|\alpha-\alpha'|^2}d^2\alpha' \tag{A.6}$$

From this, the photon number distribution for a statistical mixture of coherent states is given by

$$P_m = A\Big[\sum_{j=1}^{N} e^{-|\alpha_j|^2}\frac{|\alpha_j|^{2m}}{m!}\Big] \tag{A.7}$$

In order to detect whether the field is classical or shows quantum nature, the squeezing is a powerful parameter. It is defined using the variance in the phase space of parameters

$$\eta_1 = \frac{1}{2}(\hat{a}^\dagger + \hat{a})$$
$$\eta_2 = \frac{1}{2i}(\hat{a}^\dagger - \hat{a})$$

They satisfy the uncertainty principle with $\langle\Delta\eta_1^2\rangle\langle\Delta\eta_2^2\rangle \geq \frac{1}{16}$

For a coherent state one obtains minimal variance in both phase space directions $\eta_{1/2}$ and a circular probability distribution.

$$\langle\Delta\eta_{1/2}^2\rangle = \sqrt{\langle\alpha|\,\eta_{1/2}^2\,|\alpha\rangle - \langle\alpha|\,\eta_{1/2}\,|\alpha\rangle^2} = \frac{1}{4}$$

A sign for quantum nature of a light field is squeezing. Here, the variance is decreased in one direction at the cost of the other one, e.g.

$$\langle\Delta\eta_1^2\rangle = \frac{\gamma}{4} \qquad \langle\Delta\eta_2^2\rangle = \frac{1}{4\gamma}$$

A.2 Thermodynamic limit in the weak tunneling regime - 2D atomic lattice

In this section, we provide some analytic background for the statements about the validity of the derived system of equations Eqs. (3.25) for the thermodynamic low-hopping limit in two dimensions [Sec. 3.2.2]. This also strengthens our claim that one can expect to obtain similar steady-state results at even higher dimension and various lattice geometries.

In two dimensions, the kinetic term in the Hamiltonian can be split into parts containing the hopping along each of the lattice dimensions $\hat{H}_{\text{kin}} = \hat{H}_{\text{kin}}^x + \hat{H}_{\text{kin}}^y$. We consider $\langle j,l\rangle$ to denote neighbouring sites on the 2D square lattice.

In the weak tunneling perturbation $\mathcal{O}(J^2)$, the hopping does not mix the different lattice directions since within the second order hopping process the initial density distribution needs to be restored in order for it to contribute in the energy transfer. One thus completely separated the contributions from dynamics along each lattice dimension. We evaluate the resulting susceptibility (c.f. Eq. (3.19) in 1D) on the 2×2-unit cell, resulting in

$$\begin{aligned}
\chi_T^{\mathrm{2D}}(\omega) = \frac{-1}{\omega^2 Z_{\mathrm{2D}}}\Bigg\{ & 8\left(\frac{1}{-2g\lambda+\omega+i\epsilon}-\frac{1}{2g\lambda+\omega+i\epsilon}\right)\Big[\sinh(\beta g\lambda)\Big(e^{\beta\mu}+4e^{3\beta\mu}+e^{-\beta(3U-7\mu)}+4e^{-\beta(U-5\mu)}\Big) \\
& +2\sinh(2\beta g\lambda)\Big(e^{2\beta\mu}+e^{-\beta(2U-6\mu)}+2e^{-\beta(U-4\mu)}\Big)+\sinh(3\beta g\lambda)\Big(e^{-\beta(2U-5\mu)}+e^{-\beta(U-3\mu)}\Big)\Big] \\
& +4\left(\frac{1}{-2g\lambda-U+\omega+i\epsilon}-\frac{1}{2g\lambda+U+\omega+i\epsilon}\right)\Big[e^{2\beta\mu}-e^{-\beta(2g\lambda-6\mu+3U)}+e^{-\beta(-2g\lambda-4\mu+U)} \\
& -3e^{-\beta(2g\lambda-4\mu+U)}-e^{-\beta(4g\lambda-4\mu+2U)}-e^{-\beta(2g\lambda-2\mu+U)}-2e^{-3\beta g\lambda}\Big(e^{-\beta(2U-5\mu)}+e^{-\beta(U-3\mu)}\Big) \\
& -2e^{\beta(-g\lambda)}\Big(e^{-\beta(2U-5\mu)}+e^{-\beta(U-3\mu)}\Big)+4\cosh(\beta g\lambda)\Big(e^{3\beta\mu}+e^{-\beta(U-5\mu)}\Big)+e^{4\beta\mu}\left(4-e^{-2\beta U}\right) \\
& +e^{-\beta(2U-6\mu)}\Big] \\
& +4\left(\frac{1}{-2g\lambda+U+\omega+i\epsilon}-\frac{1}{2g\lambda-U+\omega+i\epsilon}\right)\Big[-e^{2\beta\mu}+e^{4\beta\mu}\left(e^{-2\beta U}-4\right)-e^{-\beta(2g\lambda-4\mu+U)} \\
& +e^{-\beta(-4g\lambda-4\mu+2U)}-4\cosh(\beta g\lambda)\Big(e^{3\beta\mu}+e^{-\beta(U-5\mu)}\Big)+2e^{\beta g\lambda}\Big(e^{-\beta(2U-5\mu)}+e^{-\beta(U-3\mu)}\Big) \\
& +2e^{3\beta g\lambda}\Big(e^{-\beta(2U-5\mu)}+e^{-\beta(U-3\mu)}\Big)+e^{2\beta g\lambda}\Big(e^{-\beta(3U-6\mu)}+3e^{-\beta(U-4\mu)}+e^{-\beta(U-2\mu)}\Big) \\
& -e^{-\beta(2U-6\mu)}\Big]\Bigg\}
\end{aligned}$$

Its imaginary part is thus given by

$$\begin{aligned}
\mathrm{Im}\chi_T^{\mathrm{2D}}(\omega) = & 2(\delta(2g\lambda-\omega)-\delta(2g\lambda+\omega))\Big[\sinh(\beta g\lambda)\left(e^{\beta\mu}+4e^{3\beta\mu}+e^{-\beta(3U-7\mu)}+4e^{-\beta(U-5\mu)}\right) \\
& +2\sinh(2\beta g\lambda)\left(e^{2\beta\mu}+e^{-\beta(2U-6\mu)}+2e^{-\beta(U-4\mu)}\right) \\
& +\sinh(3\beta g\lambda)\left(e^{-\beta(2U-5\mu)}+e^{-\beta(U-3\mu)}\right)\Big] \\
& +(\delta(2g\lambda-U-\omega)-\delta(2g\lambda-U+\omega))\Big[-e^{2\beta\mu}-e^{-\beta(2g\lambda-4\mu+U)}+e^{-\beta(-4g\lambda-4\mu+2U)} \\
& -4\cosh(\beta g\lambda)\left(e^{3\beta\mu}+e^{-\beta(U-5\mu)}\right)+2e^{\beta g\lambda}\left(e^{-\beta(2U-5\mu)}+e^{-\beta(U-3\mu)}\right) \\
& +2e^{3\beta g\lambda}\Big(e^{-\beta(2U-5\mu)}+e^{-\beta(U-3\mu)}\Big)+e^{2\beta g\lambda}\Big(e^{-\beta(3U-6\mu)}+3e^{-\beta(U-4\mu)}+e^{-\beta(U-2\mu)}\Big) \\
& +e^{4\beta\mu}\left(e^{-2\beta U}-4\right)-e^{-\beta(2U-6\mu)}\Big] \\
& +(\delta(2g\lambda+U-\omega)-\delta(2g\lambda+U+\omega))\Big[e^{2\beta\mu}-e^{-\beta(2g\lambda-6\mu+3U)}+e^{-\beta(-2g\lambda-4\mu+U)}-3e^{-\beta(2g\lambda-4\mu+U)} \\
& -e^{-\beta(4g\lambda-4\mu+2U)}-e^{-\beta(2g\lambda-2\mu+U)}+4\cosh(\beta g\lambda)\left(e^{3\beta\mu}+e^{-\beta(U-5\mu)}\right) \\
& -2e^{-3\beta g\lambda}\left(e^{-\beta(2U-5\mu)}+e^{-\beta(U-3\mu)}\right)-2e^{-\beta g\lambda}\left(e^{-\beta(2U-5\mu)}+e^{-\beta(U-3\mu)}\right) \\
& +e^{4\beta\mu}\left(4-e^{-2\beta U}\right)+e^{-\beta(2U-6\mu)}\Big]
\end{aligned}$$

From this it is straight forward to calculate the corresponding energy transfer equation.

$$
\begin{aligned}
\frac{\partial \hat{H}_{\text{eff}}^{\text{2D}}}{\partial t} = \frac{4\Gamma g^2}{Z_{\text{1D}}^2}\Bigg\{ & \frac{1}{2g\lambda - U}\Bigg[\frac{1}{\left(1-e^{-\beta(U-2g\lambda)}\right)\left((\Gamma/2)^2+(\delta-2g\lambda+U)^2\right)} + \frac{1}{\left(1-e^{\beta(U-2g\lambda)}\right)\left((\Gamma/2)^2+(\delta+2g\lambda-U)^2\right)}\Bigg] \\
& \times \Big(-e^{2\beta\mu} + e^{-\beta(-4g\lambda-4\mu+2U)} - e^{-\beta(2g\lambda-4\mu+U)} + 2e^{\beta g\lambda}\left(e^{-\beta(2U-5\mu)} + e^{-\beta(U-3\mu)}\right) \\
& + 2e^{3\beta g\lambda}\left(e^{-\beta(2U-5\mu)} + e^{-\beta(U-3\mu)}\right) + e^{2\beta g\lambda}\left(e^{-\beta(3U-6\mu)} + 3e^{-\beta(U-4\mu)} + e^{-\beta(U-2\mu)}\right) \\
& - 4\left(e^{3\beta\mu} + e^{-\beta(U-5\mu)}\right)\cosh(\beta g\lambda) + e^{4\beta\mu}\left(e^{-2\beta U} - 4\right) - e^{-\beta(2U-6\mu)}\Big) \\
& + \frac{1}{2g\lambda + U}\Bigg[\frac{1}{\left(e^{-\beta(2g\lambda+U)}-1\right)\left((\Gamma/2)^2+(\delta+2g\lambda+U)^2\right)} - \frac{1}{\left(e^{\beta(2g\lambda+U)}-1\right)\left((\Gamma/2)^2+(-\delta+2g\lambda+U)^2\right)}\Bigg] \\
& \times \Big(e^{2\beta\mu} + e^{-\beta(-2g\lambda-4\mu+U)} - e^{-\beta(4g\lambda-4\mu+2U)} - 2e^{-3\beta g\lambda}\left(e^{-\beta(2U-5\mu)} + e^{-\beta(U-3\mu)}\right) \\
& - 2e^{-\beta g\lambda}\left(e^{-\beta(2U-5\mu)} + e^{-\beta(U-3\mu)}\right) - e^{-2\beta g\lambda}\left(e^{-\beta(3U-6\mu)} + 3e^{-\beta(U-4\mu)} + e^{-\beta(U-2\mu)}\right) \\
& + 4\left(e^{3\beta\mu} + e^{-\beta(U-5\mu)}\right)\cosh(\beta g\lambda) - e^{4\beta\mu}\left(e^{-2\beta U} - 4\right) + e^{-\beta(2U-6\mu)}\Big) \\
& + \frac{1}{2g\lambda}\Big[\left(e^{2\beta\mu} + e^{\beta U}\right)\sinh(\beta g\lambda)\left(\frac{1-\coth(\beta g\lambda)}{\frac{\Gamma^2}{4} + (\delta - 2g\lambda)^2} + \frac{1+\coth(\beta g\lambda)}{(\Gamma/2)^2 + (\delta + 2g\lambda)^2}\right) \\
& \times \Big(2e^{2\beta(\mu-U)}\left(e^{\beta\mu}\cosh(2\beta g\lambda) + 2\left(e^{2\beta\mu} + e^{\beta U}\right)\cosh(\beta g\lambda)\right) \\
& + e^{\beta(\mu-3U)}\left(e^{4\beta\mu} + 4e^{2\beta(\mu+U)} + e^{2\beta U}\right)\Big)\Big]\Bigg\}
\end{aligned}
\tag{A.8}
$$

Pulling out a factor of

$$
Z_{\text{1D}} = 1 + 4\cosh(\beta\hbar g\lambda)\left(e^{\beta\mu} + e^{\beta(3\mu-U)}\right) + 2e^{2\beta\mu}\left(2 + e^{-\beta U}\cosh(2\beta\hbar g\lambda)\right) + e^{\beta(4\mu-2U)}
$$

we retrieve the equation for the one dimensional case Eq. (3.25a).

We further derive equations for the particle number conservation and self-consistency condition for a 2D atomic lattice.

$$
\begin{aligned}
\langle\hat{n}\rangle = & \frac{2}{Z_{\text{1D}}^2}\Bigg\{4e^{2\beta\mu} + \left[e^{\beta\mu} + 6e^{3\beta\mu}\left(e^{-\beta U} + 2\right) + 7e^{-\beta(3U-7\mu)} + 10e^{5\beta\mu}\left(e^{-2\beta U} + 2e^{-\beta U}\right)\right]\cosh(\beta g\lambda) \\
& + \left(3e^{6\beta\mu}\left(e^{-3\beta U} + 2e^{-2\beta U}\right) + 16e^{-\beta(U-4\mu)} + e^{2\beta\mu}\left(e^{-\beta U} + 2\right)\right)\cosh(2\beta g\lambda) \\
& + \left(5e^{-\beta(2U-5\mu)} + 3e^{-\beta(U-3\mu)}\right)\cosh(3\beta g\lambda) + e^{-\beta(2U-4\mu)}\cosh(4\beta g\lambda) \\
& + 2e^{4\beta\mu}\left(e^{-2\beta U} + 4e^{-\beta U} + 4\right) + e^{-\beta(4U-8\mu)} + 12e^{-\beta(2U-6\mu)}\Bigg\}
\end{aligned}
\tag{A.9}
$$

$$
\begin{aligned}
\lambda = & \frac{1}{Z_{\text{1D}}^2}\frac{4\delta g}{\left((\Gamma/2)^2+\delta^2\right)}\Bigg\{\left(e^{\beta\mu} + 2e^{3\beta\mu}\left(e^{-\beta U} + 2\right) + e^{\beta(7\mu-3U)} + 2e^{5\beta\mu}\left(e^{-2\beta U} + 2e^{-\beta U}\right)\right)\sinh(\beta g\lambda) \\
& + \left(e^{6\beta\mu}\left(e^{-3\beta U} + 2e^{-2\beta U}\right) + 8e^{\beta(4\mu-U)} + e^{2\beta\mu}\left(e^{-\beta U} + 2\right)\right)\sinh(2\beta g\lambda) \\
& + 3\left(e^{\beta(3\mu-U)} + e^{\beta(5\mu-2U)}\right)\sinh(3\beta g\lambda) + e^{\beta(4\mu-2U)}\sinh(4\beta g\lambda)\Bigg\}
\end{aligned}
\tag{A.10}
$$

Since both expressions only contain local density operators, they also reproduce the equations in one dimension Eqs. (3.25b) & (3.25c).

We confirm these calculations by computationally evaluating all term when tracing over the unit cell and obtain agreeing solution contours in the (μ, β, λ) parameter space for the system of equations in 1D and 2D [see Fig. A.1]. Since the hopping processes considered do not involve multiple lattice directions, we expect the same results for cubic lattices. For similar lattice geometries, the relative scaling of the terms might change depending on the energy spectrum of $\hat{H}_{\text{eff}}$ on the defined unit cell, the overall form of the equations however should remain unchanged.

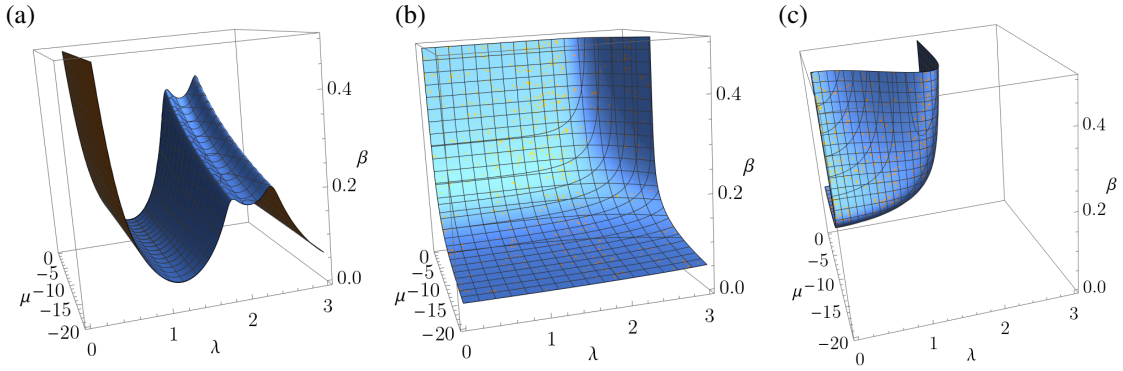

Fig. A.1: System of equations in low hopping thermodynamic limit comparing a 1D (orange) and 2D (blue) atomic lattice in the (μ, β, λ) parameter space (a) Solution of the energy transfer equation Eq. (3.25a), (b) solution of particle conservation condition Eq. (3.25b) and (c) solution of self-consistency condition Eq. (3.25c)

A.3 Thermodynamic limit in the weak tunneling regime - higher order corrections in 1D

We calculate higher order corrections to particle conservation and self-consistency condition in order to confirm the convergence of the equations $\mathcal{O}(J^2)$ derived in Sec. 3.2.

Again we consider the system hamiltonian $\hat{H} = \tilde{H}_0 + \hat{H}_{\text{kin}}$ with the kinetic part as a perturbation. In this case, a general operator expectation value can be calculated as

$$\langle \hat{A} \rangle_T = \frac{\text{Tr}\left[e^{-\beta \tilde{H}_0} \hat{U} \hat{A}\right]}{\text{Tr}\left[e^{-\beta \tilde{H}_0} \hat{U}\right]}, \qquad \hat{U}(\tau) = e^{\tau \tilde{H}_0/\hbar} e^{-\tau \hat{H}/\hbar} \tag{A.11}$$

$$\hat{U}(\beta) = 1 - \int_0^\beta \mathrm{d}\tau_1 \hat{H}_{\text{kin}}(\tau_1) + \underbrace{\int_0^\beta \mathrm{d}\tau_1 \int_0^{\tau_1} \mathrm{d}\tau_2 \hat{H}_{\text{kin}}(\tau_1)\hat{H}_{\text{kin}}(\tau_2)}_{\hat{U}^{(2)}} + \mathcal{O}(J^3) \tag{A.12}$$

The first order here will vanish in the further calculation as it does not go back to the initial state.

Inserting the definition of $\hat{H}_{\text{kin}}$ and performing the integrations yields

$$
\begin{aligned}
U(\beta) =& 1 + J^2 \sum_{j,\alpha} \beta \Bigg\{ \frac{1}{2g\lambda(-1)^j} \left(1 - n_{j\bar{\alpha}} - n_{j+1\bar{\alpha}} + 2n_{j\bar{\alpha}} n_{j+1\bar{\alpha}}\right) + \frac{1}{2g\lambda(-1)^j - U} \left(n_{j\bar{\alpha}} - n_{j\bar{\alpha}} n_{j+1\bar{\alpha}}\right) \\
&\quad + \frac{1}{2g\lambda(-1)^j + U} \left(n_{j+1\bar{\alpha}} - n_{j\bar{\alpha}} n_{j+1\bar{\alpha}}\right) \Bigg\} \left(n_{j\alpha} - n_{j+1\alpha}\right) \\
&\quad + \Bigg\{ \frac{1}{(2g\lambda)^2} \left(1 - n_{j\bar{\alpha}} - n_{j+1\bar{\alpha}} + 2n_{j\bar{\alpha}} n_{j+1\bar{\alpha}}\right) \left(e^{-2g\lambda(-1)^j \beta} - 1\right) \\
&\qquad + \frac{1}{(2g\lambda(-1)^j - U)^2} \left(n_{j\bar{\alpha}} - n_{j\bar{\alpha}} n_{j+1\bar{\alpha}}\right) \left(e^{-(2g\lambda(-1)^j - U)\beta} - 1\right) \\
&\qquad + \frac{1}{(2g\lambda(-1)^j + U)^2} \left(n_{j+1\bar{\alpha}} - n_{j\bar{\alpha}} n_{j+1\bar{\alpha}}\right) \left(e^{-(2g\lambda(-1)^j + U)\beta} - 1\right) \Bigg\} n_{j\alpha} \left(1 - n_{j+1\alpha}\right) \\
&\quad + \Bigg\{ \frac{1}{(2g\lambda)^2} \left(1 - n_{j\bar{\alpha}} - n_{j+1\bar{\alpha}} + 2n_{j\bar{\alpha}} n_{j+1\bar{\alpha}}\right) \left(e^{2g\lambda(-1)^j \beta} - 1\right) \\
&\qquad + \frac{1}{(2g\lambda(-1)^j - U)^2} \left(n_{j\bar{\alpha}} - n_{j\bar{\alpha}} n_{j+1\bar{\alpha}}\right) \left(e^{(2g\lambda(-1)^j - U)\beta} - 1\right) \\
&\qquad + \frac{1}{(2g\lambda(-1)^j + U)^2} \left(n_{j+1\bar{\alpha}} - n_{j\bar{\alpha}} n_{j+1\bar{\alpha}}\right) \left(e^{(2g\lambda(-1)^j + U)\beta} - 1\right) \Bigg\} n_{j+1\alpha} \left(1 - n_{j\alpha}\right) \\
=& 1 + U^{(2)}(\beta) + \mathcal{O}(J^3)
\end{aligned}
\tag{A.13}
$$

With this we calculate some quantities appearing in the self-consistency and particle-conservation equations

$$
\begin{aligned}
\langle \hat{n}_j \rangle_T =& \frac{1}{Z_{1\mathrm{D}}} \Big(4\cosh(\beta\hbar g\lambda) \left(e^{\beta\mu} + e^{\beta(3\mu - U)}\right) + 4e^{2\beta\mu} \left(2 + e^{-\beta U} \cosh(2\beta\hbar g\lambda)\right) + e^{\beta(4\mu - 2U)} \Big) \\
\langle \hat{\Delta} \rangle_T =& \frac{2}{Z_{1\mathrm{D}}} \Big(\sinh(\beta\hbar g\lambda) \left(e^{\beta\mu} + e^{\beta(3\mu - U)}\right) + e^{2\beta\mu} e^{-\beta U} \sinh(2\beta\hbar g\lambda) \Big) \\
\langle U^{(2)} \rangle_T =& \frac{1}{Z_{1\mathrm{D}}} \Bigg(\frac{4\beta}{2g\lambda} \sinh(\beta\hbar g\lambda) \left(e^{\beta\mu} - e^{3\beta\mu} e^{-\beta U}\right) + \beta e^{2\beta\mu} \Big(- \frac{e^{-(2g\lambda + U)\beta} + 2}{2g\lambda + U} + \frac{e^{(2g\lambda - U)\beta} + 2}{2g\lambda - U} \Big) \\
&\quad + e^{2\beta\mu} \Big(- \frac{e^{-(2g\lambda + U)\beta} - 1}{(2g\lambda + U)^2} + \frac{e^{(2g\lambda - U)\beta} - 1}{(2g\lambda - U)^2} \Big) \Bigg) \\
\langle U^{(2)} n_j \rangle_T =& \frac{1}{Z_{1\mathrm{D}}} \Bigg(\frac{2\beta}{2g\lambda} \sinh(\beta\hbar g\lambda) \left(e^{\beta\mu} - 3e^{3\beta\mu} e^{-\beta U}\right) + e^{2\beta\mu} \Big(- \frac{e^{-(2\hbar g\lambda + U)\beta} - 1}{(2g\lambda + U)^2} + \frac{e^{(2\hbar g\lambda - U)\beta} - 1}{(2g\lambda - U)^2} \Big) \Bigg) \\
\langle U^{(2)} \hat{\Delta} \rangle_T =& \frac{1}{Z_{1\mathrm{D}}} \Bigg(\frac{4}{2g\lambda} \left(\beta \cosh(\beta\hbar g\lambda) - \frac{\sinh(2\beta\hbar g\lambda)}{2g\lambda} \right) \left(e^{\beta\mu} - e^{\beta(3\mu - U)}\right) \\
&\quad + \frac{2e^{2\beta\mu}}{2g\lambda + U} \left(\beta e^{-\beta(2\hbar g\lambda + U)} - \frac{1 - e^{-(2\hbar g\lambda + U)\beta}}{2g\lambda + U} \right) \\
&\quad + \frac{2e^{2\beta\mu}}{2g\lambda - U} \left(\beta e^{-\beta(2\hbar g\lambda - U)} - \frac{1 - e^{-(2\hbar g\lambda - U)\beta}}{2g\lambda - U} \right) \Bigg)
\end{aligned}
$$

The self-consistency condition and particle number equation thus become

$$
1 = \langle n \rangle_T \left[1 - \langle U^{(2)} \rangle_T\right] + \langle U^{(2)} n \rangle_T \tag{A.14a}
$$

$$
\lambda = \frac{2g\delta}{\delta^2 + (\Gamma/2)^2} \left[\langle \hat{\Delta} \rangle_T \left[1 - \langle U^{(2)} \rangle_T\right] + \langle U^{(2)} \hat{\Delta} \rangle_T \right] \tag{A.14b}
$$

Within the parameter range shown in the following results section, the deviations between results calculated with and without the higher order corrections agree within the limits of the numerical accuracy reached when solving the system of equations. Therefore, since the calculation without corrections is faster and more stable, we will use the system of equations presented in Eqs. (3.25) if not stated otherwise.

Appendix B

Appendix "Cooling effects and fluctuation-induced bistability in the steady state phase diagrams"

B.1 System of equations $L \to \infty$ bistability empirical approximations

In this section we aim to find analytical expressions for the parameters (μ, β, λ) that solve the derived system of equations in the thermodynamic low hopping limit Eqs. (3.25). We concentrate on specific parameter regions presented in Chapter 6, setting the filling to $\langle \hat{n} \rangle = 1/2$ [see Sec. 6.1]. The equations are analyzed around the edges of the fluctuation-induced bistability at quarter filling that was described in Sec. 6.3. At a value of the atoms-cavity coupling $g_{\mathrm{bi},1}$ beside the solution $(\mu_1, \beta_1, \lambda_1)$ a second stable solution $(\mu_1, \beta_1, \lambda_1)$, that is typically characterized by a larger cavity field parameter and lower temperature appears. Both solutions coexist until at $g_{\mathrm{bi},2}$ the λ_1-solution vanishes. We start by investigating the properties of Eqs. (3.25) in the bistability region with a focus on the edges.

Determine $\mu(\beta)$ from particle conservation equation.

In the self-ordered regime for values of the atom-cavity coupling around the bistability region $g \in \{g_{\mathrm{bi},1}, g_{\mathrm{bi},2}\}$, we observe a very weak dependence of the particle conservation condition fixing the average local atomic density $\langle \hat{n} \rangle$ [Eq. (3.25b) on the cavity field parameter λ. Thus, to simplify we set $\lambda = 0$.

$$\frac{\langle \hat{n} \rangle}{2} = \frac{e^{\beta\mu} + e^{\beta(3\mu - U)} + e^{2\beta\mu}\left(2 + e^{-\beta U}\right) + e^{\beta(4\mu - 2U)}}{1 + 4\left(e^{\beta\mu} + e^{\beta(3\mu-U)}\right) + 2e^{2\beta\mu}\left(2 + e^{-\beta U}\right) + e^{\beta(4\mu-2U)}} \tag{B.1}$$

Solving for the chemical potential μ yields the analytical expression

$$\mu(\beta) = \frac{1}{\beta} \log\left[-(\langle \hat{n} \rangle - 1)e^{\beta U} + \frac{\left((\langle \hat{n} \rangle - 1)^2 e^{2\beta U} - (\langle \hat{n} \rangle - 2)\langle \hat{n} \rangle e^{\beta U}\right)^{1/2}}{\langle \hat{n} \rangle - 2} \right]. \tag{B.2}$$

The expression can be simplified considerably by assuming one is in the strong-interaction regime $\exp(\beta U) \gg 1$

$$\mu_{\mathrm{simple}}(\beta) = -\log(2)/\beta. \tag{B.3}$$

In Fig. B.1(a) we demonstrate the very good agreement of the two expressions levels of approximation for on-site interaction $U/J = 40$. In the considered parameter region the chemical potential is this growing linearly with the temperature.

We now specifically distinguish the regions around the edges of the bistability to derive individual equations for both of them.

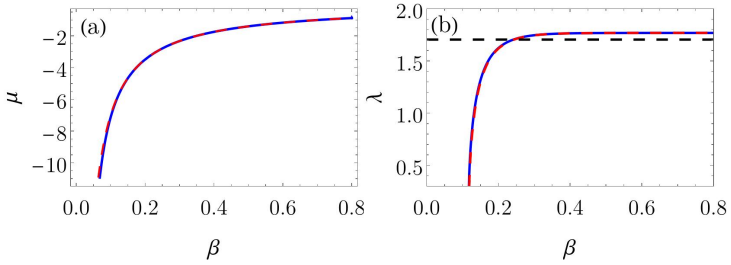

Fig. B.1: (a) $\mu(\beta)$ approximations, Eq. (B.2) (blue), Eq. (B.3) (red) (b) $\beta(\lambda)$, full numerical result from particle conservation and self-consistency Eqs. (3.25b) & (3.25c) (blue) , approximation Eq. (B.6) (red dashed), Eq. (B.9) (black dashed) at $U/J=40$, $\hbar\delta/J=5$, $\Gamma/J=3$, $\hbar g/J=9.65$

B.1.1 Onset of bistability

At the appearance of the high-λ-solution, the system of equations determining $(\mu_{\text{simple}}(\beta_2), \beta_2, \lambda_2)$ can be further approximated in order to find an analytic expression for $\lambda_2(U, g, \delta, \Gamma)$ and identify the terms in the equation of motions that cause the bistability. Additionally we obtain an approximate condition for the corresponding $g_t extbi, 1$ by identifying the parameter domain where a solution $\lambda_2(U, g, \delta, \Gamma)$ exists. Note that these approximations are often empirical and only justified by numerically investigating the functions in the specified parameter regime.

In the full solutions of the equations of motion we observed that around $g_{\text{bi},1}$ for λ_2 we have a rather low corresponding temperature [see e.g. Fig. 6.21, reasonable agreement with zero-temperature mean-field method]. Thus, as we are interested only in the terms appearing in Eqs. (3.25) with the largest contribution, we neglect in the following the states characterized by the highest energies. For the regime we are considering these are states with high unit-cell occupation, with either ≥ 3 particles per unit cell, or 2 particles on the high potential sublattice. We call this in the following as the *low-energy approximation*, denoted by the index "le".

$$\begin{aligned}\frac{\partial}{\partial t}\langle H_{\text{le}}\rangle \propto \Bigg[&\left(\frac{-\exp(\beta\hbar g\lambda)}{(2g\lambda+\delta)^2+(\Gamma/2)^2}+\frac{\exp(-\beta\hbar g\lambda)}{(2g\lambda-\delta)^2+(\Gamma/2)^2}\right)\frac{e^{\beta\mu}}{2g\lambda}\\ &+\left(\frac{-\exp[\beta(2\hbar g\lambda-U)]}{(2g\lambda-U/\hbar+\delta)^2+(\Gamma/2)^2}+\frac{1}{(2g\lambda-U/\hbar-\delta)^2+(\Gamma/2)^2}\right)\frac{e^{2\beta\mu}}{2g\lambda-U/\hbar}\\ &+\left(\frac{-\exp[\beta(2\hbar g\lambda+U)]}{(2g\lambda+U/\hbar+\delta)^2+(\Gamma/2)^2}+\frac{1}{(2g\lambda+U/\hbar-\delta)^2+(\Gamma/2)^2}\right)\frac{e^{2\beta\mu}}{2g\lambda+U/\hbar}\Bigg]\end{aligned} \tag{B.4}$$

Determine $\beta(\lambda)$ from self-consistency equation.

Within the low energy approximation and using the simplified expression Eq. (B.3) for the chemical potential μ the self-consistency condition simplifies considerably to the relation

$$\lambda = \frac{\delta g}{(\Gamma/2)^2+\delta^2}\tanh(\beta g\lambda/2). \tag{B.5}$$

Even though this relation is not analytically solvable for λ, one can obtain an expression for the temperature

$$\beta(\lambda) = \frac{1}{g\lambda}\log\left[\frac{\left((\Gamma/2)^2+\delta^2\right)\lambda+\delta g}{-\left((\Gamma/2)^2+\delta^2\right)\lambda+\delta g}\right] \tag{B.6}$$

within this approximation.

Determine $\lambda(U, g, \delta\Gamma)$ from EOM

This relation is shown in Fig. B.1 (b) and compared to the numerical solution of the full self-consistency equation beyond the low energy approximation. A good agreement is found. In particular, the value of λ rises extremely

rapidly a low inverse temperatures and then bends to saturate at larger values of the inverse temperatures corresponding to the low temperature limit to the value of $\lambda_{max} = \delta g/((\Gamma/2)^2 + \delta^2)$. We find that the second solution which gives the onset of the bistability and thus, also satisfies the equation of motions lies close to the maximal bending of the curve which lies close to the where $\beta g\lambda = 4$. We will use this point later as an expansion point.

Using Eqs. (B.3) & (B.6), we rewrite the energy transfer Eq. (6.25) as a function of λ.

Taking a look at the individual terms, we observe that taking only the terms $\propto 1/(2g\lambda)$ [first line Eq. (6.25), red, dashed line in Fig. B.2 (a)] into account, gives very good agreement of zero value of the EOM at low values of $\lambda \approx 0.69$. This approximation corresponds to the $U \to \infty$-limit since we neglect the possibility of double occupied sites and we nicely reproduce the λ_1 solution [petrol line in Fig. B.2 (c)], yielding

$$\lambda_{1\text{approx}} = \sqrt{\frac{\left((\Gamma/2)^2 + \delta^2\right)^2 - 4\delta^2 g^2}{2\left((\Gamma/2)^2 + \delta^2\right)^2 - 4g^2\left((\Gamma/2)^2 + 2\delta^2\right)}} \tag{B.7}$$

However, this does not capture the disappearance of the λ_1-solution at $g_{\text{bi},2}$ and as it is seen in Fig. B.2 (a) the additional two values at which the EOM vanishes around $\lambda \approx 1.6$ which correspond to the unstable solution and the λ_2-solution cannot be recovered by this simple approximation.

For the appearance of the λ_2-solution further contributions $\propto 1/(2g\lambda - U/\hbar)$ [second line Eq. (6.25), blue line in Fig. B.2 (a)] need to be taken into account. This shows the importance of the interaction in the generation of this bistability. Neglecting terms $\propto 1/(2g\lambda + U/\hbar)$, Eq. (6.25) simplifies to

$$\begin{aligned} 0 = &\frac{1}{4g\lambda}\left[\frac{\left((\Gamma/2)^2+\delta^2\right)\lambda - \delta g}{\left(-\left((\Gamma/2)^2+\delta^2\right)\lambda - \delta g\right)\left((\Gamma/2)^2+\delta^2\right)} - \frac{-\left((\Gamma/2)^2+\delta^2\right)\lambda - \delta g}{\left(\left((\Gamma/2)^2+\delta^2\right)\lambda - \delta g\right)\left((\Gamma/2)^2+(2g\lambda+\delta)^2\right)}\right] \\ &+ \frac{1}{4(2g\lambda - U/\hbar)}\left[\frac{1}{(\Gamma/2)^2+(2g\lambda - U/\hbar - \delta)^2} - \frac{\left(\frac{-\left((\Gamma/2)^2+\delta^2\right)\lambda - \delta g}{\left((\Gamma/2)^2+\delta^2\right)\lambda - \delta g}\right)^{\frac{2g\lambda - U/\hbar}{g\lambda}}}{(\Gamma/2)^2+(2g\lambda - U/\hbar + \delta)^2}\right] \end{aligned} \tag{B.8}$$

[blue dashed line in Fig. B.2 (b)]. This equation is still too complicated to be solved for λ_2 analytically, thus, for the terms that only slowly varying with λ we replace λ with a constant value empirically determined from Eq. (B.5) [see black dashed line in Fig. B.1 (b)].

$$\lambda_0 = \frac{\delta g}{(\Gamma/2)^2 + \delta^2}\tanh(2) \tag{B.9}$$

Furthermore, we approximate the terms in Eq. (B.8) by rational functions using a Padé-approximation [289] $[m/m]_{\text{EOM}}(\lambda)$ to order $m = 1$ around multiple expansion points λ_0, depending on the divergence points of the individual terms [green line in Fig. B.2 (b)]. For the second term in the first line of Eq. (6.25) we choose the $U \to \infty$-solution for λ_0 given in Eq. (B.7) and for the second line terms the expression for λ_0 in Eq. (B.9). The region of convergence for the approximation strongly depends on the expansion points, and we found this choice to be working the best. The approximations employed capture well the maximum and following zero-crossing exhibited by the numerically solved full system of equations, as shown comparing the black dashed and green lines in Fig. B.2 (b).

After performing the approximations described above, the resulting equations can be solved analytically. We obtain a function for λ_2 around the onset of the bistability, which nicely reproduces the numerical solution for the full system of equations up to the maximum λ_2-value [see Fig. B.2 (c)]. The approximate analytical solution $\lambda_2(U, g, \delta, \Gamma)$ has a real solution only for

$$g \geq \sqrt{\frac{(U/\hbar - \delta)}{2\delta}\left((\Gamma/2)^2 + \delta^2\right)} \tag{B.10}$$

This gives an estimate for $g_{\text{bi},1}$ [Eq. (6.14)]. Comparing to the numerically determined onset of the bistability region we see a nice agreement in the parameter regime of large interaction strengths U/J and $\delta^2 + (\Gamma/2)^2$ small [see red lines in Fig. 6.22].

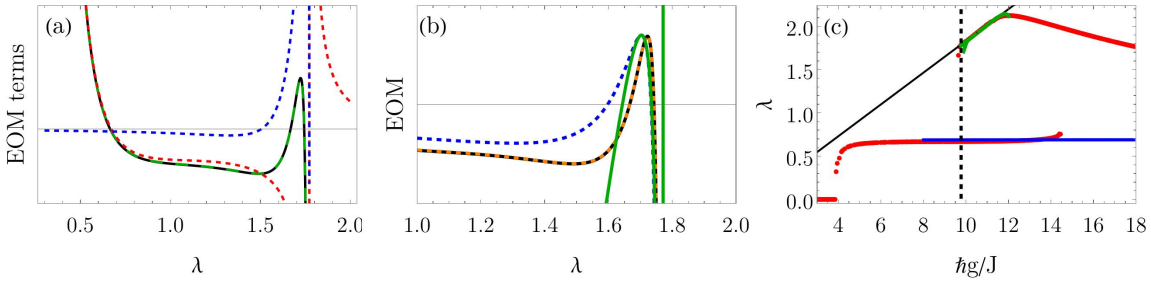

Fig. B.2: (a) terms in EOM Eq. (6.25)) using Eqs. (B.3),(B.6) all terms (black, dashed), lines 1+2 (green), line 1 (red), line 2 (blue) (b) $\mathrm{EOM}_{\mathrm{le}}[\mu_{\mathrm{simple}}(\beta(\lambda)), \beta[\lambda], \lambda]$ [Eq. (6.25)] (black), neglect terms $\propto 1/(2g\lambda+U/\hbar)$ (yellow), $\mathrm{EOM}_{\mathrm{le,\,approx}}$ simplified to Eq. (B.8) (blue), Padé-approximation of Eq. (B.8) (green) (c) full numerical solution for λ (red), $\lambda_{\mathrm{MF}} = \lambda(\Delta = N/L)$ [Eq. (3.3)] (black), solution of Padé-approx. of Eq. (B.8) (green), approximate solution $\lambda_{1,\mathrm{approx}}$ [Eq. (B.7)] (blue), vertical dashed line [Eq. (B.10)], at $U/J = 40$, $\hbar g/J = 9.65$, $\hbar\delta/J = 5$, $\hbar\Gamma/J = 3$

Taking a look at the individual terms, it shows that while taking only terms $\propto 1/(2g\lambda)$ into account nicely reproduces the λ_1 solution, for the appearance of the λ_2-solution further contributions $\propto 1/(2g\lambda - U/\hbar)$ start to dominate.

The qualitative behavior is determined by terms

$$\left(\frac{-\exp(\beta\hbar g\lambda)}{(2g\lambda+\delta)^2+(\Gamma/2)^2}\right)\frac{e^{\beta\mu}}{2g\lambda} + \left(\frac{-\exp[\beta(2\hbar g\lambda - U)]}{(2g\lambda - U/\hbar+\delta)^2+(\Gamma/2)^2} + \frac{1}{(2g\lambda - U/\hbar-\delta)^2+(\Gamma/2)^2}\right)\frac{e^{2\beta\mu}}{2g\lambda - U/\hbar}$$

where the last part mainly contributes a shift of the function, changing the $g_{bi,1}$ at which the further zero-crossings of the function occur.

Inserting the approximations previously made for μ [Eq. (B.3)] and β [Eq. (B.6)] and neglect the terms $\propto 1/(2g\lambda + U/\hbar)$.

$$\begin{aligned} 0 =& \frac{1}{4g\lambda}\left(\frac{\left((\Gamma/2)^2+\delta^2\right)\lambda - \delta g}{\left(-\left((\Gamma/2)^2+\delta^2\right)\lambda - \delta g\right)\left((\Gamma/2)^2+(2g\lambda-\delta)^2\right)} - \frac{-\left((\Gamma/2)^2+\delta^2\right)\lambda - \delta g}{\left(\left((\Gamma/2)^2+\delta^2\right)\lambda - \delta g\right)\left((\Gamma/2)^2+(2g\lambda+\delta)^2\right)}\right) \\ &+ \frac{1}{4(2g\lambda - U/\hbar)}\left(\frac{1}{(\Gamma/2)^2+(2g\lambda - U/\hbar-\delta)^2} - \frac{\left(\frac{-\left((\Gamma/2)^2+\delta^2\right)\lambda-\delta g}{\left((\Gamma/2)^2+\delta^2\right)\lambda-\delta g}\right)^{\frac{2g\lambda-U/\hbar}{g\lambda}}}{(\Gamma/2)^2+(2g\lambda - U/\hbar+\delta)^2}\right) \end{aligned} \tag{B.11}$$

Since this approximation is still not solvable analytically, further simplifications are needed. We replace $\lambda = \frac{\delta g \tanh(2)}{(\Gamma/2)^2+\delta^2}$ in the function parts that slowly vary with λ. (not choosing the also thinkable $\lambda = \frac{U/\hbar-\delta}{2g}$ to not introduce additional singularities in the function)
Also, terms $(\Gamma/2)^2$ are neglected where possible.

$$\begin{aligned} 0 =& \frac{\coth^2(2)\left((\Gamma/2)^2+\delta^2\right)^2\left((\Gamma/2)^2\coth(2)+\delta^2(1+\coth(2))\right)}{g\left(\lambda\left((\Gamma/2)^2+\delta^2\right)-\delta g\right)\left(\delta\coth(2)\left((\Gamma/2)^2+\delta^2\right)+2\delta g^2\right)^2} \\ &+ \frac{\coth(2)\left((\Gamma/2)^2+\delta^2\right)^3\left((\Gamma/2)^2-\delta^2(\tanh(2)-1)\right)}{4\delta^3 g^2\left((\Gamma/2)^2+\delta^2(1+\tanh(2))\right)\left((\Gamma/2)^2+\delta^2-2g^2\tanh(2)\right)^2} \\ &+ \frac{1}{4(2g\lambda - U/\hbar)}\left(\frac{1}{\left(-\frac{2\delta g^2\tanh(2)}{(\Gamma/2)^2+\delta^2}+\delta+U/\hbar\right)^2} - \frac{\left(-\frac{16\delta g((\Gamma/2)^2+\delta^2(1+\tanh(2)))}{4((\Gamma/2)^2+\delta^2)(\lambda((\Gamma/2)^2+\delta^2)-\delta g)}\right)^{2-\frac{U\coth(2)((\Gamma/2)^2+\delta^2)}{\hbar\delta g^2}}}{(\Gamma/2)^2+(\delta+2g\lambda-U/\hbar)^2}\right) \end{aligned} \tag{B.12}$$

The approximation captures the maximum and following zero-crossing in the EOM quite well (Fig. B.2)

The resulting equations can be solved analytically. We obtain a function for λ around the onset of the bistability, which nicely reproduces the numerical solution for the full system of equations up to the maximum λ-value.

The resulting function $\lambda(U, g, \delta, \Gamma)$ has a real solution only for

$$g \geq \sqrt{\frac{(U/\hbar - \delta)}{2\delta}\left((\Gamma/2)^2 + \delta^2\right)} \tag{B.13}$$

This gives a crude estimate for $g_{\mathrm{bi},1}$. Comparing to the numerically determined onset of the bistability region shows nice agreement for large U, low δ and $\Gamma \sim \delta$.

$$\begin{aligned}
\lambda_{\mathrm{Pade}} =& \frac{\left(-1+e^4\right)^7}{2a_4\left(1+e^4\right)(\Gamma^2+4\delta^2)^2\left(8\left(-1+e^4\right)g^2+\left(1+e^4\right)(\Gamma^2+4\delta^2)\right)^2} \\
&\times \frac{1}{\left(16a_1a_6\left(-1+e^4\right)\left(\left(1+e^4\right)\Gamma^2+8e^4\delta^2\right)\left(\left(1+e^4\right)(\Gamma^2+4\delta^2)g-8\left(-1+e^4\right)g^3\right)^2\delta^3+\ldots\right.} \\
&\left.\overline{\ldots+a_2a_5\left(1+e^4\right)^3(\Gamma^2+4\delta^2)^3\left(\left(1+e^4\right)\Gamma^2+8\delta^2\right)\right)} \\
&\times\Bigg(\frac{(\Gamma^2+4\delta^2)}{\left(-1+e^4\right)^6}\Big(128a_1a_4a_6e^4\left(\left(1+e^4\right)\Gamma^2+8e^4\delta^2\right)g^3\left(\left(1+e^4\right)^2(\Gamma^2+4\delta^2)^2-64\left(-1+e^4\right)^2g^4\right)^2\delta^4 \\
&+a_2(\Gamma^2+4\delta^2)\Big(16a_3a_6\left(-1+e^4\right)\left(\left(1+e^4\right)\Gamma^2+8e^4\delta^2\right)\left(\left(1+e^4\right)^2(\Gamma^2+4\delta^2)^2g-64\left(-1+e^4\right)^2g^5\right)^2\delta^3 \\
&+a_4\left(1+e^4\right)^2(\Gamma^2+4\delta^2)\Big(a_6\left(1+e^4\right)(\Gamma^2+4\delta^2)^2\left(\left(1+e^4\right)\Gamma^2+8\delta^2\right)\left(8\left(-1+e^4\right)g^2+\left(1+e^4\right)(\Gamma^2+4\delta^2)\right)^2 \\
&+4a_5\left(-1+e^4\right)\delta g\Big(64\left(-1+e^4\right)^2\left(\left(1+e^4\right)\Gamma^4-8e^4\delta^2\Gamma^2-64e^4\delta^4\right)g^4 \\
&+16\left(1+e^4\right)(\Gamma^2+4\delta^2)\left(\left(1+4e^4+3e^8\right)\Gamma^4+8e^4\left(5+3e^4\right)\delta^2\Gamma^2+64e^4\left(1+e^4\right)\delta^4\right)g^2 \\
&+\left(1+e^4\right)^2(\Gamma^2+4\delta^2)^2\left(\left(1+e^4\right)\Gamma^4-8e^4\delta^2\Gamma^2-64e^4\delta^4\right)\Big)\Big)\coth(2)\Big) \\
&\pm\sqrt{\frac{(\Gamma^2+4\delta^2)^2}{\left(-1+e^4\right)^{12}}\left(128a_1a_4a_6e^4\left(\left(1+e^4\right)\Gamma^2+8e^4\delta^2\right)g^3\left(\left(1+e^4\right)^2(\Gamma^2+4\delta^2)^2-64\left(-1+e^4\right)^2g^4\right)^2\delta^4\right.} \\
&\overline{+a_2(\Gamma^2+4\delta^2)\left(16a_3a_6\left(-1+e^4\right)\left(\left(1+e^4\right)\Gamma^2+8e^4\delta^2\right)\left(\left(1+e^4\right)^2(\Gamma^2+4\delta^2)^2g-64\left(-1+e^4\right)^2g^5\right)^2\delta^3} \\
&\overline{+a_4\left(1+e^4\right)^2(\Gamma^2+4\delta^2)\left(a_6\left(1+e^4\right)(\Gamma^2+4\delta^2)^2\left(\left(1+e^4\right)\Gamma^2+8\delta^2\right)\left(8\left(-1+e^4\right)g^2+\left(1+e^4\right)(\Gamma^2+4\delta^2)\right)^2\right.} \\
&\overline{+4a_5\left(-1+e^4\right)\delta g\left(64\left(-1+e^4\right)^2\left(\left(1+e^4\right)\Gamma^4-8e^4\delta^2\Gamma^2-64e^4\delta^4\right)g^4+16\left(1+e^4\right)(\Gamma^2+4\delta^2)\left(\left(1+4e^4+3e^8\right)\Gamma^4\right.\right.} \\
&\left.\overline{\left.\left.+8e^4\left(5+3e^4\right)\delta^2\Gamma^2+64e^4\left(1+e^4\right)\delta^4\right)g^2+\left(1+e^4\right)^2(\Gamma^2+4\delta^2)^2\left(\left(1+e^4\right)\Gamma^4-8e^4\delta^2\Gamma^2-64e^4\delta^4\right)\right)\right)\coth(2)\Big)^2} \\
&\overline{-\frac{64a_4\left(1+e^4\right)\delta(\Gamma^2+4\delta^2)^2g\left(8\left(-1+e^4\right)g^2+\left(1+e^4\right)(\Gamma^2+4\delta^2)\right)^2}{\left(-1+e^4\right)^{12}}} \\
&\overline{\times\left(16a_1a_6\left(-1+e^4\right)\left(\left(1+e^4\right)\Gamma^2+8e^4\delta^2\right)\left(\left(1+e^4\right)(\Gamma^2+4\delta^2)g-8\left(-1+e^4\right)g^3\right)^2\delta^3\right.} \\
&\overline{+a_2a_5\left(1+e^4\right)^3(\Gamma^2+4\delta^2)^3\left(\left(1+e^4\right)\Gamma^2+8\delta^2\right)\Big)\left(16a_1a_4a_6\left(\left(1+e^4\right)\Gamma^2+8e^4\delta^2\right)g^3\right.} \\
&\overline{\times\left(\left(1+e^4\right)^2(\Gamma^2+4\delta^2)^2-64\left(-1+e^4\right)^2g^4\right)^2\delta^4+a_2(\Gamma^2+4\delta^2)\left(4a_3a_6\delta^3\left(\left(1+e^4\right)\Gamma^2+8e^4\delta^2\right)\right.} \\
&\overline{\left(\left(1+e^4\right)^2(\Gamma^2+4\delta^2)^2g-64\left(-1+e^4\right)^2g^5\right)^2-a_4\left(1+e^4\right)(\Gamma^2+4\delta^2)\left(a_6\left(1+e^4\right)(\Gamma^2+4\delta^2)\right.} \\
&\overline{+4a_5\left(-1+e^4\right)\delta g\Big)\Big(64\left(-1+e^4\right)^2\delta^2\left(3\left(1+e^4\right)\Gamma^2+8\left(1+2e^4\right)\delta^2\right)g^4-8\left(1+e^4\right)(\Gamma^2+4\delta^2)\right.} \\
&\overline{\left(\left(1+e^4\right)^2\Gamma^4+2\left(3+8e^4+5e^8\right)\delta^2\Gamma^2+16\left(1+e^4+2e^8\right)\delta^4\right)g^2+\left(1+e^4\right)^2\delta^2(\Gamma^2+4\delta^2)^2} \\
&\overline{\left.\left.\times\left(3\left(1+e^4\right)\Gamma^2+8\left(1+2e^4\right)\delta^2\right)\right)\coth(2)\Big)\Big)}
\end{aligned} \tag{B.14a}$$

With

$$
\begin{aligned}
a_1 = {} & (\Gamma^2+4\delta^2)^2\left(\left(1+e^4\right)\Gamma^2+8e^4\delta^2\right)^2\left(e^4-\frac{(-1+e^4)\Gamma^2}{2(\Gamma^2+4\delta^2)}\right)^{-\frac{U((\Gamma/2)^2+\delta^2)\coth(2)}{\delta g^2}} \\
& \times\Bigg((\Gamma^2+4\delta^2)^2\Big(16\left(1+e^4\right)^7U^7(\Gamma^2+4\delta^2)^7-64\left(1+e^4\right)^6U^6\delta\left(\left(1+e^4\right)\Gamma^2+4\left(1+e^4\right)\delta^2\right. \\
& \left.+15\left(-1+e^4\right)g^2\right)(\Gamma^2+4\delta^2)^6+8\left(1+e^4\right)^5U^5\Big(256\left(13-25e^4+12e^8\right)\delta^2g^4+416\left(-1+e^8\right)\delta^2(\Gamma^2+4\delta^2)g^2 \\
& +\left(1+e^4\right)^2(\Gamma^2+4\delta^2)^2\left(\Gamma^2+12\delta^2\right)\Big)(\Gamma^2+4\delta^2)^5-16\left(1+e^4\right)^4U^4\delta\Big(1280\left(-1+e^4\right)^2\left(-21+17e^4\right)\delta^2g^6 \\
& +128\left(37-35e^4-37e^8+35e^{12}\right)\delta^2(\Gamma^2+4\delta^2)g^4+22\left(-1+e^4\right)\left(1+e^4\right)^2(\Gamma^2+4\delta^2)^2\left(\Gamma^2+12\delta^2\right)g^2 \\
& +\left(1+e^4\right)^3(\Gamma^2+4\delta^2)^4\Big)(\Gamma^2+4\delta^2)^4+\left(1+e^4\right)^3U^3\left(65536\left(-1+e^4\right)^2\left(67-110e^4+45e^8\right)\delta^4g^8\right. \\
& +32768\left(-1+e^4\right)^2\left(1+e^4\right)\left(-29+25e^4\right)\delta^4(\Gamma^2+4\delta^2)g^6+6144\left(-1+e^8\right)^2\delta^2(\Gamma^2+4\delta^2)^2\left(\Gamma^2+12\delta^2\right)g^4 \\
& +576\left(-1+e^4\right)\left(1+e^4\right)^3\delta^2(\Gamma^2+4\delta^2)^4g^2+\left(1+e^4\right)^4(\Gamma^2+4\delta^2)^6\Big)(\Gamma^2+4\delta^2)^3 \\
& -4\left(-1+e^4\right)\left(1+e^4\right)^2U^2\delta g^2\left(65536\left(-1+e^4\right)^2\left(109-154e^4+57e^8\right)\delta^4g^8\right. \\
& +131072\left(-1+e^4\right)^2\left(1+e^4\right)\left(-13+10e^4\right)\delta^4(\Gamma^2+4\delta^2)g^6+13312\left(-1+e^8\right)^2\delta^2(\Gamma^2+4\delta^2)^2\left(\Gamma^2+12\delta^2\right)g^4 \\
& +128\left(1+e^4\right)^3\left(-13+15e^4\right)\delta^2(\Gamma^2+4\delta^2)^4g^2+7\left(1+e^4\right)^4(\Gamma^2+4\delta^2)^6\Big)(\Gamma^2+4\delta^2)^2 \\
& +128\left(-1+e^8\right)u\delta^2g^4\left(65536\left(-1+e^4\right)^3\left(13+5e^4\left(-3+e^4\right)\right)\delta^4g^8\right. \\
& +8192\left(-1+e^4\right)^3\left(1+e^4\right)\left(-25+17e^4\right)\delta^4(\Gamma^2+4\delta^2)g^6+256\left(-1+e^4\right)\left(1+e^4\right)^2\delta^2(\Gamma^2+4\delta^2)^2 \\
& \times\left(\left(4+7e^4\left(-2+e^4\right)\right)\Gamma^2+12\left(6+7e^4\left(-2+e^4\right)\right)\delta^2\right)g^4+32(-1+e)(1+e)\left(1+e^2\right)\left(1+e^4\right)^3\left(-7+11e^4\right)\delta^2 \\
& (\Gamma^2+4\delta^2)^4g^2+\left(1+e^4\right)^4\left(-1+2e^4\right)(\Gamma^2+4\delta^2)^6\Big)(\Gamma^2+4\delta^2)-256\left(-1+e^4\right)^2\delta^3g^6\left(\left(1+e^4\right)^4\left(1+3e^4\right)\Gamma^{12}\right. \\
& +24\left(1+e^4\right)^4\left(1+3e^4\right)\delta^2\Gamma^{10}+16\left(1+e^4\right)^3\delta^2\left(15\left(1+4e^4+3e^8\right)\delta^2+8\left(-1-4e^4+3e^8\right)g^2\right)\Gamma^8 \\
& +256\left(1+e^4\right)^2\delta^2\left(5\left(1+e^4\right)^2\left(1+3e^4\right)\delta^4+8\left(1+e^4\right)\left(-1-4e^4+3e^8\right)g^2\delta^2+6\left(1+e^4-3e^8+e^{12}\right)g^4\right)\Gamma^6 \\
& +768\left(1+e^4\right)^2\delta^4\left(5\left(1+e^4\right)^2\left(1+3e^4\right)\delta^4+16\left(1+e^4\right)\left(-1-4e^4+3e^8\right)g^2\delta^2+8\left(1+9e^4+5e^8\left(-3+e^4\right)\right)g^4\right)\Gamma^4 \\
& +2048\left(1+e^4\right)\delta^4\Big(3\left(1+e^4\right)^3\left(1+3e^4\right)\delta^6+16\left(1+e^4\right)^2\left(-1-4e^4+3e^8\right)g^2\delta^4 \\
& +12\left(1+e^4\right)\left(-1+15e^4+7e^8\left(-3+e^4\right)\right)g^4\delta^2+16\left(-1+e^4\right)^3\left(-5+3e^4\right)g^6\Big)\Gamma^2 \\
& +4096\delta^4\left(\left(1+e^4\right)\delta^2+2\left(-1+e^4\right)g^2\right)^2\left(\left(1+e^4\right)^2\left(1+3e^4\right)\delta^4+4\left(1+e^4\right)\left(-1-6e^4+3e^8\right)g^2\delta^2\right. \\
& \left.+4\left(-11+21e^4-13e^8+3e^{12}\right)g^4\right)\Big)\Big)\left(e^4-\frac{(-1+e^4)\Gamma^2}{2(\Gamma^2+4\delta^2)}\right)^{\frac{(1+e^4)U(\Gamma^2+4\delta^2)}{4(-1+e^4)\delta g^2}} \\
& +\left(\left(1+e^4\right)\Gamma^2+8e^4\delta^2\right)^2\left(\left(1+e^4\right)(U+\delta)(\Gamma^2+4\delta^2)-8\left(-1+e^4\right)\delta g^2\right)^2\left(-256\left(-1+e^4\right)^2\delta^3\right. \\
& \times\left(256\left(-25+39e^4-15e^8+e^{12}\right)\delta^2g^4+64\left(13+3e^4-9e^8+e^{12}\right)\delta^2(\Gamma^2+4\delta^2)g^2+\left(-5+e^4\right)\left(1+e^4\right)^2(\Gamma^2+4\delta^2)^3\right)g^6 \\
& +128\left(-1+e^8\right)U\delta^2(\Gamma^2+4\delta^2)\Big(384\left(-9+17e^4-9e^8+e^{12}\right)\delta^2g^4+16\left(21-5e^4-21e^8+5e^{12}\right)\delta^2(\Gamma^2+4\delta^2)g^2 \\
& +\left(-2+e^4\right)\left(1+e^4\right)^2(\Gamma^2+4\delta^2)^3\Big)g^4-4\left(-1+e^4\right)\left(1+e^4\right)^2U^2\delta(\Gamma^2+4\delta^2)^2\left(512\left(25-32e^4+7e^8\right)\delta^2g^4\right. \\
& +64\left(1+e^4\right)\left(-17+9e^4\right)\delta^2(\Gamma^2+4\delta^2)g^2+5\left(1+e^4\right)^2(\Gamma^2+4\delta^2)^3\Big)g^2+4\left(1+e^4\right)^5U^5(\Gamma^2+4\delta^2)^5 \\
& +8\left(1+e^4\right)^4U^4\delta(\Gamma^2+4\delta^2)^4\left(-18\left(-1+e^4\right)g^2-\left(1+e^4\right)(\Gamma^2+4\delta^2)\right)+\left(1+e^4\right)^3U^3(\Gamma^2+4\delta^2)^3 \\
& \left.\times\left(512\left(7-11e^4+4e^8\right)\delta^2g^4+224\left(-1+e^8\right)\delta^2(\Gamma^2+4\delta^2)g^2+\left(1+e^4\right)^2(\Gamma^2+4\delta^2)^3\right)\right)\coth^4(2)
\end{aligned}
\tag{B.14b}
$$

$$
\begin{aligned}
a_2 =& 32\left(e^4-1\right)^{11}\delta^2 g^3(\coth(2)-1)^3\left(U\coth(2)(\Gamma^2+4\delta^2)-8\delta g^2\right)\Bigg(256\delta^2 g^4+64\delta g^2\coth(2)(\Gamma^2+4\delta^2)(\delta-U) \\
&+\coth^2(2)(\Gamma^2+4\delta^2)^2\left(\Gamma^2+4(U-\delta)^2\right)\Bigg)\Bigg(\left(\Gamma^2\coth(2)+4\delta^2(1+\coth(2))\right)^2\left(\coth(2)(\Gamma^2+4\delta^2)(\delta+U)-8\delta g^2\right)^2 \\
&\times\left(40960\delta^4 g^8-16\delta g^2\coth^3(2)(\Gamma^2+4\delta^2)^2\left(2\delta g^2\left(\Gamma^2+4\left(\delta^2+3U^2-4\delta U\right)\right)+U(\Gamma^2+4\delta^2)\left(\Gamma^2+4\delta^2+8U^2-12\delta U\right)\right)\right. \\
&+32\delta^2 g^4\coth^2(2)(\Gamma^2+4\delta^2)\left((\Gamma^2+4\delta^2)\left(3(\Gamma^2+4\delta^2)+60U^2-64\delta U\right)+64\delta g^2(3U-2\delta)\right) \\
&\left.+U^2\coth^4(2)(\Gamma^2+4\delta^2)^4\left(\Gamma^2+4(U-\delta)^2\right)+2048\delta^3 g^6\coth(2)\left(-12\delta g^2-(\Gamma^2+4\delta^2)(7U-4\delta)\right)\right) \\
&+\frac{64\delta^2 g^4(\Gamma^2+4\delta^2)^2}{(e^4-1)^7}\Bigg(256(e^4-1)^2\delta^2 g^4+64(e^8-1)\delta g^2(\Gamma^2+4\delta^2)(\delta-U) \\
&+(1+e^4)^2(\Gamma^2+4\delta^2)^2(\Gamma^2+4(U-\delta)^2)\Bigg)^2\left(e^4-\frac{(e^4-1)\Gamma^2}{2(\Gamma^2+4\delta^2)}\right)^{\frac{(1+e^4)U(\Gamma^2+4\delta^2)}{4(e^4-1)\delta g^2}}\Bigg)
\end{aligned}
\tag{B.14c}
$$

$$
\begin{aligned}
a_3 =& (\Gamma^2+4\delta^2)\Bigg((\Gamma^2+4\delta^2)^2\left(e^4-\frac{(e^4-1)\Gamma^2}{2(\Gamma^2+4\delta^2)}\right)^{\frac{(1+e^4)U(\Gamma^2+4\delta^2)}{4(e^4-1)\delta g^2}}\Bigg(256\left(e^4-1\right)^2\delta^2 g^4 \\
&+64\left(e^8-1\right)\delta g^2(\Gamma^2+4\delta^2)(\delta-U)+\left(1+e^4\right)^2(\Gamma^2+4\delta^2)^2\left(\Gamma^2+4(U-\delta)^2\right)\Bigg) \\
&-\left(\left(1+e^4\right)\Gamma^2+8e^4\delta^2\right)^2\left(\left(1+e^4\right)(\Gamma^2+4\delta^2)(\delta+U)-8\left(e^4-1\right)\delta g^2\right)^2\Bigg) \\
&\left(e^4-\frac{(e^4-1)\Gamma^2}{2(\Gamma^2+4\delta^2)}\right)^{-\frac{U\coth(2)((\Gamma/2)^2+\delta^2)}{\delta g^2}}
\end{aligned}
\tag{B.14d}
$$

$$
\begin{aligned}
a_4 =& \left(1+e^4\right)^4(\tanh(2)-1)^2\left((\Gamma^2+4\delta^2)(\delta+U)-8\delta g^2\tanh(2)\right)^2\left(8\delta g^2\tanh(2)-U(\Gamma^2+4\delta^2)\right) \\
&\left(256\delta^2 g^4\tanh^2(2)+64\delta g^2\tanh(2)(\Gamma^2+4\delta^2)(\delta-U)+(\Gamma^2+4\delta^2)^2\left(\Gamma^2+4(U-\delta)^2\right)\right)
\end{aligned}
\tag{B.14e}
$$

$$
\begin{aligned}
a_5 =&(\Gamma^2+4\delta^2)\coth(2)\Bigg(\frac{8192(-1+e^4)^2\delta^4(\Gamma^2+4\delta^2)^2}{(1+e^4)^{12}}\Big(e^4-\frac{(-1+e^4)\Gamma^2}{2(\Gamma^2+4\delta^2)}\Big)^{\frac{(1+e^4)U(\Gamma^2+4\delta^2)}{4(-1+e^4)\delta g^2}} g^8\Big(256\big(-1+e^4\big)^2\delta^2 g^4 \qquad \text{(B.14f)}\\
&+64\big(-1+e^8\big)\delta(\delta-U)(\Gamma^2+4\delta^2)g^2+\big(1+e^4\big)^2\big(\Gamma^2+4(U-\delta)^2\big)(\Gamma^2+4\delta^2)^2\big)^3-\big((U+\delta)(\Gamma^2+4\delta^2)\\
&-8\delta g^2\tanh(2)\big)^2\big(\Gamma^2+4\delta^2(1+\tanh(2))\big)^2\Bigg(16U^8(\Gamma^2+4\delta^2)^8+\frac{64U^7\delta}{1+e^4}\big(-17\big(-1+e^4\big)g^2-\big(1+e^4\big)(\Gamma^2+4\delta^2)\big)\\
&\times(\Gamma^2+4\delta^2)^7+\frac{8U^6}{(1+e^4)^2}\big(192\big(25-46e^4+21e^8\big)\delta^2g^4+480\big(-1+e^8\big)\delta^2(\Gamma^2+4\delta^2)g^2+\big(1+e^4\big)^2(\Gamma^2+4\delta^2)^2\\
&\times\big(\Gamma^2+12\delta^2\big)\big)(\Gamma^2+4\delta^2)^6-\frac{16U^5\delta}{(1+e^4)^3}\big(256\big(-1+e^4\big)^2\big(-205+133e^4\big)\delta^2g^6+256\big(29-24e^4-29e^8+24e^{12}\big)\\
&\times\delta^2(\Gamma^2+4\delta^2)g^4+26\big(-1+e^4\big)\big(1+e^4\big)^2(\Gamma^2+4\delta^2)^2\big(\Gamma^2+12\delta^2\big)g^2+\big(1+e^4\big)^3(\Gamma^2+4\delta^2)^4\big)(\Gamma^2+4\delta^2)^5\\
&+U^4\Big(88801128\delta^4\tanh^4(2)g^8+32768\delta^4\big(55(\Gamma^2+4\delta^2)-102g^2\big)\tanh^3(2)g^6+256\delta^2\big(768\delta^2g^4\\
&-1600\delta^2(\Gamma^2+4\delta^2)g^2+39(\Gamma^2+4\delta^2)^2\big(\Gamma^2+12\delta^2\big)\big)\tanh^2(2)g^4+64\delta^2(\Gamma^2+4\delta^2)^2\Big(11(\Gamma^2+4\delta^2)^2\\
&-16\big(\Gamma^2+12\delta^2\big)g^2\Big)\tanh(2)g^2+(\Gamma^2+4\delta^2)^6\Big)(\Gamma^2+4\delta^2)^4-4U^3\delta g^2\tanh(2)\big(19070976\delta^4\tanh^4(2)g^8\\
&+1572864\delta^4\big(3\Gamma^2+12\delta^2-7g^2\big)\tanh^3(2)g^6+1024\delta^2\big(1536\delta^2g^4-1856\delta^2(\Gamma^2+4\delta^2)g^2\\
&+33(\Gamma^2+4\delta^2)^2\big(\Gamma^2+12\delta^2\big)\big)\tanh^2(2)g^4-384\delta^2(\Gamma^2+4\delta^2)^4g^2+128\delta^2(\Gamma^2+4\delta^2)\\
&\big(1024\delta^2g^4-64\big(\Gamma^4+16\delta^2\Gamma^2+48\delta^4\big)g^2+27(\Gamma^2+4\delta^2)^3\big)\tanh(2)g^2+9(\Gamma^2+4\delta^2)^6\big)(\Gamma^2+4\delta^2)^3\\
&+32U^2\delta^2g^4\tanh(2)\Big(133038808\delta^4\tanh^5(2)g^8+32768\delta^4\big(119(\Gamma^2+4\delta^2)-324g^2\big)\tanh^4(2)g^6\\
&+256\delta^2\big(9216\delta^2g^4-9472\delta^2(\Gamma^2+4\delta^2)g^2+(\Gamma^2+4\delta^2)^2\big(131\Gamma^2+1596\delta^2\big)\big)\tanh^3(2)g^4\\
&+128\delta^2(\Gamma^2+4\delta^2)\big(3072\delta^2g^4-12(\Gamma^2+4\delta^2)\big(9\Gamma^2+116\delta^2\big)g^2+35(\Gamma^2+4\delta^2)^3\big)\tanh^2(2)g^2\\
&-2(\Gamma^2+4\delta^2)^6+(\Gamma^2+4\delta^2)^2\big(17(\Gamma^2+4\delta^2)^4-1152\delta^2g^2(\Gamma^2+4\delta^2)^2+768\delta^2\big(\Gamma^2+20\delta^2\big)g^4\big)\tanh(2)\Big)(\Gamma^2+4\delta^2)^2\\
&-256U\delta^3g^6\tanh^2(2)\Big(5439488\delta^4\tanh^5(2)g^8+98304\delta^4\big(19\Gamma^2+76\delta^2-56g^2\big)\tanh^4(2)g^6\\
&+2048\delta^2\big(768\delta^2g^4-784\delta^2(\Gamma^2+4\delta^2)g^2+3(\Gamma^2+4\delta^2)^2\big(3\Gamma^2+38\delta^2\big)\big)\tanh^3(2)g^4+192\delta^2(\Gamma^2+4\delta^2)^4g^2\\
&+64\delta^2(\Gamma^2+4\delta^2)\big(6144\delta^2g^4-16(\Gamma^2+4\delta^2)\big(11\Gamma^2+156\delta^2\big)g^2+49(\Gamma^2+4\delta^2)^3\big)\tanh^2(2)g^2-4(\Gamma^2+4\delta^2)^6\\
&+3(\Gamma^2+4\delta^2)^2\big(5(\Gamma^2+4\delta^2)^4-512\delta^2g^2(\Gamma^2+4\delta^2)^2+512\delta^2\big(\Gamma^2+20\delta^2\big)g^4\big)\tanh(2)\Big)(\Gamma^2+4\delta^2)\\
&+\frac{2048\delta^4g^8}{(1+e^4)^6}\big(196608\big(-1+e^4\big)^4\big(13-6e^4+e^8\big)\delta^4g^8+32768\big(-1+e^4\big)^3\big(1+e^4\big)\big(29-16e^4+3e^8\big)\delta^4(\Gamma^2+4\delta^2)g^6\\
&+512\big(-1+e^8\big)^2\delta^2(\Gamma^2+4\delta^2)^2\big(\big(17-14e^4+3e^8\big)\Gamma^2+12\big(21-14e^4+3e^8\big)\delta^2\big)g^4\\
&+384(-1+e)(1+e)\big(1+e^2\big)\big(1+e^4\big)^3\big(5-4e^4+e^8\big)\delta^2(\Gamma^2+4\delta^2)^4g^2\\
&+\big(1+e^4\big)^4\big(11-10e^4+3e^8\big)(\Gamma^2+4\delta^2)^6\big)\tanh^2(2)\Big)\Bigg)
\end{aligned}
$$

$$
\begin{aligned}
a_{6_2} =& 32\delta^2 g^3(\tanh(2)-1)\left(U(\Gamma^2+4\delta^2)-8\delta g^2\tanh(2)\right)\left(256\delta^2 g^4\tanh^2(2)+64\delta g^2\tanh(2)(\Gamma^2+4\delta^2)(\delta-U)\right. \\
&\left.+(\Gamma^2+4\delta^2)^2\left(\Gamma^2+4(U-\delta)^2\right)\right)\Bigg(-\left(\Gamma^2+4\delta^2(1+\tanh(2))\right)^2\left((\Gamma^2+4\delta^2)(\delta+U)-8\delta g^2\tanh(2)\right)^2 \\
&\times\Bigg(32\delta^2 g^4\tanh(2)\left(256\delta^2 g^2\tanh^2(2)\left(\Gamma^2+4\delta^2-3g^2\right)+\tanh(2)(\Gamma^2+4\delta^2)\left(3(\Gamma^2+4\delta^2)^2-128\delta^2 g^2\right)\right. \\
&\left.-(\Gamma^2+4\delta^2)^3+1280\delta^2 g^4\tanh^3(2)\right)+4U^4(\Gamma^2+4\delta^2)^4+8\delta U^3(\Gamma^2+4\delta^2)^3\left(-\Gamma^2-4\delta^2-\frac{16(e^4-1)g^2}{1+e^4}\right) \\
&+U^2(\Gamma^2+4\delta^2)^2\left(192\delta^2 g^2\tanh(2)\left(\Gamma^2+4\delta^2-2g^2\right)+(\Gamma^2+4\delta^2)^3+1920\delta^2 g^4\tanh^2(2)\right) \\
&-16\delta U g^2\tanh(2)(\Gamma^2+4\delta^2)\left(-32\delta^2 g^2(\Gamma^2+4\delta^2)+128\delta^2 g^2\tanh(2)\left(\Gamma^2+4\delta^2-3g^2\right)+(\Gamma^2+4\delta^2)^3\right. \\
&\left.+896\delta^2 g^4\tanh^2(2)\right)\Bigg)-\frac{64(e^4-1)\delta^2 g^4(\Gamma^2+4\delta^2)^2}{(1+e^4)^8}\Bigg(256\left(e^4-1\right)^2\delta^2 g^4+64\left(e^8-1\right)\delta g^2(\Gamma^2+4\delta^2)(\delta-U) \\
&+\left(1+e^4\right)^2(\Gamma^2+4\delta^2)^2\left(\Gamma^2+4(U-\delta)^2\right)\Bigg)^2\left(e^4-\frac{(e^4-1)\Gamma^2}{2(\Gamma^2+4\delta^2)}\right)^{\frac{(1+e^4)U(\Gamma^2+4\delta^2)}{4(e^4-1)\delta g^2}}\Bigg)
\end{aligned}
\tag{B.14g}
$$

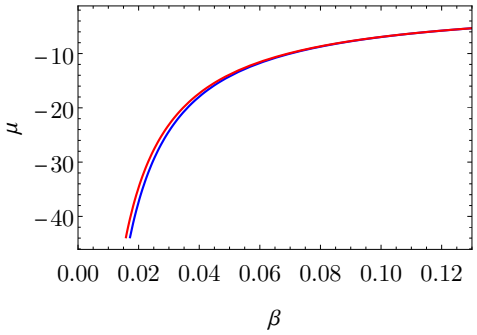

Fig. B.3: $\mu(\beta)$ approximations, Eq. (B.2) (blue), Eq. (B.3) (red) at $U/J=40$, $\hbar\delta/J=5$, $\hbar\Gamma/J=3$, $\hbar g/J=14.1$

B.1.2 End of bistability

At the disappearance of the low-λ-solution, again we try to approximate the system of equations determining (μ, β, λ) in order to find an analytic expression for $\lambda_{\mathrm{l}}(U, g, \delta, \Gamma)$ and show which terms in the equation of motions are crucial for the disappearance of the low solution. An approximate condition for the corresponding g_2 is also derived from the function domain, putting a constraint on the parameters for $\lambda_{\mathrm{l}}(U, g, \delta, \Gamma)$ to exist.

Generally we note, that the intersection line between particle-conservation- and self-consistency condition is only very weakly depending on λ. Also, the equation of motion is almost independent of the chemical potential β.

Determine $\mu(\beta)$ from particle conservation

Solving the particle conservation condition at $\lambda = 0$ as before, we obtain an approximate solution for $\mu(\beta)$ as before. However, since the temperature in this parameter region is a lot higher that at the onset of the high-λ solution, the expansion for $\exp(\beta U)$ large is a more crude approximation here. (See Fig. B.3 around $\beta \sim 0.05$)

We keep comparing the results using both $\mu(\beta)$ and $\mu_{\text{simple}}(\beta)$ [Eq. (B.2), Eq. (B.3)] to track the influence of these deviations.

Determine $\beta(\lambda)$ from self-consistency

To determine β, since the self-consistency weakly depends on λ, we insert the μ-equations into the condition at fixed $\lambda = \lambda_0$. The point λ_0 will later be set to e.g.

$$\lambda(U\to\infty) = \sqrt{\frac{\left((\Gamma/2)^2+\delta^2\right)^2 - 4\delta^2 g^2}{2\left(\left((\Gamma/2)^2+\delta^2\right)^2 - 2g^2\left((\Gamma/2)^2+2\delta^2\right)\right)}} \tag{B.15}$$

$$\lambda(U\to\infty, g\to\infty) = \frac{\delta}{\sqrt{(\Gamma/2)^2+2\delta^2}} \tag{B.16}$$

Note, that since the temperature is higher, the low-filling-approximation does not represent the system as well as at the onset. it might be necessary to consider further higher unit cell filling terms.

$$\lambda_0 = \frac{4\delta g}{((\Gamma/2)^2+\delta^2)} \times \frac{\left(1+4e^{\beta U}\right)\left(e^{\beta U/2}\left(1+2e^{\beta U}\right)+\sqrt{1+4e^{\beta U}}\cosh(\beta g\lambda_0)\right)\sinh(\beta g\lambda_0)}{4e^{\beta U/2}\left(1+6e^{\beta U}+8e^{2\beta U}\right)\cosh(\beta g\lambda_0)+\sqrt{1+4e^{\beta U}}\left(1+16e^{2\beta U}+\cosh(2\beta g\lambda_0)+2e^{\beta U}\left(3+2\cosh(2\beta g\lambda_0)\right)\right)} \tag{B.17}$$

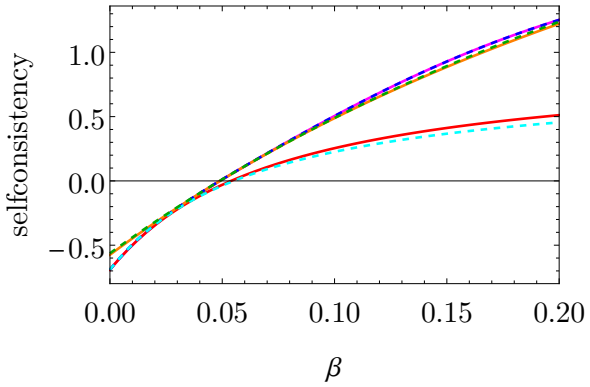

Fig. B.4: $\mathrm{sc}(\beta, \lambda_0, \beta_0)$ approx. of Eq. (B.17) at $U/J = 40$, $\hbar\delta/J = 5$, $\hbar\Gamma/J = 3$, $\hbar g/J = 14.1$, $\lambda_0(U \to \infty)$ Eq. (B.15)
magenta: $\mathrm{sc}(\mu(\beta), \beta, \lambda_0)$,
blue dashed:$\mathrm{sc}(\mu_{\mathrm{simple}}(\beta), \beta, \lambda_0)$
red: $\mathrm{sc}(\mu(\beta), \beta, \lambda_0)$ Padé-approx. $\beta_0 = 0$,
cyan dashed:$\mathrm{sc}(\mu_{\mathrm{simple}}(\beta), \beta, \lambda_0)$ Padé-approx. $\beta_0 = 0$
orange: $\mathrm{sc}(\mu(\beta), \beta, \lambda_0)$ Padé-approx. $\beta_0 = 2/U$,
green:$\mathrm{sc}(\mu_{\mathrm{simple}}(\beta), \beta, \lambda_0)$ Padé-approx. $\beta_0 = 2/U$

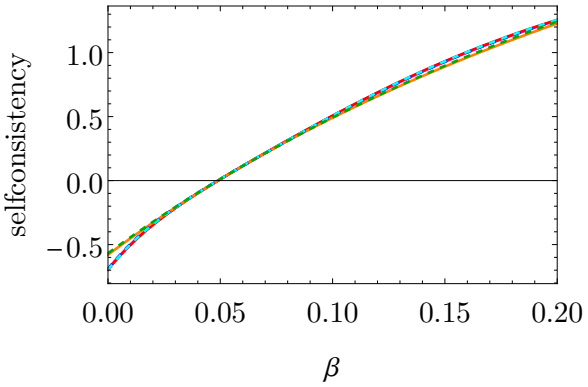

Fig. B.5: $\mathrm{sc}(\beta, \lambda_0, \beta_0)$ approx. of Eq. (B.17) at $U/J = 40$, $\hbar\delta/J = 5$, $\hbar\Gamma/J = 3$, $\hbar g/J = 14.1$ at ($\lambda_0(U \to \infty)$(B.15); $\lambda_0(U, g \to \infty)$ Eq. (B.16))
magenta: $\mathrm{sc}(\mu(\beta), \beta, \lambda_0(U \to \infty))$,
blue dashed:$\mathrm{sc}(\mu_{\mathrm{simple}}(\beta), \beta, \lambda_0(U \to \infty))$
red: $\mathrm{sc}(\mu(\beta), \beta, \lambda_0(U, g \to \infty))$,
cyan dashed:$\mathrm{sc}(\mu_{\mathrm{simple}}(\beta), \beta, \lambda_0(U, g \to \infty))$
orange: $\mathrm{sc}(\mu(\beta), \beta, \lambda_0(U, g \to \infty))$ Padé-approx. $\beta_0 = 2/U$,
green dashed:$\mathrm{sc}(\mu_{\mathrm{simple}}(\beta), \beta, \lambda_0(U, g \to \infty))$ Padé-approx. $\beta_0 = 2/U$

In order to solve for β, some approximations are necessary. We employ a Padé-approximation in β around the general expansion point β_0 to $\mathcal{O}(\beta)$. The resulting approximate self-consistency condition shows nice agreement with the original function.

Comparing the different approximations in the previous steps shows, that while the solution of the self-consistency is quite sensitive to the expansion point β_0 (comparing $\beta_0 = 0$ to $\beta_0 = 2/U$ in Fig. B.4) the more crude approximation for $\mu(\beta)$ seems to be sufficient.

´

The Padé-approximations of Eq. (B.17) can be solved for β, resulting in a function $\beta(\lambda_0, \beta_0, U, g, \delta, \Gamma)$. Comparison of the resulting curve for different expansion points (λ_0, β_0) are plotted in Fig. B.6 together with the full numerical result for β of the complete system of Eqs. (3.25). The sensitivity to the expansion point β_0 is apparent, while changes in λ_0 do not strongly effect the solutions.

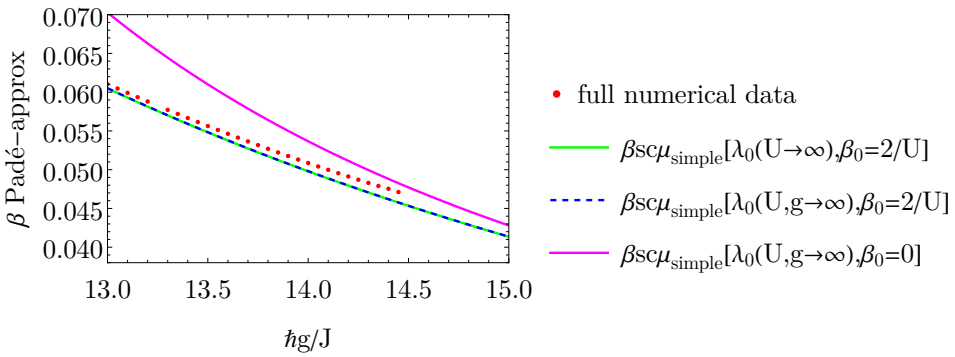

Fig. B.6: $\beta(\lambda_0, \beta_0, U, g, \delta, \Gamma)$ solutions of Padé-approx. of Eq. (B.17) around expansion points $\beta_0 = 2/U; 0$ at $U/J = 40$, $\hbar\delta/J = 5$, $\hbar\Gamma/J = 3$, $\hbar g/J = 14.1$ at ($\lambda_0(U \to \infty)$ Eq. (B.15); $\lambda_0(U, g \to \infty)$ Eq. (B.16))

Determine $\lambda(U, g, \delta\Gamma)$ from EOM

Finally, the approximations are inserted in the equation of motion. Here we see, that the qualitative behavior of the curve for the lower solution is nicely reproduced by the first four terms $\left(\propto \frac{1}{2g\lambda}, \frac{1}{2g\lambda - U}\right)$, while the remaining terms $\left(\propto \frac{1}{2g\lambda + U}\right)$ only introduce a minor shift of the function as seen in Fig. B.7.

The full low-filling-equation of motion $\mathrm{EOM}_{\mathrm{lf}}(\mu_{\mathrm{simple}}(\beta(\lambda_0, \beta_0)), \beta(\lambda_0, \beta_0), \lambda, U, g, \delta, \Gamma)$ is given by.

$$
\begin{aligned}
0 = &\frac{1}{4g\lambda}\left[\frac{e^{-\beta g\lambda}}{(\Gamma/2)^2 + (2g\lambda - \delta)^2} - \frac{e^{\beta g\lambda}}{(\Gamma/2)^2 + (2g\lambda + \delta)^2}\right] \\
&+ \frac{1}{4(2g\lambda - U)}\left[\frac{1}{(\Gamma/2)^2 + (2g\lambda - U - \delta)^2} - \frac{e^{\beta(2g\lambda - U)}}{(\Gamma/2)^2 + (2g\lambda - U + \delta)^2}\right] \\
&+ \frac{1}{4(2g\lambda + U)}\left[\frac{e^{-\beta(2g\lambda + u)}}{(\Gamma/2)^2 + (2g\lambda + U - \delta)^2} - \frac{1}{(\Gamma/2)^2 + (2g\lambda + U + \delta)^2}\right]
\end{aligned}
\tag{B.18}
$$

Not taking the low-filling limit leads to $\mathrm{EOM}(\mu_{\mathrm{simple}}(\beta(\lambda_0, \beta_0)), \beta(\lambda_0, \beta_0), \lambda, U, g, \delta, \Gamma)$

$$
\begin{aligned}
0 = &\frac{1}{4}\left[\frac{\left(e^{-\beta U} + 4\right)}{4g\lambda}\left(\frac{e^{-\beta g\lambda}}{(\Gamma/2)^2 + (2g\lambda - \delta)^2} - \frac{e^{\beta g\lambda}}{(\Gamma/2)^2 + (2g\lambda + \delta)^2}\right)\right. \\
&+ \frac{1}{2g\lambda - U}\left(\frac{1}{(\Gamma/2)^2 + (2g\lambda + U - \delta)^2} - \frac{e^{\beta(2g\lambda - U)}}{(\Gamma/2)^2 + (2g\lambda - U + \delta)^2}\right) \\
&\left.+ \frac{1}{2g\lambda + U}\left(\frac{e^{-\beta(2g\lambda + U)}}{(\Gamma/2)^2 + (2g\lambda + U - \delta)^2} - \frac{1}{(\Gamma/2)^2 + 2g\lambda + U + \delta)^2}\right)\right]
\end{aligned}
\tag{B.19}
$$

Since the behavior of the EOM/ first four terms looks to be quadratic, a series expansion around expansion point λ_0 to $\mathcal{O}(\lambda - \lambda_0)^2$ is used in order to solve for λ. Also, taking μ_{simple} is accurate enough, as replacing it by the U-dependent μ_{lf} does not lead to any noticeable improvement.

In contrast to this, it is important to consider all terms in the EOM-equation, taking only the dominating 4 terms noticeably shifts the critical coupling to lower $\hbar g/J$ (Compare dark blue, green/cyan lines in Fig. B.8)

Also, not performing the low-filling approximation slightly improves the result (Compare light green, cyan lines in Fig. B.8)

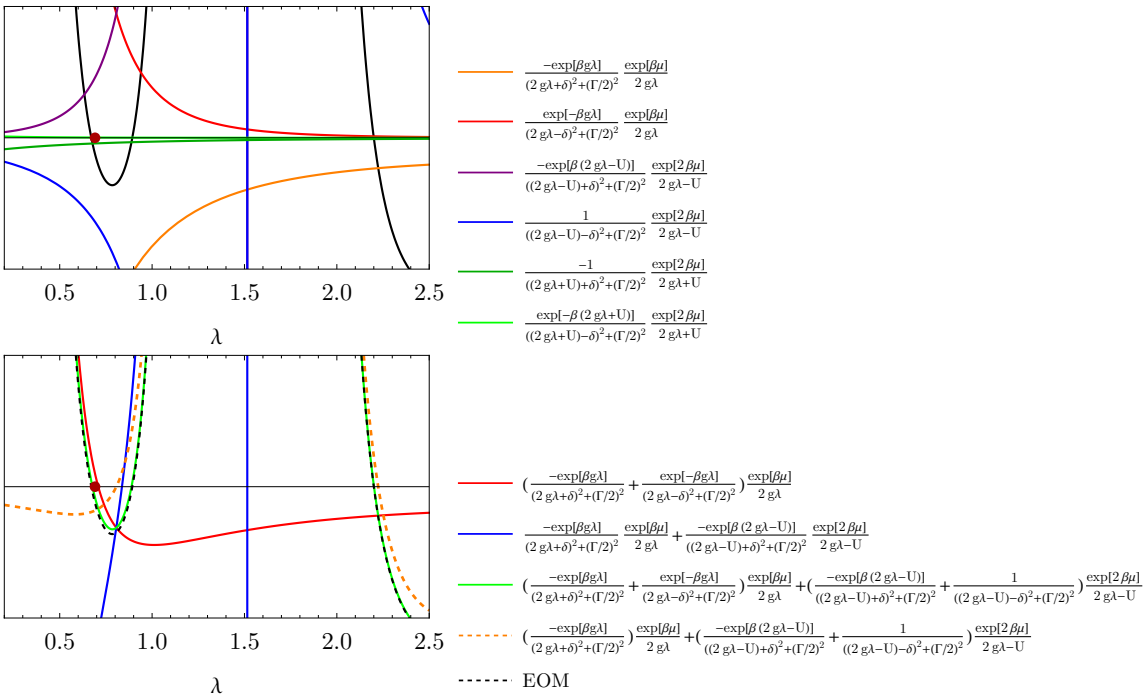

Fig. B.7: Terms and subsets of therms in Eq. (3.25a) EOM($\mu = 0, \beta(\lambda_0, \beta_0), \lambda, U, g, \delta, \Gamma$) at $U/J = 40$, $\hbar\delta/J = 5$, $\hbar\Gamma/J = 3$, $\hbar g/J = 13.2$, $\lambda_0(U \to \infty)$ from Eq. (B.15) The red dot marks λ_0, black is the full energy transfer equation

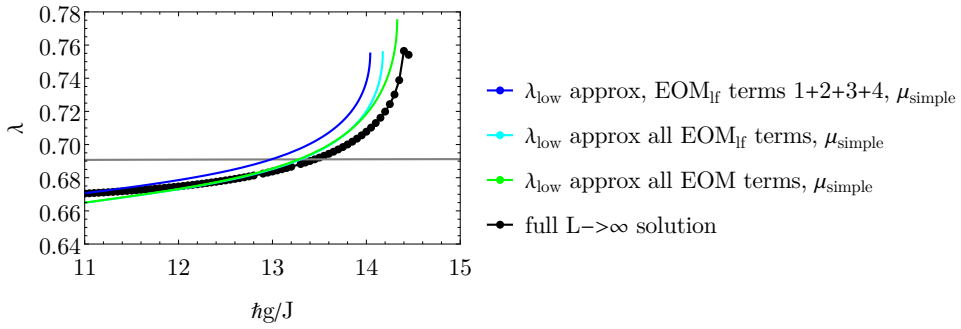

Fig. B.8: Terms in Eq. (3.25a) λ functions (various approximations) vs g¸ at $U/J = 40$, $\hbar\delta/J = 5$, $\hbar\Gamma/J = 3$, $\lambda_0(U \to \infty)$ compared to the full numerical data

$$
\begin{aligned}
\lambda = \Bigg[& \frac{e^{-\beta g\lambda_0}\big(64g(\delta-2g\lambda_0)-4\beta g\big(\Gamma^2+4(2g\lambda_0-\delta)^2\big)\big)}{4g\lambda_0\big(\Gamma^2+4(2g\lambda_0-\delta)^2\big)^2} - \frac{4e^{\beta g\lambda_0}g\big(\beta\big(\Gamma^2+4(2g\lambda_0+\delta)^2\big)-16(2g\lambda_0+\delta)\big)}{4g\lambda_0\big(\Gamma^2+4(2g\lambda_0+\delta)^2\big)^2} \\
& + \frac{1}{4}\Bigg(\frac{2g}{(2g\lambda_0-U)^2}\Big(\frac{1}{(\Gamma/2)^2+(2g\lambda_0-U-\delta)^2} - \frac{e^{\beta(2g\lambda_0-U)}}{(\Gamma/2)^2+(2g\lambda_0-U-\delta)^2}\Big) \qquad \text{(B.20)} \\
& - \frac{1}{2g\lambda_0-U}\Bigg(-\frac{2e^{\beta(2g\lambda_0-U)}\beta g}{(\Gamma/2)^2+(-2g\lambda_0+U+\delta)^2} - \frac{4(2g\lambda_0-U-\delta)g}{\big((\Gamma/2)^2+(2g\lambda_0-U-\delta)^2\big)^2} + \frac{4e^{\beta(U-2g\lambda_0)}(-2g\lambda_0+U+\delta)g}{\big((\Gamma/2)^2+(2g\lambda_0-U+\delta)^2\big)^2}\Bigg) \\
& + \frac{1}{16\lambda_0^2 g}\Big(\frac{e^{-\beta g\lambda_0}}{(\Gamma/2)^2+(2g\lambda_0-\delta)^2} - \frac{e^{\beta g\lambda_0}}{(\Gamma/2)^2+(2g\lambda_0+\delta)^2}\Big) \\
& \times \Bigg(\frac{2g}{(2g\lambda_0+U)^2}\Bigg(\frac{e^{-\beta(2g\lambda_0+U)}}{(\Gamma/2)^2+(U-2g\lambda_0+\delta)^2} - \frac{1}{(\Gamma/2)^2+(2g\lambda_0+U+\delta)^2}\Bigg) \\
& \quad - \frac{1}{2g\lambda_0+U}\Bigg(-\frac{2e^{-\beta(2g\lambda_0+U)}\beta g}{(\Gamma/2)^2+(2g\lambda_0+U-\delta)^2} - \frac{4e^{-\beta(2g\lambda_0+U)}(U-2g\lambda_0+\delta)g}{\big((\Gamma/2)^2+(U-2g\lambda_0+\delta)^2\big)^2} + \frac{4(2g\lambda_0+U+\delta)g}{\big((\Gamma/2)^2+(2g\lambda_0+U+\delta)^2\big)^2}\Bigg)\Bigg) \\
& + 2\lambda_0\Bigg[\frac{1}{4}\Bigg(-\frac{4}{(U-2g\lambda_0)^3}\Bigg(\frac{1}{(\Gamma/2)^2+(-2g\lambda_0+U-\delta)^2} - \frac{e^{\beta(2g\lambda_0-U)}}{(\Gamma/2)^2+(2g\lambda_0-U+\delta)^2}\Bigg)g^2 \\
& + \frac{g^2}{2g\lambda_0-U}\Bigg(-\frac{4e^{\beta(2g\lambda_0-U)}\beta^2}{\Gamma^2+4(2g\lambda_0-U+\delta)^2} + \frac{64e^{\beta(2g\lambda_0-U)}(-2g\lambda_0+U+\delta)\beta}{\big(\Gamma^2+4(2g\lambda_0-U+\delta)^2\big)^2} + \frac{32\big(12(2g\lambda_0-U-\delta)^2-\Gamma^2\big)}{\big(\Gamma^2+4(2g\lambda_0-U-\delta)^2\big)^3} \\
& \qquad - \frac{32e^{\beta(2g\lambda_0-U)}\big(12(2g\lambda_0-U+\delta)^2-\Gamma^2\big)}{\big(\Gamma^2+4(2g\lambda_0-U+\delta)^2\big)^3}\Bigg) \\
& - \frac{2g}{(2g\lambda_0-U)^2}\Bigg(-\frac{2e^{\beta(2g\lambda_0-U)}\beta}{(\Gamma/2)^2+(2g\lambda_0-U+\delta)^2} - \frac{4g(-2g\lambda_0+U-\delta)g}{\big((\Gamma/2)^2+(-2g\lambda_0+U-\delta)^2\big)^2} + \frac{4ge^{\beta(2g\lambda_0-U)}(-2g\lambda_0+U+\delta)}{\big((\Gamma/2)^2+(2g\lambda_0-U+\delta)^2\big)^2}\Bigg)\Bigg) \\
& + \frac{1}{4}\Bigg(\frac{4g^2}{(U+2g\lambda_0)^3}\Bigg(\frac{e^{-\beta(2g\lambda_0+U)}}{(\Gamma/2)^2+(2g\lambda_0+U-\delta)^2} - \frac{1}{(\Gamma/2)^2+(2g\lambda_0+U+\delta)^2}\Bigg) \\
& + \frac{8g^2}{U+2g\lambda_0}\Bigg(\frac{e^{-\beta(2g\lambda_0+U)}\beta^2}{\Gamma^2+4(2g\lambda_0+U-\delta)^2} + \frac{16e^{-\beta(2g\lambda_0+U)}(2g\lambda_0+U-\delta)\beta}{\big(\Gamma^2+4(2g\lambda_0+U-\delta)^2\big)^2} \\
& \qquad + \frac{8e^{-\beta(2g\lambda_0+U)}\big(12(2g\lambda_0+U-\delta)^2-\Gamma^2\big)}{\big(\Gamma^2+4(2g\lambda_0+U-\delta)^2\big)^3} - \frac{8\big(12(2g\lambda_0+U+\delta)^2-\Gamma^2\big)}{\big(\Gamma^2+4(2g\lambda_0+U+\delta)^2\big)^3}\Bigg) \\
& - \frac{2g}{(U+2g\lambda_0)^2}\Bigg(-\frac{2ge^{-\beta(2g\lambda_0+U)}\beta}{(\Gamma/2)^2+(2g\lambda_0+U-\delta)^2} - \frac{4e^{-\beta(2g\lambda_0+U)}(2g\lambda_0+U-\delta)g}{\big((\Gamma/2)^2+(2g\lambda_0+U-\delta)^2\big)^2} + \frac{4g(2g\lambda_0+U+\delta)}{\big((\Gamma/2)^2+(2g\lambda_0+U+\delta)^2\big)^2}\Bigg)\Bigg) \\
& + \frac{2g^2}{4g\lambda_0}e^{-\beta g\lambda_0}\Bigg(\frac{\beta^2}{\Gamma^2+4(2g\lambda_0-\delta)^2} - \frac{32(\delta-2g\lambda_0)\beta}{\big(\Gamma^2+4(2g\lambda_0-\delta)^2\big)^2} - \frac{32\big(\Gamma^2-12(2g\lambda_0-\delta)^2\big)}{\big(\Gamma^2+4(2g\lambda_0-\delta)^2\big)^3}\Bigg) \\
& + \frac{g}{2\lambda_0}e^{-\beta g\lambda_0}\Bigg(-\frac{e^{2\beta g\lambda_0}\beta^2}{\Gamma^2+4(2g\lambda_0+\delta)^2} + \frac{32e^{2\beta g\lambda_0}(2g\lambda_0+\delta)\beta}{\big(\Gamma^2+4(2g\lambda_0+\delta)^2\big)^2} - \frac{32e^{2\beta g\lambda_0}\big(12(2g\lambda_0+\delta)^2-\Gamma^2\big)}{\big(\Gamma^2+4(2g\lambda_0+\delta)^2\big)^3}\Bigg) \\
& + \frac{1}{\lambda_0^2}e^{-\beta g\lambda_0}\Bigg(\frac{\beta\big(\Gamma^2+4(2g\lambda_0-\delta)^2\big)-16(\delta-2g\lambda_0)}{\big(\Gamma^2+4(2g\lambda_0-\delta)^2\big)^2} + \frac{e^{2\beta g\lambda_0}\big(\beta\big(\Gamma^2+4(2g\lambda_0+\delta)^2\big)-16(2g\lambda_0+\delta)\big)}{\big(\Gamma^2+4(2g\lambda_0+\delta)^2\big)^2}\Bigg) \\
& + \frac{1}{4g\lambda_0^3}\Bigg(\frac{e^{-\beta g\lambda_0}}{(\Gamma/2)^2+(2g\lambda_0-\delta)^2} - \frac{e^{\beta g\lambda_0}}{(\Gamma/2)^2+(2g\lambda_0+\delta)^2}\Bigg)\Bigg] + \frac{4g}{4g\lambda_0^2}e^{-\beta g\lambda_0}\Bigg(\frac{\beta\big(\Gamma^2+4(2g\lambda_0-\delta)^2\big)-16(\delta-2g\lambda_0)}{\big(\Gamma^2+4(2g\lambda_0-\delta)^2\big)^2} \\
& \quad + \frac{e^{2\beta g\lambda_0}\big(\beta\big(\Gamma^2+4(2g\lambda_0+\delta)^2\big)-16(2g\lambda_0+\delta)\big)}{\big(\Gamma^2+4(2g\lambda_0+\delta)^2\big)^2}\Big) + \frac{1}{4g\lambda_0^3}\Bigg(\frac{e^{-\beta g\lambda_0}}{(\Gamma/2)^2+(2g\lambda_0-\delta)^2} - \frac{e^{\beta g\lambda_0}}{(\Gamma/2)^2+(2g\lambda_0+\delta)^2}\Bigg)\Bigg)
\end{aligned}
$$

(B.21)

$$-\sqrt{\Bigg[-\frac{1}{\lambda_0^2}\left(\frac{e^{-\beta g\lambda_0}}{(\Gamma/2)^2+(2g\lambda_0-\delta)^2}-\frac{e^{\beta g\lambda_0}}{(\Gamma/2)^2+(2g\lambda_0+\delta)^2}\right)}$$
$$+\frac{1}{\lambda_0}\left(\frac{e^{-\beta g\lambda_0}\big(64g(\delta-2g\lambda_0)-4\beta g\big(\Gamma^2+4(2g\lambda_0-\delta)^2\big)\big)}{4g\big(\Gamma^2+4(2g\lambda_0-\delta)^2\big)^2}-\frac{e^{\beta g\lambda_0}\big(\beta\big(\Gamma^2+4(2g\lambda_0+\delta)^2\big)-16(2g\lambda_0+\delta)\big)}{\big(\Gamma^2+4(2g\lambda_0+\delta)^2\big)^2}\right)$$
$$+\frac{1}{4(2g\lambda_0-U)}\left(-\frac{2e^{\beta(2g\lambda_0-U)}\beta g}{(\Gamma/2)^2+(2g\lambda_0-U+\delta)^2}-\frac{4(-2g\lambda_0+U-\delta)g}{\big((\Gamma/2)^2+(-2g\lambda_0+U-\delta)^2\big)^2}+\frac{4e^{\beta(2g\lambda_0-U)}(-2g\lambda_0+U+\delta)g}{\big((\Gamma/2)^2+(2g\lambda_0-U+\delta)^2\big)^2}\right)$$
$$-\frac{2g}{4(2g\lambda_0-U)^2}\left(\frac{1}{(\Gamma/2)^2+(-2g\lambda_0+U-\delta)^2}-\frac{e^{\beta(2g\lambda_0-U)}}{(\Gamma/2)^2+(2g\lambda_0-U+\delta)^2}\right)$$
$$+\frac{1}{4(U+2g\lambda_0)}\left(-\frac{2e^{-\beta(2g\lambda_0+U)}\beta g}{(\Gamma/2)^2+(2g\lambda_0+U-\delta)^2}-\frac{4e^{-\beta(2g\lambda_0+U)}(2g\lambda_0+U-\delta)g}{\big((\Gamma/2)^2+(U-\delta+2\lambda_0 g)^2\big)^2}+\frac{4(2g\lambda_0+U+\delta)g}{\big((\Gamma/2)^2+(2g\lambda_0+U+\delta)^2\big)^2}\right)$$
$$-\frac{2g}{4(U+2g\lambda_0)^2}\left(\frac{e^{-\beta(2g\lambda_0+U)}}{(\Gamma/2)^2+(2g\lambda_0+U-\delta)^2}-\frac{1}{(\Gamma/2)^2+(2g\lambda_0+U+\delta)^2}\right)\Bigg]^2$$
$$-4\Bigg(\frac{1}{4g\lambda_0}\left(\frac{e^{-\beta g\lambda_0}}{(\Gamma/2)^2+(2g\lambda_0-\delta)^2}-\frac{e^{\beta g\lambda_0}}{(\Gamma/2)^2+(2g\lambda_0+\delta)^2}\right)$$
$$+\frac{1}{4(2g\lambda_0-U)}\left(\frac{1}{(\Gamma/2)^2+(-2g\lambda_0+U-\delta)^2}-\frac{e^{\beta(2g\lambda_0-U)}}{(\Gamma/2)^2+(2g\lambda_0-U+\delta)^2}\right)$$
$$+\frac{1}{4(U+2g\lambda_0)}\left(\frac{e^{-\beta(2g\lambda_0+U)}}{(\Gamma/2)^2+(2g\lambda_0+U-\delta)^2}-\frac{1}{(\Gamma/2)^2+(2g\lambda_0+U+\delta)^2}\right)\Bigg)$$
$$\times\Bigg(\frac{1}{4}\left(-\frac{4g^2}{(U-2g\lambda_0)^3}\left(\frac{1}{(\Gamma/2)^2+(-2g\lambda_0+U-\delta)^2}-\frac{e^{\beta(2g\lambda_0-U)}}{(\Gamma/2)^2+(2g\lambda_0-U+\delta)^2}\right)\right.$$
$$+\frac{g^2}{2g\lambda_0-U}\left[-\frac{4e^{\beta(2g\lambda_0-U)}\beta^2}{\Gamma^2+4(2g\lambda_0-U+\delta)^2}+\frac{64e^{\beta(2g\lambda_0-U)}(-2g\lambda_0+U+\delta)\beta}{\big(\Gamma^2+4(2g\lambda_0-U+\delta)^2\big)^2}+\frac{32\big(12(U+\delta-2g\lambda_0)^2-\Gamma^2\big)}{\big(\Gamma^2+4(U+\delta-2g\lambda_0)^2\big)^3}\right.$$
$$\left.\left.-\frac{32e^{\beta(2g\lambda_0-U)}\big(12(2g\lambda_0-U+\delta)^2-\Gamma^2\big)}{\big(\Gamma^2+4(2g\lambda_0-U+\delta)^2\big)^3}\right)-\frac{2g}{(2g\lambda_0-U)^2}\left(-\frac{2e^{\beta(2g\lambda_0-U)}\beta g}{(\Gamma/2)^2+(2g\lambda_0-U+\delta)^2}\right.\right.$$
$$\left.\left.-\frac{4(-2g\lambda_0+U-\delta)g}{\big((\Gamma/2)^2+(-2g\lambda_0+U-\delta)^2\big)^2}+\frac{4e^{\beta(2g\lambda_0-U)}(-2g\lambda_0+U+\delta)g}{\big((\Gamma/2)^2+(2g\lambda_0-U+\delta)^2\big)^2}\right)\right]$$
$$+\frac{1}{4}\left[\frac{4g^2}{(U+2g\lambda_0)^3}\left(\frac{e^{-\beta(2g\lambda_0+U)}}{(\Gamma/2)^2+(2g\lambda_0+U-\delta)^2}-\frac{1}{(\Gamma/2)^2+(2g\lambda_0+U+\delta)^2}\right)\right.$$
$$+\frac{8g^2}{U+2g\lambda_0}\left(\frac{e^{-\beta(2g\lambda_0+U)}\beta^2}{\Gamma^2+4(2g\lambda_0+U-\delta)^2}+\frac{16e^{-\beta(2g\lambda_0+U)}(2g\lambda_0+U-\delta)\beta}{\big(\Gamma^2+4(2g\lambda_0+U-\delta)^2\big)^2}+\frac{8e^{-\beta(2g\lambda_0+U)}\big(12(2g\lambda_0+U-\delta)^2-\Gamma^2\big)}{\big(\Gamma^2+4(2g\lambda_0+U-\delta)^2\big)^3}\right.$$
$$\left.\left.-\frac{8\big(12(2g\lambda_0+U+\delta)^2-\Gamma^2\big)}{\big(\Gamma^2+4(2g\lambda_0+U+\delta)^2\big)^3}\right)-\frac{2g}{(U+2g\lambda_0)^2}\left(-\frac{2e^{-\beta(2g\lambda_0+U)}\beta g}{(\Gamma/2)^2+(2g\lambda_0+U-\delta)^2}-\frac{4e^{-\beta(2g\lambda_0+U)}(2g\lambda_0+U-\delta)g}{\big((\Gamma/2)^2+(2g\lambda_0+U-\delta)^2\big)^2}\right.\right.$$
$$\left.\left.+\frac{4(2g\lambda_0+U+\delta)g}{\big((\Gamma/2)^2+(2g\lambda_0+U+\delta)^2\big)^2}\right)\right]$$
$$+\frac{2g^2}{4g\lambda_0}e^{-\beta g\lambda_0}\left(\frac{\beta^2}{\Gamma^2+4(2g\lambda_0-\delta)^2}-\frac{32(\delta-2g\lambda_0)\beta}{\big(\Gamma^2+4(\delta-2g\lambda_0)^2\big)^2}-\frac{32\big(\Gamma^2-12(2g\lambda_0-\delta)^2\big)}{\big(\Gamma^2+4(\delta-2g\lambda_0)^2\big)^3}\right)$$

$$
\begin{aligned}
&+\frac{2g^2}{4g\lambda_0}e^{-\beta g\lambda_0}\left(-\frac{e^{2\beta g\lambda_0}\beta^2}{\Gamma^2+4(2g\lambda_0+\delta)^2}+\frac{32e^{2\beta g\lambda_0}(2g\lambda_0+\delta)\beta}{\left(\Gamma^2+4(2g\lambda_0+\delta)^2\right)^2}-\frac{32e^{2\beta g\lambda_0}\left(12(2g\lambda_0+\delta)^2-\Gamma^2\right)}{\left(\Gamma^2+4(2g\lambda_0+\delta)^2\right)^3}\right)\\
&+\frac{4g}{4g\lambda_0^2}e^{-\beta g\lambda_0}\left(\frac{\beta\left(\Gamma^2+4(2g\lambda_0-\delta)^2\right)-16(\delta-2g\lambda_0)}{\left(\Gamma^2+4(2g\lambda_0-\delta)^2\right)^2}+\frac{e^{2\beta g\lambda_0}\left(\beta\left(\Gamma^2+4(2g\lambda_0+\delta)^2\right)-16(2g\lambda_0+\delta)\right)}{\left(\Gamma^2+4(2g\lambda_0+\delta)^2\right)^2}\right)\\
&+\frac{1}{4g\lambda_0^3}\left(\frac{e^{-\beta g\lambda_0}}{(\Gamma/2)^2+(2g\lambda_0-\delta)^2}-\frac{e^{\beta g\lambda_0}}{(\Gamma/2)^2+(2g\lambda_0+\delta)^2}\right)\Bigg]\\
&\Bigg/\Bigg[2\left(\frac{1}{4}\left(-\frac{4g^2}{(U-2g\lambda_0)^3}\left(\frac{1}{(\Gamma/2)^2+(-2g\lambda_0+U-\delta)^2}-\frac{e^{\beta(2g\lambda_0-U)}}{(\Gamma/2)^2+(2g\lambda_0-U+\delta)^2}\right)\right.\right.\\
&+\frac{g^2}{2g\lambda_0-U}\left(-\frac{4e^{\beta(2g\lambda_0-U)}\beta^2}{\Gamma^2+4(2g\lambda_0-U+\delta)^2}+\frac{64e^{\beta(2g\lambda_0-U)}(-2g\lambda_0+U+\delta)\beta}{\left(\Gamma^2+4(2g\lambda_0-U+\delta)^2\right)^2}+\frac{32\left(12(U+\delta-2g\lambda_0)^2-\Gamma^2\right)}{\left(\Gamma^2+4(U+\delta-2g\lambda_0)^2\right)^3}\right.\\
&\left.-\frac{32e^{\beta(2g\lambda_0-U)}\left(12(2g\lambda_0-U+\delta)^2-\Gamma^2\right)}{\left(\Gamma^2+4(2g\lambda_0-U+\delta)^2\right)^3}\right)\\
&\left.-\frac{2g}{(2g\lambda_0-U)^2}\left(-\frac{2e^{\beta(2g\lambda_0-U)}\beta g}{(\Gamma/2)^2+(2g\lambda_0-U+\delta)^2}-\frac{4(-2g\lambda_0+U-\delta)g}{\left((\Gamma/2)^2+(-2g\lambda_0+U-\delta)^2\right)^2}+\frac{4e^{\beta(2g\lambda_0-U)}(-2g\lambda_0+U+\delta)g}{\left((\Gamma/2)^2+(2g\lambda_0-U+\delta)^2\right)^2}\right)\right)\\
&+\frac{1}{4}\left(\frac{4g^2}{(U+2g\lambda_0)^3}\left(\frac{e^{-\beta(2g\lambda_0+U)}}{(\Gamma/2)^2+(2g\lambda_0+U-\delta)^2}-\frac{1}{(\Gamma/2)^2+(2g\lambda_0+U+\delta)^2}\right)\right.\\
&+\frac{8g^2}{U+2g\lambda_0}\left(\frac{e^{-\beta(2g\lambda_0+U)}\beta^2}{\Gamma^2+4(2g\lambda_0+U-\delta)^2}+\frac{16e^{-\beta(2g\lambda_0+U)}(2g\lambda_0+U-\delta)\beta}{\left(\Gamma^2+4(2g\lambda_0+U-\delta)^2\right)^2}\right.\\
&\left.+\frac{8e^{-\beta(2g\lambda_0+U)}\left(12(2g\lambda_0+U-\delta)^2-\Gamma^2\right)}{\left(\Gamma^2+4(2g\lambda_0+U-\delta)^2\right)^3}-\frac{8\left(12(2g\lambda_0+U+\delta)^2-\Gamma^2\right)}{\left(\Gamma^2+4(2g\lambda_0+U+\delta)^2\right)^3}\right)\\
&\left.\left.-\frac{2g}{(U+2g\lambda_0)^2}\left(-\frac{2e^{-\beta(2g\lambda_0+U)}\beta g}{(\Gamma/2)^2+(2g\lambda_0+U-\delta)^2}-\frac{4e^{-\beta(2g\lambda_0+U)}(2g\lambda_0+U-\delta)g}{\left((\Gamma/2)^2+(2g\lambda_0+U-\delta)^2\right)^2}+\frac{4(2g\lambda_0+U+\delta)g}{\left((\Gamma/2)^2+(2g\lambda_0+U+\delta)^2\right)^2}\right)\right)\\
&\quad+\frac{2g^2}{4g\lambda_0}e^{-\beta g\lambda_0}\left(\frac{\beta^2}{\Gamma^2+4(2g\lambda_0-\delta)^2}-\frac{e^{2\beta g\lambda_0}\beta^2}{\Gamma^2+4(2g\lambda_0+\delta)^2}-\frac{32(\delta-2g\lambda_0)\beta}{\left(\Gamma^2+4(2g\lambda_0-\delta)^2\right)^2}+\frac{32e^{2\beta g\lambda_0}(2g\lambda_0+\delta)\beta}{\left(\Gamma^2+4(2g\lambda_0+\delta)^2\right)^2}\right.\\
&\quad\left.-\frac{32e^{2\beta g\lambda_0}\left(12(2g\lambda_0+\delta)^2-\Gamma^2\right)}{\left(\Gamma^2+4(2g\lambda_0+\delta)^2\right)^3}-\frac{32\left(\Gamma^2-12(2g\lambda_0-\delta)^2\right)}{\left(\Gamma^2+4(2g\lambda_0-\delta)^2\right)^3}\right)\\
&\quad+\frac{4g}{4g\lambda_0^2}e^{-\beta g\lambda_0}\left(\frac{\beta\left(\Gamma^2+4(2g\lambda_0-\delta)^2\right)-16(\delta-2g\lambda_0)}{\left(\Gamma^2+4(2g\lambda_0-\delta)^2\right)^2}+\frac{e^{2\beta g\lambda_0}\left(\beta\left(\Gamma^2+4(2g\lambda_0+\delta)^2\right)-16(2g\lambda_0+\delta)\right)}{\left(\Gamma^2+4(2g\lambda_0+\delta)^2\right)^2}\right)\\
&\quad\left.+\frac{1}{4g\lambda_0^3}\left(\frac{e^{-\beta g\lambda_0}}{(\Gamma/2)^2+(2g\lambda_0-\delta)^2}-\frac{e^{\beta g\lambda_0}}{(\Gamma/2)^2+(2g\lambda_0+\delta)^2}\right)\right)\Bigg]
\end{aligned}
$$

$$
\begin{aligned}
\lambda = \Bigg[& 2\Bigg(\frac{1}{4}\Bigg(\frac{2g}{(2g\lambda_0-U)^2}\Bigg(\frac{1}{(\Gamma/2)^2+(U+\delta-2g\lambda_0)^2}-\frac{4e^{\beta(2g\lambda_0-U)}}{\Gamma^2+4(2g\lambda_0-U+\delta)^2}\Bigg)\\
& -\frac{4g}{2g\lambda_0-U}\Bigg(-\frac{2e^{\beta(2g\lambda_0-U)}\beta}{\Gamma^2+4(2g\lambda_0-U+\delta)^2}+\frac{U+\delta-2g\lambda_0}{\big((\Gamma/2)^2+(U+\delta-2g\lambda_0)^2\big)^2}+\frac{16e^{\beta(2g\lambda_0-U)}(-2g\lambda_0+U+\delta)}{\big(\Gamma^2+4(2g\lambda_0-U+\delta)^2\big)^2}\Bigg)\\
& -\frac{8g}{(U+2g\lambda_0)^2}\Bigg(\frac{1}{\Gamma^2+4(2g\lambda_0+U+\delta)^2}-\frac{e^{-\beta(2g\lambda_0+U)}}{\Gamma^2+4(2g\lambda_0+U-\delta)^2}\Bigg)\\
& -\frac{1}{U+2g\lambda_0}\Bigg(\frac{64g(2g\lambda_0+U+\delta)}{\big(\Gamma^2+4(2g\lambda_0+U+\delta)^2\big)^2}+4\Bigg(-\frac{2e^{-\beta(2g\lambda_0+U)}\beta g}{\Gamma^2+4(2g\lambda_0+U-\delta)^2}-\frac{16e^{-\beta(2g\lambda_0+U)}(2g\lambda_0+U-\delta)g}{\big(\Gamma^2+4(2g\lambda_0+U-\delta)^2\big)^2}\Bigg)\Bigg)\\
& -\frac{e^{-\beta g\lambda_0}\big(4+e^{-U\beta}\big)}{g\lambda_0^2}\Bigg(-\frac{g\lambda_0\big(\beta\big(\Gamma^2+4(2g\lambda_0-\delta)^2\big)-16(\delta-2g\lambda_0)\big)}{\big(\Gamma^2+4(2g\lambda_0-\delta)^2\big)^2}\\
& -\frac{e^{2\beta g\lambda_0}g\lambda_0\big(\beta\big(\Gamma^2+4(2g\lambda_0+\delta)^2\big)-16(2g\lambda_0+\delta)\big)}{\big(\Gamma^2+4(2g\lambda_0+\delta)^2\big)^2}-\frac{1}{\Gamma^2+4(2g\lambda_0-\delta)^2}+\frac{e^{2\beta g\lambda_0}}{\Gamma^2+4(2g\lambda_0+\delta)^2}\Bigg)\Bigg)\\
& +\frac{1}{2}\lambda_0\Bigg(-\frac{4g^2}{(U-2g\lambda_0)^3}\Bigg(\frac{1}{(\Gamma/2)^2+(U+\delta-2g\lambda_0)^2}-\frac{4e^{\beta(2g\lambda_0-U)}}{\Gamma^2+4(2g\lambda_0-U+\delta)^2}\Bigg)\\
& -\frac{16g^2}{(U+2g\lambda_0)^2}\Bigg(-\frac{e^{-\beta(2g\lambda_0+U)}\beta}{\Gamma^2+4(2g\lambda_0+U-\delta)^2}-\frac{8e^{-\beta(2g\lambda_0+U)}(2g\lambda_0+U-\delta)}{\big(\Gamma^2+4(2g\lambda_0+U-\delta)^2\big)^2}+\frac{8(2g\lambda_0+U+\delta)}{\big(\Gamma^2+4(2g\lambda_0+U+\delta)^2\big)^2}\Bigg)\\
& +\frac{4g^2}{(U+2g\lambda_0)^3}\Bigg(\frac{4e^{-\beta(2g\lambda_0+U)}}{\Gamma^2+4(2g\lambda_0+U-\delta)^2}-\frac{4}{\Gamma^2+4(2g\lambda_0+U+\delta)^2}\Bigg)\\
& +\frac{8g^2}{U+2g\lambda_0}\Bigg(\frac{e^{-\beta(2g\lambda_0+U)}\beta^2}{\Gamma^2+4(2g\lambda_0+U-\delta)^2}+\frac{16e^{-\beta(2g\lambda_0+U)}(2g\lambda_0+U-\delta)\beta}{\big(\Gamma^2+4(2g\lambda_0+U-\delta)^2\big)^2}+\frac{8e^{-\beta(2g\lambda_0+U)}\big(12(2g\lambda_0+U-\delta)^2\Gamma^2\big)}{\big(\Gamma^2+4(2g\lambda_0+U-\delta)^2\big)^3}\\
& -\frac{8\big(12(2g\lambda_0+U+\delta)^2-\Gamma^2\big)}{\big(\Gamma^2+4(2g\lambda_0+U+\delta)^2\big)^3}\Bigg)-\frac{8g^2}{(2g\lambda_0-U)^2\big((\Gamma/2)^2+(U+\delta-2g\lambda_0)^2\big)^3\big(\Gamma^2+4(2g\lambda_0-U+\delta)^2\big)^3}\\
& \times\Big((\Gamma/2)^2+(U+\delta-2g\lambda_0)^2\big(\Gamma^2+4(2g\lambda_0-U+\delta)^2\big)\big((U+\delta-2g\lambda_0)\big(\Gamma^2+4(2g\lambda_0-U+\delta)^2\big)^2\\
& -2e^{\beta(2g\lambda_0-U)}\Big((\Gamma/2)^2+(U+\delta-2g\lambda_0)^2\Big)^2\big(8(U-\delta-2g\lambda_0)+\beta\big(\Gamma^2+4(2g\lambda_0-U+\delta)^2\big)\big)\big)\\
& +(U-2g\lambda_0)\Big(\Big((\Gamma/2)^2-3(U+\delta-2g\lambda_0)^2\Big)\big(\Gamma^2+4(2g\lambda_0-U+\delta)^2\big)^3\\
& -2e^{\beta(2g\lambda_0-U)}\Big((\Gamma/2)^2+(U+\delta-2g\lambda_0)^2\Big)^3\big(-\beta^2\big(\Gamma^2+4(2g\lambda_0-U+\delta)^2\big)^2\\
& -16\beta(U-\delta-2g\lambda_0)\big(\Gamma^2+4(2g\lambda_0-U+\delta)^2\big)+8\big(\Gamma^2-12(2g\lambda_0-U+\delta)^2\big)\big)\Big)\Big)\\
& +\frac{\big(4+e^{-U\beta}\big)}{4g}\Bigg(\frac{2e^{-\beta g\lambda_0}g^2}{\lambda_0}\Bigg(\frac{\beta^2}{\Gamma^2+4(2g\lambda_0-\delta)^2}-\frac{e^{2\beta g\lambda_0}\beta^2}{\Gamma^2+4(2g\lambda_0+\delta)^2}-\frac{32(\delta-2g\lambda_0)\beta}{\big(\Gamma^2+4(2g\lambda_0-\delta)^2\big)^2}\\
& +\frac{32e^{2\beta g\lambda_0}(2g\lambda_0+\delta)\beta}{\big(\Gamma^2+4(2g\lambda_0+\delta)^2\big)^2}-\frac{32e^{2\beta g\lambda_0}\big(12(2g\lambda_0+\delta)^2-\Gamma^2\big)}{\big(\Gamma^2+4(2g\lambda_0+\delta)^2\big)^3}-\frac{32\big(\Gamma^2-12(2g\lambda_0-\delta)^2\big)}{\big(\Gamma^2+4(2g\lambda_0-\delta)^2\big)^3}\Bigg)\\
& +\frac{4e^{-\beta g\lambda_0}g}{\lambda_0^2}\Bigg(\frac{\beta\big(\Gamma^2+4(2g\lambda_0-\delta)^2\big)-16(\delta-2g\lambda_0)}{\big(\Gamma^2+4(2g\lambda_0-\delta)^2\big)^2}+\frac{e^{2\beta g\lambda_0}\big(\beta\big(\Gamma^2+4(2g\lambda_0+\delta)^2\big)-16(2g\lambda_0+\delta)\big)}{\big(\Gamma^2+4(2g\lambda_0+\delta)^2\big)^2}\Bigg)\\
& +\frac{1}{\lambda_0^3}\Bigg(\frac{4e^{-\beta g\lambda_0}}{\Gamma^2+4(2g\lambda_0-\delta)^2}-\frac{4e^{\beta g\lambda_0}}{\Gamma^2+4(2g\lambda_0+\delta)^2}\Bigg)\Bigg)\Bigg)\\
& -\sqrt{\frac{1}{16}\Bigg(-\frac{2g\big(\frac{1}{(\Gamma/2)^2+(U+\delta-2g\lambda_0)^2}-\frac{4e^{\beta(2g\lambda_0-U)}}{\Gamma^2+4(2g\lambda_0-U+\delta)^2}\big)}{(2g\lambda_0-U)^2}+\frac{4g}{2g\lambda_0-U}\Big(-\frac{2e^{\beta(2g\lambda_0-U)}\beta}{\Gamma^2+4(2g\lambda_0-U+\delta)^2}}
\end{aligned}
$$

$$+\frac{U+\delta-2g\lambda_0}{\left((\Gamma/2)^2+(U+\delta-2g\lambda_0)^2\right)^2}+\frac{16e^{\beta(2g\lambda_0-U)}(-2g\lambda_0+U+\delta)}{\left(\Gamma^2+4(2g\lambda_0-U+\delta)^2\right)^2}\Big)$$

$$+\frac{8g}{(U+2g\lambda_0)^2}\left(\frac{1}{\Gamma^2+4(2g\lambda_0+U+\delta)^2}-\frac{e^{-\beta(2g\lambda_0+U)}}{\Gamma^2+4(2g\lambda_0+U-\delta)^2}\right)$$

$$+\frac{1}{U+2g\lambda_0}\frac{64g(2g\lambda_0+U+\delta)}{\left(\Gamma^2+4(2g\lambda_0+U+\delta)^2\right)^2}+4\Big(-\frac{2e^{-\beta(2g\lambda_0+U)}\beta g}{\Gamma^2+4(2g\lambda_0+U-\delta)^2}-\frac{16e^{-\beta(2g\lambda_0+U)}(2g\lambda_0+U-\delta)g}{\left(\Gamma^2+4(2g\lambda_0+U-\delta)^2\right)^2}\Big)$$

$$+\frac{e^{-\beta g\lambda_0}\left(4+e^{-U\beta}\right)}{g\lambda_0^2}\Bigg(-\frac{g\lambda_0\left(\beta\left(\Gamma^2+4(2g\lambda_0-\delta)^2\right)-16(\delta-2g\lambda_0)\right)}{\left(\Gamma^2+4(2g\lambda_0-\delta)^2\right)^2}-\frac{e^{2\beta g\lambda_0}g\lambda_0\left(\beta\left(\Gamma^2+4(2g\lambda_0+\delta)^2\right)\right.}{\left(\Gamma^2+4(2g\lambda_0+\delta)^2\right)^2}$$

$$\left.-\frac{16(2g\lambda_0+\delta))}{\left(\Gamma^2+4(2g\lambda_0+\delta)^2\right)^2}-\frac{1}{\Gamma^2+4(2g\lambda_0-\delta)^2}+\frac{e^{2\beta g\lambda_0}}{\Gamma^2+4(2g\lambda_0+\delta)^2}\right)\Bigg)^2$$

$$-\frac{1}{4}\Bigg[\frac{\left(4+e^{-U\beta}\right)}{4g\lambda_0}\left(\frac{4e^{-\beta g\lambda_0}}{\Gamma^2+4(2g\lambda_0-\delta)^2}-\frac{4e^{\beta g\lambda_0}}{\Gamma^2+4(2g\lambda_0+\delta)^2}\right)$$

$$+\frac{1}{2g\lambda_0-U}\left(\frac{1}{(\Gamma/2)^2+(U+\delta-2g\lambda_0)^2}-\frac{4e^{\beta(2g\lambda_0-U)}}{\Gamma^2+4(2g\lambda_0-U+\delta)^2}\right)$$

$$+\frac{1}{U+2g\lambda_0}\left(\frac{4e^{-\beta(2g\lambda_0+U)}}{\Gamma^2+4(2g\lambda_0+U-\delta)^2}-\frac{4}{\Gamma^2+4(2g\lambda_0+U+\delta)^2}\right)\Bigg]$$

$$\times\Big(-\frac{4g^2}{(U-2g\lambda_0)^3}\left(\frac{1}{(\Gamma/2)^2+(U+\delta-2g\lambda_0)^2}-\frac{4e^{\beta(2g\lambda_0-U)}}{\Gamma^2+4(2g\lambda_0-U+\delta)^2}\right)$$

$$-\frac{16g^2}{(U+2g\lambda_0)^2}\Bigg(-\frac{e^{-\beta(2g\lambda_0+U)}\beta}{\Gamma^2+4(2g\lambda_0+U-\delta)^2}-\frac{8e^{-\beta(2g\lambda_0+U)}(2g\lambda_0+U-\delta)}{\left(\Gamma^2+4(2g\lambda_0+U-\delta)^2\right)^2}$$

$$+\frac{8(2g\lambda_0+U+\delta)}{\left(\Gamma^2+4(2g\lambda_0+U+\delta)^2\right)^2}\Bigg)+\frac{4g^2}{(U+2g\lambda_0)^3}\left(\frac{4e^{-\beta(2g\lambda_0+U)}}{\Gamma^2+4(2g\lambda_0+U-\delta)^2}-\frac{4}{\Gamma^2+4(2g\lambda_0+U+\delta)^2}\right)$$

$$+\frac{8g^2}{U+2g\lambda_0}\Bigg(\frac{e^{-\beta(2g\lambda_0+U)}\beta^2}{\Gamma^2+4(2g\lambda_0+U-\delta)^2}+\frac{16e^{-\beta(2g\lambda_0+U)}(2g\lambda_0+U-\delta)\beta}{\left(\Gamma^2+4(2g\lambda_0+U-\delta)^2\right)^2}+\frac{8e^{-\beta(2g\lambda_0+U)}\left(12(2g\lambda_0+U-\delta)^2-\Gamma^2\right)}{\left(\Gamma^2+4(2g\lambda_0+U-\delta)^2\right)^3}$$

$$-\frac{8\left(12(2g\lambda_0+U+\delta)^2-\Gamma^2\right)}{\left(\Gamma^2+4(2g\lambda_0+U+\delta)^2\right)^3}\Bigg)-\frac{4g^2}{(2g\lambda_0-U)^2\left((\Gamma/2)^2+(U+\delta-2g\lambda_0)^2\right)^3\left(\Gamma^2+4(2g\lambda_0-U+\delta)^2\right)^3}$$

$$\times\Big(2\left((\Gamma/2)^2+(U+\delta-2g\lambda_0)^2\right)\left(\Gamma^2+4(2g\lambda_0-U+\delta)^2\right)\left((U+\delta-2g\lambda_0)\left(\Gamma^2+4(2g\lambda_0-U+\delta)^2\right)^2\right.$$

$$-2e^{\beta(2g\lambda_0-U)}\left((\Gamma/2)^2+(U+\delta-2g\lambda_0)^2\right)^2\left(8(U-\delta-2g\lambda_0)\right.$$

$$\left.+\beta\left(\Gamma^2+4(2g\lambda_0-U+\delta)^2\right)\right)\Big)+(U-2g\lambda_0)\Big(\left((\Gamma/2)^2-3(U+\delta-2g\lambda_0)^2\right)\left(\Gamma^2+4(2g\lambda_0-U+\delta)^2\right)^3$$

$$-2e^{\beta(2g\lambda_0-U)}\left((\Gamma/2)^2+(U+\delta-2g\lambda_0)^2\right)^3\Big(-\beta^2\left(\Gamma^2+4(2g\lambda_0-U+\delta)^2\right)^2-16\beta(U-\delta-2g\lambda_0)\left(\Gamma^2+4(2g\lambda_0-U+\delta)^2\right)$$

$$+8\left(\Gamma^2-12(2g\lambda_0-U+\delta)^2\right)\Big)\Big)\Big)+\frac{\left(4+e^{-U\beta}\right)}{4g}\Big(\frac{2e^{-\beta g\lambda_0}g^2}{\lambda_0}\Big(\frac{\beta^2}{\Gamma^2+4(2g\lambda_0-\delta)^2}-\frac{e^{2\beta g\lambda_0}\beta^2}{\Gamma^2+4(2g\lambda_0+\delta)^2}$$

$$-\frac{32(\delta-2g\lambda_0)\beta}{\left(\Gamma^2+4(2g\lambda_0-\delta)^2\right)^2}+\frac{32e^{2\beta g\lambda_0}(2g\lambda_0+\delta)\beta}{\left(\Gamma^2+4(2g\lambda_0+\delta)^2\right)^2}-\frac{32e^{2\beta g\lambda_0}\left(12(2g\lambda_0+\delta)^2-\Gamma^2\right)}{\left(\Gamma^2+4(2g\lambda_0+\delta)^2\right)^3}-\frac{32\left(\Gamma^2-12(2g\lambda_0-\delta)^2\right)}{\left(\Gamma^2+4(2g\lambda_0-\delta)^2\right)^3}\Big)$$

$$+\frac{4e^{-\beta g\lambda_0}g}{\lambda_0^2}\left(\frac{\beta\left(\Gamma^2+4(2g\lambda_0-\delta)^2\right)-16(\delta-2g\lambda_0)}{\left(\Gamma^2+4(2g\lambda_0-\delta)^2\right)^2}+\frac{e^{2\beta g\lambda_0}\left(\beta\left(\Gamma^2+4(2g\lambda_0+\delta)^2\right)-16(2g\lambda_0+\delta)\right)}{\left(\Gamma^2+4(2g\lambda_0+\delta)^2\right)^2}\right)$$

$$+\frac{1}{\lambda_0^3}\left(\frac{4e^{-\beta g\lambda_0}}{\Gamma^2+4(2g\lambda_0-\delta)^2}-\frac{4e^{\beta g\lambda_0}}{\Gamma^2+4(2g\lambda_0+\delta)^2}\right)\Big)\Big)\Big)\Bigg]$$

$$
\Bigg/\Bigg[-\frac{4g^2}{(U-2g\lambda_0)^3}\left(\frac{1}{(\Gamma/2)^2+(U+\delta-2g\lambda_0)^2}-\frac{4e^{\beta(2g\lambda_0-U)}}{\Gamma^2+4(2g\lambda_0-U+\delta)^2}\right)
$$

$$
-\frac{16g^2}{(U+2g\lambda_0)^2}\left(-\frac{e^{-\beta(2g\lambda_0+U)}\beta}{\Gamma^2+4(2g\lambda_0+U-\delta)^2}-\frac{8e^{-\beta(2g\lambda_0+U)}(2g\lambda_0+U-\delta)}{\left(\Gamma^2+4(2g\lambda_0+U-\delta)^2\right)^2}+\frac{8(2g\lambda_0+U+\delta)}{\left(\Gamma^2+4(2g\lambda_0+U+\delta)^2\right)^2}\right)
$$

$$
+\frac{4g^2}{(U+2g\lambda_0)^3}\left(\frac{4e^{-\beta(2g\lambda_0+U)}}{\Gamma^2+4(2g\lambda_0+U-\delta)^2}-\frac{4}{\Gamma^2+4(2g\lambda_0+U+\delta)^2}\right)+\frac{8g^2}{U+2g\lambda_0}\left(\frac{e^{-\beta(2g\lambda_0+U)}\beta^2}{\Gamma^2+4(2g\lambda_0+U-\delta)^2}\right.
$$

$$
\left.+\frac{16e^{-\beta(2g\lambda_0+U)}(2g\lambda_0+U-\delta)\beta}{\left(\Gamma^2+4(2g\lambda_0+U-\delta)^2\right)^2}+\frac{8e^{-\beta(2g\lambda_0+U)}\left(12(2g\lambda_0+U-\delta)^2-\Gamma^2\right)}{\left(\Gamma^2+4(2g\lambda_0+U-\delta)^2\right)^3}-\frac{8\left(12(2g\lambda_0+U+\delta)^2-\Gamma^2\right)}{\left(\Gamma^2+4(2g\lambda_0+U+\delta)^2\right)^3}\right)
$$

$$
-\frac{4g^2}{(2g\lambda_0-U)^2\left((\Gamma/2)^2+(U+\delta-2g\lambda_0)^2\right)^3\left(\Gamma^2+4(2g\lambda_0-U+\delta)^2\right)^3}\left(2\left((\Gamma/2)^2+(U+\delta-2g\lambda_0)^2\right)\right.
$$

$$
\times\left(\Gamma^2+4(2g\lambda_0-U+\delta)^2\right)\left((U+\delta-2g\lambda_0)\left(\Gamma^2+4(2g\lambda_0-U+\delta)^2\right)^2\right.
$$

$$
-2e^{\beta(2g\lambda_0-U)}\left((\Gamma/2)^2+(U+\delta-2g\lambda_0)^2\right)^2\left(8(U-\delta-2g\lambda_0)+\beta\left(\Gamma^2+4(2g\lambda_0-U+\delta)^2\right)\right)\Big)
$$

$$
+(U-2g\lambda_0)\Big(\left((\Gamma/2)^2-3(U+\delta-2g\lambda_0)^2\right)\left(\Gamma^2+4(2g\lambda_0-U+\delta)^2\right)^3
$$

$$
-2e^{\beta(2g\lambda_0-U)}\left((\Gamma/2)^2+(U+\delta-2g\lambda_0)^2\right)^3\left(-\beta^2\left(\Gamma^2+4(2g\lambda_0-U+\delta)^2\right)^2\right.
$$

$$
\left.\left.-16\beta(U-\delta-2g\lambda_0)\left(\Gamma^2+4(2g\lambda_0-U+\delta)^2\right)+8\left(\Gamma^2-12(2g\lambda_0-U+\delta)^2\right)\right)\right)
$$

$$
+\frac{\left(4+e^{-U\beta}\right)}{4g}\left[\frac{2e^{-\beta g\lambda_0}g^2}{\lambda_0}\left(\frac{\beta^2}{\Gamma^2+4(2g\lambda_0-\delta)^2}-\frac{e^{2\beta g\lambda_0}\beta^2}{\Gamma^2+4(2g\lambda_0+\delta)^2}-\frac{32(\delta-2g\lambda_0)\beta}{\left(\Gamma^2+4(2g\lambda_0-\delta)^2\right)^2}\right.\right.
$$

$$
\left.+\frac{32e^{2\beta g\lambda_0}(2g\lambda_0+\delta)\beta}{\left(\Gamma^2+4(2g\lambda_0+\delta)^2\right)^2}-\frac{32e^{2\beta g\lambda_0}\left(12(2g\lambda_0+\delta)^2-\Gamma^2\right)}{\left(\Gamma^2+4(2g\lambda_0+\delta)^2\right)^3}-\frac{32\left(\Gamma^2-12(2g\lambda_0-\delta)^2\right)}{\left(\Gamma^2+4(2g\lambda_0-\delta)^2\right)^3}\right)
$$

$$
+\frac{4g}{\lambda_0^2}e^{-\beta g\lambda_0}\left(\frac{\beta\left(\Gamma^2+4(2g\lambda_0-\delta)^2\right)-16(\delta-2g\lambda_0)}{\left(\Gamma^2+4(2g\lambda_0-\delta)^2\right)^2}+\frac{e^{2\beta g\lambda_0}\left(\beta\left(\Gamma^2+4(2g\lambda_0+\delta)^2\right)-16(2g\lambda_0+\delta)\right)}{\left(\Gamma^2+4(2g\lambda_0+\delta)^2\right)^2}\right)
$$

$$
\left.+\frac{1}{\lambda_0^3}\left(\frac{4e^{-\beta g\lambda_0}}{\Gamma^2+4(2g\lambda_0-\delta)^2}-\frac{4e^{\beta g\lambda_0}}{\Gamma^2+4(2g\lambda_0+\delta)^2}\right)\right]\Bigg]
$$

Appendix C

Appendix "Fluctuation-induced Bistability for Bosons"

C.1 Derivation of System of equations

Here we show details of the derivation of the system of equations used to describe a bosonic many-body system coupled globally to a dissipative cavity field via transverse pumping. As for fermions, we perform a perturbation calculation in the kinetic energy and go to the thermodynamic limit. We want to rewrite the susceptibility $\chi_T(\omega)$ in terms of the perturbation $\hat{H}_{\text{kin}}$. In this sense, we first compute equation of motion of the operator $\hat{\Delta}$. Since $\hat{\Delta}$ consists of local densities all terms of $\hat{H}_{\text{eff}}$ except for the kinetic part commute with it and we obtain

$$\begin{aligned}\frac{\partial}{\partial t}\hat{\Delta}(t) &= \frac{\partial}{\partial t}e^{i\hat{H}_{\text{eff}}t/\hbar}\hat{\Delta}e^{-i\hat{H}_{\text{eff}}t/\hbar} = -\frac{i}{\hbar}e^{i\hat{H}_{\text{eff}}t/\hbar}\big[\hat{H}_{\text{eff}},\hat{\Delta}\big]e^{-i\hat{H}_{\text{eff}}t/\hbar} \\ &= -\frac{i}{\hbar}e^{i\hat{H}_0t/\hbar}\big[\hat{H}_{\text{kin}},\hat{\Delta}\big]e^{-i\hat{H}_0t/\hbar} = -\frac{i}{\hbar}\big[\hat{H}_{\text{kin}},\hat{\Delta}\big](t).\end{aligned} \tag{C.1}$$

Using this result we have

$$\begin{aligned}\chi_T(\omega) &= -\frac{i}{\hbar}\int_0^\infty dt e^{i(\omega+i\epsilon)t}\left\langle\big[\hat{\Delta}(t),\hat{\Delta}(0)\big]\right\rangle_T = -\frac{1}{\hbar\omega}\int_0^\infty dt\frac{\partial}{\partial t}\big(e^{i(\omega+i\epsilon)t}\big)\left\langle\big[\hat{\Delta}(t),\hat{\Delta}(0)\big]\right\rangle_T \\ &\overset{P.I.}{=} -\frac{1}{\hbar\omega}\left[e^{i(\omega+i\epsilon)t}\left\langle\big[\hat{\Delta}(t),\hat{\Delta}(0)\big]\right\rangle_T\right]_0^\infty + \frac{1}{\hbar\omega}\int_0^\infty dt e^{i(\omega+i\epsilon)t}\frac{\partial}{\partial t}\left\langle\big[\hat{\Delta}(t),\hat{\Delta}(0)\big]\right\rangle_T \\ &= \frac{1}{\hbar\omega}\int_0^\infty dt e^{i(\omega+i\epsilon)t}\left\langle\Big[\frac{\partial\hat{\Delta}(t)}{\partial t},\hat{\Delta}(0)\Big]\right\rangle_T = -\frac{i}{\hbar^2\omega}\int_0^\infty dt e^{i(\omega+i\epsilon)t}\left\langle\big[\big[\hat{H}_{\text{kin}},\hat{\Delta}\big](t)),\hat{\Delta}(0)\big]\right\rangle_T \\ &= -\frac{1}{\hbar^2\omega^2}\int_0^\infty dt\frac{\partial}{\partial t}\big(e^{i(\omega+i\epsilon)t}\big)\left\langle\big[\big[\hat{H}_{\text{kin}},\hat{\Delta}\big](t),\hat{\Delta}(0)\big]\right\rangle_T \\ &\overset{P.I.}{=} -\frac{1}{\omega^2}\left[e^{i(\omega+i\epsilon)t}\left\langle\big[\big[\hat{H}_{\text{kin}},\hat{\Delta}\big](0),\hat{\Delta}(-t)\big]\right\rangle_T\right]_0^\infty - \frac{i}{\omega^2}\int_0^\infty dt e^{i(\omega+i\epsilon)t}\left\langle\big[\big[\hat{H}_{\text{kin}},\hat{\Delta}\big](t),\big[\hat{H}_{\text{kin}},\hat{\Delta}\big](0)\big]\right\rangle_T \\ &= -\frac{i}{\hbar^3\omega^2}\int_0^\infty dt e^{i(\omega+i\epsilon)t}\left\langle\big[\big[\hat{H}_{\text{kin}},\hat{\Delta}\big](t),\big[\hat{H}_{\text{kin}},\hat{\Delta}\big](0)\big]\right\rangle_T\end{aligned}$$

This agrees with the result for fermions. In this calculation we used the time-translational symmetry $\Big[\hat{\Delta}(t),\hat{\Delta}(0)\Big] = \Big[\hat{\Delta}(0),\hat{\Delta}(-t)\Big]$ and we performed partial integration (P.I.). The double commutator expression of the susceptibility at which we arrived provides a nice way to perform the perturbation theory. By computing the expectation

values with respect to the unperturbed Hamiltonian $\hat{H}_0$, defined as $\langle ... \rangle_{\hat{H}_0,T} = \mathrm{Tr}\Big\{ e^{-\beta \hat{H}_0} ... \Big\}$, we obtain perturbative result in the kinetic terms on the order of $\mathcal{O}(J^2)$. The explicit calculation of the commutators and expectation value results in the following

$$\begin{aligned}
\big[\hat{H}_{\text{kin}}, \hat{\Delta}(0)\big] &= -J \sum_{\langle j,l\rangle, m} (-1)^m \big[\hat{b}_j^\dagger \hat{b}_l + \hat{b}_l^\dagger \hat{b}_j, \hat{b}_m^\dagger \hat{b}_m\big] = -2J \sum_{\langle j,l\rangle} \mathrm{sgn}(l-j) \hat{b}_j^\dagger \hat{b}_l \\
\big[\hat{H}_{\text{kin}}, \hat{\Delta}\big](t) &= e^{i\hat{H}_0 t/\hbar} \big[\hat{H}_{\text{kin}}, \hat{\Delta}(0)\big] e^{-i\hat{H}_0 t/\hbar} = -2J e^{i\hat{H}_0 t/\hbar} \Big(\sum_{\langle j,l\rangle} \mathrm{sgn}(l-j) \hat{b}_j^\dagger \hat{b}_l \Big) e^{-i\hat{H}_0 t/\hbar}.
\end{aligned}$$

We determine the time evolution of the operators by considering the action on the local basis states

$$\{ |0\rangle_j, |1\rangle_j, |2\rangle_j, ..., |n_{\text{max}}\rangle_j \}$$

and obtain

$$\begin{aligned}
\hat{o}_j(t) &= e^{i\hat{H}_0 t/\hbar} \hat{o}_j e^{-i\hat{H}_0 t/\hbar} = e^{i\hat{H}_j t/\hbar} \hat{o}_j e^{-i\hat{H}_j t/\hbar} \\
&= e^{it/\hbar(\frac{U}{2}\hat{n}_j(\hat{n}_j-1) - \hbar g\lambda \hat{\Delta}_j - \mu \hat{n}_j)} \hat{o}_j e^{-it/\hbar(\frac{U}{2}\hat{n}_j(\hat{n}_j-1) - \hbar g\lambda \hat{\Delta}_j - \mu \hat{n}_j)}
\end{aligned}$$

$$\begin{aligned}
\hat{b}_j(t) |n\rangle_j &= e^{i\hat{H}_j t/\hbar} \hat{b}_j e^{-i\hat{H}_j t/\hbar} |n\rangle_j \qquad \text{(C.2a)} \\
&= e^{it/\hbar(\frac{U}{2}\hat{n}_j(\hat{n}_j-1) - \hbar g\lambda \hat{\Delta}_j - \mu \hat{n}_j)} \hat{b}_j e^{-it/\hbar(\frac{U}{2}\hat{n}_j(\hat{n}_j-1) - \hbar g\lambda \hat{\Delta}_j - \mu \hat{n}_j)} |n\rangle_j \\
&= \sqrt{n_j} e^{-it/\hbar(U(n_j-1) - \hbar g\lambda(-1)^j - \mu)} |n-1\rangle_j \\
\hat{b}_j^\dagger(t) |n\rangle_j &= e^{i\hat{H}_j t/\hbar} \hat{b}_j^\dagger e^{-i\hat{H}_j t/\hbar} |n\rangle_j \qquad \text{(C.2b)} \\
&= e^{it/\hbar(\frac{U}{2}\hat{n}_j(\hat{n}_j-1) - \hbar g\lambda \hat{\Delta}_j - \mu \hat{n}_j)} \hat{b}_j^\dagger e^{-it/\hbar(\frac{U}{2}\hat{n}_j(\hat{n}_j-1) - \hbar g\lambda \hat{\Delta}_j - \mu \hat{n}_j)} |n\rangle_j \\
&= \sqrt{n_j+1} e^{+it/\hbar(Un_j - \hbar g\lambda(-1)^j - \mu)} |n+1\rangle_j
\end{aligned}$$

$$\begin{aligned}
\big[\hat{H}_{\text{kin}}, \hat{\Delta}\big](t) &= e^{i\hat{H}_0 t/\hbar} \big[\hat{H}_{\text{kin}}, \hat{\Delta}\big](0) e^{-i\hat{H}_0 t/\hbar} = -2J \Big(\sum_{\langle j,l\rangle} \mathrm{sgn}(l-j) e^{i\hat{H}_j t/\hbar} \hat{b}_j^\dagger e^{-i\hat{H}_j t/\hbar} e^{i\hat{H}_l t/\hbar} \hat{b}_l e^{-i\hat{H}_l t/\hbar} \Big) \\
&= -2J \Big(\sum_{\langle j,l\rangle} \mathrm{sgn}(l-j) \hat{b}_j^\dagger(t) \hat{b}_l(t) \Big) \qquad \text{(C.3)}
\end{aligned}$$

with this

$$\big[\big[\hat{H}_{\text{kin}}, \hat{\Delta}\big](t), \big[\hat{H}_{\text{kin}}, \hat{\Delta}\big](0)\big] = e^{i\hat{H}_0 t/\hbar} \big[\hat{H}_{\text{kin}}, \hat{\Delta}\big](0) e^{-i\hat{H}_0 t/\hbar} = 4J^2 \Big(\sum_{\substack{\langle j,l\rangle \\ \langle n,m\rangle}} \mathrm{sgn}(l-j)\mathrm{sgn}(n-m) \big[\hat{b}_j^\dagger(t) \hat{b}_l(t), \hat{b}_n^\dagger \hat{b}_m\big] \Big)$$

For notation simplicity, restrict to $1D$,

$$\begin{aligned}
\big[\big[\hat{H}_{\text{kin}}, \hat{\Delta}\big](t), \big[\hat{H}_{\text{kin}}, \hat{\Delta}\big](0)\big] &= 4J^2 \Big(\sum_{j,l} (-1)^{j+l} \big[\hat{b}_j^\dagger(t) \hat{b}_{j+1}(t) - \hat{b}_{j+1}^\dagger(t) \hat{b}_j(t), \hat{b}_l^\dagger \hat{b}_{l+1} - \hat{b}_{l+1}^\dagger \hat{b}_l\big] \Big) \\
&= 4J^2 \sum_{j,l} (-1)^{j+l} \Big(\underbrace{\big[\hat{b}_j^\dagger(t) \hat{b}_{j+1}(t), \hat{b}_l^\dagger \hat{b}_{l+1}\big] + \big[\hat{b}_{j+1}^\dagger(t) \hat{b}_j(t), \hat{b}_{l+1}^\dagger \hat{b}_l\big]}_{\text{does not go back to initial state}} \\
&\qquad - \big[\hat{b}_j^\dagger(t) \hat{b}_{j+1}(t), \hat{b}_{l+1}^\dagger \hat{b}_l\big] - \big[\hat{b}_{j+1}^\dagger(t) \hat{b}_j(t), \hat{b}_l^\dagger \hat{b}_{l+1}\big] \Big)
\end{aligned}$$

$$\Big\langle\big[[\hat{H}_{\text{kin}},\hat{\Delta}](t),[\hat{H}_{\text{kin}},\hat{\Delta}](0)\big]\Big\rangle_T = -4J^2\sum_{j,l}(-1)^{j+l}\Big(\Big\langle[\hat{b}_j^\dagger(t)\hat{b}_{j+1}(t),\hat{b}_{l+1}^\dagger\hat{b}_l]\Big\rangle_T+\Big\langle[\hat{b}_{j+1}^\dagger(t)\hat{b}_j(t),\hat{b}_l^\dagger\hat{b}_{l+1}]\Big\rangle_T\Big)$$
$$= -\frac{4J^2}{\text{Tr}\Big(\prod_m e^{-\beta\hat{H}_m}\Big)}\sum_{j,l}(-1)^{j+l}\Bigg(\text{Tr}\Bigg(\prod_m e^{-\beta\hat{H}_m}[\hat{b}_j^\dagger(t)\hat{b}_{j+1}(t),\hat{b}_{l+1}^\dagger\hat{b}_l]\Bigg)$$
$$+\text{Tr}\Bigg(\prod_m e^{-\beta\hat{H}_m}[\hat{b}_{j+1}^\dagger(t)\hat{b}_j(t),\hat{b}_l^\dagger\hat{b}_{l+1}]\Bigg)\Bigg)$$

$$\langle n_j,n_{j+1}|\,[[\hat{H}_{\text{kin}}^{j,j+1},\hat{\Delta}^{j,j+1}](t),[\hat{H}_{\text{kin}}^{j,j+1},\hat{\Delta}^{j,j+1}](0)]\,|n_j,n_{j+1}\rangle$$
$$= -4J^2\Big(\langle n_j,n_{j+1}|\,[\hat{b}_j^\dagger(t)\hat{b}_{j+1}(t),\hat{b}_{j+1}^\dagger\hat{b}_j]\,|n_j,n_{j+1}\rangle$$
$$+\langle n_j,n_{j+1}|\,[\hat{b}_{j+1}^\dagger(t)\hat{b}_j(t),\hat{b}_j^\dagger\hat{b}_{j+1}]\,|n_j,n_{j+1}\rangle\Big)$$

from here for simplicity ($\hbar=1$, $\eta_j=2g\lambda(-1)^j$)

$$\langle n,m|\,[\hat{b}_j^\dagger(t)\hat{b}_{j+1}(t),\hat{b}_{j+1}^\dagger\hat{b}_j]\,|n,m\rangle = \sqrt{n}\sqrt{m+1}\,\langle n,m|\,\hat{b}_j^\dagger(t)\hat{b}_{j+1}(t)\,|n-1,m+1\rangle \tag{C.4a}$$
$$-\sqrt{n+1}\sqrt{m}e^{-it(U(m-1)-\eta_{j+1}/2-\mu)}e^{+it(Un-\eta_j/2-\mu)}\,\langle n,m|\,\hat{b}_{j+1}^\dagger\hat{b}_j\,|n+1,m-1\rangle$$
$$= n(m+1)e^{-it(U(m-n+1)+\eta_j)}-(n+1)me^{-it(U(m-n-1)+\eta_j)}$$
$$\langle n,m|\,[\hat{b}_{j+1}^\dagger(t)\hat{b}_j(t),\hat{b}_j^\dagger\hat{b}_{j+1}]\,|n,m\rangle = -n(m+1)e^{it(U(m-n+1)+\eta_j)}+(n+1)me^{it(U(m-n-1)+\eta_j)} \tag{C.4b}$$

Note: Need to consider that $\hat{b}_j^\dagger(t)\hat{b}_{j+1}(t)\hat{b}_{j+1}^\dagger\hat{b}_j\,|n,m\rangle$ vanishes for $m=n_{\text{max}}$, $\hat{b}_{j+1}^\dagger\hat{b}_j\hat{b}_j^\dagger(t)\hat{b}_{j+1}(t)\,|n,m\rangle$ vanishes for $n=n_{\text{max}}$.

$$\Big\langle[\,[\hat{H}_{\text{kin}},\hat{\Delta}](t),[\hat{H}_{\text{kin}},\hat{\Delta}](0)]\Big\rangle_{j,j+1} = \frac{-4J^2}{Z}\Big[\sum_{\substack{\{n,m\}\\ n,m\neq n_{\text{max}}}}e^{-\beta H_{j,j+1}(\{n,m\})}\big(n(m+1)\sin(t(U(m-n+1)+\eta_j))$$
$$-(n+1)m(\sin(t(U(m-n-1)+\eta_j)))\big)$$
$$-\sum_{\substack{\{n,n_{\text{max}}\}\\ n\neq n_{\text{max}}}}e^{-\beta H_{j,j+1}(\{n,n_{\text{max}}\})}(n+1)n_{\text{max}}(\sin(t(U(n_{\text{max}}-n-1)+\eta_j)))$$
$$+\sum_{\substack{\{n_{\text{max}},m\}\\ m\neq n_{\text{max}}}}e^{-\beta H_{j,j+1}(\{n_{\text{max}},m\})}n_{\text{max}}(m+1)\sin(t(U(m-n_{\text{max}}+1)+\eta_j))\Big] \tag{C.5}$$

and $Z=\text{Tr}\Big\{e^{-\beta\hat{H}_{l,l+1}}\Big\}$

sum over configurations $\{n, m\}$, averaging over j even/odd and rescaling with system size

$$\begin{aligned}
\big\langle \big[\big[\hat{H}_{\text{kin}}, \hat{\Delta}\big](t), \big[\hat{H}_{\text{kin}}, \hat{\Delta}\big](0)\big]\big\rangle_T &= -\frac{4iJ^2}{Z}\Big(\sum_{n,m=0}^{n_{\max}-1} e^{-\beta(\frac{U}{2}(n(n-1)+m(m-1))-\mu(n+m))} && \text{(C.6a)}\\
&\times \Big[e^{\beta\eta/2(n-m)}\big(n(m+1)\sin(t(U(m-n+1)+\eta))-(n+1)m\sin(t(U(m-n-1)+\eta))\big)\\
&\quad + e^{-\beta\eta/2(n-m)}\big(n(m+1)\sin(t(U(m-n+1)-\eta))-(n+1)m\sin(t(U(m-n-1)-\eta))\big)\Big]\\
&- \sum_{n=0}^{n_{\max}-1} e^{-\beta(\frac{U}{2}(n(n-1)+n_{\max}(n_{\max}-1))-\mu(n+n_{\max}))} \times \Big[e^{\beta\eta/2(n-n_{\max})}(n+1)n_{\max}\sin(t(U(n_{\max}-n-1)+\eta))\\
&\quad + e^{-\beta\eta/2(n-n_{\max})}(n+1)n_{\max}\sin(t(U(n_{\max}-n-1)-\eta))\Big]\\
&+ \sum_{m=0}^{n_{\max}-1} e^{-\beta(\frac{U}{2}(n_{\max}(n_{\max}-1)+m(m-1))-\mu(n_{\max}+m))} \times \Big[e^{\beta\eta/2(n_{\max}-m)}n_{\max}(m+1)\sin(t(U(m-n_{\max}+1)+\eta))\\
&\quad + e^{-\beta\eta/2(n_{\max}-m)}n_{\max}(m+1)\sin(t(U(m-n_{\max}+1)-\eta))\Big]\Big)
\end{aligned}$$

rename $m \to n$ in last sum

$$\begin{aligned}
&= -\frac{4iJ^2}{Z}\Big(\sum_{n,m=0}^{n_{\max}-1} e^{-\beta(\frac{U}{2}(n(n-1)+m(m-1))-\mu(n+m))} && \text{(C.6b)}\\
&\times \Big[e^{\beta\eta/2(n-m)}\big(n(m+1)\sin(t(U(m-n+1)+\eta))-(n+1)m\sin(t(U(m-n-1)+\eta))\big)\\
&\quad + e^{-\beta\eta/2(n-m)}\big(n(m+1)\sin(t(U(m-n+1)-\eta))-(n+1)m\sin(t(U(m-n-1)-\eta))\big)\Big]\\
&- 2\sum_{n=0}^{n_{\max}-1} e^{-\beta(\frac{U}{2}(n(n-1)+n_{\max}(n_{\max}-1))-\mu(n+n_{\max}))} \times \Big[e^{\beta\eta/2(n-n_{\max})}(n+1)n_{\max}\sin(t(U(n_{\max}-n-1)+\eta))\\
&\quad + e^{-\beta\eta/2(n-n_{\max})}(n+1)n_{\max}\sin(t(U(n_{\max}-n-1)-\eta))\Big]\Big)
\end{aligned}$$

Use this to calculate susceptibility

$$
\begin{aligned}
\chi_T(\omega) &= -\frac{i}{\omega^2}\int_0^\infty dt e^{i(\omega+i\epsilon)t}\left\langle\left[\left[\hat{H}_{\text{kin}},\hat{\Delta}\right](t),\left[\hat{H}_{\text{kin}},\hat{\Delta}\right](0)\right]\right\rangle_T \\
&= \frac{4J^2}{Z\omega^2}\int_0^\infty dt e^{i(\omega+i\epsilon)t}\Big(\sum_{n,m=0}^{n_{\max}-1} e^{-\beta(\frac{U}{2}(n(n-1)+m(m-1))-\mu(n+m))} \\
&\qquad\times\left(e^{\beta g\lambda(n-m)}\big(n(m+1)\sin(t(U(m-n+1)+\eta))-(n+1)m\sin(t(U(m-n-1)+\eta))\big)\right. \\
&\qquad\left.+\,e^{-\beta g\lambda(n-m)}\big(n(m+1)\sin(t(U(m-n+1)-\eta))-(n+1)m\sin(t(U(m-n-1)-\eta))\big)\right) \\
&\quad-2\sum_{n=0}^{n_{\max}-1} e^{-\beta(\frac{U}{2}(n(n-1)+n_{\max}(n_{\max}-1))-\mu(n+n_{\max}))}(n+1)n_{\max} \\
&\qquad\times\left(e^{\beta g\lambda(n-n_{\max})}\sin(t(U(n_{\max}-n-1)+\eta))+e^{-\beta g\lambda(n-n_{\max})}\sin(t(U(n_{\max}-n-1)-\eta))\right)\Big) \\
&= \frac{2J^2}{Z\omega^2}\Big(\sum_{n,m=0}^{n_{\max}-1} e^{-\beta(\frac{U}{2}(n(n-1)+m(m-1))-\mu(n+m))}\Big(\frac{n(m+1)e^{\beta g\lambda(n-m)}}{i\epsilon+(U(m-n+1)+2g\lambda+\omega)} \\
&\quad-\frac{n(m+1)e^{\beta g\lambda(n-m)}}{i\epsilon+(-U(m-n+1)-2g\lambda+\omega)}-\frac{(n+1)me^{\beta g\lambda(n-m)}}{i\epsilon+(U(m-n-1)+2g\lambda+\omega)}+\frac{(n+1)me^{\beta g\lambda(n-m)}}{i\epsilon+(-U(m-n-1)-2g\lambda+\omega)} \\
&\quad+\frac{n(m+1)e^{-\beta g\lambda(n-m)}}{i\epsilon+(U(m-n+1)-2g\lambda+\omega)}-\frac{n(m+1)e^{-\beta g\lambda(n-m)}}{i\epsilon+(-U(m-n+1)+2g\lambda+\omega)}-\frac{(n+1)me^{-\beta g\lambda(n-m)}}{i\epsilon+(U(m-n-1)-2g\lambda+\omega)} \\
&\quad+\frac{(n+1)me^{-\beta g\lambda(n-m)}}{i\epsilon+(-U(m-n-1)+2g\lambda+\omega)}\Big) \\
&\quad-2\sum_{n=0}^{n_{\max}-1} e^{-\beta(\frac{U}{2}(n(n-1)+n_{\max}(n_{\max}-1))-\mu(n+n_{\max}))}(n+1)n_{\max}\Big(\frac{e^{\beta g\lambda(n-n_{\max})}}{i\epsilon+(U(n_{\max}-n-1)+2g\lambda+\omega)} \\
&\quad+\frac{e^{\beta g\lambda(n-n_{\max})}}{i\epsilon+(-U(n_{\max}-n-1)-2g\lambda+\omega)}-\frac{e^{-\beta g\lambda(n-n_{\max})}}{i\epsilon+(U(n_{\max}-n-1)-2g\lambda+\omega)} \\
&\quad+\frac{e^{-\beta g\lambda(n-n_{\max})}}{i\epsilon+(-U(n_{\max}-n-1)+2g\lambda+\omega)}\Big)\Big)
\end{aligned}
$$

use $\lim_{\epsilon\to 0^+}\left[\text{Im}\left[\frac{1}{x+i\epsilon}\right]\right]=-\pi\delta(x)$.

$$
\begin{aligned}
\text{Im}[\chi_T(\omega)] &= \frac{2J^2}{Z\omega^2}\Big(\sum_{n,m=0}^{n_{\max}-1} e^{-\beta(\frac{U}{2}(n(n-1)+m(m-1))-\mu(n+m))} \\
&\qquad\times\Big(e^{\beta g\lambda(n-m)}n(m+1)\big(\delta(U(m-n+1)+2g\lambda+\omega)-\delta(-U(m-n+1)-2g\lambda+\omega)\big) \\
&\qquad\quad+e^{\beta g\lambda(n-m)}(n+1)m\big(!-\delta(U(m-n-1)+2g\lambda+\omega)+\delta(-U(m-n-1)-2g\lambda+\omega)\big) \\
&\qquad\quad+e^{-\beta g\lambda(n-m)}n(m+1)\big(\delta(U(m-n+1)-2g\lambda+\omega)-\delta(-U(m-n+1)+2g\lambda+\omega)\big) \\
&\qquad\quad+e^{-\beta g\lambda(n-m)}(n+1)m\big(-\delta(U(m-n-1)-2g\lambda+\omega)+\delta(-U(m-n-1)+2g\lambda+\omega)\big)\Big) \\
&\quad-2\sum_{n=0}^{n_{\max}-1} e^{-\beta(\frac{U}{2}(n(n-1)+n_{\max}(n_{\max}-1))-\mu(n+n_{\max}))}(n+1)n_{\max} \\
&\qquad\times\Big(e^{\beta g\lambda(n-n_{\max})}\big(\delta(U(n_{\max}-n-1)+2g\lambda+\omega)-\delta(-U(n_{\max}-n-1)-2g\lambda+\omega)\big) \\
&\qquad\quad+e^{-\beta g\lambda(n-n_{\max})}\big(\delta(U(n_{\max}-n-1)-2g\lambda+\omega)-\delta(-U(n_{\max}-n-1)+2g\lambda+\omega)\big)\Big)\Big)
\end{aligned}
$$

inserting this in Eq. (6.17) and integrating over ω one arrives at Eq. (6.21)

$$
\begin{aligned}
\frac{\partial}{\partial t}\langle \hat{H}_{\text{eff}}\rangle_T = &-\frac{2\Gamma g^2 J^2}{L^d Z}\sum_{n,m=0}^{n_{\max}-1} e^{-\beta(\frac{U}{2}(n(n-1)+m(m-1))-\mu(n+m))} \\
&\times\Bigg[-\frac{e^{\beta g\lambda(n-m)}n(m+1)}{U(m-n+1)+2g\lambda}\left[\frac{\left(1-e^{\beta(U(m-n+1)+2g\lambda)}\right)^{-1}}{(U(m-n+1)+2g\lambda-\delta)^2+(\Gamma/2)^2}+\frac{\left(1-e^{-\beta(U(m-n+1)+2g\lambda)}\right)^{-1}}{(U(m-n+1)+2g\lambda+\delta)^2+(\Gamma/2)^2}\right] \\
&\quad+\frac{e^{\beta g\lambda(n-m)}(n+1)m}{U(m-n-1)+2g\lambda}\left[\frac{\left(1-e^{\beta(U(m-n-1)+2g\lambda)}\right)^{-1}}{(U(m-n-1)+2g\lambda-\delta)^2+(\Gamma/2)^2}+\frac{\left(1-e^{-\beta(U(m-n-1)+2g\lambda)}\right)^{-1}}{(U(m-n-1)+2g\lambda+\delta)^2+(\Gamma/2)^2}\right] \\
&\quad-\frac{e^{-\beta g\lambda(n-m)}n(m+1)}{U(m-n+1)-2g\lambda}\left[\frac{\left(1-e^{\beta(U(m-n+1)-2g\lambda)}\right)^{-1}}{(U(m-n+1)-2g\lambda-\delta)^2+(\Gamma/2)^2}+\frac{\left(1-e^{-\beta(U(m-n+1)-2g\lambda)}\right)^{-1}}{(U(m-n+1)-2g\lambda+\delta)^2+(\Gamma/2)^2}\right] \\
&\quad+\frac{e^{-\beta g\lambda(n-m)}(n+1)m}{U(m-n-1)-2g\lambda}\left[\frac{\left(1-e^{\beta(U(m-n-1)-2g\lambda)}\right)^{-1}}{(U(m-n-1)-2g\lambda-\delta)^2+(\Gamma/2)^2}+\frac{\left(1-e^{-\beta(U(m-n-1)-2g\lambda)}\right)^{-1}}{(U(m-n-1)-2g\lambda+\delta)^2+(\Gamma/2)^2}\right]\Bigg] \\
&+\frac{4\Gamma g^2 J^2}{L^d Z}\sum_{n=0}^{n_{\max}-1} e^{-\beta(\frac{U}{2}(n(n-1)+n_{\max}(n_{\max}-1))-\mu(n+n_{\max}))}(n+1)n_{\max} \\
&\times\Bigg[\frac{e^{\beta g\lambda(n-n_{\max})}}{U(n_{\max}-n-1)+2g\lambda}\left[\frac{\left(1-e^{\beta(U(n_{\max}-n-1)+2g\lambda)}\right)^{-1}}{(U(n_{\max}-n-1)+2g\lambda-\delta)^2+(\Gamma/2)^2}+\frac{\left(1-e^{-\beta(U(n_{\max}-n-1)+2g\lambda)}\right)^{-1}}{(U(n_{\max}-n-1)+2g\lambda+\delta)^2+(\Gamma/2)^2}\right] \\
&\quad+\frac{e^{-\beta g\lambda(n-n_{\max})}}{U(n_{\max}-n-1)-2g\lambda}\left[\frac{\left(1-e^{\beta(U(n_{\max}-n-1)-2g\lambda)}\right)^{-1}}{(U(n_{\max}-n-1)-2g\lambda-\delta)^2+(\Gamma/2)^2}+\frac{\left(1-e^{-\beta(U(n_{\max}-n-1)-2g\lambda)}\right)^{-1}}{(U(n_{\max}-n-1)-2g\lambda+\delta)^2+(\Gamma/2)^2}\right]\Bigg]
\end{aligned}
$$

Appendix D

Appendix "Time evolution with tensor network methods and comparison to the steady state"

D.1 Numerical parameters of long-time values

$\hbar g/J$	$\tau J/\hbar$	$t_{\text{end}} J/\hbar$	$N_{\text{pho,max}}$	m	method	comment
5	0.01	200	25	600	trotter	
6	0.01	200	40	600	trotter	
7	0.01	200	35	600	trotter	
8	0.015	250	40	500	trotter	
9	0.01	200	50	600	trotter	
10	0.015	250	50	500	trotter	
11	0.005	100	40	500	tdvp	$n_{\text{iter}} = 3$
11.5	0.015	250	50	600	trotter	
12.25	0.015	250	50	600	trotter	
12.25	0.01	100	60	600	trotter	
13	0.015	250	50	500	trotter	
13.5	0.015	250	50	500	trotter	
14.25	0.01	50	80	650	trotter	
14.7	0.01	50	80	650	trotter	
16	0.0075	100	90	650	trotter	
17	0.0075	100	95	650	trotter	
18	0.005	50	120	800	trotter	

Table D.1: Convergence parameters for individual points in Fig. 7.15. For all points the system parameters are, $L = 12$, quarter filling, $U/J = 40$, $\hbar\delta/J = 5$, $\hbar\Gamma/J = 3$. The average is built from 500 trajectories.

References

[1] Luisa Tolle, Ameneh Sheikhan, Thierry Giamarchi, Corinna Kollath, and Catalin-Mihai Halati. Fluctuation-induced bistability of fermionic atoms coupled to a dissipative cavity. *Phys. Rev. Lett.*, 134:133602, Mar 2025.

[2] T. Zwettler, G. Del Pace, F. Marijanovic, S. Chattopadhyay, T. Bühler, C.-M. Halati, L. Skolc, L. Tolle, V. Helson, G. Bolognini, A. Fabre, S. Uchino, T. Giamarchi, E. Demler, and J. P. Brantut. Nonequilibrium dynamics of long-range interacting fermions. *Phys. Rev. X*, 15:021089, Jun 2025.

[3] Jeannette De Marco, Luisa Tolle, Catalin-Mihai Halati, Ameneh Sheikhan, Andreas M. Läuchli, and Corinna Kollath. Level statistics of the one-dimensional ionic hubbard model. *Phys. Rev. Res.*, 4:033119, Aug 2022.

[4] H. P. Breuer and F. Petruccione. *The theory of open quantum systems*. Oxford University Press, Oxford, 2002.

[5] Christian Gross and Immanuel Bloch. Quantum simulations with ultracold atoms in optical lattices. *Science*, 357(6355):995–1001, 2017.

[6] Markus Müller, Sebastian Diehl, Guido Pupillo, and Peter Zoller. Engineered open systems and quantum simulations with atoms and ions. 61:1–80, 2012.

[7] Julio T. Barreiro, Markus Müller, Philipp Schindler, Daniel Nigg, Thomas Monz, Michael Chwalla, Markus Hennrich, Christian F. Roos, Peter Zoller, and Rainer Blatt. An open-system quantum simulator with trapped ions. *Nature*, 470:486, 2011.

[8] Kevin Roux, Hideki Konishi, Victor Helson, and Jean-Philippe Brantut. Strongly correlated fermions strongly coupled to light. *Nature Communications*, 11(1):2974, Jun 2020.

[9] Jens Klinder, Hans Keßler, Matthias Wolke, Ludwig Mathey, and Andreas Hemmerich. Dynamical phase transition in the open dicke model. *Proceedings of the National Academy of Sciences*, 112(11):3290–3295, 2015.

[10] Katrin Kroeger, Nishant Dogra, Rodrigo Rosa-Medina, Marcin Paluch, Francesco Ferri, Tobias Donner, and Tilman Esslinger. Continuous feedback on a quantum gas coupled to an optical cavity. *New Journal of Physics*, 22(3):033020, 2020.

[11] Andreas Bayer, Marcel Pozimski, Simon Schambeck, Dieter Schuh, Rupert Huber, Dominique Bougeard, and Christoph Lange. Terahertz light–matter interaction beyond unity coupling strength. *Nano Letters*, 17(10):6340–6344, Oct 2017.

[12] G. Scalari, C. Maissen, D. Turčinková, D. Hagenmüller, S. De Liberato, C. Ciuti, C. Reichl, D. Schuh, W. Wegscheider, M. Beck, and J. Faist. Ultrastrong coupling of the cyclotron transition of a 2d electron gas to a thz metamaterial. *Science*, 335(6074):1323–1326, 2012.

[13] P. Forn-Díaz, L. Lamata, E. Rico, J. Kono, and E. Solano. Ultrastrong coupling regimes of light-matter interaction. *Rev. Mod. Phys.*, 91:025005, Jun 2019.

[14] K. Baumann, C. Guerlin, F. Brennecke, and T. Esslinger. Dicke quantum phase transition with a superfluid gas in an optical cavity. *Nature*, 464:1301, 2010.

[15] Ronen M. Kroeze, Yudan Guo, Varun D. Vaidya, Jonathan Keeling, and Benjamin L. Lev. Spinor self-ordering of a quantum gas in a cavity. *Phys. Rev. Lett.*, 121:163601, Oct 2018.

[16] Varun D. Vaidya, Yudan Guo, Ronen M. Kroeze, Kyle E. Ballantine, Alicia J. Kollár, Jonathan Keeling, and Benjamin L. Lev. Tunable-range, photon-mediated atomic interactions in multimode cavity qed. *Phys. Rev. X*, 8:011002, Jan 2018.

[17] Hans Keßler, Phatthamon Kongkhambut, Christoph Georges, Ludwig Mathey, Jayson G. Cosme, and Andreas Hemmerich. Observation of a dissipative time crystal. *Phys. Rev. Lett.*, 127:043602, Jul 2021.

[18] Francesco Ferri, Rodrigo Rosa-Medina, Fabian Finger, Nishant Dogra, Matteo Soriente, Oded Zilberberg, Tobias Donner, and Tilman Esslinger. Emerging dissipative phases in a superradiant quantum gas with tunable decay. *Phys. Rev. X*, 11:041046, Dec 2021.

[19] Davide Dreon, Alexander Baumgärtner, Xiangliang Li, Simon Hertlein, Tilman Esslinger, and Tobias Donner. Self-oscillating pump in a topological dissipative atom–cavity system. *Nature*, 608(7923):494–498, Aug 2022.

[20] Phatthamon Kongkhambut, Jim Skulte, Ludwig Mathey, Jayson G. Cosme, Andreas Hemmerich, and Hans Keßler. Observation of a continuous time crystal. *Science*, 377(6606):670–673, August 2022.

[21] Renate Landig, Lorenz Hruby, Nishant Dogra, Manuele Landini, Rafael Mottl, Tobias Donner, and Tilman Esslinger. Quantum phases from competing short- and long-range interactions in an optical lattice. *Nature*, 532(7600):476–479, Apr 2016. Letter.

[22] Lorenz Hruby, Nishant Dogra, Manuele Landini, Tobias Donner, and Tilman Esslinger. Metastability and avalanche dynamics in strongly correlated gases with long-range interactions. *Proceedings of the National Academy of Sciences*, 115(13):3279–3284, 2018.

[23] J. Klinder, H. Keßler, M. Reza Bakhtiari, M. Thorwart, and A. Hemmerich. Observation of a superradiant mott insulator in the dicke-hubbard model. *Phys. Rev. Lett.*, 115:230403, Dec 2015.

[24] Victor Helson, Timo Zwettler, Kevin Roux, Hideki Konishi, Shun Uchino, and Jean-Philippe Brantut. Optomechanical response of a strongly interacting fermi gas. *Phys. Rev. Res.*, 4:033199, Sep 2022.

[25] Victor Helson, Timo Zwettler, Farokh Mivehvar, Elvia Colella, Kevin Roux, Hideki Konishi, Helmut Ritsch, and Jean-Philippe Brantut. Density-wave ordering in a unitary fermi gas with photon-mediated interactions. *Nature*, 618(7966):716–720, Jun 2023.

[26] Timo Zwettler, Giulia del Pace, Filip Marijanovic, Sambuddha Chattopadhyay, Tabea Bühler, Catalin-Mihai Halati, Luka Skolc, Luisa Tolle, Victor Helson, Gaia Bolognini, Aurélien Fabre, Shun Uchino, Thierry Giamarchi, Eugene Demler, and Jean-Philippe Brantut. Non-equilibrium dynamics of long-range interacting fermions, 2024.

[27] Xiaotian Zhang, Yu Chen, Zemao Wu, Juan Wang, Jijie Fan, Shujin Deng, and Haibin Wu. Observation of a superradiant quantum phase transition in an intracavity degenerate fermi gas. *Science (New York, N.Y.)*, 373, 08 2021.

[28] Zemao Wu, Jijie Fan, Xue Zhang, Jiansheng Qi, and Haibin Wu. Signatures of prethermalization in a quenched cavity-mediated long-range interacting fermi gas. *Phys. Rev. Lett.*, 131:243401, Dec 2023.

[29] Peter Domokos and Helmut Ritsch. Collective cooling and self-organization of atoms in a cavity. *Phys. Rev. Lett.*, 89:253003, Dec 2002.

[30] D. Nagy, G. Szirmai, and P. Domokos. Self-organization of a bose-einstein condensate in an optical cavity. *The European Physical Journal D*, 48(1):127–137, Jun 2008.

[31] C. Maschler, I. B. Mekhov, and H. Ritsch. Ultracold atoms in optical lattices generated by quantized light fields. *The European Physical Journal D*, 46(3):545–560, 2008.

[32] J. Keeling, M. J. Bhaseen, and B. D. Simons. Collective dynamics of bose-einstein condensates in optical cavities. *Phys. Rev. Lett.*, 105:043001, Jul 2010.

[33] T. Esslinger. Fermi-Hubbard physics with atoms in an optical lattice. *Annual Revies of Condensed Matter Physics*, 1:129, 2010.

[34] Andreas Hemmerich. Effective time-independent description of optical lattices with periodic driving. *Phys. Rev. A*, 81:063626, Jun 2010.

[35] R. H. Dicke. Coherence in spontaneous radiation processes. *Phys. Rev.*, 93:99–110, Jan 1954.

[36] Klaus Hepp and Elliott H Lieb. On the superradiant phase transition for molecules in a quantized radiation field: the dicke maser model. *Annals of Physics*, 76(2):360 – 404, 1973.

[37] Y. K. Wang and F. T. Hioe. Phase transition in the dicke model of superradiance. *Phys. Rev. A*, 7:831–836, Mar 1973.

[38] F. Dimer, B. Estienne, A. S. Parkins, and H. J. Carmichael. Proposed realization of the dicke-model quantum phase transition in an optical cavity qed system. *Phys. Rev. A*, 75:013804, Jan 2007.

[39] Emanuele G. Dalla Torre, Sebastian Diehl, Mikhail D. Lukin, Subir Sachdev, and Philipp Strack. Keldysh approach for nonequilibrium phase transitions in quantum optics: Beyond the dicke model in optical cavities. *Phys. Rev. A*, 87:023831, Feb 2013.

[40] Fabrizio Minganti, Alberto Biella, Nicola Bartolo, and Cristiano Ciuti. Spectral theory of liouvillians for dissipative phase transitions. *Phys. Rev. A*, 98:042118, Oct 2018.

[41] Jonas Larson, Bogdan Damski, Giovanna Morigi, and Maciej Lewenstein. Mott-insulator states of ultracold atoms in optical resonators. *Phys. Rev. Lett.*, 100:050401, Feb 2008.

[42] Titas Chanda, Rebecca Kraus, Giovanna Morigi, and Jakub Zakrzewski. Self-organized topological insulator due to cavity-mediated correlated tunneling. *Quantum*, 5:501, July 2021.

[43] Jonas Larson, Giovanna Morigi, and Maciej Lewenstein. Cold fermi atomic gases in a pumped optical resonator. *Phys. Rev. A*, 78:023815, Aug 2008.

[44] R. Kanamoto and P. Meystre. Optomechanics of a quantum-degenerate fermi gas. *Phys. Rev. Lett.*, 104:063601, Feb 2010.

[45] Qing Sun, Xing-Hua Hu, An-Chun Ji, and W. M. Liu. Dynamics of a degenerate fermi gas in a one-dimensional optical lattice coupled to a cavity. *Phys. Rev. A*, 83:043606, Apr 2011.

[46] Francesco Piazza and Philipp Strack. Umklapp superradiance with a collisionless quantum degenerate fermi gas. *Phys. Rev. Lett.*, 112:143003, Apr 2014.

[47] Francesco Piazza and Philipp Strack. Quantum kinetics of ultracold fermions coupled to an optical resonator. *Phys. Rev. A*, 90:043823, Oct 2014.

[48] Yu Chen, Zhenhua Yu, and Hui Zhai. Superradiance of degenerate fermi gases in a cavity. *Phys. Rev. Lett.*, 112:143004, Apr 2014.

[49] J. Keeling, J. Bhaseen, M., and D. Simons, B. Fermionic superradiance in a transversely pumped optical cavity. *Phys. Rev. Lett.*, 112:143002, Apr 2014.

[50] Yu Chen, Hui Zhai, and Zhenhua Yu. Superradiant phase transition of fermi gases in a cavity across a feshbach resonance. *Phys. Rev. A*, 91:021602, Feb 2015.

[51] Stefan Wolff, Ameneh Sheikhan, and Corinna Kollath. Dissipative time evolution of a chiral state after a quantum quench. *Phys. Rev. A*, 94:043609, Oct 2016.

[52] Filip Marijanović, Sambuddha Chattopadhyay, Luka Skolc, Timo Zwettler, Catalin-Mihai Halati, Simon B. Jäger, Thierry Giamarchi, Jean-Philippe Brantut, and Eugene Demler. Dynamical instabilities of strongly interacting ultracold fermions in an optical cavity, 2024.

[53] Xiaoyong Guo, Zhongzhou Ren, Guangjie Guo, and Jie Peng. Ultracold fermi gas in a single-mode cavity: Cavity-mediated interaction and bcs-bec evolution. *Phys. Rev. A*, 86:053605, Nov 2012.

[54] Frank Schlawin and Dieter Jaksch. Cavity-mediated unconventional pairing in ultracold fermionic atoms. *Phys. Rev. Lett.*, 123:133601, Sep 2019.

[55] Corinna Kollath, Ameneh Sheikhan, Stefan Wolff, and Ferdinand Brennecke. Ultracold fermions in a cavity-induced artificial magnetic field. *Phys. Rev. Lett.*, 116:060401, Feb 2016.

[56] Ameneh Sheikhan, Ferdinand Brennecke, and Corinna Kollath. Cavity-induced generation of nontrivial topological states in a two-dimensional fermi gas. *Phys. Rev. A*, 94:061603, Dec 2016.

[57] A. Sheikhan, F. Brennecke, and C. Kollath. Cavity-induced chiral states of fermionic quantum gases. *Phys. Rev. A*, 93:043609, 2016.

[58] F. P. M. Mendez-Cordoba, J. J. Mendoza-Arenas, F. J. Gomez-Ruiz, F. J. Rodriguez, C. Tejedor, and L. Quiroga. Renyi entropy singularities as signatures of topological criticality in coupled photon-fermion systems. *Phys. Rev. Res.*, 2:043264, Nov 2020.

[59] Jian-Song Pan, Xiong-Jun Liu, Wei Zhang, Wei Yi, and Guang-Can Guo. Topological superradiant states in a degenerate fermi gas. *Phys. Rev. Lett.*, 115:045303, Jul 2015.

[60] Lin Dong, Lu Zhou, Biao Wu, B. Ramachandhran, and Han Pu. Cavity-assisted dynamical spin-orbit coupling in cold atoms. *Phys. Rev. A*, 89:011602, Jan 2014.

[61] Jingtao Fan, Xiaofan Zhou, Wei Zheng, Wei Yi, Gang Chen, and Suotang Jia. Magnetic order in a fermi gas induced by cavity-field fluctuations. *Physical Review A*, 98(4), October 2018.

[62] E. Colella, R. Citro, M. Barsanti, D. Rossini, and M.-L. Chiofalo. Quantum phases of spinful fermi gases in optical cavities. *Phys. Rev. B*, 97:134502, Apr 2018.

[63] Elvia Colella, Farokh Mivehvar, Francesco Piazza, and Helmut Ritsch. Hofstadter butterfly in a cavity-induced dynamic synthetic magnetic field. *Phys. Rev. B*, 100:224306, Dec 2019.

[64] Frank Schlawin, Andrea Cavalleri, and Dieter Jaksch. Cavity-mediated electron-photon superconductivity. *Phys. Rev. Lett.*, 122:133602, Apr 2019.

[65] Zhen Zheng and Z. D. Wang. Cavity-induced fulde-ferrell-larkin-ovchinnikov superfluids of ultracold fermi gases. *Phys. Rev. A*, 101:023612, Feb 2020.

[66] Xiaotian Nie and Wei Zheng. Nonequilibrium phases of a fermi gas inside a cavity with imbalanced pumping. *Phys. Rev. A*, 108:043312, Oct 2023.

[67] Elvia Colella, Stefan Ostermann, Wolfang Niedenzu, Farokh Mivehvar, and Helmut Ritsch. Antiferromagnetic self-ordering of a fermi gas in a ring cavity. *New Journal of Physics*, 21(4):043019, apr 2019.

[68] Farokh Mivehvar, Helmut Ritsch, and Francesco Piazza. Superradiant topological peierls insulator inside an optical cavity. *Phys. Rev. Lett.*, 118:073602, Feb 2017.

[69] Bikash Padhi and Sankalpa Ghosh. Spin-orbit-coupled bose-einstein condensates in a cavity: Route to magnetic phases through cavity transmission. *Phys. Rev. A*, 90:023627, Aug 2014.

[70] Haowei Li, Haojie Wu, Wei Zheng, and Wei Yi. Many-body non-hermitian skin effect under dynamic gauge coupling. *Phys. Rev. Res.*, 5:033173, Sep 2023.

[71] Yongqiang Li, Liang He, and Walter Hofstetter. Lattice-supersolid phase of strongly correlated bosons in an optical cavity. *Phys. Rev. A*, 87:051604, May 2013.

[72] Igor B. Mekhov, Christoph Maschler, and Helmut Ritsch. Cavity-enhanced light scattering in optical lattices to probe atomic quantum statistics. *Phys. Rev. Lett.*, 98:100402, Mar 2007.

[73] Florian Marquardt, Joe P. Chen, A. A. Clerk, and S. M. Girvin. Quantum theory of cavity-assisted sideband cooling of mechanical motion. *Phys. Rev. Lett.*, 99:093902, Aug 2007.

[74] P. Maunz, T. Puppe, I. Schuster, N. Syassen, P. W. H. Pinkse, and G. Rempe. Cavity cooling of a single atom. *Nature*, 428(6978):50–52, March 2004.

[75] Monika H. Schleier-Smith, Ian D. Leroux, Hao Zhang, Mackenzie A. Van Camp, and Vladan Vuletić. Optomechanical cavity cooling of an atomic ensemble. *Phys. Rev. Lett.*, 107:143005, Sep 2011.

[76] Mahdi Hosseini, Yiheng Duan, Kristin M. Beck, Yu-Ting Chen, and Vladan Vuletić. Cavity cooling of many atoms. *Phys. Rev. Lett.*, 118:183601, May 2017.

[77] Peter Domokos and Helmut Ritsch. Mechanical effects of light in optical resonators. *J. Opt. Soc. Am. B*, 20(5):1098–1130, May 2003.

[78] Helmut Ritsch, Peter Domokos, Ferdinand Brennecke, and Tilman Esslinger. Cold atoms in cavity-generated dynamical optical potentials. *Rev. Mod. Phys.*, 85:553–601, Apr 2013.

[79] Stefan Schütz, Hessam Habibian, and Giovanna Morigi. Cooling of atomic ensembles in optical cavities: Semiclassical limit. *Phys. Rev. A*, 88:033427, Sep 2013.

[80] Minghui Xu, Simon B. Jäger, S. Schütz, J. Cooper, Giovanna Morigi, and M. J. Holland. Supercooling of atoms in an optical resonator. *Phys. Rev. Lett.*, 116:153002, Apr 2016.

[81] Guang S. He. *Optical Bistability*, pages 359–385. 10 2014.

[82] Ralf Labouvie, Bodhaditya Santra, Simon Heun, and Herwig Ott. Bistability in a driven-dissipative superfluid. *Phys. Rev. Lett.*, 116:235302, Jun 2016.

[83] Matteo Biondi, Gianni Blatter, Hakan E. Türeci, and Sebastian Schmidt. Nonequilibrium gas-liquid transition in the driven-dissipative photonic lattice. *Phys. Rev. A*, 96:043809, Oct 2017.

[84] Thomas Fink, Anne Schade, Sven Höfling, Christian Schneider, and Ataç Imamoglu. Signatures of a dissipative phase transition in photon correlation measurements. *Nature Physics*, 14(4):365–369, December 2017.

[85] M. Foss-Feig, P. Niroula, J. T. Young, M. Hafezi, A. V. Gorshkov, R. M. Wilson, and M. F. Maghrebi. Emergent equilibrium in many-body optical bistability. *Phys. Rev. A*, 95:043826, Apr 2017.

[86] Julia Hannukainen and Jonas Larson. Dissipation-driven quantum phase transitions and symmetry breaking. *Phys. Rev. A*, 98:042113, Oct 2018.

[87] Andrea Nava and Michele Fabrizio. Lindblad dissipative dynamics in the presence of phase coexistence. *Phys. Rev. B*, 100:125102, Sep 2019.

[88] Louis Garbe, Peregrine Wade, Fabrizio Minganti, Nathan Shammah, Simone Felicetti, and Franco Nori. Dissipation-induced bistability in the two-photon dicke model. *Scientific Reports*, 10, 08 2020.

[89] J Benary, C Baals, E Bernhart, J Jiang, M Röhrle, and H Ott. Experimental observation of a dissipative phase transition in a multi-mode many-body quantum system. *New Journal of Physics*, 24(10):103034, oct 2022.

[90] B. Gábor, D. Nagy, A. Dombi, T. W. Clark, F. I. B. Williams, K. V. Adwaith, A. Vukics, and P. Domokos. Ground-state bistability of cold atoms in a cavity. *Phys. Rev. A*, 107:023713, Feb 2023.

[91] Alexandre Le Boité, Giuliano Orso, and Cristiano Ciuti. Steady-state phases and tunneling-induced instabilities in the driven dissipative bose-hubbard model. *Phys. Rev. Lett.*, 110:233601, Jun 2013.

[92] Mónica Benito, Carlos Sánchez Muñoz, and Carlos Navarrete-Benlloch. Degenerate parametric oscillation in quantum membrane optomechanics. *Phys. Rev. A*, 93:023846, Feb 2016.

[93] Myung-Joong Hwang, Peter Rabl, and Martin B. Plenio. Dissipative phase transition in the open quantum rabi model. *Phys. Rev. A*, 97:013825, Jan 2018.

[94] Henrik Wilming, Michael J. Kastoryano, Albert H. Werner, and Jens Eisert. Emergence of spontaneous symmetry breaking in dissipative lattice systems. *Journal of Mathematical Physics*, 58(3):033302, 2017.

[95] Mattias Fitzpatrick, Neereja M. Sundaresan, Andy C. Y. Li, Jens Koch, and Andrew A. Houck. Observation of a dissipative phase transition in a one-dimensional circuit qed lattice. *Phys. Rev. X*, 7:011016, Feb 2017.

[96] João S. Ferreira and Pedro Ribeiro. Lipkin-meshkov-glick model with markovian dissipation: A description of a collective spin on a metallic surface. *Phys. Rev. B*, 100:184422, Nov 2019.

[97] Kevin C. Stitely, Andrus Giraldo, Bernd Krauskopf, and Scott Parkins. Nonlinear semiclassical dynamics of the unbalanced, open dicke model. *Phys. Rev. Res.*, 2:033131, Jul 2020.

[98] Matteo Soriente, Toni L. Heugel, Keita Omiya, R. Chitra, and Oded Zilberberg. Distinctive class of dissipation-induced phase transitions and their universal characteristics. *Phys. Rev. Res.*, 3:023100, May 2021.

[99] Farokh Mivehvar. Conventional and unconventional dicke models: Multistabilities and nonequilibrium dynamics. *Phys. Rev. Lett.*, 132:073602, Feb 2024.

[100] J. J. Mendoza-Arenas, S. R. Clark, S. Felicetti, G. Romero, E. Solano, D. G. Angelakis, and D. Jaksch. Beyond mean-field bistability in driven-dissipative lattices: Bunching-antibunching transition and quantum simulation. *Phys. Rev. A*, 93:023821, Feb 2016.

[101] Haggai Landa, Marco Schiró, and Grégoire Misguich. Multistability of driven-dissipative quantum spins. *Phys. Rev. Lett.*, 124:043601, Jan 2020.

[102] Catalin-Mihai Halati, Ameneh Sheikhan, Helmut Ritsch, and Corinna Kollath. Numerically exact treatment of many-body self-organization in a cavity. *Phys. Rev. Lett.*, 125:093604, Aug 2020.

[103] Berislav Buča and Tomaž Prosen. A note on symmetry reductions of the lindblad equation: transport in constrained open spin chains. *New Journal of Physics*, 14(7):073007, jul 2012.

[104] Victor V. Albert and Liang Jiang. Symmetries and conserved quantities in lindblad master equations. *Phys. Rev. A*, 89:022118, Feb 2014.

[105] David Roberts and Aashish A. Clerk. Driven-dissipative quantum kerr resonators: New exact solutions, photon blockade and quantum bistability. *Phys. Rev. X*, 10:021022, Apr 2020.

[106] Catalin-Mihai Halati, Ameneh Sheikhan, and Corinna Kollath. Breaking strong symmetries in dissipative quantum systems: Bosonic atoms coupled to a cavity. *Phys. Rev. Research*, 4:L012015, Feb 2022.

[107] S. Brazovskii. Phase transition of an isotropic system to a nonuniform state - jetp 41, 85 (1975). *Soviet Phys JETP.*, 41, 01 1996.

[108] K Binder. Theory of first-order phase transitions. *Reports on Progress in Physics*, 50(7):783, jul 1987.

[109] B. I. Halperin, T. C. Lubensky, and Shang-keng Ma. First-order phase transitions in superconductors and smectic-a liquid crystals. *Phys. Rev. Lett.*, 32:292–295, Feb 1974.

[110] I. F Herbut, A Yethiraj, and J Bechhoefer. Effect of order parameter fluctuations on the halperin-lubensky-ma first-order transition in superconductors and liquid crystals. *Europhysics Letters (EPL)*, 55(3):317–323, August 2001.

[111] M. Janoschek, M. Garst, A. Bauer, P. Krautscheid, R. Georgii, P. Böni, and C. Pfleiderer. Fluctuation-induced first-order phase transition in dzyaloshinskii-moriya helimagnets. *Phys. Rev. B*, 87:134407, Apr 2013.

[112] P. C. Hohenberg and J. B. Swift. Metastability in fluctuation-driven first-order transitions: Nucleation of lamellar phases. *Phys. Rev. E*, 52:1828–1845, Aug 1995.

[113] Filippo Vicentini, Fabrizio Minganti, Riccardo Rota, Giuliano Orso, and Cristiano Ciuti. Critical slowing down in driven-dissipative bose-hubbard lattices. *Phys. Rev. A*, 97:013853, Jan 2018.

[114] Guifré Vidal. Efficient simulation of one-dimensional quantum many-body systems. *Phys. Rev. Lett.*, 93:040502, Jul 2004.

[115] Steven R. White and Adrian E. Feiguin. Real-time evolution using the density matrix renormalization group. *Phys. Rev. Lett.*, 93:076401, Aug 2004.

[116] F. Verstraete, J. J. García-Ripoll, and J. I. Cirac. Matrix product density operators: Simulation of finite-temperature and dissipative systems. *Phys. Rev. Lett.*, 93:207204, Nov 2004.

[117] F. Verstraete and J. I. Cirac. Matrix product states represent ground states faithfully. *Phys. Rev. B*, 73:094423, Mar 2006.

[118] F. Verstraete, V. Murg, and J.I. Cirac. Matrix product states, projected entangled pair states, and variational renormalization group methods for quantum spin systems. *Advances in Physics*, 57(2):143–224, 2008.

[119] Román Orús. A practical introduction to tensor networks: Matrix product states and projected entangled pair states. *Annals of Physics*, 349:117–158, October 2014.

[120] J. Ignacio Cirac, David Pérez-García, Norbert Schuch, and Frank Verstraete. Matrix product states and projected entangled pair states: Concepts, symmetries, theorems. *Rev. Mod. Phys.*, 93:045003, Dec 2021.

[121] Steven R. White. Density matrix formulation for quantum renormalization groups. *Phys. Rev. Lett.*, 69:2863–2866, Nov 1992.

[122] U. Schollwöck. The density-matrix renormalization group. *Rev. Mod. Phys.*, 77:259–315, Apr 2005.

[123] Ulrich Schollwöck. The density-matrix renormalization group in the age of matrix product states. *Annals of Physics*, 326(1):96–192, Jan 2011.

[124] I. Peschel, X. Wang, M. Kaulke, and K. Hallberg, editors. *Density-matrix Renormalization*. Springer, 1998.

[125] W. Janke and T. Sauer. Properties of higher-order trotter formulas. *Physics Letters A*, 165(3):199 – 205, 1992.

[126] Florian Schäfer, Takeshi Fukuhara, Seiji Sugawa, Yosuke Takasu, and Yoshiro Takahashi. Tools for quantum simulation with ultracold atoms in optical lattices. *Nature Reviews Physics*, 2(8):411–425, Aug 2020.

[127] Jutho Haegeman, J. Ignacio Cirac, Tobias J. Osborne, Iztok Pižorn, Henri Verschelde, and Frank Verstraete. Time-dependent variational principle for quantum lattices. *Phys. Rev. Lett.*, 107:070601, Aug 2011.

[128] Laurens Vanderstraeten, Jutho Haegeman, and Frank Verstraete. Tangent-space methods for uniform matrix product states. *SciPost Physics Lecture Notes*, January 2019.

[129] Mingru Yang and Steven R. White. Time-dependent variational principle with ancillary krylov subspace. *Phys. Rev. B*, 102:094315, Sep 2020.

[130] Jheng-Wei Li, Andreas Gleis, and Jan von Delft. Time-dependent variational principle with controlled bond expansion for matrix product states. *Phys. Rev. Lett.*, 133:026401, Jul 2024.

[131] A J Daley, C Kollath, U Schollwöck, and G Vidal. Time-dependent density-matrix renormalization-group using adaptive effective hilbert spaces. *Journal of Statistical Mechanics: Theory and Experiment*, 2004(04):P04005, apr 2004.

[132] F. Verstraete, M. Popp, and J. I. Cirac. Entanglement versus correlations in spin systems. *Phys. Rev. Lett.*, 92:027901, 2004.

[133] Michael Zwolak and Guifré Vidal. Mixed-state dynamics in one-dimensional quantum lattice systems: A time-dependent superoperator renormalization algorithm. *Physical Review Letters*, 93(20), Nov 2004.

[134] Alan A Dzhioev and D S Kosov. Superoperator coupled cluster method for nonequilibrium density matrix. *Journal of Physics A: Mathematical and Theoretical*, 48(1):015004, dec 2014.

[135] B. Meng and W. H. Weinberg. Monte carlo simulations of temperature programmed desorption spectra. *The Journal of Chemical Physics*, 100(7):5280–5289, 04 1994.

[136] Dario Poletti, Jean-Sébastien Bernier, Antoine Georges, and Corinna Kollath. Interaction-induced impeding of decoherence and anomalous diffusion. *Phys. Rev. Lett.*, 109:045302, Jul 2012.

[137] Jean-Sébastien Bernier, Peter Barmettler, Dario Poletti, and Corinna Kollath. Emergence of spatially extended pair coherence through incoherent local environmental coupling. *Phys. Rev. A*, 87:063608, Jun 2013.

[138] Andrew J. Daley. Quantum trajectories and open many-body quantum systems. *Advances in Physics*, 63(2):77–149, 2014.

[139] Lars Bonnes and Andreas M. Läuchli. Superoperators vs. trajectories for matrix product state simulations of open quantum system: A case study. 2014.

[140] Michael L. Wall, Arghavan Safavi-Naini, and Ana Maria Rey. Simulating generic spin-boson models with matrix product states. *Phys. Rev. A*, 94:053637, Nov 2016.

[141] Marco T. Manzoni, Darrick E. Chang, and James S. Douglas. Simulating quantum light propagation through atomic ensembles using matrix product states. *Nature Communications*, 8(1):1743, Nov 2017.

[142] Benjamin Everest, Igor Lesanovsky, Juan P. Garrahan, and Emanuele Levi. Role of interactions in a dissipative many-body localized system. *Phys. Rev. B*, 95:024310, Jan 2017.

[143] Daniel Jaschke, Simone Montangero, and Lincoln D Carr. One-dimensional many-body entangled open quantum systems with tensor network methods. *Quantum Science and Technology*, 4(1):013001, nov 2018.

[144] J. Tindall, B. Buča, J. R. Coulthard, and D. Jaksch. Heating-induced long-range η pairing in the hubbard model. *Phys. Rev. Lett.*, 123:030603, Jul 2019.

[145] Stefan Wolff, Ameneh Sheikhan, and Corinna Kollath. Numerical evaluation of two-time correlation functions in open quantum systems with matrix product state methods: a comparison. *SciPost Phys. Core*, 3:010, 2020.

[146] Berislav Buča, Cameron Booker, and Dieter Jaksch. Algebraic theory of quantum synchronization and limit cycles under dissipation. *SciPost Phys.*, 12:097, 2022.

[147] Catalin-Mihai Halati, Ameneh Sheikhan, Giovanna Morigi, and Corinna Kollath. Controlling the dynamics of atomic correlations via the coupling to a dissipative cavity. *Phys. Rev. Lett.*, 134:073604, Feb 2025.

[148] Catalin-Mihai Halati, Ameneh Sheikhan, and Corinna Kollath. Cavity-induced spin-orbit coupling in an interacting bosonic wire. *Phys. Rev. A*, 99:033604, Mar 2019.

[149] Catalin-Mihai Halati, Ameneh Sheikhan, and Corinna Kollath. Theoretical methods to treat a single dissipative bosonic mode coupled globally to an interacting many-body system. *Phys. Rev. Research*, 2:043255, Nov 2020.

[150] C.-M. Halati. *External Control of Many-Body Quantum Systems*. PhD thesis, University of Bonn, 2021.

[151] Catalin-Mihai Halati, Ameneh Sheikhan, Giovanna Morigi, Corinna Kollath, and Simon B. Jäger. From light-cone to supersonic propagation of correlations by competing short- and long-range couplings, 2025.

[152] Farokh Mivehvar, Francesco Piazza, Tobias Donner, and Helmut Ritsch. Cavity qed with quantum gases: new paradigms in many-body physics. *Advances in Physics*, 70(1):1–153, 2021.

[153] Haruka Tanji-Suzuki, Ian D Leroux, Monika H Schleier-Smith, Marko Cetina, Andrew T Grier, Jonathan Simon, and Vladan Vuletić. Interaction between atomic ensembles and optical resonators: Classical description. *Advances in atomic, molecular, and optical physics*, 60:201–237, 2011.

[154] E. T. Jaynes and F. W. Cummings. Comparison of quantum and semiclassical radiation theories with application to the beam maser. *Proceedings of the IEEE*, 51(1):89–109, 1963.

[155] Christoph Maschler and Helmut Ritsch. Cold atom dynamics in a quantum optical lattice potential. *Phys. Rev. Lett.*, 95:260401, Dec 2005.

[156] H. Carmichael. *An open systems approach to quantum optics*. Springer Verlag, Berlin Heidelberg, 1991.

[157] Cătălin-Mihai Halaţi. *External Control of Many-Body Quantum Systems*. PhD thesis, Rheinische Friedrich-Wilhelms-Universität Bonn, oct 2021.

[158] E. H. Lieb and F. Y. Wu. The one-dimensional Hubbard model: a reminiscence. *cond-mat/0207529*, 2002.

[159] J J García-Ripoll, S Dürr, N Syassen, D M Bauer, M Lettner, G Rempe, and J I Cirac. Dissipation-induced hard-core boson gas in an optical lattice. *New Journal of Physics*, 11(1):013053, 2009.

[160] Florentin Reiter and Anders S. Sørensen. Effective operator formalism for open quantum systems. *Phys. Rev. A*, 85:032111, Mar 2012.

[161] E. M. Kessler. Generalized schrieffer-wolff formalism for dissipative systems. *Phys. Rev. A*, 86:012126, Jul 2012.

[162] Dario Poletti, Peter Barmettler, Antoine Georges, and Corinna Kollath. Emergence of glasslike dynamics for dissipative and strongly interacting bosons. *Phys. Rev. Lett.*, 111:195301, Nov 2013.

[163] Bruno Sciolla, Dario Poletti, and Corinna Kollath. Two-time correlations probing the dynamics of dissipative many-body quantum systems: Aging and fast relaxation. *Phys. Rev. Lett.*, 114:170401, Apr 2015.

[164] Alla V. Bezvershenko, Catalin-Mihai Halati, Ameneh Sheikhan, Corinna Kollath, and Achim Rosch. Dicke transition in open many-body systems determined by fluctuation effects. *Phys. Rev. Lett.*, 127:173606, Oct 2021.

[165] François Damanet, Andrew J. Daley, and Jonathan Keeling. Atom-only descriptions of the driven-dissipative dicke model. *Phys. Rev. A*, 99:033845, Mar 2019.

[166] Simon B. Jäger, Tom Schmit, Giovanna Morigi, Murray J. Holland, and Ralf Betzholz. Lindblad master equations for quantum systems coupled to dissipative bosonic modes. *Phys. Rev. Lett.*, 129:063601, Aug 2022.

[167] Valentin Link, Kai Müller, Rosaria G. Lena, Kimmo Luoma, François Damanet, Walter T. Strunz, and Andrew J. Daley. Non-markovian quantum dynamics in strongly coupled multimode cavities conditioned on continuous measurement. *PRX Quantum*, 3:020348, Jun 2022.

[168] Florian Lange, Zala Lenarčič, and Achim Rosch. Time-dependent generalized gibbs ensembles in open quantum systems. *Phys. Rev. B*, 97:165138, Apr 2018.

[169] Ryogo Kubo. Statistical-mechanical theory of irreversible processes. i. general theory and simple applications to magnetic and conduction problems. *Journal of the Physical Society of Japan*, 12(6):570–586, 1957.

[170] Florian Lange, Zala Lenarčič, and Achim Rosch. Pumping approximately integrable systems. *Nature Communications*, 8(1):15767, Jun 2017.

[171] Lin Tian. Cavity-assisted dynamical quantum phase transition at bifurcation points. *Phys. Rev. A*, 93:043850, Apr 2016.

[172] Catalin-Mihai Halati, Ameneh Sheikhan, and Corinna Kollath. Cavity-induced artificial gauge field in a bose-hubbard ladder. *Phys. Rev. A*, 96:063621, Dec 2017.

[173] Matthew Fishman, Steven R. White, and E. Miles Stoudenmire. The ITensor software library for tensor network calculations, 2020.

[174] E M Stoudenmire and Steven R White. Minimally entangled typical thermal state algorithms. *New Journal of Physics*, 12(5):055026, may 2010.

[175] Ulrich Schollwöck. The density-matrix renormalization group in the age of matrix product states. *Annals of Physics*, 326(1):96 – 192, 2011.

[176] Roger Penrose. Applications of negative dimensional tensors, in combinatorial mathematics and its applications. *Academic Press, New York*, page 221–244, 1971.

[177] P. Jordan and E. Wigner. Über das paulische äquivalenzverbot. *Zeitschrift für Physik*, 47(9):631–651, Sep 1928.

[178] C. Lanczos. An iteration method for the solution of the eigenvalue problem of linear differential and integral operators. *J. Res. Natl. Bur. Stand.*, 45:225, 1950.

[179] P. W. Langhoff, S. T. Epstein, and M. Karplus. Aspects of time-dependent perturbation theory. *Rev. Mod. Phys.*, 44:602–644, Jul 1972.

[180] E. Gerjuoy, A. R. P. Rau, and Larry Spruch. A unified formulation of the construction of variational principles. *Rev. Mod. Phys.*, 55:725–774, Jul 1983.

[181] Shimpei Goto and Ippei Danshita. Performance of the time-dependent variational principle for matrix product states in the long-time evolution of a pure state. *Physical Review B*, 99(5), February 2019.

[182] Sebastian Paeckel, Thomas Köhler, Andreas Swoboda, Salvatore R. Manmana, Ulrich Schollwöck, and Claudius Hubig. Time-evolution methods for matrix-product states. *Annals of Physics*, 411:167998, 2019.

[183] Jutho Haegeman, Christian Lubich, Ivan Oseledets, Bart Vandereycken, and Frank Verstraete. Unifying time evolution and optimization with matrix product states. *Phys. Rev. B*, 94:165116, Oct 2016.

[184] L. Tolle. Developing tmps-methods for a fermi-hubbard model coupled to a dissipative photonic mode. Master's thesis, University of Bonn, 2021.

[185] Jean Dalibard, Yvan Castin, and Klaus Mølmer. Wave-function approach to dissipative processes in quantum optics. *Phys. Rev. Lett.*, 68:580–583, Feb 1992.

[186] C. W. Gardiner, A. S. Parkins, and P. Zoller. Wave-function quantum stochastic differential equations and quantum-jump simulation methods. *Phys. Rev. A*, 46:4363–4381, Oct 1992.

[187] Jan Stolpp, Thomas Köhler, Salvatore R. Manmana, Eric Jeckelmann, Fabian Heidrich-Meisner, and Sebastian Paeckel. Comparative study of state-of-the-art matrix-product-state methods for lattice models with large local hilbert spaces without u(1) symmetry. *Computer Physics Communications*, 269:108106, 2021.

[188] D. Gobert, C. Kollath, U. Schollwöck, and G. Schütz. Real-time dynamics in spin-1/2 chains with adaptive time-dependent DMRG. *Phys. Rev. E*, 71:036102, 2005.

[189] D. Pertot, A. Sheikhan, E. Cocchi, L. A. Miller, J. E. Bohn, M. Koschorreck, M. Köhl, and C. Kollath. Relaxation dynamics of a fermi gas in an optical superlattice. *Phys. Rev. Lett.*, 113:170403, Oct 2014.

[190] Michael Messer, Rémi Desbuquois, Thomas Uehlinger, Gregor Jotzu, Sebastian Huber, Daniel Greif, and Tilman Esslinger. Exploring competing density order in the ionic hubbard model with ultracold fermions. *Phys. Rev. Lett.*, 115:115303, Sep 2015.

[191] J. B. Torrance, A. Girlando, J. J. Mayerle, J. I. Crowley, V. Y. Lee, P. Batail, and S. J. LaPlaca. Anomalous nature of neutral-to-ionic phase transition in tetrathiafulvalene-chloranil. *Phys. Rev. Lett.*, 47:1747–1750, Dec 1981.

[192] Naoto Nagaosa and Jun-ichi Takimoto. Theory of neutral-ionic transition in organic crystals. i. monte carlo simulation of modified hubbard model. *Journal of the Physical Society of Japan*, 55(8):2735–2744, 1986.

[193] T. Egami, S. Ishihara, and M. Tachiki. Lattice effect of strong electron correlation: Implication for ferroelectricity and superconductivity. *Science*, 261(5126):1307–1310, 1993.

[194] John Kogut and Leonard Susskind. Hamiltonian formulation of wilson's lattice gauge theories. *Phys. Rev. D*, 11:395–408, Jan 1975.

[195] M. E. Torio, A. A. Aligia, and H. A. Ceccatto. Phase diagram of the hubbard chain with two atoms per cell. *Phys. Rev. B*, 64:121105, Sep 2001.

[196] Tim Wilkens and Richard M. Martin. Quantum monte carlo study of the one-dimensional ionic hubbard model. *Phys. Rev. B*, 63:235108, May 2001.

[197] S. R. Manmana, V. Meden, R. M. Noack, and K. Schönhammer. Quantum critical behavior of the one-dimensional ionic hubbard model. *Phys. Rev. B*, 70:155115, Oct 2004.

[198] Hiromi Otsuka and Masaaki Nakamura. Ground-state phase diagram of the one-dimensional hubbard model with an alternating chemical potential. *Physical Review B*, 71(15), April 2005.

[199] M C Refolio, J M Lòpez Sancho, and J Rubio. Modelling one-dimensional insulating materials with the ionic hubbard model. *Journal of Physics: Condensed Matter*, 17(42):6635–6644, oct 2005.

[200] Ara Go and Gun Sang Jeon. Phase transitions and spectral properties of the ionic hubbard model in one dimension. *Phys. Rev. B*, 84:195102, Nov 2011.

[201] N. Gidopoulos S. Sorella and E. Tosatti. Born effective charge reversal and metallic threshold state at a band insulator-mott insulator transition, 1999.

[202] Ö. Legeza, K. Buchta, and J. Sólyom. Unified phase diagram of models exhibiting a neutral-ionic transition. *Phys. Rev. B*, 73:165124, Apr 2006.

[203] L. Tincani, R. M. Noack, and D. Baeriswyl. Critical properties of the band-insulator-to-mott-insulator transition in the strong-coupling limit of the ionic hubbard model. *Physical Review B*, 79(16), April 2009.

[204] M. Hafez, S. A. Jafari, Sh. Adibi, and F. Shahbazi. Classical analogue of the ionic hubbard model. *Phys. Rev. B*, 81:245131, Jun 2010.

[205] Aaram J. Kim, M. Y. Choi, and Gun Sang Jeon. Finite-temperature phase transitions in the ionic hubbard model. *Phys. Rev. B*, 89:165117, Apr 2014.

[206] M. Hafez Torbati, Nils A. Drescher, and Götz S. Uhrig. Dispersive excitations in one-dimensional ionic hubbard model. *Phys. Rev. B*, 89:245126, Jun 2014.

[207] Mohsen Hafez-Torbati, Nils A. Drescher, and Götz S. Uhrig. From gapped excitons to gapless triplons in one dimension. *The European Physical Journal B*, 88(2), February 2015.

[208] Y. Z. Zhang, C. Q. Wu, and H. Q. Lin. Inducement of bond-order wave due to electron correlation in one dimension. *Phys. Rev. B*, 67:205109, May 2003.

[209] C. D. Batista and A. A. Aligia. Exact bond ordered ground state for the transition between the band and the mott insulator. *Phys. Rev. Lett.*, 92:246405, Jun 2004.

[210] A. A. Aligia and C. D. Batista. Dimerized phase of ionic hubbard models. *Phys. Rev. B*, 71:125110, Mar 2005.

[211] C. Schuster and U. Schwingenschlögl. One-dimensional hubbard model at quarter filling on periodic potentials. *Phys. Rev. B*, 75:045124, Jan 2007.

[212] M. E. Torio, A. A. Aligia, G. I. Japaridze, and B. Normand. Quantum phase diagram of the generalized ionic hubbard model for abn chains. *Physical Review B*, 73(11), March 2006.

[213] M. Ménard and C. Bourbonnais. One-dimensional alternating extended hubbard model at quarter-filling and its applications to structural instabilities of organic conductors. *Crystals*, 10(10), 2020.

[214] Myung-Hoon Chung. Phase transitions in the one-dimensional ionic hubbard model. *Journal of the Korean Physical Society*, 78(8):700–705, February 2021.

[215] Soumen Bag, Arti Garg, and H. R. Krishnamurthy. Phase diagram of the half-filled ionic hubbard model. *Phys. Rev. B*, 91:235108, Jun 2015.

[216] Anwesha Chattopadhyay, Soumen Bag, H. R. Krishnamurthy, and Arti Garg. Phase diagram of the half-filled ionic hubbard model in the limit of strong correlations. *Phys. Rev. B*, 99:155127, Apr 2019.

[217] A P Kampf, M Sekania, G I Japaridze, and Ph Brune. Nature of the insulating phases in the half-filled ionic hubbard model. *Journal of Physics: Condensed Matter*, 15(34):5895–5907, August 2003.

[218] M. Tsuchiizu and Akira Furusaki. Ground-state phase diagram of the one-dimensional half-filled extended hubbard model. *Physical review. B, Condensed matter*, 69, 09 2003.

[219] Michele Fabrizio, Alexander O. Gogolin, and Alexander A. Nersesyan. From band insulator to mott insulator in one dimension. *Phys. Rev. Lett.*, 83:2014–2017, Sep 1999.

[220] M. Fabrizio, A.O. Gogolin, and A.A. Nersesyan. Critical properties of the double-frequency sine-gordon model with applications. *Nuclear Physics B*, 580(3):647–687, August 2000.

[221] Karla Loida, Jean-Sébastien Bernier, Roberta Citro, Edmond Orignac, and Corinna Kollath. Probing the bond order wave phase transitions of the ionic hubbard model by superlattice modulation spectroscopy. *Phys. Rev. Lett.*, 119:230403, Dec 2017.

[222] Jeannette DeMarco, Luisa Tolle, Catalin-Mihai Halati, Ameneh Sheikhan, Andreas Läuchli, and Corinna Kollath. Level statistics of the one-dimensional ionic hubbard model. *Physical Review Research*, 4, 08 2022.

[223] Karin Haderlein, David J Luitz, Corinna Kollath, and Ameneh Sheikhan. Level statistics of the one-dimensional dimerized hubbard model. *Journal of Statistical Mechanics: Theory and Experiment*, 2024(7):073101, jul 2024.

[224] Mark Srednicki. Chaos and quantum thermalization. *Phys. Rev. E*, 50:888–901, Aug 1994.

[225] Corinna Kollath, Andreas M. Läuchli, and Ehud Altman. Quench dynamics and nonequilibrium phase diagram of the bose-hubbard model. *Phys. Rev. Lett.*, 98:180601, Apr 2007.

[226] Anatoli Polkovnikov, Krishnendu Sengupta, Alessandro Silva, and Mukund Vengalattore. Colloquium: Nonequilibrium dynamics of closed interacting quantum systems. *Rev. Mod. Phys.*, 83:863–883, Aug 2011.

[227] Rahul Nandkishore and David A. Huse. Many-body localization and thermalization in quantum statistical mechanics. *Annual Review of Condensed Matter Physics*, 6(1):15–38, 2015.

[228] Dmitry A. Abanin, Ehud Altman, Immanuel Bloch, and Maksym Serbyn. Colloquium: Many-body localization, thermalization, and entanglement. *Rev. Mod. Phys.*, 91:021001, May 2019.

[229] F. Haake. *Quantum Signatures of Chaos*. Springer, Berlin Heidelberg New York, 2000.

[230] D.M. Basko, I.L. Aleiner, and B.L. Altshuler. Metal–insulator transition in a weakly interacting many-electron system with localized single-particle states. *Annals of Physics*, 321(5):1126–1205, 2006.

[231] I. V. Gornyi, A. D. Mirlin, and D. G. Polyakov. Interacting electrons in disordered wires: Anderson localization and low-t transport. *Phys. Rev. Lett.*, 95:206603, Nov 2005.

[232] Arijeet Pal and David A. Huse. Many-body localization phase transition. *Phys. Rev. B*, 82:174411, Nov 2010.

[233] Pablo Sala, Tibor Rakovszky, Ruben Verresen, Michael Knap, and Frank Pollmann. Ergodicity breaking arising from hilbert space fragmentation in dipole-conserving hamiltonians. *Phys. Rev. X*, 10:011047, Feb 2020.

[234] Vedika Khemani, Michael Hermele, and Rahul Nandkishore. Localization from hilbert space shattering: From theory to physical realizations. *Phys. Rev. B*, 101:174204, May 2020.

[235] Naoto Shiraishi and Takashi Mori. Systematic construction of counterexamples to the eigenstate thermalization hypothesis. *Phys. Rev. Lett.*, 119:030601, Jul 2017.

[236] C. J. Turner, A. A. Michailidis, D. A. Abanin, M. Serbyn, and Z. Papić. Weak ergodicity breaking from quantum many-body scars. *Nature Physics*, 14(7):745–749, Jul 2018.

[237] Vedika Khemani, Chris R. Laumann, and Anushya Chandran. Signatures of integrability in the dynamics of rydberg-blockaded chains. *Phys. Rev. B*, 99:161101, Apr 2019.

[238] Wen Wei Ho, Soonwon Choi, Hannes Pichler, and Mikhail D. Lukin. Periodic orbits, entanglement, and quantum many-body scars in constrained models: Matrix product state approach. *Phys. Rev. Lett.*, 122:040603, Jan 2019.

[239] Hannes Bernien, Sylvain Schwartz, Alexander Keesling, Harry Levine, Ahmed Omran, Hannes Pichler, Soonwon Choi, Alexander S. Zibrov, Manuel Endres, Markus Greiner, Vladan Vuletić, and Mikhail D. Lukin. Probing many-body dynamics on a 51-atom quantum simulator. *Nature*, 551(7682):579–584, Nov 2017.

[240] M. L. Mehta. *Random Matrices*. Academic Press, 2 edition, 1991.

[241] Michael Victor Berry, M. Tabor, and John Michael Ziman. Level clustering in the regular spectrum. *Proceedings of the Royal Society of London. A. Mathematical and Physical Sciences*, 356(1686):375–394, 1977.

[242] O. Bohigas, M. J. Giannoni, and C. Schmit. Characterization of chaotic quantum spectra and universality of level fluctuation laws. *Phys. Rev. Lett.*, 52:1–4, Jan 1984.

[243] Abolfath Hosseinzadeh and Seyed Akbar Jafari. Quantum integrability of 1d ionic hubbard model. *Annalen der Physik*, 532(3):1900601, 2020.

[244] Oriol Bohigas, Marie-Joya Giannoni, and Charles Schmit. *Spectral fluctuations of classically chaotic quantum systems*. Springer Berlin Heidelberg, Berlin, Heidelberg, 1986.

[245] Thomas Guhr, Axel Müller–Groeling, and Hans A. Weidenmüller. Random-matrix theories in quantum physics: common concepts. *Physics Reports*, 299(4):189–425, 1998.

[246] D Poilblanc, T Ziman, J Bellissard, F Mila, and G Montambaux. Poisson vs. GOE statistics in integrable and non-integrable quantum hamiltonians. *Europhysics Letters (EPL)*, 22(7):537–542, jun 1993.

[247] Theodore C. Hsu and J. C. Angle's d'Auriac. Level repulsion in integrable and almost-integrable quantum spin models. *Phys. Rev. B*, 47:14291–14296, Jun 1993.

[248] Gilles Montambaux, Didier Poilblanc, Jean Bellissard, and Clément Sire. Quantum chaos in spin-fermion models. *Phys. Rev. Lett.*, 70:497–500, Jan 1993.

[249] Vadim Oganesyan and David A. Huse. Localization of interacting fermions at high temperature. *Physical Review B (Condensed Matter and Materials Physics)*, 75(15):155111, 2007.

[250] Corinna Kollath, Guillaume Roux, Giulio Biroli, and Andreas M Läuchli. Statistical properties of the spectrum of the extended bose–hubbard model. *Journal of Statistical Mechanics: Theory and Experiment*, 2010(08):P08011, aug 2010.

[251] Maksym Serbyn and Joel E. Moore. Spectral statistics across the many-body localization transition. *Phys. Rev. B*, 93:041424, Jan 2016.

[252] Toma ž Prosen. Ergodic properties of a generic nonintegrable quantum many-body system in the thermodynamic limit. *Phys. Rev. E*, 60:3949–3968, Oct 1999.

[253] Masudul Haque and P. A. McClarty. Eigenstate thermalization scaling in majorana clusters: From chaotic to integrable sachdev-ye-kitaev models. *Phys. Rev. B*, 100:115122, Sep 2019.

[254] Bruus, H. and Anglès d'Auriac, J.-C. The spectrum of the two-dimensional hubbard model at low filling. *Europhys. Lett.*, 35(5):321–326, 1996.

[255] J. M. G. Gómez, R. A. Molina, A. Relaño, and J. Retamosa. Misleading signatures of quantum chaos. *Phys. Rev. E*, 66:036209, Sep 2002.

[256] Y. Y. Atas, E. Bogomolny, O. Giraud, and G. Roux. Distribution of the ratio of consecutive level spacings in random matrix ensembles. *Phys. Rev. Lett.*, 110:084101, Feb 2013.

[257] Olivier Giraud, Nicolas Macé, Éric Vernier, and Fabien Alet. Probing symmetries of quantum many-body systems through gap ratio statistics. *Phys. Rev. X*, 12:011006, Jan 2022.

[258] Norbert Rosenzweig and Charles E. Porter. "repulsion of energy levels" in complex atomic spectra. *Phys. Rev.*, 120:1698–1714, Dec 1960.

[259] M V Berry and M Robnik. Semiclassical level spacings when regular and chaotic orbits coexist. *Journal of Physics A: Mathematical and General*, 17(12):2413–2421, aug 1984.

[260] Fadi Sun, Yu Yi-Xiang, Jinwu Ye, and Wu-Ming Liu. Classification of the quantum chaos in colored sachdev-ye-kitaev models. *Phys. Rev. D*, 101:026009, Jan 2020.

[261] J. K. Asbóth, P. Domokos, H. Ritsch, and A. Vukics. Self-organization of atoms in a cavity field: Threshold, bistability, and scaling laws. *Phys. Rev. A*, 72:053417, Nov 2005.

[262] W. Niedenzu, T. Grießer, and H. Ritsch. Kinetic theory of cavity cooling and self-organisation of a cold gas. *Europhysics Letters*, 96(4):43001, nov 2011.

[263] Peter Kirton, Mor M. Roses, Jonathan Keeling, and Emanuele G. Dalla Torre. Introduction to the dicke model: From equilibrium to nonequilibrium, and vice versa. *Advanced Quantum Technologies*, 2(1-2):1800043, 2019.

[264] J. Vidal and S. Dusuel. Finite-size scaling exponents in the dicke model. *Europhysics Letters*, 74(5):817, may 2006.

[265] Qing-Hu Chen, Yu-Yu Zhang, Tao Liu, and Ke-Lin Wang. Numerically exact solution to the finite-size dicke model. *Phys. Rev. A*, 78:051801, Nov 2008.

[266] Matthias Wolke, Julian Klinner, Hans Keßler, and Andreas Hemmerich. Cavity cooling below the recoil limit. *Science*, 337(6090):75–78, 2012.

[267] Fabian H. L. Essler, Holger Frahm, Frank Göhmann, Andreas Klümper, and Vladimir E. Korepin. *The One-Dimensional Hubbard Model*. Cambridge University Press, 2005.

[268] Kevin C. Stitely, Andrus Giraldo, Bernd Krauskopf, and Scott Parkins. Nonlinear semiclassical dynamics of the unbalanced, open dicke model. *Phys. Rev. Res.*, 2:033131, Jul 2020.

[269] Thomas Fink, Anne Schade, Sven Höfling, Christian Schneider, and Ataç Imamoglu. Signatures of a dissipative phase transition in photon correlation measurements. *Nature Physics*, 14(4):365–369, Apr 2018.

[270] M. Foss-Feig, P. Niroula, J. T. Young, M. Hafezi, A. V. Gorshkov, R. M. Wilson, and M. F. Maghrebi. Emergent equilibrium in many-body optical bistability. *Phys. Rev. A*, 95:043826, Apr 2017.

[271] J. J. Mendoza-Arenas, S. R. Clark, S. Felicetti, G. Romero, E. Solano, D. G. Angelakis, and D. Jaksch. Beyond mean-field bistability in driven-dissipative lattices: Bunching-antibunching transition and quantum simulation. *Phys. Rev. A*, 93:023821, Feb 2016.

[272] Christoph Georges, Jayson G. Cosme, Ludwig Mathey, and Andreas Hemmerich. Light-induced coherence in an atom-cavity system. *Phys. Rev. Lett.*, 121:220405, Nov 2018.

[273] Christoph Georges, Jayson G. Cosme, Hans Keßler, Ludwig Mathey, and Andreas Hemmerich. Dynamical density wave order in an atom-cavity system. *arXiv:2003.14135*, 2021.

[274] Anton Mazurenko, Christie S. Chiu, Geoffrey Ji, Maxwell F. Parsons, Márton Kanász-Nagy, Richard Schmidt, Fabian Grusdt, Eugene Demler, Daniel Greif, and Markus Greiner. A cold-atom fermi–hubbard antiferromagnet. *Nature*, 545(7655):462–466, May 2017.

[275] Václav Janiš, Antonín Klíč, and Jiawei Yan. Antiferromagnetic fluctuations in the one-dimensional hubbard model. *AIP Advances*, 10(12), December 2020.

[276] Jacques des Cloizeaux and J. J. Pearson. Spin-wave spectrum of the antiferromagnetic linear chain. *Phys. Rev.*, 128:2131–2135, Dec 1962.

[277] F.H.L. Essler, H. Frahm, F. Göhmann, A. Klümper, and V. Korepin. *The One-Dimensional Hubbard Model*. Cambridge University Press, 2005.

[278] L. E. Sadler, J. M. Higbie, S. R. Leslie, M. Vengalattore, and D. M. Stamper-Kurn. Spontaneous symmetry breaking in a quenched ferromagnetic spinor bose–einstein condensate. *Nature*, 443(7109):312–315, September 2006.

[279] Junjiro Kanamori. Electron correlation and ferromagnetism of transition metals. *Progress of Theoretical Physics*, 30(3):275–289, 09 1963.

[280] Steven R. White. Density matrix formulation for quantum renormalization groups. *Phys. Rev. Lett.*, 69:2863–2866, Nov 1992.

[281] Jacek Dziarmaga. Dynamics of a quantum phase transition and relaxation to a steady state. *Advances in Physics*, 59(6):1063–1189, 2010.

[282] Federico Carollo, Antonio Lasanta, and Igor Lesanovsky. Exponentially accelerated approach to stationarity in markovian open quantum systems through the mpemba effect. *Phys. Rev. Lett.*, 127:060401, Aug 2021.

[283] Mattia Moroder, Oisín Culhane, Krissia Zawadzki, and John Goold. Thermodynamics of the quantum mpemba effect. *Phys. Rev. Lett.*, 133:140404, Oct 2024.

[284] Filiberto Ares, Pasquale Calabrese, and Sara Murciano. The quantum mpemba effects. *Nature Reviews Physics*, 07 2025.

[285] Katarzyna Macieszczak, M Guţă, Igor Lesanovsky, and Juan P. Garrahan. Towards a theory of metastability in open quantum dynamics. *Phys. Rev. Lett.*, 116:240404, Jun 2016.

[286] M. Rigol. Breakdown of thermalization in finite one-dimensional systems. *arXiv:0904.3746*, 2009.

[287] Simon J. D. Phoenix and P. L. Knight. Establishment of an entangled atom-field state in the jaynes-cummings model. *Phys. Rev. A*, 44:6023–6029, Nov 1991.

[288] V. Bužek and P.L. Knight. The origin of squeezing in a superposition of coherent states. *Optics Communications*, 81(5):331–336, 1991.

[289] George A. Baker and Peter Graves-Morris. *Padé Approximants*. Encyclopedia of Mathematics and its Applications. Cambridge University Press, 2 edition, 1996.